



Delft University of Technology

**Document Version**

Final published version

**Citation (APA)**

Karanth, P. (2025). *Optimizing Electrode-Electrolyte Interfaces in Lithium Batteries*. [Dissertation (TU Delft), Delft University of Technology]. <https://doi.org/10.4233/uuid:62918903-e42d-4d9a-9599-d0a1cfde3ef0>

**Important note**

To cite this publication, please use the final published version (if applicable).  
Please check the document version above.

**Copyright**

In case the licence states "Dutch Copyright Act (Article 25fa)", this publication was made available Green Open Access via the TU Delft Institutional Repository pursuant to Dutch Copyright Act (Article 25fa, the Taverne amendment). This provision does not affect copyright ownership.  
Unless copyright is transferred by contract or statute, it remains with the copyright holder.

**Sharing and reuse**

Other than for strictly personal use, it is not permitted to download, forward or distribute the text or part of it, without the consent of the author(s) and/or copyright holder(s), unless the work is under an open content license such as Creative Commons.

**Takedown policy**

Please contact us and provide details if you believe this document breaches copyrights.  
We will remove access to the work immediately and investigate your claim.

*This work is downloaded from Delft University of Technology.*

# **Optimizing Electrode-Electrolyte Interfaces in Lithium Batteries**

**Pranav Karanth**

# **Optimizing Electrode-Electrolyte Interfaces in Lithium Batteries**

**Pranav Karanth**

**2025**



# Optimizing Electrode-Electrolyte Interfaces in Lithium Batteries

## Dissertation

for the purpose of obtaining the degree of doctor

at Delft University of Technology

by the authority of the Rector Magnificus, prof. dr. ir. T.H.J.J. van der Hagen,

chair of the Board for Doctorates

to be defended publicly on

Tuesday 3 June 2025 at 10:00 o'clock

by

**Pranav KARANTH**

Master of Science in Sustainable Energy Technology,

Delft University of Technology, the Netherlands

born in Mangalore, India

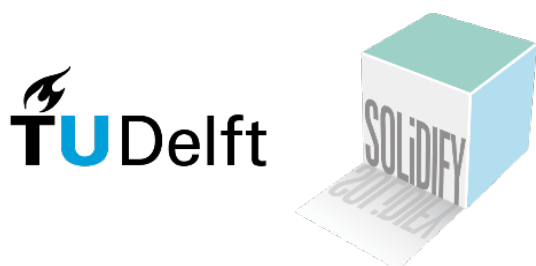
This dissertation has been approved by the promotor.

Composition of the doctoral committee:

Rector Magnificus,	chairperson
Prof. dr. F.M. Mulder	Delft University of Technology, <i>promotor</i>
Prof. dr. ir. M. Wagemaker	Delft University of Technology, <i>promotor</i>

*Independent members:*

Prof. dr. E. H. Brück	Delft University of Technology
Dr. E. M. Kelder	Delft University of Technology
Prof. dr. ir. M. Huijben	University of Twente
Prof. Dr. P. M. Vereecken	Katholieke Universiteit (KU) Leuven, Belgium
Dr. ir. Y. Xu	Aalto University, Finland
Prof. dr. A. J. Houtepen	Delft University of Technology, <i>reserve member</i>



The research presented in this thesis was performed at Materials for Energy Conversion and Storage (MECS) and Storage of Electrochemical Energy (SEE) groups, Faculty of Applied Sciences, Delft University of Technology, the Netherlands, and funded by the European Union's H2020 research and innovation program 'SOLiDIFY' project under grant agreement No. 875557.

**Keywords:** Lithium ion batteries, electrode-electrolyte interface, polymerized ionic liquid, solid-state batteries, NMR, XPS

*Printed by:* ProefschriftMaken | [www.proefschriftmaken.nl](http://www.proefschriftmaken.nl)

*Cover by:* Pranav Karanth. Artwork created using ChatGPT o3

Copyright © 2025 by P. Karanth

ISBN 000-00-0000-000-0

An electronic copy of this dissertation is available at

<https://repository.tudelft.nl/>.



# Contents

<b>1. Introduction</b> .....	<b>1</b>
1.1 The necessity of energy storage technologies.....	2
1.2 Lithium-ion batteries: past, present and future (challenges) .....	2
1.3 Electrode/Electrolyte interfaces and interphases in lithium batteries .....	4
1.3.1 The cathode/electrolyte interface.....	4
1.3.2 The lithium/electrolyte interface.....	6
1.4 Outline of this thesis.....	8
References.....	9
<b>2. A phase inversion strategy for low tortuosity, ultrahigh mass loading Nickel-rich layered oxide electrodes</b> .....	<b>15</b>
<b>Abstract</b> .....	<b>16</b>
<b>2.1 Introduction</b> .....	<b>17</b>
<b>2.2 Results</b> .....	<b>19</b>
2.2.1 Optimization of the phase inversion process for Ni-rich layered oxides .....	19
2.2.2 Changes to the electrode structure upon phase inversion and the effect of calendaring ...	20
2.2.3 Differences in electrochemical rate performance.....	23
2.2.4 Differences in the tortuosity factor .....	26
2.2.5 Long-term cycling performance .....	29
<b>2.3 Discussion</b> .....	<b>30</b>
<b>2.4 Experimental Procedures</b> .....	<b>33</b>
2.4.1 Electrode Manufacturing.....	33
2.4.2 Electrode Characterization .....	33
2.4.3 Electrochemical characterization .....	34
2.4.4 P2D Modelling.....	34
References .....	35
Supporting Information .....	41
<b>3. Multifunctional ion-conductive polymer coatings for high-performance sulfide solid-state batteries</b> .....	<b>57</b>
<b>Abstract</b> .....	<b>58</b>
<b>3.1 Introduction</b> .....	<b>59</b>
<b>3.2 Results and Discussion</b> .....	<b>60</b>
3.2.1 Materials selection and design for polymeric coatings on Ni-rich CAMs:.....	60
3.2.2 Surface Analysis of NMC82 with Polymeric Coatings .....	63
3.2.3 Electrochemical Cycling Performance .....	65
3.2.4 Effect on (electro)chemical stability .....	69

3.2.5 Effect on mechanical and structural stability .....	70
<b>3.3 Conclusions .....</b>	<b>72</b>
<b>3.4 Experimental Procedures.....</b>	<b>73</b>
3.4.1 Sample preparation .....	73
3.4.2 Electrochemical characterization .....	73
3.4.3 Surface and Bulk Characterization.....	74
<b>References .....</b>	<b>75</b>
<b>Supplementary Information .....</b>	<b>82</b>
<b>4. Understanding the effect of salt concentration on the Li metal interface in gel polymer electrolytes .....</b>	<b>97</b>
Abstract .....	98
4.1 Introduction.....	99
4.2 System Definition .....	100
4.3 Electrochemical Performance .....	101
4.4 Differences at the Li interface with initial (formation) cycling:.....	102
4.4.1 Charge transfer kinetics.....	102
4.4.2 SEI Composition.....	104
4.4.3 Lithium morphology evolution .....	106
4.5 Lithium interface evolution with extended cycling.....	109
4.6 Conclusion .....	113
4.7 Experimental Procedures .....	115
4.7.1 PIL separator synthesis.....	115
4.7.2 Cell assembly and electrochemical characterization.....	115
4.7.3 SEI Characterization.....	115
4.7.4 Operando NMR.....	116
4.7.5 Li density and morphology characterization .....	116
<b>References .....</b>	<b>118</b>
<b>Supplementary Information .....</b>	<b>123</b>
<b>5. Rational design of safe, fluorine-free dual salt electrolytes for Lithium metal batteries.....</b>	<b>133</b>
Abstract .....	134
5.1 Introduction.....	135
<b>5.2 Results and discussion .....</b>	<b>137</b>
5.2.1 Choice of salts, solvents and salt concentration.....	137
5.2.2 Lithium plating/stripping in Li/Li and Li/Cu cells.....	142
5.2.3 Effect of salt ratios on SEI composition and Li microstructure .....	145
5.2.4 Electrochemical performance in half and full cells.....	148

5.3 Conclusions .....	150
5.4 Experimental Details.....	150
5.4.1 Electrolyte preparation.....	150
5.4.2 Electrolyte characterization.....	150
5.4.3 Cell assembly and electrochemical characterization.....	152
5.4.4 Li interface characterization .....	153
References.....	153
Supplementary Information .....	161
<b>Summary .....</b>	<b>167</b>
<b>Samenvatting .....</b>	<b>170</b>
<b>Acknowledgements.....</b>	<b>174</b>
<b>List of Publications .....</b>	<b>178</b>
<b>Curriculum Vitae .....</b>	<b>181</b>

# 1. Introduction

### 1.1 The necessity of energy storage technologies

Human-caused climate change is one of the most critical and complex challenges facing humanity today<sup>1</sup>. To address its impact, it is essential to reduce global carbon dioxide (CO<sub>2</sub>) emissions in accordance with the Paris Agreement, which sets an ambitious goal of limiting global temperature rise to 1.5°C above pre-industrial levels<sup>2</sup>. This, however, coincides with a growing global energy demand, particularly from the developing nations. As these countries continue to urbanize and improve their living standards,<sup>3</sup> the need for sustainable energy technologies becomes even more crucial.

Transport and electricity generation are the two main sectors where the shift from fossil fuels to sustainable energy must occur. For these sectors, energy storage—primarily through battery technologies—is expected to play a pivotal role in facilitating this transition. The concept of battery-powered vehicles is far from new. In fact, some of the earliest passenger cars, dating back to the late 19th/early 20th centuries, were powered by rechargeable batteries.<sup>4</sup> However, with the advent of gasoline/ diesel engines that offered higher volumetric/gravimetric energy densities and faster refuel times, they eventually became the dominant technology. Today, with the development of lithium-ion batteries and the urgent need to reduce CO<sub>2</sub> emissions, the automotive landscape is shifting dramatically. Governments around the world have introduced comprehensive plans to encourage the widespread adoption of electric vehicles (EVs), with many setting ambitious targets for phasing out gasoline/diesel-powered cars over the next 10-20 years.<sup>5,6</sup> This transition would mark an important step towards achieving a sustainable, low-carbon future.

The need for energy storage is equally important for electricity grids of the future, which will increasingly depend on renewable sources such as solar and wind power. Both these energy sources, while sustainable, are known for their intermittency. Addressing this challenge requires different storage solutions for short-term (diurnal) and long-term (seasonal) energy needs.<sup>7</sup> For short-term storage, in particular, systems that can be turned on and off on very short timescales are essential, and rechargeable batteries are again at the forefront of options available in this regard.

### 1.2 Lithium-ion batteries: past, present and future (challenges)

The motivation for using Lithium in batteries came from the fact that lithium is the most electropositive (-3.04V vs the standard hydrogen electrode) and the lightest metal (density = 0.53 g/cc) in the periodic table, which would lead to high energy densities.<sup>8</sup> The first rechargeable Lithium-ion battery was reported by Prof. Stanley Whittingham in the 1970s with Li metal as the negative electrode, lithium perchlorate (LiClO<sub>4</sub>) in Dioxolane (DOL) as the electrolyte, and TiS<sub>2</sub>, a layered Sulfide material as the positive electrode.<sup>9</sup> The Lithium metal, however, owing to its safety concerns and poor cyclability, eventually gave way to Graphite as the negative electrode of choice<sup>10,11</sup>, while the TiS<sub>2</sub> was replaced by better-performing layered oxide materials (such as LiCoO<sub>2</sub><sup>12</sup> and LiNi<sub>x</sub>Mn<sub>y</sub>Co<sub>1-x-y</sub>O<sub>2</sub><sup>13</sup>) as the positive electrode of choice, and these two classes of materials continue to be the mainstay of state-of-the-art

lithium-ion batteries to this day. Further, the search for 'greener' materials with easier-to-source transition metals and improved cycle life led to the development of olivine type  $\text{LiFePO}_4$ , which has also made its mark as an alternative positive electrode material for batteries focussed more on durability and less on cell-level energy density.

Going forward, three main challenges can be identified for current Li-ion batteries, i.e.

- a) **Increasing the cell/pack level energy density:** The increase towards higher cell/pack level energy densities is mainly driven by applications such as the automotive sector, where an increase in the current pack level energy densities of 100-150 Wh/kg to >250 Wh/kg is strongly desired<sup>14,15</sup> in order to improve the adoption rate of electric vehicles. Several options often discussed in this regard include the use of higher energy density materials as negative electrodes (with a strong focus on Li metal and silicon), increasing the thickness of electrodes, reducing the electrode porosity, reducing the amount of inactive components per cell etc.<sup>16</sup> Of these, while a switch to Li metal and increasing the electrode thickness hold great promise, several challenges need to be addressed, particularly at the electrode-electrolyte interface, which will be discussed further.
- b) **Improving battery safety:** Battery safety has remained a major barrier to the adoption of Lithium-ion batteries in the automotive and grid storage sectors. The state-of-the-art Lithium-ion batteries employ carbonates such as dimethyl carbonate (DMC) and ethyl methyl carbonate (EMC) as solvents, which typically have low flash and boiling points, and are easily susceptible to thermal runaways caused by overcharging, heat exposure, internal short circuits etc., which can result in electrolyte decomposition, followed by enormous heat/gas release and fires.<sup>17</sup>  
In this respect, solid-state electrolytes, both inorganic and polymer-based, known to possess much higher thermal stabilities, present a potentially safer alternative.<sup>18</sup> However, these electrolytes also suffer from chemomechanical issues at the electrode/electrolyte interfaces, even more so than their liquid counterparts owing to the solid/solid interfaces, prone to contact loss with successive cycling due to the volume changes induced.<sup>19</sup>
- c) **Greener batteries:** State-of-the-art Li-ion batteries have several chemical components and manufacturing methods that do not adhere to the twelve principles of Green chemistry.<sup>20</sup> These include the use of toxic materials such as LCO and NMC as electrode materials<sup>21</sup>, the use of fluorinated compounds in electrolytes and binders,<sup>22</sup> and the use of toxic solvents such as N-methyl pyrrolidone (NMP) in the manufacture and recycling of these electrodes.<sup>23</sup> Among the proposed measures towards greener lithium batteries, the elimination of fluorinated, or specifically Per- and poly-fluoroalkyl substances (PFAS) is gaining significant research and commercial interest, partly driven by the proposed ban on the use of PFAS materials in the EU.<sup>24</sup> It is, however, important to recognize the vital role currently played by fluorinated/PFAS compounds in achieving appreciable long-term performance in current batteries,

particularly by stabilizing the electrode-electrolyte interfaces. Any redesign/replacement strategy targeting the elimination of fluorine would, therefore, have to pay close attention to its effects on the stability of the electrode/electrolyte interfaces.

## 1.3 Electrode/Electrolyte interfaces and interphases in lithium batteries

### 1.3.1 The cathode/electrolyte interface

The cathode-electrolyte interface in both liquid electrolyte-based and solid-state batteries presents a complex system that can be studied across multiple scales—namely, the mesoscale, particle scale, and nanoscale. At the mesoscale, the primary focus is on understanding the ion and electron percolation networks through the cathode composite (i.e. cathode in contact with electrolyte). At the particle scale, research is mainly focused towards studying the contact between the active material and the electrolyte and/or the conductive binder domain (CBD), and examining how these evolve over time. Finally, at the nanoscale, the interfacial stability between the cathode active material (CAM) and the electrolyte, both chemically and electrochemically, becomes critical.

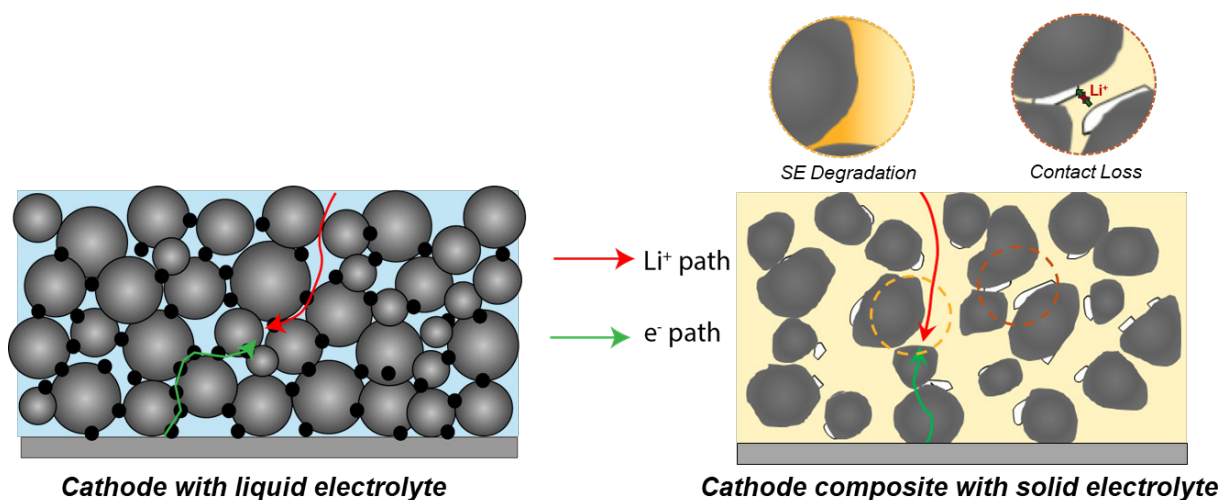


**Figure 1:** A comparison of cathode-electrolyte composites in liquid and solid electrolyte systems. Lithium ion pathways are indicated in red and electronic pathways are indicated in green

For liquid-electrolyte-based systems, where a lot of optimization has already been carried out at the CEI and particle levels, there is considerable interest in increasing the thickness of electrodes and improving the cell/pack level energy densities, as previously suggested. However, doing so using conventional fabrication methods results in further performance limitations, mainly due to the **poor ionic conduction through the electrolyte** in the tortuous porous network (Figure 1) and the higher **electronic resistance** due to the increasing electrode thickness<sup>25</sup>. Of the two, the former is typically considered the bigger limitation for

## 1. Introduction

thick electrodes.<sup>26,27</sup> Producing NMC-based Li-ion batteries with high energy density that do not compromise on the fast charging aspirations can, therefore, be very challenging.

Producing high mass loading electrode architectures that can enable good electrolyte infiltration requires a low resistance to electrolyte diffusivity through the network, and a measure of this given by the **Macmullin number**,  $N_M$

$$N_M = \frac{\tau}{\varepsilon} = \frac{D_0}{D_{eff}} = \frac{K_0}{K_{eff}}$$

where  $D_0$  = diffusion coefficient of the pure electrolyte,  $K_0$  = conductivity of the pure electrolyte,  $D_{eff}$  and  $K_{eff}$  are their corresponding “effective” values in the porous network,  $\varepsilon$  = Porosity,  $\tau$  = Tortuosity factor<sup>28</sup>

The two parameters that can be controlled to reduce the Macmullin number are **porosity and tortuosity**. For battery electrodes, there is generally an optimum with respect to porosity and an increase beyond this value would result in reduced overall conductivity, as the electronic conductivity keeps decreasing with increase in porosity<sup>29</sup>. Further, the practical porosities of electrodes can tend to be lower than this value in view of obtaining reasonable volumetric energy density values; after all, there is no active material in the pores. It is, therefore, desirable to have a minimal, optimized porosity with a reduced Tortuosity Factor, the measure of tortuousness of the porous network, to obtain electrodes with a better rate performance.

In comparison, the cathode/electrolyte interface in solid-state batteries has a relatively higher degree of challenges at the particle and CEI levels in addition to those at the mesoscale.<sup>30</sup> Here, the particle size and distribution of CAM and SE influence the percolation pathways, affecting the tortuosity and, thereby, effective ionic/electronic conductivity. Further, the ratio between CAM and SE could also be tuned to optimize these conductivities.<sup>31</sup>

At the particle level, the chemomechanics of volume change/pressure evolution and subsequent void formation/cracking become important for cathode design. Interparticle cracking and voids at the CAM-SE interface increase resistance (Figure 1), which occurs to a lesser extent with liquids as they can penetrate into voids/cracks and re-establish contact.

At the CEI level, oxidative SE decomposition (Figure 1) and the formation of an unstable, poorly conducting CEI must be avoided. These aspects can be dependent on the composition of the solid electrolyte used; while oxide and halide-based are relatively stable against high-voltage cathode materials, sulfides, otherwise known for their high ionic conductivities and ease of processability, are highly prone to oxidation against high-voltage cathodes.<sup>32</sup> Artificial coatings, both inorganic and organic, have been applied to overcome this challenge, but designing coatings that can also address the other concerns (contact loss,  $\text{Li}^+$  conduction) related to the SE-cathode interface can be challenging, as discussed further in Chapter 3.

### 1.3.2 The lithium/electrolyte interface

Enabling long-term reversible plating/stripping of Lithium metal in batteries at high current densities has remained one of the greatest challenges. The tendency of Li metal to form dendrites is well known, and several possible strategies to alleviate this phenomenon and improve cycle life have been and are still being proposed<sup>33</sup>. When it comes to solid electrolytes, the set of challenges to overcome is arguably much bigger as summarized in Figure 2 below<sup>34</sup>. While the picture specifically refers to inorganic SEs, these challenges also hold true for other types such as gel polymer electrolytes studied in this thesis.

In terms of **interface stability**, almost all solid electrolytes tend to become reduced electrochemically by Lithium, and often produce a multicomponent solid electrolyte interphase (SEI) both in terms of depth and cross section. This interphase would ideally have to be of low impedance to enable facile **ion transport**, and of self-limiting nature in terms of growth over time, but this is often not the case<sup>34</sup>.

Other than the interface stability and kinetics, the other major challenge, as already noted, is the mechanics of Li plating and stripping in contact with the solid electrolyte. With liquid electrolytes, the limiting conditions for Li plating have previously been described in terms of limiting current and Sand's time<sup>35</sup> and the mosaic like SEI structure leading to nonhomogeneous electric fields is known to result in **dendrite formation** at currents and times lower than the limiting values<sup>33</sup>. Li dendrites can still happen under limiting conditions in Inorganic SEs along the grain boundaries, and solid polymer or gel polymer electrolytes may perform better in this aspect, depending on the Young modulus and the nature of the porous structure (nano-mesoporous) of these systems.

But with solid electrolytes, an even bigger limitation on current densities could be imposed due to **void formation** during Lithium stripping. Lithium, being a soft metal, is known to display creep deformation behaviour when subjected to stresses below the yield strength value<sup>36</sup>. As it turns out, the rate of Li replenishment at the surface of Li metal is more dependent on the creep rather than the Lithium diffusion, and voids are formed on the metal surface whenever the rate of Li migration due to the stripping current is greater than the rate of replenishment due to the creep and the diffusion, i.e. when  $J_{\text{migration}} > J_{\text{creep}} + J_{\text{diffusion}}$ <sup>36</sup>. This results in loss of contact area between the metal anode and the electrolyte, resulting in increased local current densities.

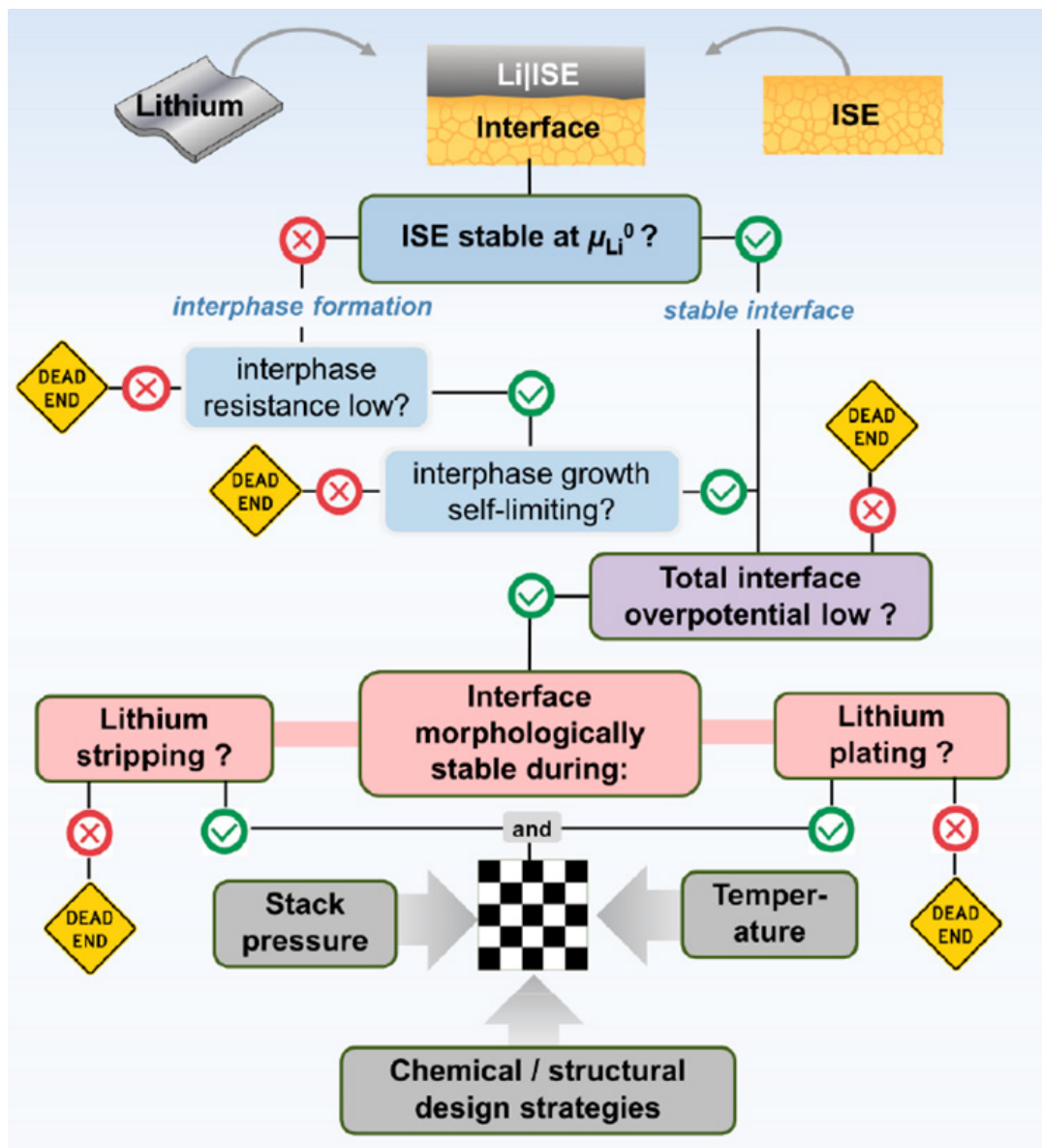


**Figure 2:** Illustration of Li metal anode – solid electrolyte interface challenges with solid electrolytes. Reprinted with permission from Reference 34, © 2020 American Chemical Society

A common approach to overcome this has been to increase the stack pressure of the cell, as this results in a greater Li creep and greater replenishment<sup>37</sup>. Parameters such as critical stack pressure have also been proposed for inorganic solid electrolytes to overcome void formation<sup>38</sup>. However, for gel polymer electrolytes, the use of high pressures could also have implications in terms of mechanical integrity, and it is therefore important to find solutions complementary to this approach.

While several works have focused on constructing artificial SEI with desirable ion conducting and mechanical properties<sup>39</sup>, a more popular approach that has worked quite well is tuning the salt concentration/solvation structure to generate an SEI that has the right balance of inorganic/organic components and provides both (electro)chemical and mechanical stability.<sup>40</sup> While a high salt concentration either throughout the electrolyte<sup>41</sup> or locally<sup>42</sup>, is

known to result in dense Li plating with large grain size, recent works advocate for moderate salt concentrations, which could result in both dense Li plating and sufficient area coverage.<sup>43</sup> In contrast, the effect of salt concentration on the chemomechanics of Li plating /stripping remains underexplored for gel polymer electrolytes.

A common feature of the above approach is the use of Fluorinated compounds (salts, solvents, cosolvents) to generate a LiF-containing SEI, and the improved electrochemical performance is typically attributed to the LiF content/structure in the SEI. However, increasing evidence suggests that LiF may not be playing a direct role in Li conduction through the SEI<sup>44,45</sup>, and other SEI components such as Li<sub>2</sub>O show a stronger correlation with Li plating/stripping coulombic efficiency<sup>46</sup>. The design of Fluorine-free electrolytes for Li metal batteries, is, therefore, an interesting proposition, given the EU-wide push towards 'greener' energy storage and conversion systems.

### 1.4 Outline of this thesis

As discussed so far, optimizing electrode/electrolyte interfaces holds the key to designing next-generation Lithium batteries. This thesis aims at studying and optimizing key aspects and bottlenecks both at the cathode electrolyte interface and anode/electrolyte interface for different battery chemistries/configurations.

**Chapter 2** looks at the non-solvent-induced phase inversion as a simple yet effective technique to lower the tortuosity of thick Ni-rich layered oxide (NMC811 in this case) electrodes. Here the exchange of solvent NMP with a non-solvent benign to Ni-rich electrodes (ethanol) is shown to result in an alteration to the CBD structure, which lowers the tortuosity factor for these electrodes (as evidenced by electrochemical tortuosity measurements and modelling) and results in significantly improved performances for the phase inversion based electrodes at high mass loadings (7 mAh/cm<sup>2</sup> and higher) compared to the conventionally made electrodes.

**Chapter 3** looks at the cathode/electrolyte interface in sulfide (Li<sub>6</sub>PS<sub>5</sub>Cl) based solid state batteries, where performance degradation of the cathode composite with Ni-rich NMC82 (LiNi<sub>0.82</sub>Mn<sub>0.07</sub>Co<sub>0.11</sub>O<sub>2</sub>) as the CAM can occur due to contact loss and (electro)chemical degradation of the SE at the interface as discussed earlier. Here, Li-salt-containing polymerized ionic liquids (PILs) are proposed as multifunctional cathode coatings to alleviate these challenges. While PILs can buffer volume change in such systems as shown in this work and in previous works<sup>47</sup>, the Li salt containing PIL (Li-PIL) is also shown to improve Li<sup>+</sup> conduction over the SE/NMC82 interface, as evidenced by 2D exchange NMR and electrochemical impedance spectroscopy (EIS) measurements, which results in both improved discharge capacities and higher capacity retention.

**Chapters 4 and 5** focus on the interface of Li metal anode with a gel polymer electrolyte and fluorine-free liquid electrolyte respectively. In **Chapter 4**, the focus is on studying the effect of salt concentration (i.e. of LiFSI) in the polymer host and its effects on SEI composition and

## 1. Introduction

Li morphology. Here, ex-situ characterization results (SEM, XPS, ssNMR, NDP) are combined with operando techniques (NMR, NDP) to understand the evolution of Li metal with cycling, and the results provide an explanation as to why intermediate salt concentrations results in the best coulombic efficiencies and capacity retentions for these systems.

Finally, in **Chapter 5**, a fluorine-free electrolyte based on LiNO<sub>3</sub> and LiBOB salts is designed for Li metal batteries, with a focus on understanding the effect of salt ratios on the Li metal morphology, the SEI composition, and their impact on the long-term cycling of Li metal. Here the two salts show synergistic effects, particularly at equimolar salt concentrations, on both the ionic conductivity and the Li metal/electrolyte interface, which results in good capacity retention in Li/Li symmetric cells, Li/LFP half cells and Li/LFP full cells, establishing the dual salt approach as a viable pathway towards fluorine-free Lithium metal batteries.

## References

- (1) *AR5 Climate Change 2014: Impacts, Adaptation, and Vulnerability — IPCC*. <https://www.ipcc.ch/report/ar5/wg2/> (accessed 2024-09-15).
- (2) *The Paris Agreement | UNFCCC*. <https://unfccc.int/process-and-meetings/the-paris-agreement> (accessed 2024-09-15).
- (3) Vanegas Cantarero, M. M. Of Renewable Energy, Energy Democracy, and Sustainable Development: A Roadmap to Accelerate the Energy Transition in Developing Countries. *Energy Res. Soc. Sci.* **2020**, *70*, 101716. <https://doi.org/10.1016/j.erss.2020.101716>.
- (4) Høyer, K. G. The History of Alternative Fuels in Transportation: The Case of Electric and Hybrid Cars. *Util. Policy* **2008**, *16* (2), 63–71. <https://doi.org/10.1016/j.jup.2007.11.001>.
- (5) *EU deal to end sale of new CO2 emitting cars by 2035*. European Commission - European Commission. [https://ec.europa.eu/commission/presscorner/detail/en/ip\\_22\\_6462](https://ec.europa.eu/commission/presscorner/detail/en/ip_22_6462) (accessed 2024-09-15).
- (6) *C: Electric Vehicles*. Guide to Chinese Climate Policy. <https://chineseclimatepolicy.oxfordenergy.org/book-content/domestic-policies/vehicles/electric-vehicles/> (accessed 2024-09-15).
- (7) Mulder, F. M. Implications of Diurnal and Seasonal Variations in Renewable Energy Generation for Large Scale Energy Storage. *J. Renew. Sustain. Energy* **2014**, *6* (3), 033105. <https://doi.org/10.1063/1.4874845>.
- (8) Tarascon, J.-M.; Armand, M. Issues and Challenges Facing Rechargeable Lithium Batteries. *Nature* **2001**, *414* (6861), 359–367. <https://doi.org/10.1038/35104644>.
- (9) Whittingham, M. S. Electrical Energy Storage and Intercalation Chemistry. *Science* **1976**, *192* (4244), 1126–1127. <https://doi.org/10.1126/science.192.4244.1126>.

## 1. Introduction

(10) Mohri, M.; Yanagisawa, N.; Tajima, Y.; Tanaka, H.; Mitate, T.; Nakajima, S.; Yoshida, M.; Yoshimoto, Y.; Suzuki, T.; Wada, H. Rechargeable Lithium Battery Based on Pyrolytic Carbon as a Negative Electrode. *J. Power Sources* **1989**, *26* (3), 545–551. [https://doi.org/10.1016/0378-7753\(89\)80176-4](https://doi.org/10.1016/0378-7753(89)80176-4).

(11) Ozawa, K. Lithium-Ion Rechargeable Batteries with LiCoO<sub>2</sub> and Carbon Electrodes: The LiCoO<sub>2</sub>/C System. *Solid State Ion.* **1994**, *69* (3), 212–221. [https://doi.org/10.1016/0167-2738\(94\)90411-1](https://doi.org/10.1016/0167-2738(94)90411-1).

(12) Mizushima, K.; Jones, P. C.; Wiseman, P. J.; Goodenough, J. B. Li<sub>x</sub>CoO<sub>2</sub> (0 < x < 1): A New Cathode Material for Batteries of High Energy Density. *Mater. Res. Bull.* **1980**, *15* (6), 783–789. [https://doi.org/10.1016/0025-5408\(80\)90012-4](https://doi.org/10.1016/0025-5408(80)90012-4).

(13) Lu, Z.; Beaulieu, L. Y.; Donaberger, R. A.; Thomas, C. L.; Dahn, J. R. Synthesis, Structure, and Electrochemical Behavior of Li [ Ni<sub>x</sub>Li<sub>1/3 - 2x/3</sub>Mn<sub>2/3 - x/3</sub> ] O<sub>2</sub>. *J. Electrochem. Soc.* **2002**, *149* (6), A778. <https://doi.org/10.1149/1.1471541>.

(14) Masias, A.; Marcicki, J.; Paxton, W. A. Opportunities and Challenges of Lithium Ion Batteries in Automotive Applications. *ACS Energy Lett.* **2021**, *6* (2), 621–630. <https://doi.org/10.1021/acsenergylett.0c02584>.

(15) Frith, J. T.; Lacey, M. J.; Ulissi, U. A Non-Academic Perspective on the Future of Lithium-Based Batteries. *Nat. Commun.* **2023**, *14* (1), 420. <https://doi.org/10.1038/s41467-023-35933-2>.

(16) Liu, J.; Bao, Z.; Cui, Y.; Dufek, E. J.; Goodenough, J. B.; Khalifah, P.; Li, Q.; Liaw, B. Y.; Liu, P.; Manthiram, A.; Meng, Y. S.; Subramanian, V. R.; Toney, M. F.; Viswanathan, V. V.; Whittingham, M. S.; Xiao, J.; Xu, W.; Yang, J.; Yang, X.-Q.; Zhang, J.-G. Pathways for Practical High-Energy Long-Cycling Lithium Metal Batteries. *Nat. Energy* **2019**, *4* (3), 180–186. <https://doi.org/10.1038/s41560-019-0338-x>.

(17) Duan, J.; Tang, X.; Dai, H.; Yang, Y.; Wu, W.; Wei, X.; Huang, Y. Building Safe Lithium-Ion Batteries for Electric Vehicles: A Review. *Electrochem. Energy Rev.* **2020**, *3* (1), 1–42. <https://doi.org/10.1007/s41918-019-00060-4>.

(18) Janek, J.; Zeier, W. G. A Solid Future for Battery Development. *Nat. Energy* **2016**, *1* (9), 1–4. <https://doi.org/10.1038/nenergy.2016.141>.

(19) Janek, J.; Zeier, W. G. Challenges in Speeding up Solid-State Battery Development. *Nat. Energy* **2023**, *8* (3), 230–240. <https://doi.org/10.1038/s41560-023-01208-9>.

(20) Anastas, P.; Eghbali, N. Green Chemistry: Principles and Practice. *Chem. Soc. Rev.* **2010**, *39* (1), 301–312. <https://doi.org/10.1039/B918763B>.

(21) Mroziak, W.; Ali Rajaeifar, M.; Heidrich, O.; Christensen, P. Environmental Impacts, Pollution Sources and Pathways of Spent Lithium-Ion Batteries. *Energy Environ. Sci.* **2021**, *14* (12), 6099–6121. <https://doi.org/10.1039/D1EE00691F>.

## 1. Introduction

(22) Rensmo, A.; Savidou, E. K.; Cousins, I. T.; Hu, X.; Schellenberger, S.; Benskin, J. P. Lithium-Ion Battery Recycling: A Source of per- and Polyfluoroalkyl Substances (PFAS) to the Environment? *Environ. Sci. Process. Impacts* **2023**, *25* (6), 1015–1030. <https://doi.org/10.1039/D2EM00511E>.

(23) Dühnen, S.; Betz, J.; Kolek, M.; Schmuch, R.; Winter, M.; Placke, T. Toward Green Battery Cells: Perspective on Materials and Technologies. *Small Methods* **2020**, *4* (7), 2000039. <https://doi.org/10.1002/smt.202000039>.

(24) *Registry of restriction intentions until outcome - ECHA*. <https://echa.europa.eu/registry-of-restriction-intentions/-/dislist/details/0b0236e18663449b> (accessed 2024-08-23).

(25) Kremer, L. S.; Hoffmann, A.; Danner, T.; Hein, S.; Prifling, B.; Westhoff, D.; Dreer, C.; Latz, A.; Schmidt, V.; Wohlfahrt-Mehrens, M. Manufacturing Process for Improved Ultra-Thick Cathodes in High-Energy Lithium-Ion Batteries. *Energy Technol.* **2020**, *8* (2), 1900167. <https://doi.org/10.1002/ente.201900167>.

(26) Gao, H.; Wu, Q.; Hu, Y.; Zheng, J. P.; Amine, K.; Chen, Z. Revealing the Rate-Limiting Li-Ion Diffusion Pathway in Ultrathick Electrodes for Li-Ion Batteries. *J. Phys. Chem. Lett.* **2018**, *9* (17), 5100–5104. <https://doi.org/10.1021/acs.jpcclett.8b02229>.

(27) Weiss, M.; Ruess, R.; Kasnatscheew, J.; Levartovsky, Y.; Levy, N. R.; Minnmann, P.; Stolz, L.; Waldmann, T.; Wohlfahrt-Mehrens, M.; Aurbach, D.; Winter, M.; Ein-Eli, Y.; Janek, J. Fast Charging of Lithium-Ion Batteries: A Review of Materials Aspects. *Adv. Energy Mater.* **2021**, *11* (33), 2101126. <https://doi.org/10.1002/aenm.202101126>.

(28) Nguyen, T.-T.; Demortière, A.; Fleutot, B.; Delobel, B.; Delacourt, C.; Cooper, S. J. The Electrode Tortuosity Factor: Why the Conventional Tortuosity Factor Is Not Well Suited for Quantifying Transport in Porous Li-Ion Battery Electrodes and What to Use Instead. *Npj Comput. Mater.* **2020**, *6* (1), 1–12. <https://doi.org/10.1038/s41524-020-00386-4>.

(29) Fongy, C.; Gaillot, A.-C.; Jouanneau, S.; Guyomard, D.; Lestriez, B. Ionic vs Electronic Power Limitations and Analysis of the Fraction of Wired Grains in LiFePO<sub>4</sub> Composite Electrodes. *J. Electrochem. Soc.* **2010**, *157* (7), A885. <https://doi.org/10.1149/1.3432559>.

(30) Minnmann, P.; Strauss, F.; Bielefeld, A.; Ruess, R.; Adelhelm, P.; Burkhardt, S.; Dreyer, S. L.; Trevisanetto, E.; Ehrenberg, H.; Brezesinski, T.; Richter, F. H.; Janek, J. Designing Cathodes and Cathode Active Materials for Solid-State Batteries. *Adv. Energy Mater.* **2022**, *12* (35), 2201425. <https://doi.org/10.1002/aenm.202201425>.

(31) Minnmann, P.; Quillman, L.; Burkhardt, S.; Richter, F. H.; Janek, J. Editors' Choice—Quantifying the Impact of Charge Transport Bottlenecks in Composite Cathodes of All-Solid-State Batteries. *J. Electrochem. Soc.* **2021**, *168* (4), 040537. <https://doi.org/10.1149/1945-7111/abf8d7>.

## 1. Introduction

(32) Walther, F.; Koerver, R.; Fuchs, T.; Ohno, S.; Sann, J.; Rohnke, M.; Zeier, W. G.; Janek, J. Visualization of the Interfacial Decomposition of Composite Cathodes in Argyrodite-Based All-Solid-State Batteries Using Time-of-Flight Secondary-Ion Mass Spectrometry. *Chem. Mater.* **2019**, *31* (10), 3745–3755. <https://doi.org/10.1021/acs.chemmater.9b00770>.

(33) Lin, D.; Liu, Y.; Cui, Y. Reviving the Lithium Metal Anode for High-Energy Batteries. *Nat. Nanotechnol.* **2017**, *12* (3), 194–206. <https://doi.org/10.1038/nnano.2017.16>.

(34) Krauskopf, T.; Richter, F. H.; Zeier, W. G.; Janek, J. Physicochemical Concepts of the Lithium Metal Anode in Solid-State Batteries. *Chem. Rev.* **2020**. <https://doi.org/10.1021/acs.chemrev.0c00431>.

(35) Brissot, C.; Rosso, M.; Chazalviel, J.-N.; Lascaud, S. Dendritic Growth Mechanisms in Lithium/Polymer Cells. *J. Power Sources* **1999**, *81–82*, 925–929. [https://doi.org/10.1016/S0378-7753\(98\)00242-0](https://doi.org/10.1016/S0378-7753(98)00242-0).

(36) Kasemchainan, J.; Zekoll, S.; Spencer Jolly, D.; Ning, Z.; Hartley, G. O.; Marrow, J.; Bruce, P. G. Critical Stripping Current Leads to Dendrite Formation on Plating in Lithium Anode Solid Electrolyte Cells. *Nat. Mater.* **2019**, *18* (10), 1105–1111. <https://doi.org/10.1038/s41563-019-0438-9>.

(37) Krauskopf, T.; Hartmann, H.; Zeier, W. G.; Janek, J. Toward a Fundamental Understanding of the Lithium Metal Anode in Solid-State Batteries—An Electrochemo-Mechanical Study on the Garnet-Type Solid Electrolyte Li<sub>6</sub>.<sub>25</sub>Al<sub>0.25</sub>La<sub>3</sub>Zr<sub>2</sub>O<sub>12</sub>. *ACS Appl. Mater. Interfaces* **2019**, *11* (15), 14463–14477. <https://doi.org/10.1021/acsami.9b02537>.

(38) Wang, M. J.; Choudhury, R.; Sakamoto, J. Characterizing the Li-Solid-Electrolyte Interface Dynamics as a Function of Stack Pressure and Current Density. *Joule* **2019**, *3* (9), 2165–2178. <https://doi.org/10.1016/j.joule.2019.06.017>.

(39) Tu, Z.; Choudhury, S.; Zachman, M. J.; Wei, S.; Zhang, K.; Kourkoutis, L. F.; Archer, L. A. Designing Artificial Solid-Electrolyte Interphases for Single-Ion and High-Efficiency Transport in Batteries. *Joule* **2017**, *1* (2), 394–406. <https://doi.org/10.1016/j.joule.2017.06.002>.

(40) Chen, Y.; Li, M.; Liu, Y.; Jie, Y.; Li, W.; Huang, F.; Li, X.; He, Z.; Ren, X.; Chen, Y.; Meng, X.; Cheng, T.; Gu, M.; Jiao, S.; Cao, R. Origin of Dendrite-Free Lithium Deposition in Concentrated Electrolytes. *Nat. Commun.* **2023**, *14* (1), 2655. <https://doi.org/10.1038/s41467-023-38387-8>.

(41) Qian, J.; Henderson, W. A.; Xu, W.; Bhattacharya, P.; Engelhard, M.; Borodin, O.; Zhang, J.-G. High Rate and Stable Cycling of Lithium Metal Anode. *Nat. Commun.* **2015**, *6* (1), 6362. <https://doi.org/10.1038/ncomms7362>.

(42) Cao, X.; Jia, H.; Xu, W.; Zhang, J.-G. Review—Localized High-Concentration Electrolytes for Lithium Batteries. *J. Electrochem. Soc.* **2021**, *168* (1), 010522. <https://doi.org/10.1149/1945-7111/abd60e>.

## 1. Introduction

(43) Wang, Q.; Zhao, C.; Wang, S.; Wang, J.; Liu, M.; Ganapathy, S.; Bai, X.; Li, B.; Wagemaker, M. Clarifying the Relationship between the Lithium Deposition Coverage and Microstructure in Lithium Metal Batteries. *J. Am. Chem. Soc.* **2022**, *144* (48), 21961–21971. <https://doi.org/10.1021/jacs.2c08849>.

(44) Huang, W.; Wang, H.; Boyle, D. T.; Li, Y.; Cui, Y. Resolving Nanoscopic and Mesoscopic Heterogeneity of Fluorinated Species in Battery Solid-Electrolyte Interphases by Cryogenic Electron Microscopy. *ACS Energy Lett.* **2020**, *5* (4), 1128–1135. <https://doi.org/10.1021/acsenergylett.0c00194>.

(45) Surace, Y.; Leanza, D.; Mirolo, M.; Kondracki, Ł.; Vaz, C. A. F.; El Kazzi, M.; Novák, P.; Trabesinger, S. Evidence for Stepwise Formation of Solid Electrolyte Interphase in a Li-Ion Battery. *Energy Storage Mater.* **2022**, *44*, 156–167. <https://doi.org/10.1016/j.ensm.2021.10.013>.

(46) Hobold, G. M.; Wang, C.; Steinberg, K.; Li, Y.; Gallant, B. M. High Lithium Oxide Prevalence in the Lithium Solid–Electrolyte Interphase for High Coulombic Efficiency. *Nat. Energy* **2024**, *9* (5), 580–591. <https://doi.org/10.1038/s41560-024-01494-x>.

(47) Shi, B.-X.; Yusim, Y.; Sen, S.; Demuth, T.; Ruess, R.; Volz, K.; Henss, A.; Richter, F. H. Mitigating Contact Loss in Li6PS5Cl-Based Solid-State Batteries Using a Thin Cationic Polymer Coating on NCM. *Adv. Energy Mater.* **2023**, *13* (24), 2300310. <https://doi.org/10.1002/aenm.202300310>.

## 1. Introduction

1

2. A phase inversion  
strategy for low tortuosity,  
ultrahigh mass loading  
Nickel-rich layered oxide  
electrodes

2. A phase inversion strategy for low tortuosity, ultrahigh mass loading Nickel-rich layered oxide electrodes

## Abstract

Increasing the electrode thickness, thereby reducing the proportion of inactive cell components is one way to achieve higher energy density Li-ion batteries. This, however, results in higher electronic and ionic overpotentials and/or mechanical failure induced by binder migration. Here, we report Ethanol-induced phase inversion (EPI) as an effective method for making high-mass loading Nickel-rich layered oxide (NMC811) electrodes. The EPI electrodes significantly outperform their conventionally processed counterparts with similar loading ( $35 \text{ mg/cm}^2$ ) and porosity (30%) in Li/NMC half cells ( $131.7 \text{ mAh/g}$  vs  $56.7 \text{ mAh/g}$ ) at 1C ( $7 \text{ mA/cm}^2$ ) discharge. The binder structure induced by the nonsolvent improves the pore connectivity and results in lower tortuosity factors. The rapid solvent removal reduces the binder migration during drying, enabling ultrahigh active mass loadings up to  $60 \text{ mg/cm}^2$  ( $12 \text{ mAh/cm}^2$ ). Further, the excellent compatibility of the phase inversion process with current roll-to-roll coating setups makes this a processing technique with high industrial feasibility.

2

The contents of this chapter has previously been published in:

P Karanth\*, M Weijers\*, P Ombrini, D Ripepi, F Ooms, FM Mulder, Cell Reports Physical Science 5 (2024) 101972.

\* These authors contributed equally.

## 2.1 Introduction

Increasing the energy density of Lithium-ion batteries is a widely researched area today, thanks to the ever-increasing demand for higher driving ranges in electric cars<sup>1</sup> and a push for increased adoption of batteries in heavy-duty vehicles such as commercial aircraft.<sup>2,3</sup> A significant part of this research is dedicated to the development of high energy density electrodes.<sup>4</sup> From a materials perspective, while a transition to Li metal or Si anodes (from Graphite) would significantly boost the pack level energy densities, Ni-rich layered oxides such as  $\text{LiNi}_{0.8}\text{Mn}_{0.1}\text{Co}_{0.1}\text{O}_2$  (hereafter referred to as NMC811) remain the active material of choice on the cathode side, owing to a combination of factors such as high specific capacity, high intercalation voltages vs Li (3.6-4.3V) and good electronic/ionic conductivities. A way to further enhance the cell and pack energy density in terms of electrode architecture, particularly for the cathodes, is increasing the electrode thickness, thereby increasing the active mass loading and reducing the proportion of inactive components (current collectors, casing, etc.).<sup>5</sup>

Increasing the thickness of battery electrodes, however, comes with its own set of technical challenges that can impact the power density and the cycle life of these electrodes. An increase in electrode thickness would increase the path length for the electronic transport through the percolation network (consisting mainly of carbon additives) and the ionic transport through the electrolyte-filled porous network.<sup>5</sup> While the former issue can be addressed using 1D and 2D long-range conductive additives,<sup>6,7</sup> ion concentration polarization is generally considered the bigger challenge for thick electrodes, especially when moderate to high charge/discharge rates are desired.<sup>5,8,9</sup>

Ion transport through a porous network is influenced by its porosity and tortuosity factor, which in turn affect the Macmullin number, i.e., the ratio of bulk ionic conductivity to effective ionic conductivity of the electrolyte in the porous network.<sup>10</sup> In thick slurry cast electrodes, binder migration towards the separator side, induced by a relatively stronger association of the binder (typically PVDF) with the solvent (typically NMP) than with the active material, is also reported.<sup>11,12</sup> Binder migration in electrodes would typically result in an unfavorable Carbon-binder domain (CBD) and porosity distribution across the depth of the electrode, resulting in higher tortuosity factors.<sup>13</sup> While calendaring is an essential step in battery electrode processing, necessary to improve electrical and mechanical contacts, this often negatively affects the electrode tortuosity,<sup>14</sup> particularly in the case of thick electrodes with a nonhomogeneous CBD distribution. Further, the binder migration can also negatively affect the overall mechanical strength of the electrode and its adhesion to the current collector. With the successive electrode volume changes induced over extended cycling periods, both these factors can aggravate contact loss and capacity fade.<sup>15</sup>

## 2. A phase inversion strategy for low tortuosity, ultrahigh mass loading Nickel-rich layered oxide electrodes

Many efforts in the recent past have already focused on developing electrodes with lower tortuosities. The various approaches tried in this regard include freeze casting,<sup>16,17</sup> magnetic alignment,<sup>18–20</sup> laser etching,<sup>21</sup> mold templating<sup>22</sup>, and reactive templating<sup>23</sup> among others. However, many of these techniques also result in high electrode porosities and face challenges in terms of scalability. High electrode porosities can be undesirable in the context of volumetric energy density, and it is therefore necessary to develop techniques that can induce lower tortuosities at standard electrode porosities (25–30%).<sup>24</sup> It is also important to consider the costs involved and the compatibility of the electrode casting technique with the current industrial roll-to-roll processing for battery electrodes.<sup>25</sup>

Nonsolvent-induced phase inversion/separation (also known as NIPS/Immersion precipitation), a well-known technique in the membrane processing industry,<sup>26–28</sup> is another such technique that has been used to make high-performance battery electrodes. When the polymer-based (either pure or inorganic/polymer mix) coating is contacted with a binder nonsolvent, liquid-liquid demixing in the metastable region results in a Polymer-rich phase (polymer backbone) and a polymer-lean phase (pores).<sup>27,29</sup> Different nonsolvents under different process conditions (temperature, dilution, presence of additives, etc.) result in different demixing rates, which consequently affect the pore connectivity and the pore size distribution.<sup>29,30</sup> In addition to being used for making battery separators, fuel cell electrodes, and flow battery electrodes,<sup>30,31</sup> phase inversion has already been used to produce high-performance Sulfur/Carbon,<sup>32,33</sup>  $\text{Li}_4\text{Ti}_5\text{O}_{12}$ ,<sup>34</sup>  $\text{LiFePO}_4$ ,<sup>34,35</sup> and Silicon<sup>36</sup> electrodes for Li-ion batteries, typically using water as the binder nonsolvent. However, to our knowledge, the technique has not yet been applied to state-of-the-art but water-sensitive Ni-rich layered oxide materials (Ni-rich NMC, NCA, LNO, etc.), where a move towards higher mass-loading architectures is of significant interest to enable cell-level specific energies of 500 Wh/kg and higher.<sup>4</sup>

In this work, we report high-mass loading, high-rate performance Ni-rich NMC811 electrodes prepared using a novel ethanol-induced phase inversion method. The origin of the improved rate performance for the phase inversion-based electrodes with high active mass loadings (35 mg/cm<sup>2</sup> and higher) is elucidated using a combination of techniques (porosimetry, FIB-SEM, P2D modeling, symmetric cell EIS, solid-state NMR). The altered carbon binder domain structure for the phase inversion electrodes is shown to significantly reduce the tortuosity factor. Further, stable long-term cycling of the phase inversion electrodes is also observed for these high loadings, demonstrating the potential of phase inversion as a scalable, effective technique to obtain high mass-loading Ni-rich layered oxide electrodes.

2. A phase inversion strategy for low tortuosity, ultrahigh mass loading Nickel-rich layered oxide electrodes

## 2.2 Results

### 2.2.1 Optimization of the phase inversion process for Ni-rich layered oxides

Through the solvent/antisolvent screening for electrode slurries with PVDF as the binder, NMP and DMSO solvents were considered. DMSO is considered a green alternative to the conventionally used NMP<sup>37,38</sup> and is also typically miscible with the nonsolvent of PVDF/NMP. Miscibility of solvent and nonsolvent is necessary to ingress the nonsolvent in the cathode slurry. As opposed to previously investigated battery active materials (such as LFP) where water has often been used as the binder nonsolvent for making phase inversion-based electrodes,<sup>34,35</sup> options for suitable nonsolvents can be more limited for Ni-rich layered oxide materials such as NMC811. NMC811 is alkaline in nature as it exchanges lithium ions with protons in a protic nonsolvent medium such as water. This Li<sup>+</sup> leaching, leading to the formation of LiOH and Li<sub>2</sub>CO<sub>3</sub>, and the resulting alkaline environment (pH >12) subsequently results in corrosion of both the aluminum current collector and the native alumina layer on its surface.<sup>39,40</sup> Also, water phase inversion showed delamination of the electrode from the aluminum current collector after about 15 seconds, making the manufacturing process more error-prone.

The solubility parameters calculated based on the Hansen solubility index<sup>41,42</sup> (see **Note S1** and **Table S1**) indicate that alcohols are suitable nonsolvents for PVDF. The alcohol hydroxyl group generally has a higher pKa (15.9)<sup>43</sup> compared to the NMC alkalinity measured in an aqueous environment,<sup>39</sup> where relatively more acidic nonsolvents would form lithium salts upon contact. Among alcohols, ethanol was selected owing to its relatively higher abundance, safety, and non-solubility with PVDF. The low enthalpy of evaporation of ethanol, its low viscosity, and ease of separation with NMP and DMSO solvents by extractive distillation<sup>44</sup> or membrane filtration<sup>45</sup> make it a suitable nonsolvent. Also, no delamination from the Al current collector was observed after extended periods of nonsolvent contact.

Further, the choice of dilution decides the viscosity of the slurry and the proximity of the active material particles in the solution during precipitation. The viscosity of DMSO shows a higher dilution dependence and a high temperature dependence (**Note S2** and **Figure S1**). NMP slurries show only a slight viscosity difference upon dilution, and only for low dilutions (1:10 PVDF:NMP), a significant temperature dependence is observed. With a 1:10 m:m PVDF:solvent ratio, the electrode height and pore distribution were uneven. Such high viscosities may also not be applicable using conventional slot dye coating processing. A sufficiently low dilution of 1:12 or ideally 1:14 m:m PVDF:NMP showed the best distribution in pores (Figure S1). Dilutions up to 1:20 m:m were tried, and too high dilutions led to a non-binding precipitation. NMP is chosen as the solvent for the rest of this work, as the slurry viscosity shows a smaller temperature and dilution dependence, which improves the repeatability of the experiments.

2. A phase inversion strategy for low tortuosity, ultrahigh mass loading Nickel-rich layered oxide electrodes

### 2.2.2 Changes to the electrode structure upon phase inversion and the effect of calendaring

The phase inversion processing of NMC811 electrodes resulted in changes to both the CBD microstructure and the CBD distribution across the depth of the electrode in comparison to the conventional electrodes. Cross-section FIB-SEM images show channel structures throughout the uncalendered ethanol phase inversion-based (EPI) electrodes (**Figure 1c**), and no significant binder migration is observed (SI, **Figure S2c**). Further, ethanol phase inversion also causes macropores (pores in the micron range) throughout the cathode material (**Figure 1c**). Such macropores are not observed in the conventional electrodes. In conventional electrodes, a thick CBD layer is observed on the electrode surface (**Figure S2a**), and the CBD interconnects the particles with a porous microstructure (**Figure 1a**). For the EPI electrodes, the rapid precipitation of PVDF upon nonsolvent contact prevents binder migration by causing a rapid polymer-rich phase precipitation, creating a more evenly distributed CB structure throughout the electrode and negligible binder migration.

The immersion time (or solvent/nonsolvent exchange time) optimization also plays a crucial role in the effectiveness of the phase inversion process in generating the intended binder microstructure, as exchange times lesser than the binder precipitation time could result in partial/complete reversal of the binder structure generation, making the phase inversion processing ineffective.<sup>46</sup> Here, setting the immersion time to 5 minutes resulted in a good overall balance in terms of phase inversion/precipitation completeness, electrode adhesion, and overall processing time, resulting in binder microstructures observed in **Figure 1a** (cross-section) and **Figure S2c** (top view). With lower exchange times (1 min), while the binder migration is still reduced in comparison to the conventional electrode (**Figure S2a**), the CBD still had a porous microstructure similar to the conventional electrodes (**Figure S2b**), suggesting an incomplete binder precipitation during phase inversion.

## 2. A phase inversion strategy for low tortuosity, ultrahigh mass loading Nickel-rich layered oxide electrodes

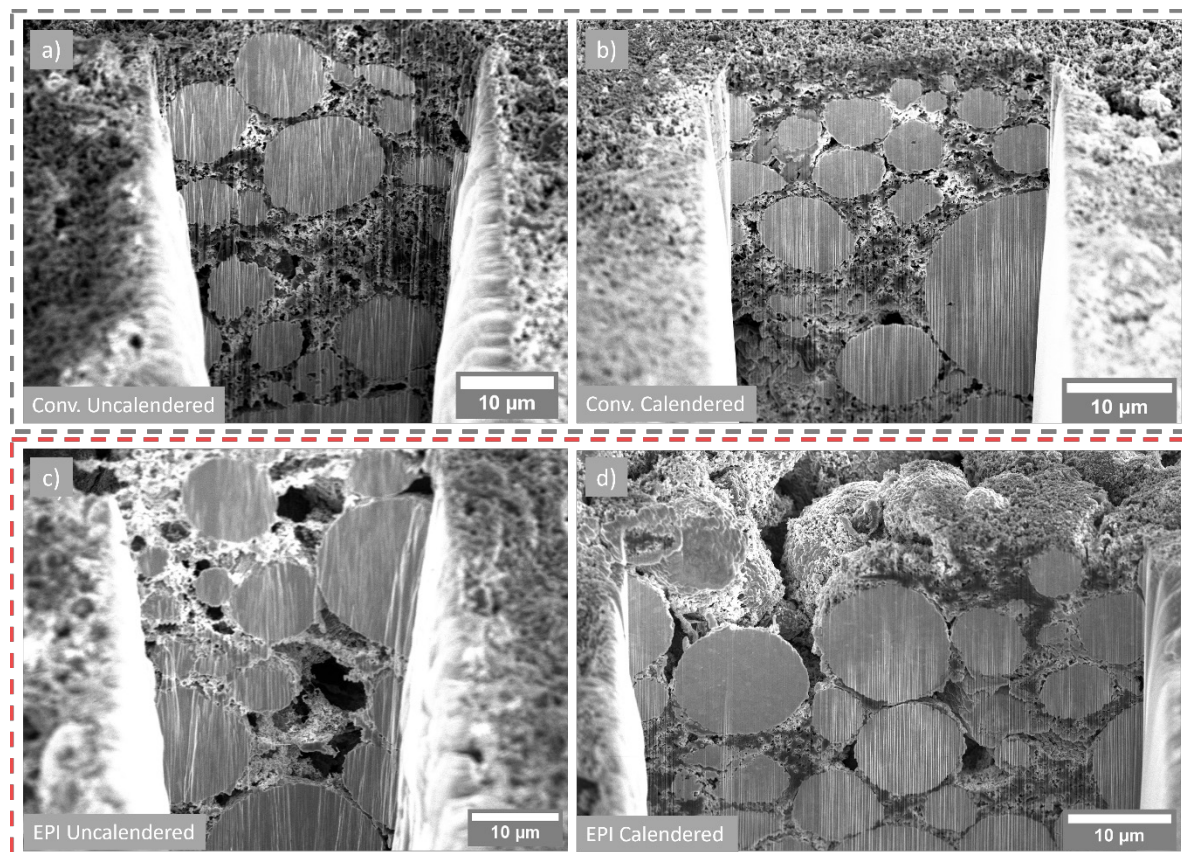


**Figure 1. Cross-section FIB-SEM of NMC811 Electrodes:** a) Conventional uncalendered, b) Conventional calendered, c) EPI uncalendered, d) EPI calendered. While the conventional electrodes show a high degree of intra-CBD microporosity before and after calendering (a,b), uncalendered EPI electrodes show a channeled structure with macropores (c). These macropores are retained to some extent with calendering while the CBD microstructure densifies (d).

For the EPI electrodes, calendering yields an evenly distributed electrode structure, and the macropores between the active material and the CBD phase are partly retained after calendering (Figure 1d, Figure S3). The CBD microstructure becomes denser after calendering for the EPI electrodes, while the conventional electrodes retain a porous CBD microstructure (Figure 1b, Figure S3).

## 2. A phase inversion strategy for low tortuosity, ultrahigh mass loading Nickel-rich layered oxide electrodes

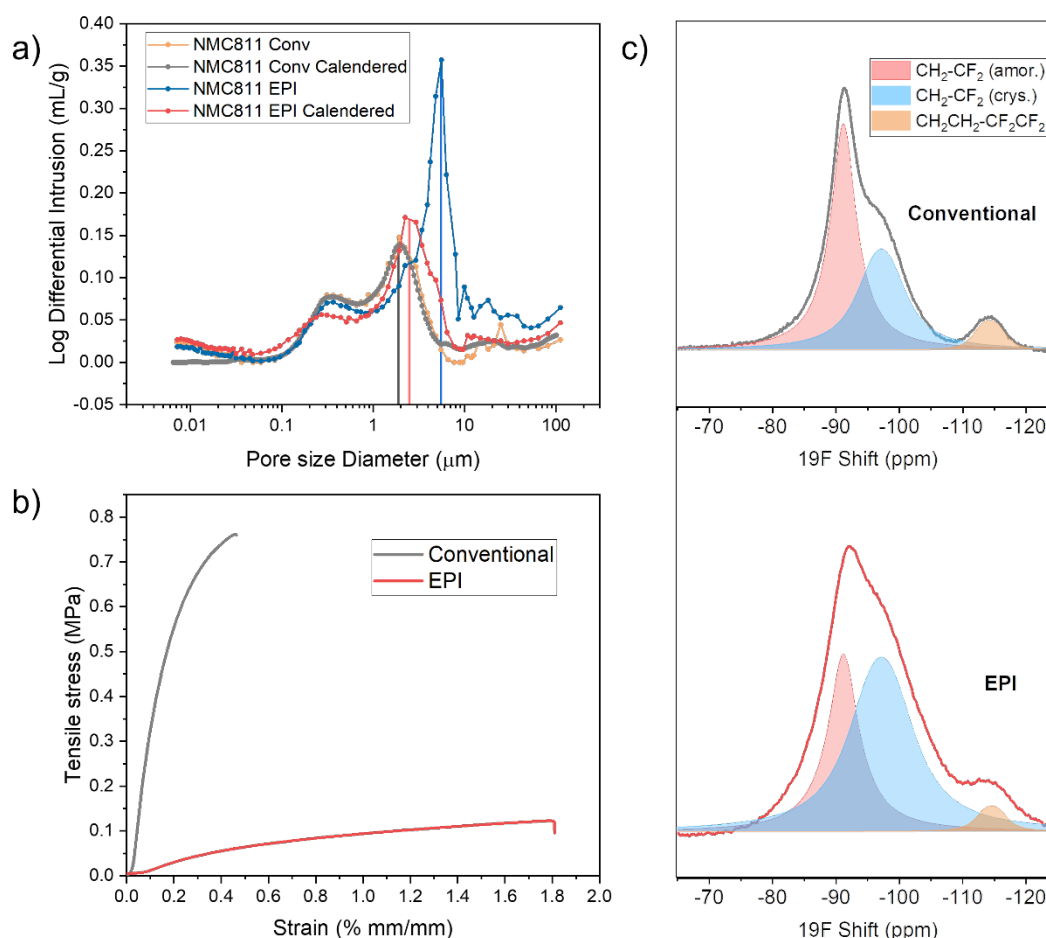


**Figure 2. Characterization of NMC811 electrodes:** a) Pore size distribution obtained by MIP of conventional and EPI electrodes before and after calendaring. b) Tensile stress-strain curves for 35 mg/cm<sup>2</sup>, 30% porosity freestanding Conventional and EPI electrodes. c) <sup>19</sup>F NMR spectra at 32 kHz spinning speed for NMC811 Electrodes (4 wt% PVDF) with the conventional drying method (top) and the EPI method (bottom), showing the differences in the amorphous/crystalline CH<sub>2</sub>-CF<sub>2</sub> fractions for the two methods

Further, a significant change to the pore size distribution in the electrodes because of phase inversion is observed by Mercury Intrusion Porosimetry (MIP). MIP shows the preferred liquid pathway in the porous structure as a function of applied pressure. Cathode structures before and after calendaring (more details on the target porosity estimation in **Note S3**) were subjected to MIP to map the changes to the pore size distribution in the CBD phase upon calendaring. A cutoff of 10 microns was chosen, as pores above this diameter were never observed with microscopy, and mercury intrusion commences first between the cathode sheets. Mercury intrusion porosimetry shows a shift in the macropore (pore sizes >1 μm) size from 1.8 μm for calendered conventional electrodes towards 2.6 μm for calendered EPI electrodes (indicated with lines in **Figure 2a**). The CBD phase with micropores (pore sizes of 0.1 to 0.8 μm) is also smaller in the EPI electrodes. This corroborates well with the FIB-SEM.

## 2. A phase inversion strategy for low tortuosity, ultrahigh mass loading Nickel-rich layered oxide electrodes

The EPI pore size distribution thus shows a lowered CBD porosity and increased macropores, which is beneficial for achieving lower tortuosities in thicker electrodes without affecting the net porosity.

Ethanol-based phase inversion in NMC811 electrodes also results in a change in the degree of crystallinity of PVDF, and this is clearly observed with the  $^{19}\text{F}$  MAS NMR measurements (Figure 2c, d). For both the samples, three environments are observed at -91.2 ppm, 97 ppm, and -114.3 ppm, and these have been previously attributed to the amorphous  $\text{CH}_2\text{-CF}_2$  component in PVDF, the crystalline  $\text{CH}_2\text{-CF}_2$  component and the defect environment ( $\text{CH}_2\text{-CH}_2$  and  $\text{CF}_2\text{-CF}_2$  units instead of alternating  $\text{CH}_2\text{-CF}_2$ ) respectively.<sup>47</sup> Clearly, a greater extent of the crystalline environment is observed for the electrode that underwent Ethanol phase inversion. These results agree well with the FIB-SEM and porosimetry observations that indicate lesser intra-CBD micropores and a denser CBD structure.

The changes to the CBD microstructure and distribution upon ethanol phase inversion were also found to affect the mechanical properties of the EPI NMC811 electrode. In general, for electrodes with  $35\text{ mg/cm}^2$  active mass loading and 30% apparent porosity, the EPI electrodes displayed better flexibility (higher Strain tolerance until fracture), i.e., 1.8% in the case of EPI as compared to 0.5% for the conventional electrode (**Figure 2b**). This could be relevant for roll-to-roll processing of these electrodes and for the application of these electrodes in non-planar cell architectures in which higher electrode flexibility is desired. Further, EPI electrodes at these loadings showed a more uniform adhesion to the Al current collector along the length of the electrode (uniform peeling force) than the conventional electrode (**Note S4** and **Figure S5**) at these loadings. These favorable properties for the EPI electrodes enable robust-crack-free electrodes at ultrahigh mass loadings of up to  $60\text{ mg/cm}^2$  ( $280\text{ }\mu\text{m}$  at 30% porosity), while conventional electrodes with a similar loading showed several cracks on the surface. (**Figure S4**).

### 2.2.3 Differences in electrochemical rate performance

The observed changes to the CBD microstructure in the EPI electrodes are expected to influence the tortuosity of the pore network and the surface coverage (by CBD) of the NMC particles, thereby the  $\text{Li}^+$  charge transfer resistance. The tortuosity factor of NMC electrodes has previously been observed to be a major bottleneck, particularly at high discharge (Lithiation) rates,<sup>14</sup> while any differences in  $\text{Li}^+$  charge transfer area would influence both the charge and the discharge rates. In this regard, the NMC811 electrodes were tested for their rate performance under both varying charge and discharge conditions at active mass loadings of  $35\text{ mg/cm}^2$  ( $7\text{ mAh/cm}^2$ ) and apparent porosities of  $\sim 30\%$ .

For the varying discharge rate tests, the electrodes were tested up to 1C, with C/10 being the constant charge rate (**Figure 3a**). For discharge rates up to C/3, not much difference is

## 2. A phase inversion strategy for low tortuosity, ultrahigh mass loading Nickel-rich layered oxide electrodes

observed for the discharge capacities. However, higher discharge capacities are observed for the EPI electrode starting from  $C/2$ . At  $1C$ , a clear difference in the discharge capacities is observed for the EPI electrodes (131.7 mAh/g vs. 56.7 mAh/g for EPI and Conv. respectively at cycle 14). From the discharge voltage traces for the two electrodes at  $1C$  (**Figure 3b**), it can be observed that the ohmic drop during the initial stage of discharge is nearly the same after charging at  $C/10$ . During discharge, however, the slope of the discharge curve is lower for the EPI electrode, indicating a lower ionic resistance across the porous electrode network for the EPI electrodes.

In the case of varying charge rate tests (with  $C/10$  constant discharge rate) shown in **Figure 3c**, while the discharge capacities remain similar for  $C/10$ , higher discharge capacities are observed at  $C/5$  and higher charge rates for the EPI electrodes. At  $C/2$ , the EPI electrode shows a discharge capacity of 142 mAh/g as opposed to 88 mAh/g for the conventional electrode. A comparison of the charge/discharge curves of the two electrodes at  $C/2$  charging is shown in **Figure 3d**. Again, while the ohmic polarization observed for the EPI electrodes is similar to that of the conventional electrodes, a lower slope is observed for the charging curve, corresponding to a higher charge capacity, which could be attributed to higher effective ion migration along the porous electrode network, influenced by the tortuosity factor and/or the porosity, which in this case lowers the Macmullin number.

## 2. A phase inversion strategy for low tortuosity, ultrahigh mass loading Nickel-rich layered oxide electrodes

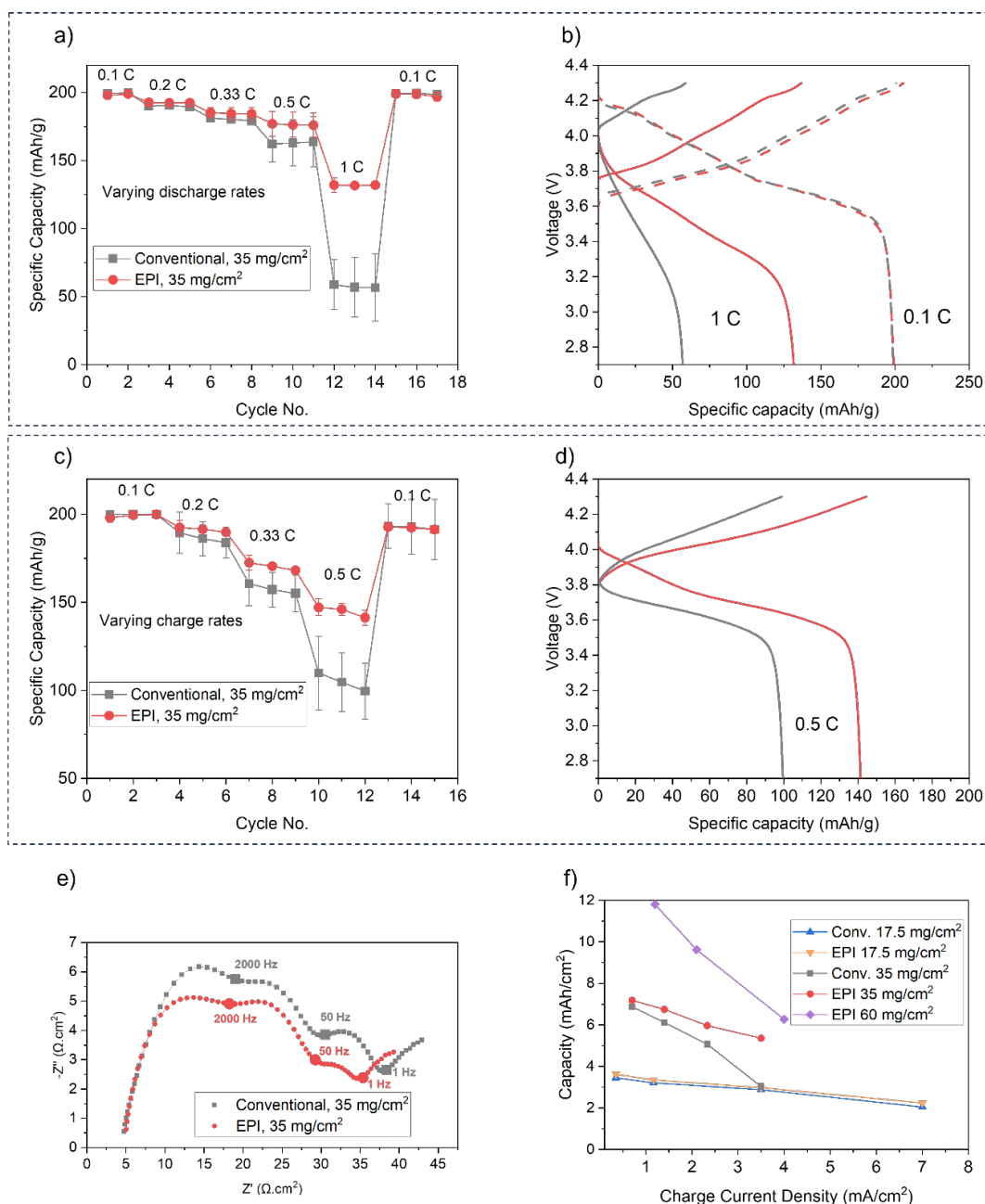


**Figure 3. Electrochemical rate performance comparison:** a) Rate performances of  $35 \text{ mg/cm}^2$  NMC811 electrodes in Li half cells at varying discharge rates and a constant C/10 charge rate. b) The voltage traces of Figure a, cycle 13 for both electrodes. c) Rate performances of  $35 \text{ mg/cm}^2$  NMC811 electrodes in Li half cells at varying charge rates and a constant C/10 discharge rate. d) The voltage traces of figure c, cycle 11 for both electrodes. e) EIS Nyquist plots at 3.7 V for the conventional and EPI based Li/LP57/NMC811 cells. f) Overview of the specific (discharge) capacities for NMC811 electrodes obtained at varying charge rates and mass loadings.

Electrochemical impedance spectroscopy (EIS) performed on the  $35 \text{ mg/cm}^2$  half cells at 3.7 V after the formation cycles also sheds light on the differences in the impedance contributions

## 2. A phase inversion strategy for low tortuosity, ultrahigh mass loading Nickel-rich layered oxide electrodes

for the two electrodes (**Figure 3e**, see **Note S5** for equivalent circuit shown in **Figure S6** and fit values in **Table S4**). The curved features occurring between 500k – 2kHz, 2 kHz- 50 Hz and 50 Hz – 1 Hz have been attributed to the total electronic resistance  $R_{elec}$  of the electrodes (including the contact resistance between the NMC811 electrode film and Al current collector), the Li SEI film resistance  $R_{SEI}$  and the charge transfer resistance at the cathode-electrolyte interface  $R_{CT}$  respectively (based on time constants typically reported for these components<sup>48</sup>).

2

Both the electrodes are observed to have similar electronic resistance values perpendicular to the plane ( $R_{elec}$ ), with the value for the EPI cell being slightly lower ( $12.0 \Omega \cdot \text{cm}^2$ ) compared to the conventional cell ( $13.1 \Omega \cdot \text{cm}^2$ ). The electronic resistance obtained with EIS is in line with through-plane DC electronic resistances for the electrodes measured in an ion-blocking setup ( $18.2 \Omega \cdot \text{cm}^2$  and  $18.4 \Omega \cdot \text{cm}^2$  for EPI and conventional electrodes respectively; further details can be found in **Note S6** and **Table S5**). Further, the  $R_{CT}$  value for the EPI electrode is observed to be lower ( $5.50 \Omega \cdot \text{cm}^2$ ) compared to the conventional cell ( $7.79 \Omega \cdot \text{cm}^2$ ).  $R_{CT}$  can depend on several factors, such as the active material, the state of charge, and the available surface area for charge transfer. In this case, the lower  $R_{CT}$  in the case of the EPI electrode could be explained by the enhanced surface area for  $\text{Li}^+$  exchange, caused by a lower CBD coverage of the active material surface and/or the improved electrolyte uptake in its pore network resulting in a better active surface utilization.

Further, **Figure 3f** provides an overview of the discharge capacities at different charging currents for NMC811 electrodes at different active mass loadings ( $17.5 - 60 \text{ mg/cm}^2$ ). It can be observed that while the rate performance of both the conventional and the EPI electrodes are similar for  $17.5 \text{ mg/cm}^2$  ( $3.5 \text{ mAh/cm}^2$ ), a clear improvement in discharge capacities is observed for the electrodes at  $35 \text{ mg/cm}^2$  ( $7 \text{ mAh/cm}^2$ ), particularly at higher charge rates. EPI electrodes with ultra-high mass loadings of  $60 \text{ mg/cm}^2$  ( $12 \text{ mAh/cm}^2$ ) also show a remarkable discharge capacity of  $9.62 \text{ mAh/cm}^2$  ( $160.3 \text{ mAh/g}$ ) capacity at charge current densities of  $\sim 2.1 \text{ mAh/cm}^2$ , whereas the conventional electrodes cast at these loadings did not show enough mechanical integrity to be tested in coin cells.

### 2.2.4 Differences in the tortuosity factor

The symmetric cell EIS (eSCM) measurements for the two electrodes also reveal differences in the ionic resistance contributions from the porous network and the CBD, and thereby, the electrode tortuosity factor. **Figures 4a** and **b** show the Nyquist plots obtained for the conventional and EPI electrodes.

Both plots show three features, i.e., two curved features in the high-mid frequency region and a sloping line in the mid-low frequency region. Similar feature(s) have been observed previously for porous Li-ion electrodes, and their physicochemical interpretation has been

## 2. A phase inversion strategy for low tortuosity, ultrahigh mass loading Nickel-rich layered oxide electrodes

subject to wide debate. Some possible reasons for such a feature include electrical contact resistance,<sup>49,50</sup> uneven CBD distribution through the depth of the electrode resulting in a depth-wise difference in the ionic resistance,<sup>13,51</sup> and the intrinsic porosity/electrolyte uptake of the CBD.<sup>52</sup>

In this case, the high-frequency feature (up to 6250 Hz) is attributed to the electronic (contact) resistance of the electrode. The second (mid-frequency) curved feature (6250 – 125 Hz) is attributed to the impedances coming from the carbon binder domain (CBD). The magnitude of this feature is observed to be higher for the EPI electrode than for the conventional one. A possible origin of this feature here could be the non-homogenous distribution of the CBD phase along the depth of the electrode, which is known to occur for thick electrodes with drying. While a migrated binder layer was indeed observed for the Conventional electrodes with the FIB-SEM, a nonuniform distribution of the CBD was not observable for the EPI electrodes at mass loadings of 7-7.5 mAh/cm<sup>2</sup> (**Figure 1a**).

When it comes to the CBD structure, however, the FIB-SEM (**Figure 1c**) reveals a more dense CBD structure in terms of microporosity for the EPI electrodes. This observation is also supported by the MIP results (**Figure 2a**) that show a lower pore size distribution in the 10-200 nm range (typically corresponding to intra-CBD pores) and also the <sup>19</sup>F ssNMR results (**Figure 2c, d**) that show a more crystalline PVDF structure produced by the EPI process. This results in a lower surface area offered by the CBD phase for the EPI electrodes, explaining the higher real axis value for the second curved feature.

Finally, the sloping line feature occurring at medium to low frequencies denotes the resistance to ion migration through the long-range (macro)porous network along the electrode, and here, the value of ionic resistance appears to be lower for the EPI electrode.

The tortuosity factors are estimated by approximating the sum of the real axis (x-axis) lengths of the sloping line and the mid-frequency curve to be  $R_{ion}/3$ , where  $R_{ion}$  is the total ionic resistance of the two electrodes in the symmetric cell.<sup>13,49</sup> This value is then used to calculate the tortuosity factors (further details can be found in **Note S7, Table S6**). The EPI electrode displays a lower tortuosity factor of 2.58 compared to a value of 3.79 for the conventional electrode.

2. A phase inversion strategy for low tortuosity, ultrahigh mass loading Nickel-rich layered oxide electrodes

2

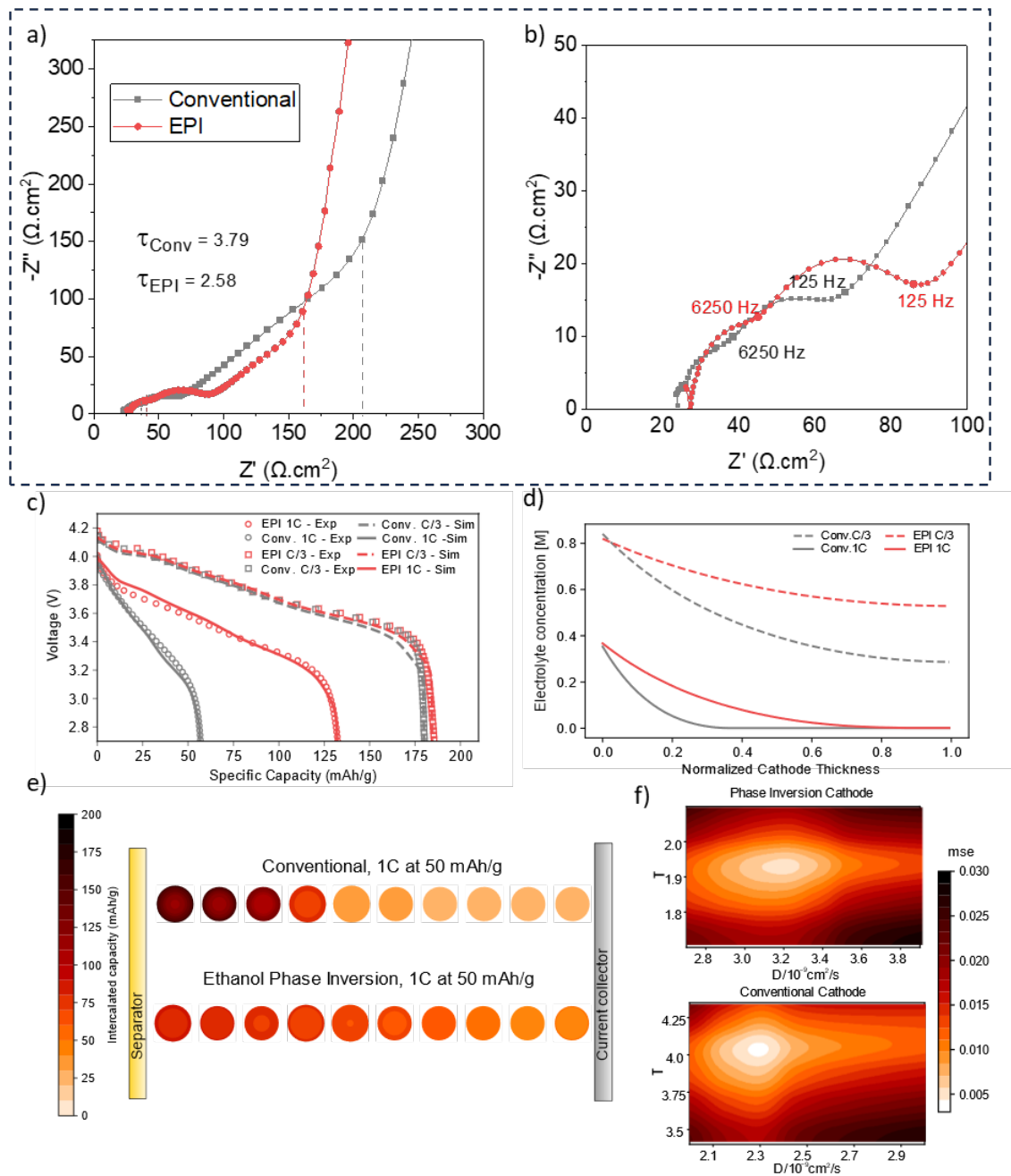


**Figure 4. Tortuosity factor measurements:** a) EIS Nyquist plots for the NMC811 symmetric coin cells with 25mM TBAClO<sub>4</sub> in EC:DEC electrolyte. The drop-down values indicate the real axis length considered for the  $R_{ion}$  calculations b) The zoomed inset of the high-to-mid frequency region for the NMC811 symmetric cells. c) Comparison between the experimental and the simulated voltage curves. d) Electrolyte concentration along the cathode at 25% DOD. e) Particle concentrations, expressed in terms of capacity delivered during discharge, along the cathode at 25% DOD for conventional and EPI electrodes. f) Mean square error landscape for varying diffusivities ( $D$ ) and tortuosity factor ( $\tau$ ) for conventional and EPI electrodes.

## 2. A phase inversion strategy for low tortuosity, ultrahigh mass loading Nickel-rich layered oxide electrodes

The rate performance and the difference in obtainable tortuosity factors for Ethanol phase inversion can be further compared to conventional processing through porous electrode modeling.<sup>53–60</sup> The physical constants of the model were found by fitting the unknown parameters, such as effective diffusivity, exchange current density, Li metal charge transfer resistance, and tortuosity factor, to match the experimental voltage curves. The result is shown in **Figure 4c-f**.

The effect of the most sensitive parameters (effective diffusivity  $D$  and tortuosity factor  $\tau$ ) on the mean square error (mse) between the simulated and the experimental voltage curve (**Figure 4f**) clarifies the importance of tortuosity factor in the correct fitting of the experimental results, revealing the best fit for the conventional and the phase-inversion to have tortuosity factors of 4.05 and 1.92, respectively.

Despite the intrinsic assumption underlying the P2D model,<sup>61,62</sup> which considers every particle in an ideal electrolyte bath, the relation between the fitted tortuosity factor is in line with the results of the EIS (**Figure 4a**), showing the effect of the phase inversion on the performance. Moreover, an optimal fit (**Figure 4c**) is achieved by decreasing the effective diffusivity and the exchange current densities of the conventional electrode compared to the EPI electrode, obtaining values of  $2.28 \cdot 10^{-9} \text{ cm}^2/\text{s}$  and  $3.19 \cdot 10^{-9} \text{ cm}^2/\text{s}$  for the effective diffusivities and  $2.48 \text{ A}/\text{m}^2$  and  $3.5 \text{ A}/\text{m}^2$  for the exchange current densities, respectively (see **Note S8**). This result, coming from the unbounded parameter estimation, aligns well with the (cathode) charge transfer resistance calculated from the EIS.

Finally, the validated model shows the effect of the microstructural changes on the  $\text{Li}^+$  concentration in the electrolyte along the cathode (**Figure 4d**), also capturing the consequences in terms of Li concentration in the particles (**Figure 4e**). This result underlines the advantages of phase inversion in reducing CBD inhomogeneities and the tortuosity factor in thick electrodes.

### 2.2.5 Long-term cycling performance

A comparison of the long-term electrochemical performances of the conventional and EPI NMC811 electrodes at high active mass loadings of  $7 \text{ mAh}/\text{cm}^2$  ( $35 \text{ mg}/\text{cm}^2$ ) is shown in **Figure 5**. In this case, Li foil ( $250 \mu\text{m}$ ) was again selected as the anode due to the unavailability of other suitable candidates that can deliver these high capacities without undergoing performance limitations of their own. The electrolyte was changed to a high-entropy electrolyte, i.e.  $1 \text{ M LiPF}_6 + 0.1 \text{ M LiDFOB} + 0.1 \text{ M LiTFSI} + 0.1 \text{ M LiFSI} + 0.1 \text{ M LiNO}_3$  in EC:DMC (1:1 wt%) + 5 wt% FEC (hereafter referred to as 1.4 M HE electrolyte) salt electrolyte previously reported by Wang et. al.<sup>63</sup>, as high-entropy multi salt electrolytes were shown to enable uniform Li plating/stripping at high current densities and capacities.<sup>63,64</sup>

## 2. A phase inversion strategy for low tortuosity, ultrahigh mass loading Nickel-rich layered oxide electrodes

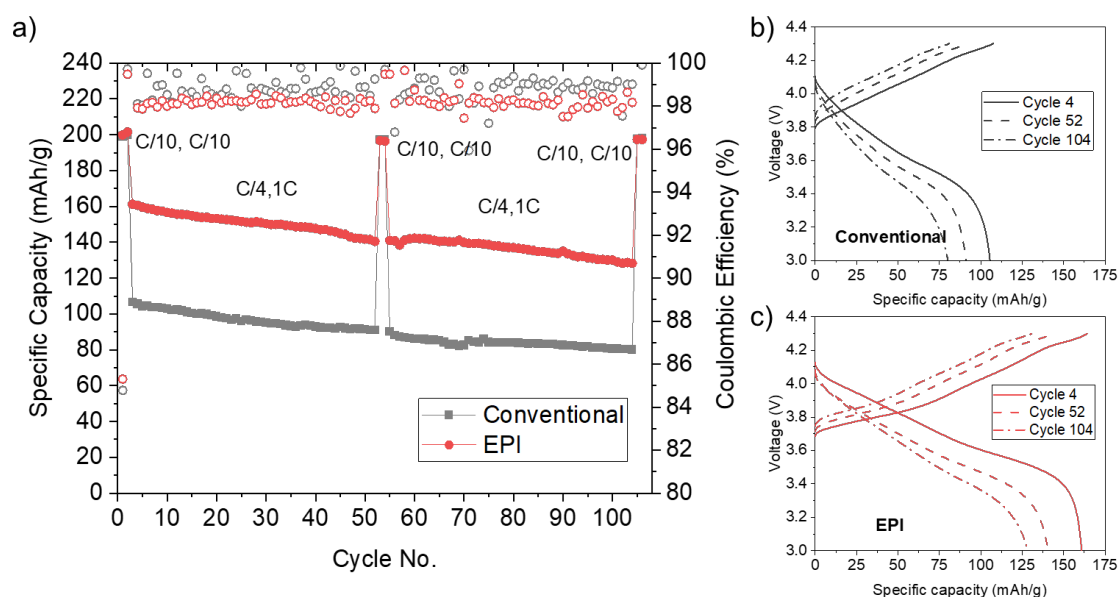


**Figure 5. Long-term cycling comparison:** a) Discharge capacities and coulombic efficiencies in Li/NMC811 half cells with 35 mg/cm<sup>2</sup> (7 mAh/cm<sup>2</sup>) active mass loading and 1.4 M HE electrolyte cycled at 20 °C. b) Voltage traces for the Conventional Li/NMC811 cells at 10, 52, and 104 cycles. c) Voltage traces for the EPI Li/NMC811 cells at 4, 52, and 104 cycles (C/4 C, 1C D).

Here, a clear improvement in the discharge capacity at 1C is observed for the EPI NMC811 electrode for over 100 cycles (**Figure 5a**). A gradual capacity fade is observed for both electrodes over the high cycling rates, and such capacity fade is typically observed due to the increase of polarization at the Li interface, due to the buildup of dead Lithium and/or gradual salt consumption at these high plating/stripping rates.<sup>65</sup> This phenomenon contributes to the increase of ohmic polarization during charge, going from cycle 4 to 104 for both electrodes (**Figure 5b, c**). However, the original capacities are observed to be nearly retained for both electrodes at low rates (0.1 C) after the 100 cycles. Remarkably, the EPI electrodes show a capacity retention of 98.65% (197.3 mAh/g) even after cycling with significantly higher discharge capacities compared to the conventional electrodes for over 100 cycles.

### 2.3 Discussion

Ethanol phase inversion (EPI) processing on casted NMC811 slurries causes rapid precipitation of the Carbon binder domain (CBD). As the nonsolvent enters, the low miscibility of the binder with the solvent/nonsolvent phase results in the formation of a polymer-rich phase in the solution and subsequent precipitation of the binder. The solvent/nonsolvent phase penetrates throughout the electrode, solidifying the constituents of the final electrode.

## 2. A phase inversion strategy for low tortuosity, ultrahigh mass loading Nickel-rich layered oxide electrodes

As a result, phase inversion processing shows a substantial change in the CBD phase (**Figure 6b**), as shown with FIB-SEM, Mercury intrusion porosimetry, and solid-state NMR. The rapid precipitation of the binder with ethanol phase inversion results in electrodes with a higher degree of (connected) macropores but a lower degree of micropores, even after calendaring (**Figure 6b**). The reduction in the degree of microporosity for the EPI electrodes was also further confirmed by  $^{19}\text{F}$  NMR, which shows a higher degree of PVDF crystallinity, increasing the overall volumetric density of the PVDF binder. The FIB-SEM also reveals a reduction in the degree of binder migration for the EPI NMC811 electrodes.

The EPI electrodes show an improved flexibility, essential for roll-to-roll processing thick electrode architectures. The structure maintains its integrity during calendaring and results in electrodes with improved rate performances at both high charge and discharge rates.

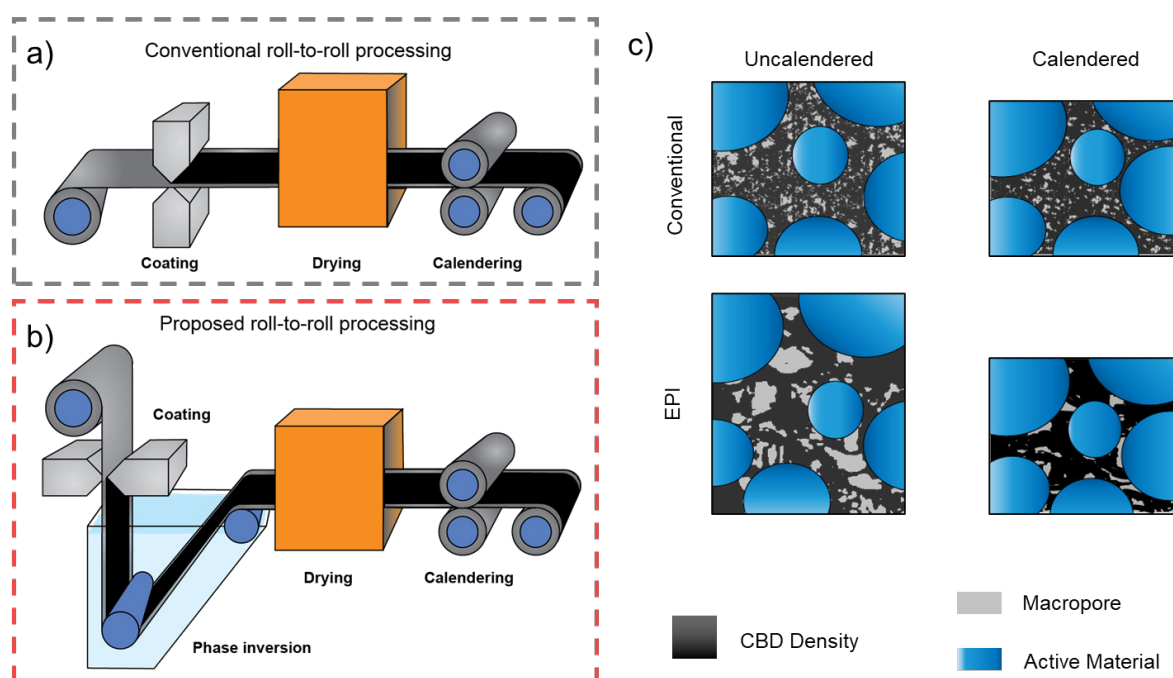


**Figure 6. Differences between Conventional and EPI processes:** a) Schematic procedure of the current roll-to-roll process based on conventional drying b) Schematic procedure of the proposed roll-to-roll process based on phase inversion c) Electrode microstructures obtained before and after calendaring for the conventional and ethanol phase inversion processes

The eSCM (EIS) using a non-intercalating electrolyte showed a significant decrease in tortuosity factor for the EPI electrodes. The lower tortuosity results in a higher charge capacity at high charge rates, but the capacity gain is more evident during high discharge. During fast discharge,  $\text{Li}^+$  concentration depletion due to insufficient influx in a tortuous pore network causes uneven charge distribution across the depth of the electrode and a rapid (concentration) overpotential buildup. In this regard, a lower tortuosity of the pore network is beneficial for maintaining sufficient ion flux deeper in the cathode. The effect of tortuosity

## 2. A phase inversion strategy for low tortuosity, ultrahigh mass loading Nickel-rich layered oxide electrodes

is shown using the P2D model, and the computed tortuosity factors nearly match the experimental values for both conventional and phase inversion electrodes.

The EPI electrodes consistently maintain a higher discharge capacity over 100+ cycles during long-term cycling tests of high mass loading (35 mg/cm<sup>2</sup>). While both EPI and conventional electrodes show the same gradual capacity fade mechanism at high discharge rates (1C, 7 mA/cm<sup>2</sup>) originating from the increase in impedance from the Li metal anode, the EPI electrode shows an excellent capacity retention of 98.65%. An estimate of the cell level volumetric and weight density of batteries fitted with double-sided EPI electrodes shown in this work are 1210 Wh/L and 503 Wh/kg, respectively without casing. Here, the calculation assumes a zero-excess lithium configuration and Celgard separators filled with conventional liquid electrolyte (see **Note S9, Table S8**). For lithium excess architectures, using twice the lithium inventory needed for the rated capacity, the energy density will slightly lower to 1054 Wh/L and 487 Wh/kg. These values highlight the benefit of high mass loadings enabled by Ethanol phase inversion, as the inactive components in a cell lower from 43% to 37% of the total cell when going from 4 to 7 mAh/cm<sup>2</sup>.

To implement phase inversion processing in current industrial practice, the conventional roll-to-roll electrode manufacturing setup would need an additional nonsolvent processing step. As typical solvents are replaced with more volatile and/or benign nonsolvents, introducing phase inversion would lower the energy investment of subsequent drying and ease solvent recovery. In this work and previous works,<sup>30-36</sup> it is shown that phase inversion processing is compatible with a wide range of materials and compositions. Finally, the available literature on membrane processing using phase inversion steps allows a steep learning curve in a roll-to-roll setup.

In summary, we have developed a new Ethanol-based phase inversion (EPI) strategy for making ultrahigh-loading, high-performance electrodes out of Ni-rich layered oxide materials. We show high active mass loading (35 mg/cm<sup>2</sup>) EPI NMC811 electrodes which outperform conventional NMC811 electrodes during fast charge (50% improvement at 0.5C) and discharge (120% improvement at 1C) at similar porosities (~30%). Unlike conventional electrodes, EPI electrodes can be made ultrathick (60 mg/cm<sup>2</sup>, 12 mAh/cm<sup>2</sup>) without having delamination or cracking issues. The EPI electrodes show a higher gravimetric capacity and similar capacity retention as the conventional electrodes on extensive cycling, which indicates that the processing does not adversely affect the cathode active material. The improved rate performance originates from the lower tortuosity of the electrode. With the addition of a phase inversion processing step in conventional battery manufacturing processes, it is possible to increase the rate performance of battery electrodes at high mass loadings, and this presents a viable path toward future batteries with both high energy and power densities.

2. A phase inversion strategy for low tortuosity, ultrahigh mass loading Nickel-rich layered oxide electrodes

## 2.4 Experimental Procedures

### 2.4.1 Electrode Manufacturing

NMC811 electrodes were made with a 92:4:3:1 mass ratio of active material (AM) : binder: carbon black: graphite using a dry and wet mixing step. First, NMC811 (Umicore) AM was mixed with the conductive additive Carbon black C45 (Imerys) in a mortar, followed by the addition and mixing of KS4 Graphite (Imerys) and Solef 5130 (Solvay) PVDF respectively. NMP (Sigma Aldrich) was added to this mixture in a 1:14 PVDF:NMP mass ratio, and subsequently, the suspension was mixed using a high-shear top stirrer (IKA Microstar 7.5) for 1 hour at 1000 RPM to create a homogeneous slurry. The obtained slurry was cast on aluminum foil using a doctor blade. To obtain freestanding electrodes for the purpose of tensile strength and mercury intrusion porosimetry measurements, the slurry was cast on clean glass plates. Immediately after casting, the sheet was either immersed in a bath of ethanol (96%, VWR) for 60-300 seconds (Ethanol phase inversion, EPI) or was not subjected to an immersion treatment (Conventional). The electrode sheets were dried in two steps. NMP/nonsolvent was evaporated in an oven at 70 °C for an hour, and subsequently, the electrode sheets were dried in a vacuum oven at 60 °C for 24 hours. Finally, the electrodes were calendered to 30% apparent porosity using a calender press (MTI). Details on the porosity estimation are provided in the Supplementary Information (**Table S2, Table S3**).

### 2.4.2 Electrode Characterization

Electrode porosity and pore size distribution of freestanding NMC811 electrodes were tested using mercury intrusion porosimetry (Autopore 9500, Micromeritics). Approximately 1 gram of freestanding electrode sample was loaded in strips of 3x1 cm in a 15 mL penetrometer with the surface perpendicular to the entry side of the mercury. The stem volume of 0.39 mL was utilized between 40 - 88% during pressurization between 3.7 kPa and 210 MPa. Rheometry was performed on the slurries using a 40 mm Peltier plate with 0° cone angle and 500 μm gap width on a Discovery HR10 rheometer (TA Instruments). The shear rate was varied between 0.01 and 10/s. Scanning electron microscopy (SEM) pictures were taken using a JEOL JSM-IT700HR FE-SEM setup either in scattering electron imaging (Acc. Voltage: 1- 5 kV) or Backscattered electron imaging (Acc. voltage: 5 kV) mode. Focused Ion Beam SEM (FIB-SEM) images were taken using a Helios G4 CX. Ion milling times were referenced to 0.8 times the silicon etching duration for a specific depth. The ion beam was set to 30 kV with 65 nA beam strength.

Solid-state MAS NMR measurements were carried out on a Bruker Avance 500 Spectrometer. NMC811 electrodes coated on Al foil were scraped off and packed into 1.9 mm rotors. <sup>19</sup>F NMR (Larmor frequency: 475 MHz) was carried out at 32 kHz spinning speeds. A zgbs (background subtraction) protocol was used with a recycle delay of 2 seconds. All spectra were processed and fitted using Mestrenova 14 software.

2. A phase inversion strategy for low tortuosity, ultrahigh mass loading Nickel-rich layered oxide electrodes

The tensile strength measurements were performed on a ZwickRoell 10 kN universal testing machine. For these measurements, freestanding electrodes were calendered between two Ni foils to a porosity of 30% and cut according to ASTM D412 type F,<sup>66</sup> with the target test area being about 6x50 mm. The tensile force test was performed at a speed of 1 mm/min.

### 2.4.3 Electrochemical characterization

Coin cells (CR2032) were assembled to study the rate performance of the NMC811 electrodes in a half-cell configuration. NMC811 electrodes were punched as 12.7 mm discs and assembled versus a 250  $\mu\text{m}$  Lithium disc (Tobmachine) in an Argon-filled glove box. One Celgard 2400 and one Whatman separator (Grade Gf/C) each were used, with 110  $\mu\text{l}$  of 1 M  $\text{LiPF}_6$  in 3:7 EC:EMC (vol%) electrolyte (LP57, Elyte) per cell. After 24 hours of rest, the cells underwent two formation cycles at C/10 on a MACCOR 3400 galvanostat. Rate performance tests were then carried out on the Maccor 3400 at 20 °C.

Long term cycling performance of the NMC811 electrodes was also tested in a half-cell configuration (vs. Li) similarly, except that the electrolyte used was changed to 1 M  $\text{LiPF}_6$  + 0.1 M  $\text{LiDFOB}$  + 0.1 M  $\text{LiTFSI}$  + 0.1 M  $\text{LiFSI}$  + 0.1 M  $\text{LiNO}_3$  in EC:DMC (1:1 wt%) + 5 wt% FEC (1.4 M HE) for the sake of improved long-term stability with the Li metal anode at high plating and stripping currents. The 1.4 M HE electrolyte was prepared as described elsewhere.<sup>63</sup> The long-term cycling was carried out at 20 °C. Following the formation cycles at C/10, the protocol used was as follows: first 2 cycles at C/10 charge-discharge, followed by 50 cycles at C/4 charge and 1C discharge, and the protocol repeats every 52 cycles.

Electrochemical impedance spectroscopy (EIS) was performed on a potentiostat (Metrohm Autolab) after the formation cycles. First, a voltage hold (until  $I < 0.01\text{C}$ ) at 3.7 V was carried out. A frequency range from 500 kHz to 100 mHz was used. The analysis and fitting of the spectra was carried out using Zview (Scribner). Tortuosity factors were measured for these electrodes based on the symmetric cell method often applied to Li-ion battery electrodes.<sup>49,67</sup> A non-intercalating electrolyte, 25 mM  $\text{TBAClO}_4$  in EC:DEC (1:1 vol%), is used along with fully intercalated NMC811 electrodes of interest to achieve the desired blocking conditions for ion flow. Both the electrodes had mass loadings around 7.5  $\text{mAh}/\text{cm}^2$  and were calendered to an apparent porosity of 30%.

### 2.4.4 P2D Modelling

Simulations were carried out using the open-source software MPET<sup>68</sup>, which uses a standard pseudo-2-dimensional (P2D) model.<sup>60,69</sup> The parameters (**Table S7**) were obtained as follows: the electrolyte parameters for the Stefan-Maxwell model<sup>70</sup> were obtained from the work of Nyman et. al.<sup>71</sup> the dependence on the concentration of the reaction resistivity and the solid-state diffusivity were taken from the fitting of McClelland et. al.<sup>72</sup>; electrical conductivity, thickness, porosity and particle size distribution were taken from measured values; the rest

2. A phase inversion strategy for low tortuosity, ultrahigh mass loading Nickel-rich layered oxide electrodes

of the parameters, such as the tortuosity factor were estimated by minimization of the weighted mean square error. The details of the model can be found in the supplementary information (**Note S8**).

The code developed for this work is based on the open-source MPET model of which a branch specific to this work is available at [www.doi.org/10.5281/zenodo.10932567](http://www.doi.org/10.5281/zenodo.10932567).

## References

- (1) Masias, A., Marcicki, J., and Paxton, W.A. (2021). Opportunities and Challenges of Lithium Ion Batteries in Automotive Applications. *ACS Energy Lett.* *6*, 621–630. [10.1021/acsenergylett.0c02584](https://doi.org/10.1021/acsenergylett.0c02584).
- (2) Viswanathan, V., Epstein, A.H., Chiang, Y.-M., Takeuchi, E., Bradley, M., Langford, J., and Winter, M. (2022). The challenges and opportunities of battery-powered flight. *Nature* *601*, 519–525. [10.1038/s41586-021-04139-1](https://doi.org/10.1038/s41586-021-04139-1).
- (3) Bills, A., Sripad, S., Fredericks, W.L., Singh, M., and Viswanathan, V. (2020). Performance Metrics Required of Next-Generation Batteries to Electrify Commercial Aircraft. *ACS Energy Lett.* *5*, 663–668. [10.1021/acsenergylett.9b02574](https://doi.org/10.1021/acsenergylett.9b02574).
- (4) Liu, J., Bao, Z., Cui, Y., Dufek, E.J., Goodenough, J.B., Khalifah, P., Li, Q., Liaw, B.Y., Liu, P., Manthiram, A., et al. (2019). Pathways for practical high-energy long-cycling lithium metal batteries. *Nat. Energy* *4*, 180–186. [10.1038/s41560-019-0338-x](https://doi.org/10.1038/s41560-019-0338-x).
- (5) Kuang, Y., Chen, C., Kirsch, D., and Hu, L. (2019). Thick Electrode Batteries: Principles, Opportunities, and Challenges. *Adv. Energy Mater.* *9*, 1901457. [10.1002/aenm.201901457](https://doi.org/10.1002/aenm.201901457).
- (6) Park, S.-H., King, P.J., Tian, R., Boland, C.S., Coelho, J., Zhang, C. (John), McBean, P., McEvoy, N., Kremer, M.P., Daly, D., et al. (2019). High areal capacity battery electrodes enabled by segregated nanotube networks. *Nat. Energy* *4*, 560–567. [10.1038/s41560-019-0398-y](https://doi.org/10.1038/s41560-019-0398-y).
- (7) Yao, W., Chouchane, M., Li, W., Bai, S., Liu, Z., Li, L., Chen, A.X., Sayahpour, B., Shimizu, R., Raghavendran, G., et al. (2023). A 5 V-class cobalt-free battery cathode with high loading enabled by dry coating. *Energy Environ. Sci.* *16*, 1620–1630. [10.1039/D2EE03840D](https://doi.org/10.1039/D2EE03840D).
- (8) Gao, H., Wu, Q., Hu, Y., Zheng, J.P., Amine, K., and Chen, Z. (2018). Revealing the Rate-Limiting Li-Ion Diffusion Pathway in Ultrathick Electrodes for Li-Ion Batteries. *J. Phys. Chem. Lett.* *9*, 5100–5104. [10.1021/acs.jpcllett.8b02229](https://doi.org/10.1021/acs.jpcllett.8b02229).
- (9) Weiss, M., Ruess, R., Kasnatscheew, J., Levartovsky, Y., Levy, N.R., Minnmann, P., Stolz, L., Waldmann, T., Wohlfahrt-Mehrens, M., Aurbach, D., et al. (2021). Fast Charging of Lithium-Ion Batteries: A Review of Materials Aspects. *Adv. Energy Mater.* *11*, 2101126. [10.1002/aenm.202101126](https://doi.org/10.1002/aenm.202101126).
- (10) Tjaden, B., Brett, D.J.L., and Shearing, P.R. (2018). Tortuosity in electrochemical devices: a review of calculation approaches. *Int. Mater. Rev.* *63*, 47–67. [10.1080/09506608.2016.1249995](https://doi.org/10.1080/09506608.2016.1249995).

## 2. A phase inversion strategy for low tortuosity, ultrahigh mass loading Nickel-rich layered oxide electrodes

- (11) Kremer, L.S., Hoffmann, A., Danner, T., Hein, S., Prifling, B., Westhoff, D., Dreer, C., Latz, A., Schmidt, V., and Wohlfahrt-Mehrens, M. (2020). Manufacturing Process for Improved Ultra-Thick Cathodes in High-Energy Lithium-Ion Batteries. *Energy Technol.* *8*, 1900167. [10.1002/ente.201900167](https://doi.org/10.1002/ente.201900167).
- (12) Jaiser, S., Müller, M., Baunach, M., Bauer, W., Scharfer, P., and Schabel, W. (2016). Investigation of film solidification and binder migration during drying of Li-Ion battery anodes. *J. Power Sources* *318*, 210–219. [10.1016/j.jpowsour.2016.04.018](https://doi.org/10.1016/j.jpowsour.2016.04.018).
- (13) Nguyen, T.-T., Demortière, A., Fleutot, B., Delobel, B., Delacourt, C., and Cooper, S.J. (2020). The electrode tortuosity factor: why the conventional tortuosity factor is not well suited for quantifying transport in porous Li-ion battery electrodes and what to use instead. *Npj Comput. Mater.* *6*, 1–12. [10.1038/s41524-020-00386-4](https://doi.org/10.1038/s41524-020-00386-4).
- (14) Lu, X., Daemi, S.R., Bertei, A., Kok, M.D.R., O'Regan, K.B., Rasha, L., Park, J., Hinds, G., Kendrick, E., Brett, D.J.L., et al. (2020). Microstructural Evolution of Battery Electrodes During Calendering. *Joule* *4*, 2746–2768. [10.1016/j.joule.2020.10.010](https://doi.org/10.1016/j.joule.2020.10.010).
- (15) Xu, R., Yang, Y., Yin, F., Liu, P., Cloetens, P., Liu, Y., Lin, F., and Zhao, K. (2019). Heterogeneous damage in Li-ion batteries: Experimental analysis and theoretical modeling. *J. Mech. Phys. Solids* *129*, 160–183. [10.1016/j.jmps.2019.05.003](https://doi.org/10.1016/j.jmps.2019.05.003).
- (16) Huang, C., Leung, C.L.A., Leung, P., and Grant, P.S. (2021). A Solid-State Battery Cathode with a Polymer Composite Electrolyte and Low Tortuosity Microstructure by Directional Freezing and Polymerization. *Adv. Energy Mater.* *11*, 2002387. [10.1002/aenm.202002387](https://doi.org/10.1002/aenm.202002387).
- (17) Delattre, B., Amin, R., Sander, J., Coninck, J.D., Tomsia, A.P., and Chiang, Y.-M. (2018). Impact of Pore Tortuosity on Electrode Kinetics in Lithium Battery Electrodes: Study in Directionally Freeze-Cast  $\text{LiNi}_0.8\text{Co}_0.15\text{Al}_0.05\text{O}_2$  (NCA). *J. Electrochem. Soc.* *165*, A388. [10.1149/2.1321802jes](https://doi.org/10.1149/2.1321802jes).
- (18) Billaud, J., Bouville, F., Magrini, T., Villeveille, C., and Studart, A.R. (2016). Magnetically aligned graphite electrodes for high-rate performance Li-ion batteries. *Nat. Energy* *1*, 1–6. [10.1038/nenergy.2016.97](https://doi.org/10.1038/nenergy.2016.97).
- (19) Li, L., Erb, R.M., Wang, J., Wang, J., and Chiang, Y.-M. (2019). Fabrication of Low-Tortuosity Ultrahigh-Area-Capacity Battery Electrodes through Magnetic Alignment of Emulsion-Based Slurries. *Adv. Energy Mater.* *9*, 1802472. [10.1002/aenm.201802472](https://doi.org/10.1002/aenm.201802472).
- (20) Sander, J.S., Erb, R.M., Li, L., Gurijala, A., and Chiang, Y.-M. (2016). High-performance battery electrodes via magnetic templating. *Nat. Energy* *1*, 1–7. [10.1038/nenergy.2016.99](https://doi.org/10.1038/nenergy.2016.99).
- (21) Chen, K.-H., Namkoong, M.J., Goel, V., Yang, C., Kazemiabnavi, S., Mortuza, S.M., Kazyak, E., Mazumder, J., Thornton, K., Sakamoto, J., et al. (2020). Efficient fast-charging of lithium-ion batteries enabled by laser-patterned three-dimensional graphite anode architectures. *J. Power Sources* *471*, 228475. [10.1016/j.jpowsour.2020.228475](https://doi.org/10.1016/j.jpowsour.2020.228475).
- (22) Singh, D.P., George, A., Kumar, R.V., ten Elshof, J.E., and Wagemaker, M. (2013). Nanostructured  $\text{TiO}_2$  Anatase Micropatterned Three-Dimensional Electrodes for High-Performance Li-Ion Batteries. *J. Phys. Chem. C* *117*, 19809–19815. [10.1021/jp3118659](https://doi.org/10.1021/jp3118659).

2. A phase inversion strategy for low tortuosity, ultrahigh mass loading Nickel-rich layered oxide electrodes

- (23) Singh, D.P., Mulder, F.M., Abdelkader, A.M., and Wagemaker, M. (2013). Facile Micro Templating LiFePO<sub>4</sub> Electrodes for High Performance Li-Ion Batteries. *Adv. Energy Mater.* *3*, 572–578. 10.1002/aenm.201200704.
- (24) Boyce, A.M., Cumming, D.J., Huang, C., Zankowski, S.P., Grant, P.S., Brett, D.J.L., and Shearing, P.R. (2021). Design of Scalable, Next-Generation Thick Electrodes: Opportunities and Challenges. *ACS Nano* *15*, 18624–18632. 10.1021/acsnano.1c09687.
- (25) Kwade, A., Haselrieder, W., Leithoff, R., Modlinger, A., Dietrich, F., and Droeder, K. (2018). Current status and challenges for automotive battery production technologies. *Nat. Energy* *3*, 290–300. 10.1038/s41560-018-0130-3.
- (26) Kingsbury, B.F.K., and Li, K. (2009). A morphological study of ceramic hollow fibre membranes. *J. Membr. Sci.* *328*, 134–140. 10.1016/j.memsci.2008.11.050.
- (27) van de Witte, P., Dijkstra, P.J., van den Berg, J.W.A., and Feijen, J. (1996). Phase separation processes in polymer solutions in relation to membrane formation. *J. Membr. Sci.* *117*, 1–31. 10.1016/0376-7388(96)00088-9.
- (28) Lee, M., Wang, B., Wu, Z., and Li, K. (2015). Formation of micro-channels in ceramic membranes – Spatial structure, simulation, and potential use in water treatment. *J. Membr. Sci.* *483*, 1–14. 10.1016/j.memsci.2015.02.023.
- (29) Hołda, A.K., and Vankelecom, I.F.J. (2015). Understanding and guiding the phase inversion process for synthesis of solvent resistant nanofiltration membranes. *J. Appl. Polym. Sci.* *132*. 10.1002/app.42130.
- (30) Jacquemond, R.R., Wan, C.T.-C., Chiang, Y.-M., Borneman, Z., Brushett, F.R., Nijmeijer, K., and Forner-Cuenca, A. (2022). Microstructural engineering of high-power redox flow battery electrodes via non-solvent induced phase separation. *Cell Rep. Phys. Sci.* *3*, 100943. 10.1016/j.xcrp.2022.100943.
- (31) Wan, C.T.-C., Jacquemond, R.R., Chiang, Y.-M., Nijmeijer, K., Brushett, F.R., and Forner-Cuenca, A. (2021). Non-Solvent Induced Phase Separation Enables Designer Redox Flow Battery Electrodes. *Adv. Mater.* *33*, 2006716. 10.1002/adma.202006716.
- (32) Yang, X., Chen, Y., Wang, M., Zhang, H., Li, X., and Zhang, H. (2016). Phase Inversion: A Universal Method to Create High-Performance Porous Electrodes for Nanoparticle-Based Energy Storage Devices. *Adv. Funct. Mater.* *26*, 8427–8434. 10.1002/adfm.201604229.
- (33) Wahyudi, W., Cao, Z., Kumar, P., Li, M., Wu, Y., Hedhili, M.N., Anthopoulos, T.D., Cavallo, L., Li, L.-J., and Ming, J. (2018). Phase Inversion Strategy to Flexible Freestanding Electrode: Critical Coupling of Binders and Electrolytes for High Performance Li–S Battery. *Adv. Funct. Mater.* *28*, 1802244. 10.1002/adfm.201802244.
- (34) Harks, P.-P.R.M.L., Robledo, C.B., George, C., Wang, C., van Dijk, T., Sturkenboom, L., Roesink, E.D.W., and Mulder, F.M. (2019). Immersion precipitation route towards high performance thick and flexible electrodes for Li-ion batteries. *J. Power Sources* *441*, 227200. 10.1016/j.jpowsour.2019.227200.
- (35) Wu, J., Ju, Z., Zhang, X., Quilty, C., Takeuchi, K.J., Bock, D.C., Marschilok, A.C., Takeuchi, E.S., and Yu, G. (2021). Ultrahigh-Capacity and Scalable Architected Battery Electrodes via Tortuosity Modulation. *ACS Nano* *15*, 19109–19118. 10.1021/acsnano.1c06491.

2. A phase inversion strategy for low tortuosity, ultrahigh mass loading Nickel-rich layered oxide electrodes

- (36) Jimenez, N.P., Balogh, M.P., and Halalay, I.C. (2021). High Porosity Single-Phase Silicon Negative Electrode Made with Phase-Inversion. *J. Electrochem. Soc.* 168, 040507. 10.1149/1945-7111/abe3f1.
- (37) Evenepoel, N., Wen, S., Tilahun Tsehaye, M., and Van der Bruggen, B. (2018). Potential of DMSO as greener solvent for PES ultra- and nanofiltration membrane preparation. *J. Appl. Polym. Sci.* 135, 46494. 10.1002/app.46494.
- (38) Wang, M., Dong, X., Escobar, I.C., and Cheng, Y.-T. (2020). Lithium Ion Battery Electrodes Made Using Dimethyl Sulfoxide (DMSO)—A Green Solvent. *ACS Sustain. Chem. Eng.* 8, 11046–11051. 10.1021/acssuschemeng.0c02884.
- (39) Li, S.Y., and Church, B.C. (2016). Effect of aqueous-based cathode slurry pH and immersion time on corrosion of aluminum current collector in lithium-ion batteries. *Mater. Corros.* 67, 978–987. 10.1002/maco.201608843.
- (40) Bresser, D., Buchholz, D., Moretti, A., Varzi, A., and Passerini, S. (2018). Alternative binders for sustainable electrochemical energy storage – the transition to aqueous electrode processing and bio-derived polymers. *Energy Environ. Sci.* 11, 3096–3127. 10.1039/C8EE00640G.
- (41) Hansen, C.M. (2007). *Hansen Solubility Parameters: A User's Handbook*, Second Edition 2nd ed. (CRC Press) 10.1201/9781420006834.
- (42) Bottino, A., Capannelli, G., Munari, S., and Turturro, A. (1988). Solubility parameters of poly(vinylidene fluoride). *J. Polym. Sci. Part B Polym. Phys.* 26, 785–794. <https://doi.org/10.1002/polb.1988.090260405>.
- (43) PubChem Ethanol. <https://pubchem.ncbi.nlm.nih.gov/compound/702>.
- (44) Yuan, S., Zou, C., Yin, H., Chen, Z., and Yang, W. (2015). Study on the separation of binary azeotropic mixtures by continuous extractive distillation. *Chem. Eng. Res. Des.* 93, 113–119. 10.1016/j.cherd.2014.05.005.
- (45) Chau, J., and Sirkar, K.K. (2021). Organic solvent mixture separation during reverse osmosis and nanofiltration by a perfluorodioxole copolymer membrane. *J. Membr. Sci.* 618, 118663. 10.1016/j.memsci.2020.118663.
- (46) Wang, B., and Lai, Z. (2012). Finger-like voids induced by viscous fingering during phase inversion of alumina/PES/NMP suspensions. *J. Membr. Sci.* 405–406, 275–283. 10.1016/j.memsci.2012.03.020.
- (47) Montina, T., Wormald, P., and Hazendonk, P. (2012). <sup>13</sup>C Solid-State NMR of the Mobile Phase of Poly(vinylidene fluoride). *Macromolecules* 45, 6002–6007. 10.1021/ma3013477.
- (48) Moškon, J., Žuntar, J., Talian, S.D., Dominko, R., and Gaberšček, M. (2020). A Powerful Transmission Line Model for Analysis of Impedance of Insertion Battery Cells: A Case Study on the NMC-Li System. *J. Electrochem. Soc.* 167, 140539. 10.1149/1945-7111/abc769.J.
- (49) Landesfeind, J., Hattendorff, J., Ehrl, A., Wall, W.A., and Gasteiger, H.A. (2016). Tortuosity Determination of Battery Electrodes and Separators by Impedance Spectroscopy. *J. Electrochem. Soc.* 163, A1373. 10.1149/2.1141607jes.

2. A phase inversion strategy for low tortuosity, ultrahigh mass loading Nickel-rich layered oxide electrodes

- (50) Pouraghajan, F., Knight, H., Wray, M., Mazzeo, B., Subbaraman, R., Christensen, J., and Wheeler, D. (2018). Quantifying Tortuosity of Porous Li-Ion Battery Electrodes: Comparing Polarization-Interrupt and Blocking-Electrolyte Methods. *J. Electrochem. Soc.* 165, A2644. 10.1149/2.0611811jes.
- (51) Morasch, R., Landesfeind, J., Suthar, B., and Gasteiger, H.A. (2018). Detection of Binder Gradients Using Impedance Spectroscopy and Their Influence on the Tortuosity of Li-Ion Battery Graphite Electrodes. *J. Electrochem. Soc.* 165, A3459. 10.1149/2.1021814jes.
- (52) Shodiev, A., Primo, E.N., Chouchane, M., Lombardo, T., Ngandjong, A.C., Rucci, A., and Franco, A.A. (2020). 4D-resolved physical model for Electrochemical Impedance Spectroscopy of Li(Ni<sub>1-x</sub>YMn<sub>x</sub>Co<sub>y</sub>)O<sub>2</sub>-based cathodes in symmetric cells: Consequences in tortuosity calculations. *J. Power Sources* 454, 227871. 10.1016/j.jpowsour.2020.227871.
- (53) Doyle, M., Fuller, T.F., and Newman, J. (1993). Modeling of Galvanostatic Charge and Discharge of the Lithium/Polymer/Insertion Cell. *J. Electrochem. Soc.* 140, 1526–1533. 10.1149/1.2221597.
- (54) Fuller, T.F., Doyle, M., and Newman, J. (1994). Simulation and Optimization of the Dual Lithium Ion Insertion Cell. *J. Electrochem. Soc.* 141, 1–10. 10.1149/1.2054684.
- (55) Ferguson, T.R., and Bazant, M.Z. (2012). Nonequilibrium Thermodynamics of Porous Electrodes. *J. Electrochem. Soc.* 159, A1967–A1985. 10.1149/2.048212jes.
- (56) Vasileiadis, A., de Klerk, N.J.J., Smith, R.B., Ganapathy, S., Harks, P.P.R.M.L., Bazant, M.Z., and Wagemaker, M. (2018). Toward Optimal Performance and In-Depth Understanding of Spinel Li<sub>4</sub>Ti<sub>5</sub>O<sub>12</sub> Electrodes through Phase Field Modeling. *Adv. Funct. Mater.* 28, 1705992. 10.1002/adfm.201705992.
- (57) Ombrini, P., Bazant, M.Z., Wagemaker, M., and Vasileiadis, A. (2023). Thermodynamics of multi-sublattice battery active materials: from an extended regular solution theory to a phase-field model of LiMnyFe<sub>1-y</sub>PO<sub>4</sub>. *Npj Comput. Mater.* 9, 148. 10.1038/s41524-023-01109-1.
- (58) Schwietert, T.K., Ombrini, P., Ootes, L.S., Oostrum, L., Azizi, V., Cogswell, D., Zhu, J., Bazant, M.Z., Wagemaker, M., and Vasileiadis, A. (2023). Phase-Field Computational Framework for Addressing Challenges in Solid-State Batteries. *PRX Energy* 2, 033014. 10.1103/PRXEnergy.2.033014.
- (59) Galuppini, G., Berliner, M.D., Cogswell, D.A., Zhuang, D., Bazant, M.Z., and Braatz, R.D. (2023). Nonlinear identifiability analysis of Multiphase Porous Electrode Theory-based battery models: A Lithium Iron Phosphate case study. *J. Power Sources* 573, 233009. 10.1016/j.jpowsour.2023.233009.
- (60) Sulzer, V., Marquis, S.G., Timms, R., Robinson, M., and Chapman, S.J. (2021). Python Battery Mathematical Modelling (PyBaMM). 9, 14. 10.5334/jors.309.
- (61) Andersson, M., Streb, M., Ko, J.Y., Löfqvist Klass, V., Klett, M., Ekström, H., Johansson, M., and Lindbergh, G. (2022). Parametrization of physics-based battery models from input–output data: A review of methodology and current research. *J. Power Sources* 521, 230859. 10.1016/j.jpowsour.2021.230859.

2. A phase inversion strategy for low tortuosity, ultrahigh mass loading Nickel-rich layered oxide electrodes

- (62) Wang, A.A., O’Kane, S.E.J., Planella, F.B., Houx, J.L., O’Regan, K., Zyskin, M., Edge, J., Monroe, C.W., Cooper, S.J., Howey, D.A., et al. (2022). Review of parameterisation and a novel database (LiionDB) for continuum Li-ion battery models. *Prog. Energy* 4, 032004. 10.1088/2516-1083/ac692c.
- (63) Wang, Q., Zhao, C., Yao, Z., Wang, J., Wu, F., Kumar, S.G.H., Ganapathy, S., Eustace, S., Bai, X., Li, B., et al. (2023). Entropy-Driven Liquid Electrolytes for Lithium Batteries. *Adv. Mater.* 35, 2210677. 10.1002/adma.202210677.
- (64) Wang, Q., Zhao, C., Wang, J., Yao, Z., Wang, S., Kumar, S.G.H., Ganapathy, S., Eustace, S., Bai, X., Li, B., et al. (2023). High entropy liquid electrolytes for lithium batteries. *Nat. Commun.* 14, 440. 10.1038/s41467-023-36075-1.
- (65) Louli, A.J., Eldesoky, A., Weber, R., Genovese, M., Coon, M., deGooyer, J., Deng, Z., White, R.T., Lee, J., Rodgers, T., et al. (2020). Diagnosing and correcting anode-free cell failure via electrolyte and morphological analysis. *Nat. Energy*, 1–10. 10.1038/s41560-020-0668-8.
- (66) Standard Test Methods for Vulcanized Rubber and Thermoplastic Elastomers—Tension <https://www.astm.org/d0412-16r21.html>.
- (67) Ogihara, N., Kawauchi, S., Okuda, C., Itou, Y., Takeuchi, Y., and Ukyo, Y. (2012). Theoretical and Experimental Analysis of Porous Electrodes for Lithium-Ion Batteries by Electrochemical Impedance Spectroscopy Using a Symmetric Cell. *J. Electrochem. Soc.* 159, A1034. 10.1149/2.057207jes.
- (68) Smith, R.B., and Bazant, M.Z. (2017). Multiphase Porous Electrode Theory. *J. Electrochem. Soc.* 164, E3291. 10.1149/2.0171711jes.
- (69) Doyle, M., Fuller, T.F., and Newman, J. (1993). Modeling of Galvanostatic Charge and Discharge of the Lithium/Polymer/Insertion Cell. *J. Electrochem. Soc.* 140, 1526. 10.1149/1.2221597.
- (70) Balu, B., and Khair, A.S. (2018). Role of Stefan–Maxwell fluxes in the dynamics of concentrated electrolytes. *Soft Matter* 14, 8267–8275. 10.1039/C8SM01222A
- (71) Nyman, A., Behm, M., and Lindbergh, G. (2008). Electrochemical characterisation and modelling of the mass transport phenomena in LiPF<sub>6</sub>–EC–EMC electrolyte. *Electrochimica Acta* 53, 6356–6365. 10.1016/j.electacta.2008.04.023.
- (72) McClelland, I., Booth, S.G., Anthonisamy, N.N., Middlemiss, L.A., Pérez, G.E., Cussen, E.J., Baker, P.J., and Cussen, S.A. (2023). Direct Observation of Dynamic Lithium Diffusion Behavior in Nickel-Rich, LiNi<sub>0.8</sub>Mn<sub>0.1</sub>Co<sub>0.1</sub>O<sub>2</sub> (NMC811) Cathodes Using *Operando* Muon Spectroscopy. *Chem. Mater.* 35, 4149–4158. 10.1021/acs.chemmater.2c03834.
- (73) R. Jung, M. Metzger, F. Maglia, C. Stinner, H.A. Gasteiger, Oxygen Release and Its Effect on the Cycling Stability of LiNixMnyCozO2 (NMC) Cathode Materials for Li-Ion Batteries, *J. Electrochem. Soc.* 164 (2017) A1361. <https://doi.org/10.1149/2.0021707jes>.
- (74) R.J. Good, R.Sh. Mikhail, The contact angle in mercury intrusion porosimetry, *Powder Technol.* 29 (1981) 53–62. [https://doi.org/10.1016/0032-5910\(81\)85004-8](https://doi.org/10.1016/0032-5910(81)85004-8).
- (75) Standard Test Method for Peel Resistance of Adhesives (T-Peel Test), (n.d.). <https://www.astm.org/d1876-08r15e01.html> (accessed August 10, 2023).

## Supporting Information

### Hansen Solubility Parameters for common solvents/non-solvents and their solubility with PVDF

Hansen Solubility parameters, developed by Charles Hansen, provide a measure of the relative solubility of two materials. Each material is defined by three Hansen parameters (typically measured in MPa), i.e.,  $\delta_d$  corresponds to intermolecular dispersion forces,  $\delta_p$  corresponds to intermolecular dipolar forces, and  $\delta_h$  corresponds to intermolecular hydrogen bond forces.

The relative solubility between the parameters is then given by the parameters Ra, the distance between the Hansen parameters of the two materials in the 3D Hansen space, which is calculated as:

$$(Ra)^2 = 4(\delta_{d2} - \delta_{d1})^2 + (\delta_{p2} - \delta_{p1})^2 + (\delta_{h2} - \delta_{h1})^2$$

The Hansen solubility parameters for commonly used solvents are obtained from the Hansen Solubility Parameters Handbook,<sup>[41]</sup> while the solubility parameters of PVDF are obtained from the work of Bottino et. al.<sup>[42]</sup>

**Table S1.** Hansen solubility parameters for commonly used solvents, non-solvents, and PVDF

Compound	$\delta_d$ (MPa)	$\delta_p$ (MPa)	$\delta_h$ (MPa)	Ra (solubility parameter) with PVDF
PVDF	17.2	12.5	9.2	0
N, N-dimethylacetamide (DMAc)	16.8	11.5	10.2	1.62
N, N-dimethylformamide (DMF)	17.4	13.7	11.3	2.45
N-methyl-2-pyrrolidone (NMP)	18	12.3	7.2	2.57
Acetone	15.5	10.4	7	4.56
Dimethylsulfoxide (DMSO)	18.4	16.4	10.2	4.69
Tetrahydrofuran (THF)	16.8	5.7	8	6.95
Acetic acid	14.5	8	13.5	8.24
Propylene- 1,2-carbonate (PC)	20	18	4.1	9.36
1-Butanol	16	5.7	15.8	9.77
1-Propanol	16	6.8	17.4	10.27
Ethanol	15.8	8.8	19.4	11.21
Methanol	15.1	12.3	22.3	13.76
Ethylene glycol	17	11	26	16.87
Glycerol	17.4	12.1	29.3	20.11
Water	15.5	16	42.3	33.46

2. A phase inversion strategy for low tortuosity, ultrahigh mass loading Nickel-rich layered oxide electrodes

### Viscosity effects on phase inversion processing

The cathode slurry solvent-to-binder ratio is an adjustable parameter that changes cathode structures significantly during phase inversion. High viscosity slurries with 1:10 PVDF:Solvent ratio yield uneven pore and height distributions (Figure S1, top left). A solvent ratio of 1:12 yields targeted pore diameters of a few micrometers (Figure S1, top left), which serve as ion channels to the deeper layers of the electrode. Higher dilutions barely show structural change, which can be explained by the minor change in the viscosity of the slurry above the 1:12 binder-to-solvent ratio (Figure S1, bottom left). DMSO shows a more significant temperature dependence than NMP-based slurries (Figure S1, bottom right). NMP is chosen as the solvent for subsequent slurry processing to prevent this large temperature-induced effect.

2

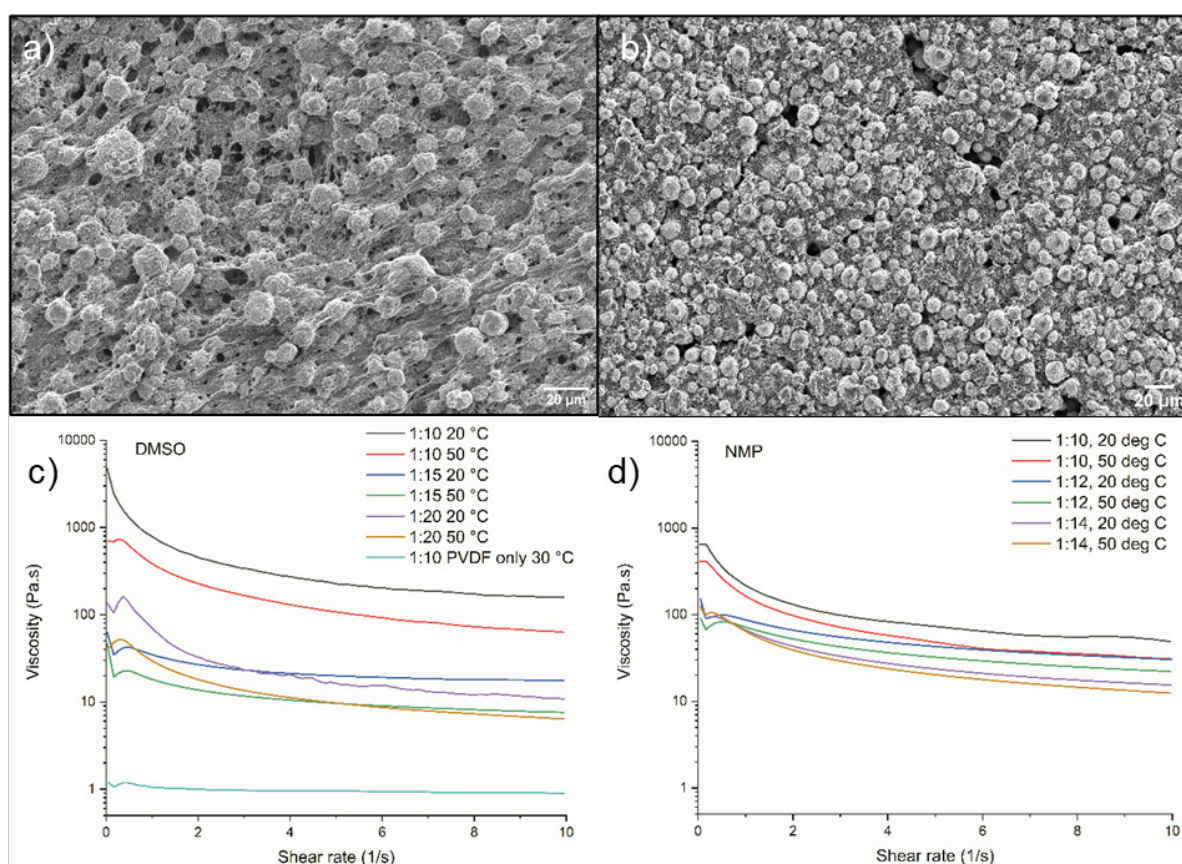
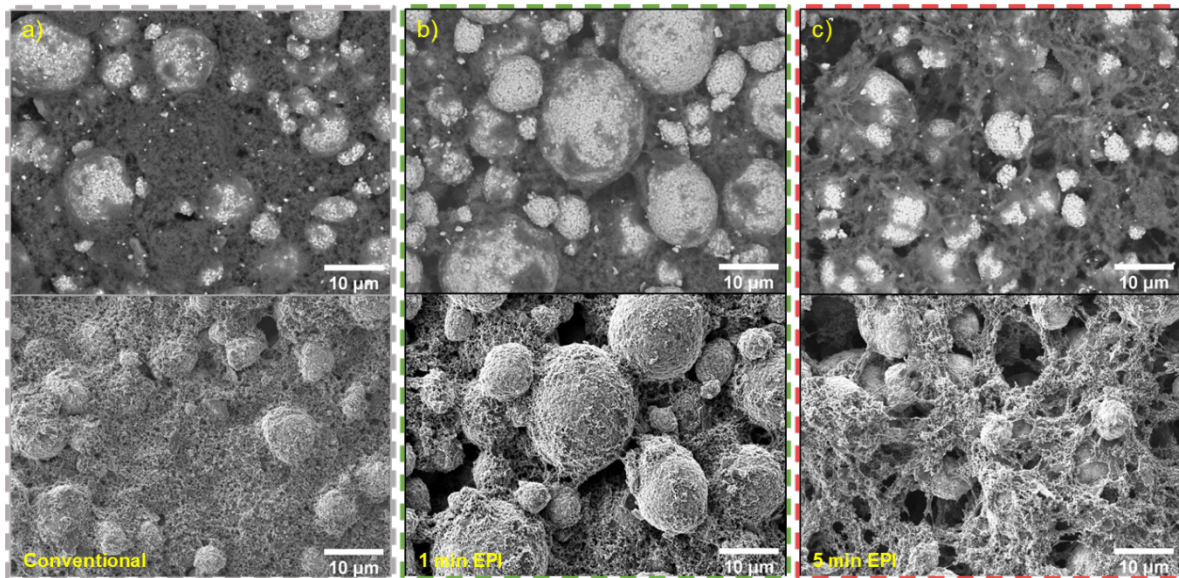


**Figure S1. Influence of viscosity on phase inversion processing.** The low solvent-to-binder ratio (1:10 PVDF:DMSO) causes uneven pore distributions (a) during the phase inversion processing compared to processing using a higher solvent-to-binder ratio (1:12 PVDF:DMSO, b). This can be explained by the viscosity change of DMSO, which has a high temperature and binder/solvent ratio dependence (c). For NMP, this dependence is much lower (d).

2. A phase inversion strategy for low tortuosity, ultrahigh mass loading Nickel-rich layered oxide electrodes



2

**Figure S2. Top view SEM images (Backscattered electron mode on top, secondary electron incidence mode below) of uncalendered NMC811 electrodes: a) conventional, b) phase inversion (1 min exchange), c) phase inversion (5 min exchange) electrodes**

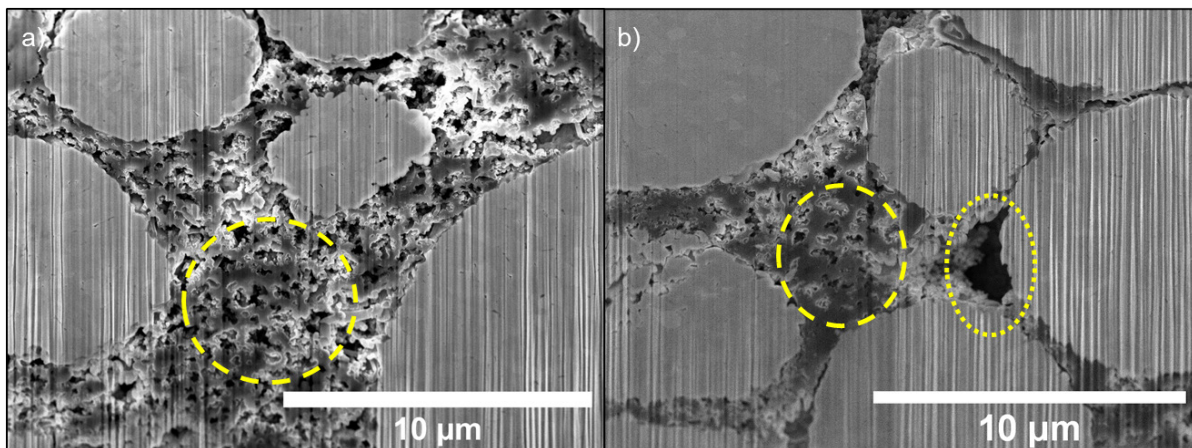


**Figure S3. Zoomed cross-section FIB-SEM of CBD structures after calendaring: a) conventional electrodes, b) EPI electrodes. The dashed ellipse indicates CBD with micropores, and the dotted ellipse indicates macropores.**

2. A phase inversion strategy for low tortuosity, ultrahigh mass loading Nickel-rich layered oxide electrodes

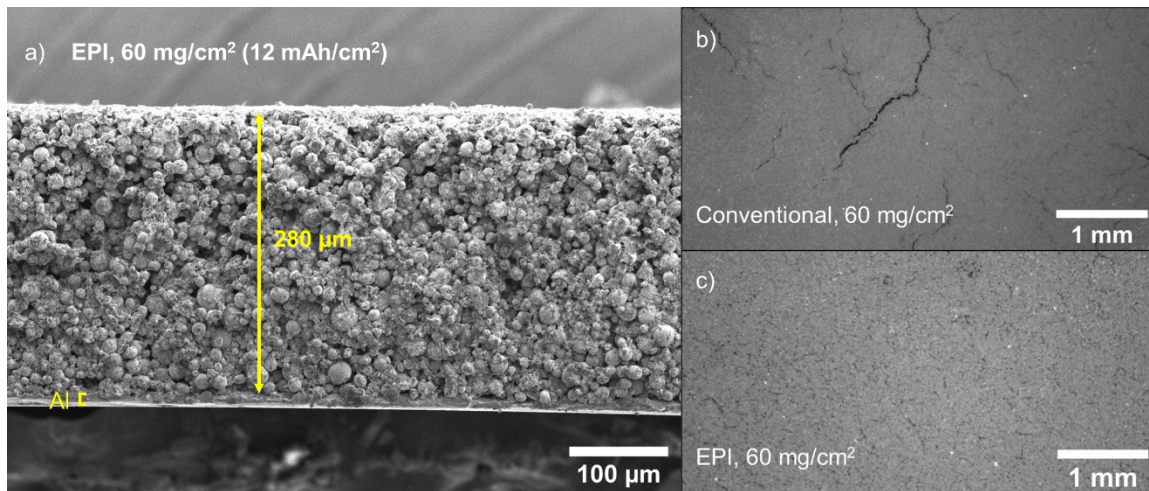


**Figure S4. NMC811 electrodes at ultrahigh mass loadings:** a) Cross-section SEM of EPI NMC811 electrode with active mass loading of 60 mg/cm<sup>2</sup> and 30% porosity. b) Top view optical micrograph of 60 mg/cm<sup>2</sup> Conventional NMC811 electrode (30% porosity) c) Top view optical micrograph of 60 mg/cm<sup>2</sup> EPI NMC811 electrode (30% porosity)

2. A phase inversion strategy for low tortuosity, ultrahigh mass loading Nickel-rich layered oxide electrodes

### Porosity calculation and MIP porosity measurements

For apparent porosity, the cathode volume is first calculated from thickness measurements by multiplying a representative area  $A_{cat}$  with thickness  $d_{cat}$ . Volume fractions of the cathode body are calculated by dividing the mass fractions  $x_{m,x}$  with the components' individual densities  $\rho_x$ , summation, and multiplication with the weighed cathode mass. Dividing the cathode body mass with the cathode volume then gives the volume fraction of the body, of which the porosity is calculated by subtracting 1 minus this value.

$$d_{cat} = \frac{M_{cat}}{A_{cat}} \left( \frac{x_{m,AM}}{\rho_{AM}} + \frac{x_{m,CB}}{\rho_{CB}} + \frac{x_{m,PVDF}}{\rho_{PVDF}} + \frac{x_{m,KS4}}{\rho_{KS4}} \right) / (1 - \varepsilon) = d_{cat,body} / (1 - \varepsilon)$$

While the particle density typically used in apparent porosity calculations for NMC/NCA electrodes is the secondary particle density (3.75 kg/dm<sup>3</sup> in this case), the intrusion of mercury at high pressures can also provide it access to the void volume between the primary crystallites of these particles, typically not accessible to the electrolyte on assembly using these electrodes. Therefore, the single crystallite particle density of 4.8 kg/dm<sup>3</sup> has been considered for estimating the cathode body volume fraction used in the case of MIP.<sup>[73]</sup>

The mercury extrusion volume provides a measure of the amount of mercury expelled from the microporous structure because of the high surface tension (contact angles near 180°)<sup>[74]</sup>. With this volume, the fraction of fine structural porosity can be estimated. On calendered cathodes, the extrusion volume fraction yields 28% porosity for conventional cathodes and 31% for EPI cathodes. In comparison, the apparent porosities, as measured by comparing the areal mass loading and the cathode thickness, were 29% and 31% respectively. With the EPI uncalendered sample, the apparent porosity of 46%, however, exceeds the MIP extrusion porosity of 18% as the droplet size of mercury becomes smaller than the size of the macropores (>15 μm at 0.1 MPa) and the mercury is not expelled as a result.

**Table S2.** Densities of NMC811 electrode components

Compound	Density (kg/dm <sup>3</sup> )
NMC811 (crystallographic density)	4.8
NMC811 (secondary particle density)	3.75
PVDF	1.78
Carbon (used for KS4 and CB)	1.9

2. A phase inversion strategy for low tortuosity, ultrahigh mass loading Nickel-rich layered oxide electrodes

**Table S3.** Apparent porosities and Microporosities of freestanding NMC811 electrodes calculated from Mercury intrusion porosimetry

Electrode	Extrusion volume (mL/g)	Loading (mg/cm <sup>2</sup> )	Measured Thickness (μm)	Mass / body volume of cathode (mg/mm <sup>3</sup> )	Body Volume cathode (mm <sup>3</sup> /cm <sup>2</sup> )	Total Volume cathode (mm <sup>3</sup> /cm <sup>2</sup> )	Apparent porosity (mm/mm)	Microporosity (mm/mm)
Conventional calendered	0.09	53.41	175.33	0.24	12.55	17.53	0.28	0.29
Conventional uncalendered	0.09	53.41	178.20	0.24	12.55	17.82	0.30	0.27
EPI calendered	0.11	47.54	163.00	0.24	11.17	14.90	0.31	0.31
EPI mild calendered	0.15	47.54	174.20	0.24	11.17	17.42	0.36	0.40
EPI uncalendered	0.08	47.54	200.00	0.24	11.17	20.00	0.44	0.18

2. A phase inversion strategy for low tortuosity, ultrahigh mass loading Nickel-rich layered oxide electrodes

### Adhesion strength measurements

Similar to the tensile strength measurements, the t-peel adhesion strength measurements were performed on the ZwickRoell 10 kN universal testing machine. For the adhesion strength measurement, the electrodes were cut into strips of 100x15 mm. A 3M VHB double-sided tape was applied onto the strips, with about 20 mm of the tape/electrode remaining unbound. These strips were placed under ~1 kg steel blocks overnight to ensure good adhesion. The peel test was performed similar to ASTM D1876-08.<sup>[75]</sup> The unbound part of the tape/electrode was used to clamp the sample onto the test setup in a t-position, with a 20 mm gap between the clamps. A 100N loadcell (Zwick) was connected to the setup. The tape was peeled off from the electrode at a constant speed of 200 mm/min.

2

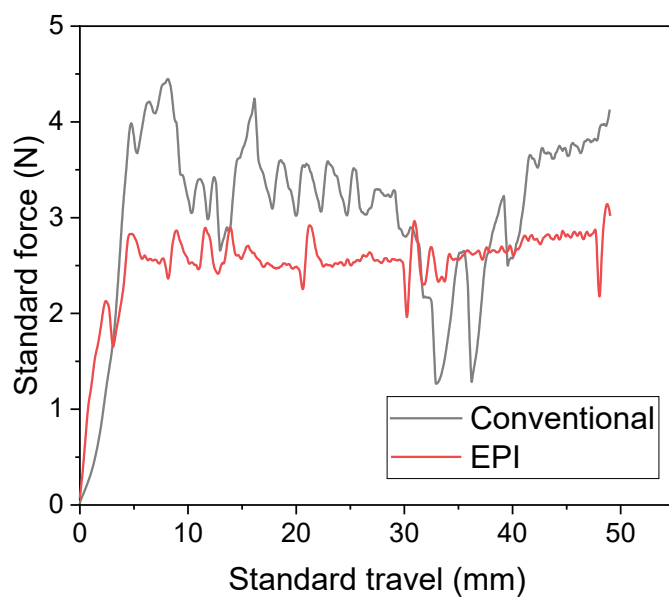


**Figure S5. Peel off force vs. travel distance for 35 mg/cm<sup>2</sup> active mass loading NMC811 electrodes on Al current collector.**

With the T-peel adhesion strength measurements, it was observed that while the EPI electrodes with active mass loading of 35 mg/cm<sup>2</sup> and 30% porosity) peeled off from the current collector at a nearly constant force, the conventional electrode peeled off at highly varying forces, highlighting uneven adhesion of the electrode to the current collector at these thicknesses.

2. A phase inversion strategy for low tortuosity, ultrahigh mass loading Nickel-rich layered oxide electrodes

### Electrochemical Impedance Spectroscopy for Li/LP57 electrolyte/NMC811 cells

The equivalent circuit used in fitting the EIS spectra is displayed in Figure 3e, and the corresponding resistance values are shown below:

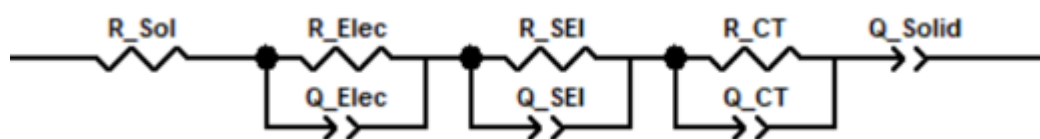


Figure S6. The equivalent circuit used for fitting the EIS data.

Table S4. Fitted R values for the EIS spectra shown in Figure 3e

Component	Conventional	EPI
Electrolyte Resistance, $R_{Sol}$ ( $\Omega \cdot \text{cm}^2$ )	4.51	4.76
Electronic Resistance (overall), $R_{Elec}$ ( $\Omega \cdot \text{cm}^2$ )	13.07	12.03
Li-SEI Resistance, $R_{SEI}$ ( $\Omega \cdot \text{cm}^2$ )	11.48	12.46
Cathode charge transfer Resistance, $R_{CT}$ ( $\Omega \cdot \text{cm}^2$ )	7.79	5.5

2. A phase inversion strategy for low tortuosity, ultrahigh mass loading Nickel-rich layered oxide electrodes

### DC electronic resistance of electrodes

The through-plane (two-point) electronic conductivity was measured by pressing the electrode(s) between two stainless steel metal plates (**Table S5**). To mitigate contact resistance due to surface roughness, the electrodes were subjected to gold sputtering (~ 10 nm). Gold sputtering indeed leads to a lower measured electronic resistance. This, however, may be a combined effect of gold plating on the electrode surface and on the material at the pore entrance. Therefore, the electronic resistance values for the non-gold-plated electrodes are reported in the main text.

**Table S5.** DC electronic resistance of electrodes perpendicular to the plane

Component	Conventional	EPI
Non gold plated [ $\Omega\cdot\text{cm}^2$ ]	18.42	18.16
Gold plated [ $\Omega\cdot\text{cm}^2$ ]	11.11	6.11

2. A phase inversion strategy for low tortuosity, ultrahigh mass loading Nickel-rich layered oxide electrodes

### Electrochemical tortuosity factor measurements

Electrochemical tortuosity factors were calculated according to the following equation:<sup>[49]</sup>

$$\tau = \frac{\varepsilon \cdot R \cdot A \cdot \kappa}{2 \cdot d}$$

The terms and their corresponding values for the conventional and EPI electrodes are provided in the table below.

**Table S6.** Details of the electrochemical tortuosity factor calculations for the EIS plots shown in Figure 4a

Property	Conventional	EPI
Avg. Thickness, d ( $\mu\text{m}$ )	170	173
Avg. weight (mg)	55	56
Electrode (geometric) area, A ( $\text{cm}^2$ )	1.27	
Avg. porosity, $\varepsilon$	0.302	0.3015
Electrolyte conductivity, $\kappa$ (mS/cm)	0.77	
Ionic Resistance ( $\Omega \cdot \text{cm}^2$ ), R.A	512.48	357.28
Tortuosity factor, $\tau$	3.79	2.58

2. A phase inversion strategy for low tortuosity, ultrahigh mass loading Nickel-rich layered oxide electrodes

### Details of the P2D model

The P2D model (also known as the Doyle-Fuller-Newman model<sup>[54,69]</sup>) uses volume averaging to simulate a complete porous electrode. A set of particles is set along the simulation axes such that they react with the surrounding electrolyte depending on the local electrolyte potential. The electrolyte transport is simulated considering the porosity and the tortuosity factor as parameters that, respectively, multiply and divide the electrolyte conductivity and diffusivity. These models can be used to optimize the battery (dis)charge protocols or obtain information about the limiting factors of specific morphologies or materials. The computational efficiency of P2D models allows broad parameter estimation, such that variables like diffusivity, charge-transfer resistance, and tortuosity factor can be subjected to sensitivity analysis by fitting voltage curves at different rates.

The P2D model<sup>[54,69]</sup> was implemented in the open-source software MPET,<sup>[54,69]</sup> the complete set of porous electrode equations is shown by Smith et. al.,<sup>[68]</sup> we here summarize the tailored NMC811 model developed for this study. The particles were considered spherical and homogenous, following then the Fick's law of diffusion:

$$\frac{dc}{dt} = \nabla \cdot (D(c)\nabla c)$$

Where  $c$  is the Li concentration normalized to the maximum Li concentration, and  $D(c)$  is a concentration-dependent diffusivity.

The reaction rate was modeled using the Butler-Volmer equation with a concentration-dependent exchange current density  $k_0(c)$ :

$$j = k_0(c) c_{\text{elyte}}^{0.5} \left( e^{\frac{1}{2} \frac{e\eta}{k_B T}} - e^{-\frac{1}{2} \frac{e\eta}{k_B T}} \right)$$

Where  $c_{\text{elyte}}$  is the electrolyte concentration at the particle-electrolyte interface,  $\eta$  is the reaction overpotential,  $k_B$  is the Boltzmann constant,  $T$  is the temperature, and  $e$  is the electron charge.

Both diffusivities and exchange current density are given in literature<sup>[72]</sup> as relative values, since the absolute values can change depending on exposed surface area and particle shape. The model is then considering

$$D(c) = D_0 f_D(c)$$

And

$$k_0(c) = k_0^* f_{k_0}(c)$$

And fitting the experiments by changing the pre-factors. The values of the fitted parameters for the simulations are listed in **Table S7**.

## 2. A phase inversion strategy for low tortuosity, ultrahigh mass loading Nickel-rich layered oxide electrodes

The single discharge mean square error was calculated considering the square of the difference between the experimental and the simulated voltages,  $V_{\text{exp}}$  and  $V_{\text{sim}}$  in the collected  $N$  data points  $p$ . The total mean square error (MSE) for the various C-rates was calculated by summing them and multiplying for the square root of the C-rate in order to increase the weight of the higher rates, which contain more physical information about the transport limitations.

$$\text{MSE} = \sum_{C_{\text{rate}}} \left\{ \left[ \sum_p \frac{(V_{\text{exp}}(p) - V_{\text{sim}}(p))^2}{N} \right] \sqrt{C_{\text{rate}}} \right\}$$

To further clarify the parameter estimation, a summary of the effect of varying tortuosity factor and diffusivity on the simulated voltage curves is reported in Figure S7.

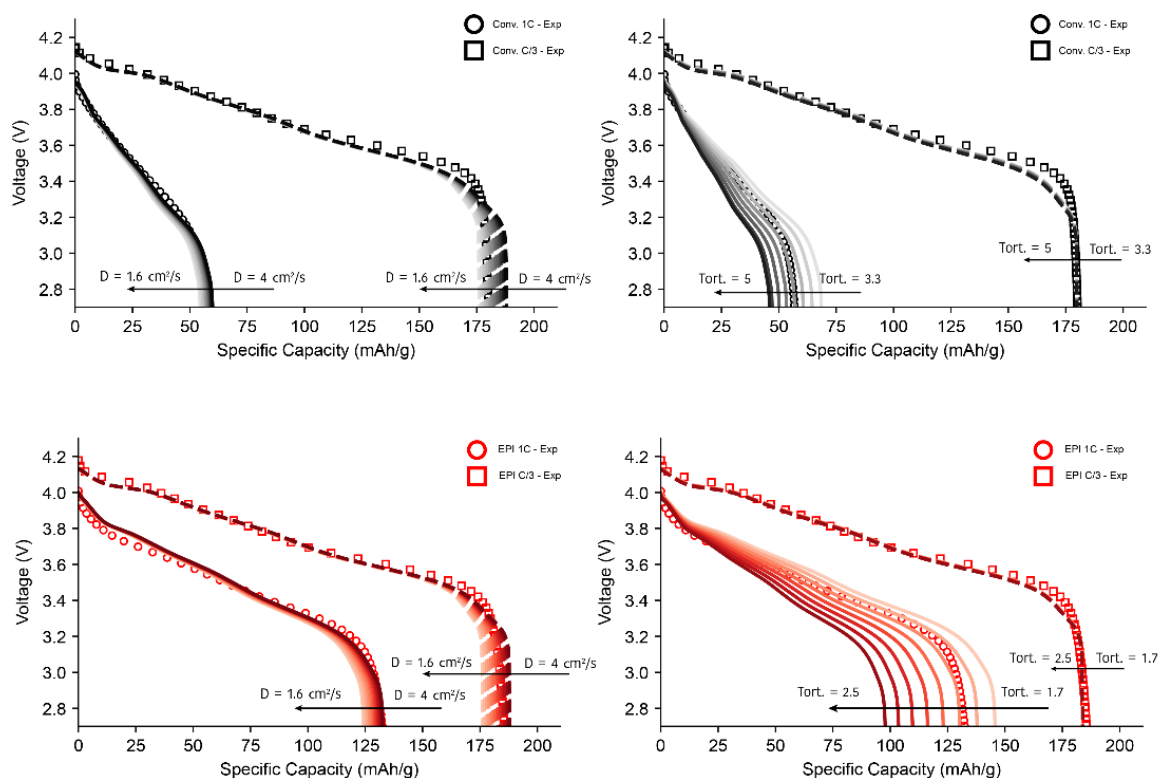


**Figure S7. Comparison of simulated and experimental voltage curves at different tortuosity and diffusivities.**

The simulated voltage curves show a non-linear effect of the variation of diffusivity and tortuosity factor. The change in diffusivity has a limited impact on the 1C curve since the main bottleneck for this rate is the electrolyte conductivity, which shows an increased sensitivity for the tortuosity factor. On the contrary, the diffusivity presents a greater effect on the utilized capacity of the C/3 discharge, since the transport overpotential for this rate is not the

2. A phase inversion strategy for low tortuosity, ultrahigh mass loading Nickel-rich layered oxide electrodes

main driver of the capacity losses, while the low diffusivity at high Li concentrations contributes greatly to the final drop of the voltage curve.

**Table S7.** P2D Simulation parameters

Parameter name	Value	Unit of measure	Origin
Particle Diffusion coefficient function, $f_D(c)$	$10^{(-66631.56 c^9 + 317224.13 c^8 + -647127.91 c^7 + 740625.61 c^6 + -522889.49 c^5 + 235652.79 c^4 + -67638.171 c^3 + 11887.013 c^2 + -1155.894 c + 37.601)}$	-	[72]
Particle Diffusion coefficient pre-factor conventional, $D_0$	$2.28 \cdot 10^{-9}$	$\text{cm}^2 \text{s}^{-1}$	Fitted
Particle Diffusion coefficient pre-factor EPI, $D_0$	$3.19 \cdot 10^{-9}$		Fitted
Exchange current density function, $f_{k_0}(c)$	$87.15 c^5 - 445.05 c^4 + 815.43 c^3 - 669.95 c^2 + 236.09 c - 23.67$	-	[72]
Exchange current density pre-factor conventional, $k_0^*$	2.48	$\text{A m}^{-2}$	Fitted
Exchange current density pre-factor EPI, $k_0^*$	3.5	$\text{A m}^{-2}$	Fitted
OCV	$(-0.8090 c + 4.4875 - 0.0428 \tanh(18.5138 (c - 0.5542)) \pm 17.7326 \tanh(15.7890 (c - 0.3117)) + 17.5842 \tanh(15.9308 (c - 0.3120)))$		[72]
Particle size	11.5	$\mu\text{m}$	Measured
Electrolyte conductivity	9.48 (for electrolyte concentration of 1 M)	$\text{mS/cm}$	[71]
Li metal\Li <sup>+</sup> exchange current density	2.056	$\text{A m}^{-2}$	Fitted

2. A phase inversion strategy for low tortuosity, ultrahigh mass loading Nickel-rich layered oxide electrodes

<b>Electronic conductivity</b>	1	mS cm <sup>-1</sup>	Measured
<b>Number of simulated particles</b>	20	-	
<b>Starting stoichiometry</b>	Li <sub>0.26</sub> Ni <sub>0.8</sub> Mn <sub>0.1</sub> Co <sub>0.1</sub> O <sub>2</sub>	-	Measured
<b>Cathode Thickness EPI</b>	152	μm	Measured
<b>Cathode Thickness Conv</b>	147	μm	Measured
<b>Cathode porosity EPI</b>	0.316	-	Measured
<b>Cathode porosity Conv</b>	0.2976	-	Measured

2

## 2. A phase inversion strategy for low tortuosity, ultrahigh mass loading Nickel-rich layered oxide electrodes

### Long Term cycling reproducibility

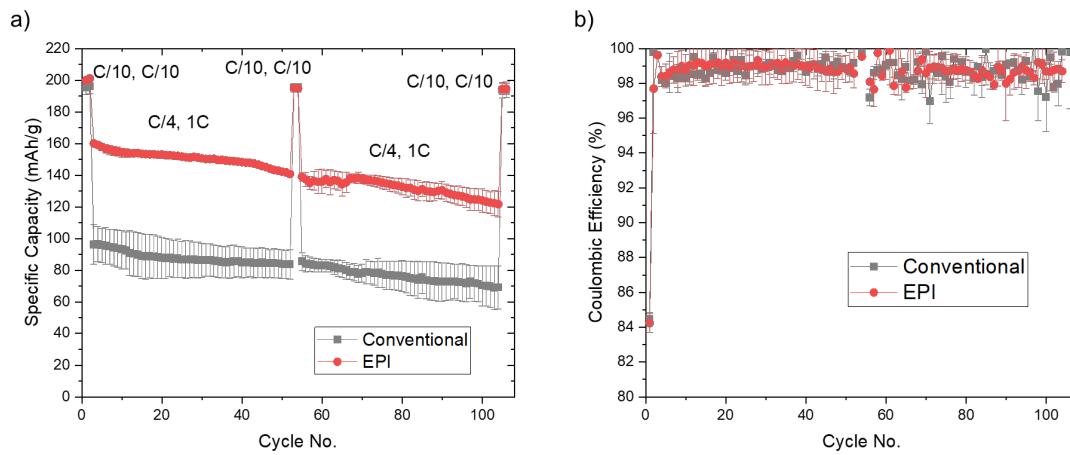


**Figure S8. Long-term cycling reproducibility:** a) Discharge capacity reproducibility and b) Coulombic efficiency reproducibility for Li/NMC811 half cells with 35 -37.5 mg/cm<sup>2</sup> (7-7.5 mAh/cm<sup>2</sup>) active mass loading and 1.4 M HE electrolyte cycled at 20 °C. Error bars indicate standard deviation.

2. A phase inversion strategy for low tortuosity, ultrahigh mass loading Nickel-rich layered oxide electrodes

### Electrode energy density calculation

The electrode energy density calculations are performed using the values listed in **Table S8**.

**Table S8.** Electrode parameters used for energy density calculations

Name	Unit	Value
<b>Key design parameters:</b>		
Areal capacity	mAh/cm <sup>2</sup>	7
Porosity	%	30
Body fraction	%	70
Active material fraction in body	%	92
<b>Densities:</b>		
Density of cathode body	g/cm <sup>3</sup>	3.46
Density of anode body	g/cm <sup>3</sup>	0.543
Density of electrolyte	g/cm <sup>3</sup>	1.22
Density of current collector	g/cm <sup>3</sup>	2.7 (Al), 8.96 (Cu)
<b>Electrochemical Performance parameters:</b>		
Average discharge potential	V	3.8
Charge density of AM	mAh/g	208 (NMC811) 3862 (Li)
Electrolyte conductivity	S/cm	0.01
<b>Thicknesses</b>		
Separator	μm	25
Current collector	μm	10
Cathode (calculated)	μm	151
Anode (calculated)	μm	33.4 (zero excess)
Cell (calculated)	μm	219.4
<b>Projected cell architecture and performance (calculated)</b>		
Volumetric fraction cathode	%	69
Volumetric fraction anode	%	15
Net vol. charge density	mAh/cm <sup>3</sup>	319
Volumetric energy density	Wh/L	1210
Density of battery cell	g/cm <sup>3</sup>	2.41
Gravimetric energy density	Wh/kg	503

### 3. Multifunctional ion-conductive polymer coatings for high-performance sulfide solid-state batteries

### 3. Multifunctional ion-conductive polymer coatings for high-performance sulfide solid-state batteries

#### Abstract

Sulfide-based solid-state batteries (SSBs) are emerging as a top contender for next-generation rechargeable batteries with improved safety and higher energy densities. However, SSBs with Ni-rich cathode materials such as  $\text{LiNi}_{0.82}\text{Mn}_{0.07}\text{Co}_{0.11}\text{O}_2$  (NMC82), exhibit several chemomechanical challenges at cathode-electrolyte interface, such as contact loss and solid-electrolyte decomposition, resulting in poor interfacial  $\text{Li}^+$  ion transport.

To overcome these challenges, we used polymerized ionic liquids (PIL) as coatings at the NMC82 cathode surface, with and without incorporating a lithium salt. The thin ( $\sim 10$  nm),  $\text{Li}^+$  ion-conductive Li-PIL coating shows excellent compatibility with sulfide solid electrolytes and enables efficient  $\text{Li}^+$  transfer over the cathode-solid electrolyte interface, as demonstrated by 2D solid-state exchange NMR. It also improves contact retention between the cathode-solid electrolyte particles and mitigates electrolyte oxidation-induced degradation. This is reflected in the electrochemical performance of coated NMC82 in sulfide SSBs, where both a higher rate performance (190 mAh/g vs 163 mAh/g for uncoated at 0.1C) and a remarkable capacity retention of 82.7% after 500 cycles at 0.2C and ambient conditions (20 °C) are observed. These results emphasize the effectiveness of PILs with Li salts as multifunctional coatings that enable high-performance sulfide-based SSBs with Ni-rich cathode materials at ambient temperature.

3

This chapter is under review at Journal of Materials Chemistry A.

### 3.1 Introduction

In the last few years, Solid-State Batteries (SSBs) have emerged as a potential electrochemical energy storage technology that could surpass the performance and safety levels of state-of-the-art Lithium-ion Batteries (LIBs).<sup>1,2</sup> Among the solid electrolytes investigated, sulfides have been receiving widespread attention, owing to the high  $\text{Li}^+$  ionic conductivity at room temperature ( $> 1 \text{ mS/cm}$ ), coupled with their relative ease of processing and lower gravimetric density compared to other solid electrolytes such as oxides and halides.<sup>2,3</sup> The cathode is the decisive component in SSBs for battery capacity and energy density.<sup>4,5</sup> One of the key challenges, therefore, in speeding up the adoption of sulfide-based solid-state batteries is the chemomechanics of the cathode-electrolyte interface.<sup>6,7</sup> During lithiation and delithiation of the cathode active material (CAM) in all-solid-state-batteries (ASSBs), the resulting volumetric and morphology changes lead to several detrimental effects. Interparticle cracking in polycrystalline CAMs in contact of rigid SE particles, creates voids both between the primary CAM particles and at the interface of the CAM and the SE, increasing ionic resistance across the interface.<sup>6,8</sup> While a move towards single crystal CAMs having a higher primary particle size has been shown to mitigate interparticle cracking,<sup>2,9</sup> void formation at the CAM/SE interface can still occur due to successive volumetric changes of the CAM, resulting in a loss of surface contact between the SE and the CAM with continuous cycling. One solution that is already widely applied in SSB research is applying high external stack pressure; however, this is considered impractical and does not resolve the issue in its totality.<sup>10</sup> Furthermore, oxidative decomposition of sulfide-based SEs at the CAM/SE interface leads to the formation of a resistive Cathode Electrolyte Interphase (CEI), leading to irreversible capacity loss.<sup>11</sup> Oxidation of the widely investigated sulfide electrolyte argyrodite  $\text{Li}_6\text{PS}_5\text{Cl}$  typically results in species such as polysulfides ( $\text{Li}_x\text{P}_y\text{S}_z$ ) and elemental sulfur ( $\text{S}^0$ ).<sup>12</sup> Furthermore, phosphates ( $-\text{PO}_x$ ) and sulfates ( $-\text{SO}_x$ ) are also reported as oxidation products in combination with  $\text{LiNi}_x\text{Mn}_y\text{Co}_z\text{O}_2$  (NMC hereafter) as the CAM upon extensive cycling. These contribute to a highly resistive CEI with sluggish  $\text{Li}^+$  diffusion.<sup>13</sup> While inorganic, electronically insulating coatings based on  $\text{LiNbO}_3$ ,<sup>14</sup>  $\text{LiZrO}_3$ ,<sup>15</sup>  $\text{LiHfO}_2$ ,<sup>16,17</sup> and others have been successfully employed to mitigate these processes, application of these coatings typically also results in lowered ionic conductivity at the interface and a lower electronic percolation through the composite, prompting the use of electronic conductive additives in the cathode composite, which could further aggravate the electrochemical instability at the CAM/SE interface.

Therefore, it is desirable to have multifunctional CAM/SE interlayers that possess sufficient (electro)chemical stability and ionic conductivity, which can also buffer volume changes at the CAM/SE interface. In this regard, the CAM particles or the SE could be coated with a polymeric buffer layer.<sup>18</sup> This polymeric protective coating, when applied on the CAM can inhibit the decomposition reactions of the SE and reduce interfacial resistance between CAM and SE, similar to the inorganic coating. In addition, the polymeric interlayers could also buffer volume change during cycling, thanks to their flexibility.<sup>19</sup> The polymers used as interlayers can also possess higher ionic conductivity than inorganic coatings, and in some cases, also reasonable electronic conductivity.<sup>18</sup> Ionically conducting and mixed conducting polymers have already been used as interlayers in both Li-ion batteries and solid-state batteries, resulting in significant performance improvements. Some examples include mixed conducting

### 3. Multifunctional ion-conductive polymer coatings for high-performance sulfide solid-state batteries

polymers such as Poly(3,4-ethylenedioxythiophene) (PEDOT),<sup>20,21</sup> PANI-PVP,<sup>22</sup> cyclized polyacrylonitrile (cPAN),<sup>23</sup> and single-ion conducting polymers such as lithium polyacrylate (LiPAA) and lithiated sulfonated polyphenylene sulfone (sPPSLi).<sup>24,25</sup>

Polymerized ionic liquids (PILs) present an interesting class of conducting polymers, where the polymeric backbone is either positively or negatively charged, and a counter ion acts as a plasticizer.<sup>26</sup> Cationic PILs such as Poly(diallyldimethylammonium) bis(trifluoromethanesulfonyl)imide (PDDATFSI hereafter) and Poly(diallyldimethylammonium) bis(fluoromethanesulfonyl)imide (PDDAFSI) have already found wide application in lithium ion batteries, from being used as solid polymer electrolytes to alternate binders for cathodes.<sup>27–33</sup> As solid polymer electrolytes, they possess excellent high-voltage stability and show good Li<sup>+</sup> conductivity and transference at optimized salt concentrations.<sup>29</sup> In addition, they have been used as interlayers in Li-S batteries, where they have been shown to inhibit polysulfide shuttling, thanks to the charged cationic backbone.<sup>34,35</sup> Cationic PILs have also been used as interlayers for sulfide-based ASSBs. Shi et al. coated PVBA-TFSI on NMC811 using spray drying, and with an optimum loading of 1 wt%, the long-term performance of the ASSBs improved, and this was attributed to the lower buildup of charge transfer resistance at the cathode electrolyte interface.<sup>36</sup> However, some fundamental questions remain over the role(s) of these coatings. In particular, further light needs to be shed on the potential role of PILs in (electro)chemically stabilizing the CAM/SE interface, and the effect of Li salt addition on Li transport through the coating and over the CAM/SE interface.

In this work, we address the above questions by designing and studying thin (~10 nm) polymeric coatings based on PDDATFSI with and without the incorporation of Li salt lithium bis(trifluoromethanesulfonyl)imide (LiTFSI) on commercial Ni-rich LiNi<sub>0.82</sub>Mn<sub>0.07</sub>Co<sub>0.11</sub>O<sub>2</sub> (NMC82 hereafter). The coatings with and without Li salt, referred to hereafter as Li-PIL and PIL respectively, are characterized to understand their structure, composition, and orientation on NMC82. We also study the ion transport properties in the Li-PIL coating and demonstrate facile Li-ion transport across the Li-PIL coating/SE interface using two-dimensional exchange NMR. The pristine and (Li)PIL coated NMC82 powders are further tested electrochemically in In-Li alloy/Li<sub>6</sub>PS<sub>5</sub>Cl/NMC82 solid-state cells, and the resulting performance is analysed further with detailed post-mortem characterization to elucidate the beneficial effects of (Li)PIL coatings on the cell performance.

## 3.2 Results and Discussion

### 3.2.1 Materials selection and design for polymeric coatings on Ni-rich CAMs:

An important criterion to be fulfilled by polymeric surface coatings for Ni-rich CAMs is high oxidative (anodic) stability. In this regard, the polymer investigated here, i.e. PDDATFSI, has previously shown high anodic stability of up to 5V vs Li<sup>+</sup>/Li,<sup>27</sup> and this can be attributed to the presence of cyclic quaternary ammonium cations in its polymeric backbone and -CF<sub>3</sub> moieties.<sup>39</sup> We limited the polymer loading on the cathode surface to 1-2 wt% of the cathode active mass, as non-lithiated PIL coatings with similar mass loading ranges were shown to result in optimal long-term cycling for Sulfide SSBs.<sup>36</sup> For Li salt containing PILs, the

### 3. Multifunctional ion-conductive polymer coatings for high-performance sulfide solid-state batteries

optimization of salt concentration is also necessary to balance ionic conductivity and transference while avoiding local salt crystallization. Previously, PIL repeat unit : salt ratio (mol%) of 1:1.5 resulted in optimal performance for LiFSI:PDDAFSI and LiTFSI:PDDATFSI based systems.<sup>29,30</sup> In our case, a salt ratio of 1:1 (mol%) was chosen, given the high surface-to-volume ratios expected for thin (nanometer range) coatings and possible confinement effects in this range, leading to lower solubility and undesirable salt precipitation.<sup>40</sup>

For the chosen salt concentration, the <sup>7</sup>Li and <sup>19</sup>F PFG NMR results of Li-PIL performed at a temperature range of 35 – 75 °C (**Figure 1a**) show a high Li\* diffusivity of 9.27 x 10<sup>-14</sup> to 1.56 x 10<sup>-12</sup> m<sup>2</sup>/s and F\* diffusivity of 3.43 x 10<sup>-13</sup> to 1.07 x 10<sup>-12</sup> m<sup>2</sup>/s (55 - 75 °C) respectively. When extrapolated to 20 °C, the Li\* diffusivity obtained is around 3.3 x 10<sup>-14</sup> m<sup>2</sup>/s, which is higher than that of most inorganic coatings typically applied on Ni-rich CAMs.<sup>41</sup> The Li\* transport numbers (ratio of Li\* diffusivity to the total diffusivity) based on these diffusivities are also high, i.e. 0.49 – 0.59 for the probed temperature range (**Figure S1**). The electrochemically measured ionic conductivity ranges from 5.02 x 10<sup>-7</sup> S/cm at 20 °C to 3.19 x 10<sup>-5</sup> S/cm at 70 °C (**Figure S2a**), while the Bruce-Vincent Li<sup>+</sup> transference number is about 0.48 at 60 °C (**Figure S2b**).

Overall, our results highlight the favourable Li<sup>+</sup> ion transport properties for the chosen Li-PIL composition over a wide temperature range.

Consequently, the use of Li-PIL results in minimal potential drops (of up to 0.03V) and no concentration polarization across the coating layer after 2 mAh/cm<sup>2</sup> of electrochemical cycling at 20 °C for current densities up to 10 mA/cm<sup>2</sup> and coating thicknesses of up to 100 nm, as shown by the analytical solution results for the Nernst-Planck transport equation (**Figure 1b, c**, methodology further described under **Supplementary Note 1**).<sup>42</sup> This is despite our assumption of a conservative lower bound of 10<sup>-15</sup> m<sup>2</sup>/s for Li<sup>+</sup> diffusivity, to account for changes in ion transport properties due to ion-ion correlations at these concentrations and possible ion confinement effects at low coating thicknesses.<sup>29,40,43</sup> These results suggest that the Li-PIL, with its good balance of Li<sup>+</sup> conductivity and transference, presents a competitive alternative to other commonly probed polymer (electrolyte) materials for application as surface coatings in SSBs operated under ambient temperature conditions.<sup>44</sup>

### 3. Multifunctional ion-conductive polymer coatings for high-performance sulfide solid-state batteries

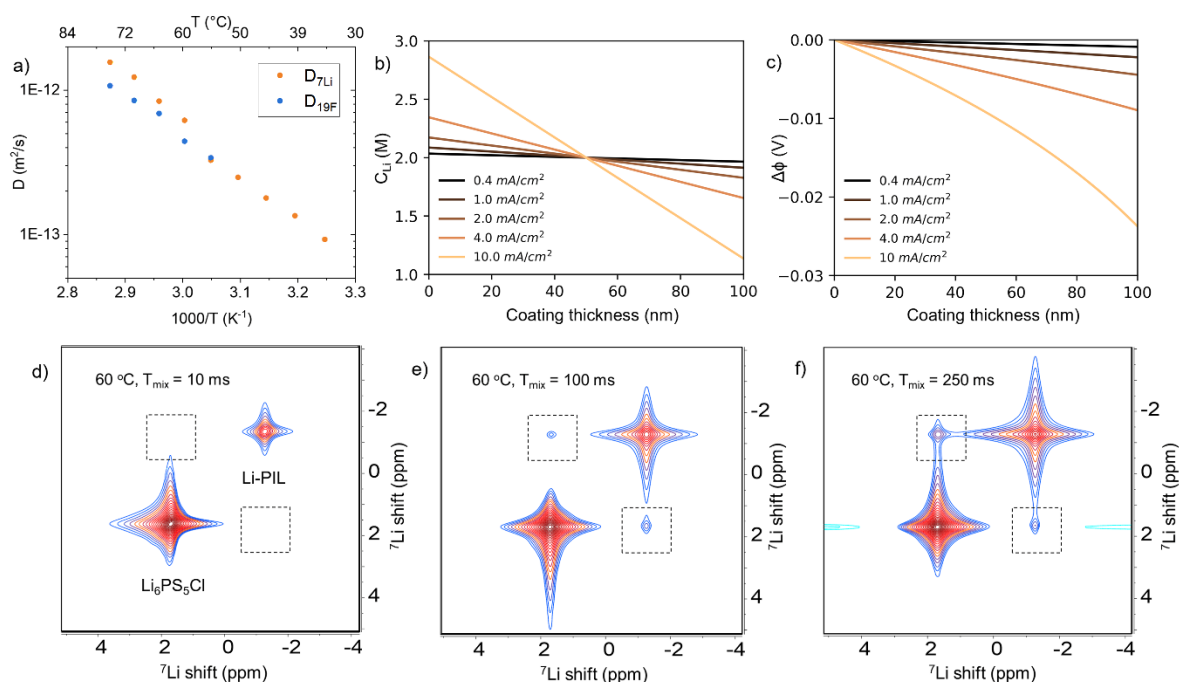


**Figure 1:** a)  $^{7}\text{Li}$  and  $^{19}\text{F}$  PFG NMR diffusivities of 1:1 Li-PDDATFSI PIL (Li-PIL) as a function of temperature. b) Concentration profiles and c) Potential drops after 2 mAh/cm<sup>2</sup> of electrochemical cycling at different current densities across a 100 nm Li-PIL coating. Bottom:  $^{7}\text{Li}$ - $^{7}\text{Li}$  2D EXSY NMR spectra at 60 °C performed on Li-PIL – 30 wt% Li<sub>6</sub>PS<sub>5</sub>Cl hybrid electrolyte films with mixing times of d) 10 ms, e) 100 ms and f) 250 ms.

It is to be noted that adequate Li<sup>+</sup> transport properties in the bulk polymer electrolyte do not always translate into sufficient Li<sup>+</sup> transport properties across the Polymer/SE interface, as previously observed for PEO-LiTFSI systems, where the nucleophilic attack-induced decomposition products formed between PEO and Li<sub>6</sub>PS<sub>5</sub>Cl impede interfacial transport.<sup>45,46</sup> However, the Li-PIL coating, with its less nucleophilic, positively charged polymer backbone and higher (electro)chemical stability, is expected to contribute positively to Li<sup>+</sup> transport across the CAM/SE interface. 2D exchange (EXSY)  $^{7}\text{Li}$  NMR, previously employed to probe Li<sup>+</sup> ion exchange across different chemical environments including Li<sub>6</sub>PS<sub>5</sub>Cl/electrode and Li<sub>6</sub>PS<sub>5</sub>Cl/polymer interfaces,<sup>45,47–49</sup> was employed to provide confirmation of Li<sup>+</sup> transfer over the Li-PIL/LPSC interface. These measurements were performed at 60 °C on Li<sub>6</sub>PS<sub>5</sub>Cl/Li-PIL hybrid solid electrolytes (with 30 wt% Li<sub>6</sub>PS<sub>5</sub>Cl). Here, the mixing time, i.e. Li self-diffusion period, is varied between 10 ms and 250 ms to probe the typical time scales of Li transport over the Li<sub>6</sub>PS<sub>5</sub>Cl/Li-PIL interface (**Figure 1d-f**). These mixing times are short enough compared to the  $T_1$  relaxation time of Li<sub>6</sub>PS<sub>5</sub>Cl (~ 500 ms) but long enough to show Li diffusion between Li<sub>6</sub>PS<sub>5</sub>Cl and Li-PIL, i.e. diffuse over similar 10 – 20 nm thicknesses of Li-PIL coating layers.

With a short mixing time of 10 ms, cross peaks, which correspond to Li<sup>+</sup> exchange over the LPSC/PIL interface do not yet appear (**Figure 1d**). However, they are observed with a longer mixing time of 100 ms and further intensify with a longer mixing time of 250 ms (**Figure 1e,f**). This is in sharp contrast to PEO-LiTFSI/Li<sub>6</sub>PS<sub>5</sub>Cl systems, where no Li<sup>+</sup> exchange was observed even after 2000 ms of mixing time at 55 °C.<sup>45</sup> These results indicate that the addition of Li salt

### 3. Multifunctional ion-conductive polymer coatings for high-performance sulfide solid-state batteries

to the PDDATFSI coating results in the participation of the PIL phase in Li<sup>+</sup> conduction and facile Li<sup>+</sup> transfer over the Li-PIL/LPSC interface.

#### 3.2.2 Surface Analysis of NMC82 with Polymeric Coatings

The 2 wt% Li-PIL and 1wt% PIL coatings deposited on the surface of NMC82 were analysed to determine its nature, composition, and possible effects on the NMC crystal structure, and the results are summarized in **Figure 2**. Transmission Electron Microscopy (TEM) was performed using a Cs-corrected Thermo Fisher Scientific Titan operated at 300 kV equipped with a super-X EDX detector in the ChemiSTEM™ configuration, with a focus on determining the thickness, morphology, and elemental distribution of the PIL coating. The surface of the NMC82 particle is shown to be covered by a PIL coating, with a thickness ranging from 10 to 20 nanometers (**Figure 2a**).

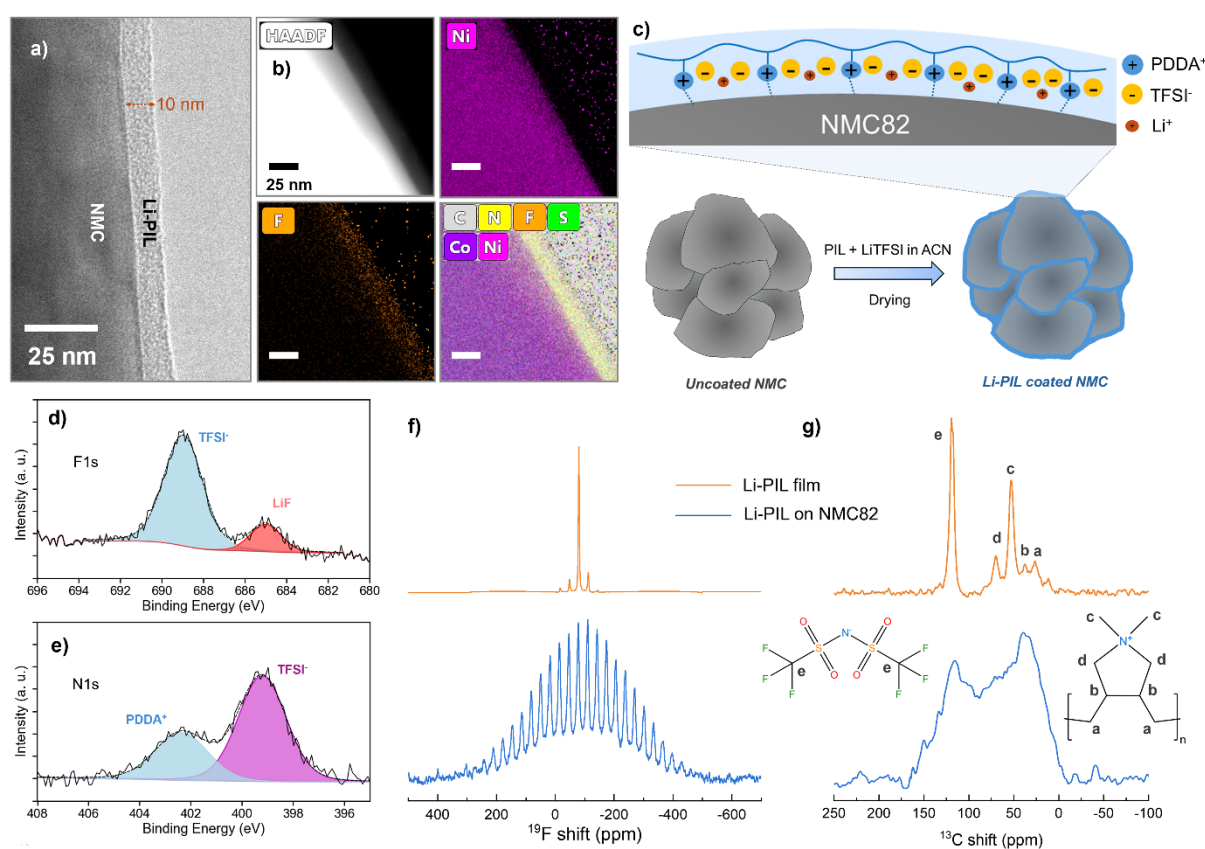


**Figure 2:** Characterization of PIL coatings on NMC82: a) TEM image of 2 wt% Li-PIL coating on NMC82 b) HAADF, and STEM elemental at% mapping of Ni, F, S and N, for Li-PIL on NMC82. c) Schematic diagram depicting the changes to the NMC82 surface before and after coating with Li-PIL d) High-resolution F1s and e) High-resolution N1s XPS spectra of NMC82 powder coated with Li-PIL. f) <sup>19</sup>F Hahn echo MAS NMR spectra of Li-PIL film (top) and NMC82 coated with Li-PIL (bottom). g) <sup>13</sup>C proton decoupled (60 W) MAS NMR spectra of Li-PIL film (top) and NMC82 coated with Li-PIL (bottom). All measurements were performed at 15 – 20 kHz spinning speeds.

The High Angle Annular Dark Field Scanning Transmission Electron Microscopy (HAADF-STEM) and the Energy Dispersive X-ray spectroscopy (EDX) atomic percentage (at%) map images

### 3. Multifunctional ion-conductive polymer coatings for high-performance sulfide solid-state batteries

(**Figure 2b**) reveal a thin, uniform distribution of F, S, C and N elements on the particle surface with Ni and Co present in the bulk (**Figure 2b and Figure S4**). Furthermore, the Li-PIL coating was also observed to deposit between the NMC82 grains, in this case with a higher thickness (**Figure S5**). It is to be noted, as observed from the Scanning Electron Microscopy (SEM) images (**Figure S6**), that the commercial NMC82 consists of aggregates of particles, and this structure is retained after the coating. The employed wet coating method is, therefore, expected to coat mainly the outer surfaces of the aggregate with a higher coating thickness between the primary particles (**Figure 2c**).

To further elucidate the chemical environment of the observed coating in comparison to that of the bare NMC82 powder, we performed X-ray Photoelectron Spectroscopy (XPS) measurements on the coated and uncoated NMC82 powders (**Figure 2d,e and S7**). The F1s spectrum of Li-PIL coated NMC82 (**Figure 2d**) shows a main peak at  $\approx 689$  eV corresponding to the TFSI<sup>-</sup>, and a secondary peak corresponding to LiF ( $\approx 685$  eV), which could be present due to LiTFSI degradation under X-rays.<sup>50</sup> In the N1s spectrum (**Figure 2e**), the peak at  $\approx 402.5$  eV corresponds to the quaternary amine from PDDA<sup>+</sup>, while the peak at  $\approx 399$  eV corresponds to nitrogen in the TFSI<sup>-</sup>.<sup>51</sup> Furthermore, the C1s spectrum shows an increased presence of C-N and C-F groups for the Li-PIL coated powders, and these findings are further corroborated by the elemental atomic percentages from the survey spectra of the uncoated and coated powders (**Figure S8**).

Magic angle spinning (MAS) solid-state NMR results provide further insights into the uniformity of Li-PIL coating and its possible orientation on the NMC82 surface. <sup>1</sup>H, <sup>19</sup>F, and <sup>13</sup>C spectra of Li-PIL coated NMC82 are compared with those of the Li-PIL film (LiTFSI/PDDATFSI (1:1 mol%) solid polymer electrolyte film prepared using wet coating/drying (with acetonitrile as the solvent)). For the Li-PIL coated NMC82, a broad background of  $\sim 800$  ppm is observed for the <sup>19</sup>F Hahn echo spectrum (**Figure 2f**), while the spinning sideband manifold also has a similar range and is wider in comparison to that of the PIL film. Moreover, the diamagnetic peak corresponding to TFSI<sup>-</sup> at  $\sim 80$  ppm is broader for the coated powder. A similar phenomenon is observed for <sup>1</sup>H Hahn echo NMR; a much broader background signal is observed for the Li-PIL coated NMC82 (**Figure S9**), and this feature is absent for the Li-PIL film. For the <sup>13</sup>C spectra with high power (60 W) proton decoupling (**Figure 2g**), five distinct peaks are observed for the Li-PIL film, with the peaks at  $\sim 52.5$  ppm (corresponding to the CH<sub>3</sub> groups dangling from N<sup>+</sup>) and  $\sim 125$  ppm (corresponding to TFSI<sup>-</sup>) being the most intense, but this changes for the coated powders. Instead of sharp peaks, a broad manifold is observed, with the highest intensity for the region corresponding to the PDDA environments occurring close to 25 - 40 ppm. The TFSI<sup>-</sup> peak at  $\sim 125$  ppm also appears broader. The lineshape broadening of the PDDA carbons on coated powders is also further confirmed with <sup>1</sup>H-<sup>13</sup>C cross-polarization (**Figure S10a**) where a broad manifold is again observed instead of individual peaks for the coated powders. The broad background observed for <sup>1</sup>H and <sup>19</sup>F, and the broader lineshapes observed for <sup>19</sup>F and <sup>13</sup>C can both be attributed to the influence of the paramagnetic interactions with the NMC82 core. This implies that most of the coating applied on NMC82 is in sufficient proximity (few nanometers) to be influenced by the paramagnetism of NMC82, which further corroborates the TEM results.

### 3. Multifunctional ion-conductive polymer coatings for high-performance sulfide solid-state batteries

It is interesting to note the change in the relative intensities for the  $^{13}\text{C}$  environments going from Li-PIL film to the coated NMC82 powder, which could offer insights into the orientation of the Li-PIL coating on NMC82 surface. To further study this phenomenon,  $^{13}\text{C}$  cross-polarization dynamics NMR (sensitive to polymer dynamics) experiments were performed on the Li-PIL film and 2 wt% Li-PIL coated on non-paramagnetic  $\text{LiCoO}_2$  (**Figure S10b,c**) to exclude the effects of paramagnetic line broadening. Here, the results show that the intensity for the  $-\text{CH}_3$  groups directly bonded to N (52.5 ppm) stays nearly the same after a small increase, and does not decrease with increasing contact times for cross-polarization from 0.05 to 1 ms, indicating a relative decrease in mobility for this environment (**Figure S10d,e**).<sup>52</sup> This could mean that the Li-PIL coating has the positively charged polymer backbone (with the quaternary  $\text{N}^+$ ) drawn towards the NMC82 surface (**Figure 2c**). This could be due to the electrostatic attractive forces induced by the negatively charged outer surface, which can be expected for layered oxides like NMC82. For the effect to be discernible by NMR, it is required that such electrostatic interaction propagates throughout the Li-PIL layer. If so, this could be a part of the explanation why the NMC82 particles can be successfully coated with Li-PIL, and it can be argued that cationic polymers hold an intrinsic advantage over anionic and neutral polymers for applications as coatings on layered oxides. However, further experiments would be necessary to establish this hypothesis.

We also investigated the structural stability of NMC82 before and after coating with X-ray Diffraction (XRD) (**Figure S11**). The characteristic peaks (003), (101), and (110) at around  $18.8^\circ$ ,  $36.6^\circ$ , and  $64.8^\circ$  respectively, corresponding to the R-3m space group of NMC82, were used to study the evolution of the lattice parameters  $a$ ,  $b$ , and  $c$ .<sup>53</sup> It is observed that the calculated lattice parameters (**Figure S11**, insets) stay nearly the same before and after coating (2.8726 Å vs 2.8732 Å for  $a,b$ ; 14.1909 Å vs 14.1917 Å for  $c$ ). This implies that the NMC82 retains its original crystal structure and particle size after the coating. Moreover, no additional environments corresponding to crystalline LiTFSI were observed in the spectrum, implying that the chosen salt ratio for the coating does not result in localized salt precipitation when coated on NMC82.

Together, the above results suggest that Li-PIL has been deposited on the surface of NMC82 particles as a thin ( $\sim 10$  nm) coating with the intended chemical composition, and no changes to the NMC82 crystal structure.

#### 3.2.3 Electrochemical Cycling Performance

To investigate the impact of (Li) PIL coatings on the rate capability and the long-term performance of solid-state batteries, we performed galvanostatic cycling of coated and uncoated NMC82 in InLi/  $\text{Li}_6\text{PS}_5\text{Cl}$ /NMC82 cells. The long-term cycling performance of these solid-state cells is compared over 100 cycles at 0.2C and at  $20^\circ\text{C}$  (**Figure 3a**). Here, the initial discharge capacity of Li-PIL coated NMC82 is the highest at 155.2 mAh/g, followed by the pristine NMC82 at 144.9 mAh/g and then the PIL-coated NMC82 at 137.3 mAh/g. After 100 cycles, the capacity retention of the sample with Li-PIL and PIL are similar at about 94%, and 95%, respectively. However, the Li-PIL coating also improves the initial capacity, whereas the

### 3. Multifunctional ion-conductive polymer coatings for high-performance sulfide solid-state batteries

PIL coating reduces the initial capacity. The capacity retention of the pristine NMC82 is only  $\approx 84\%$ .

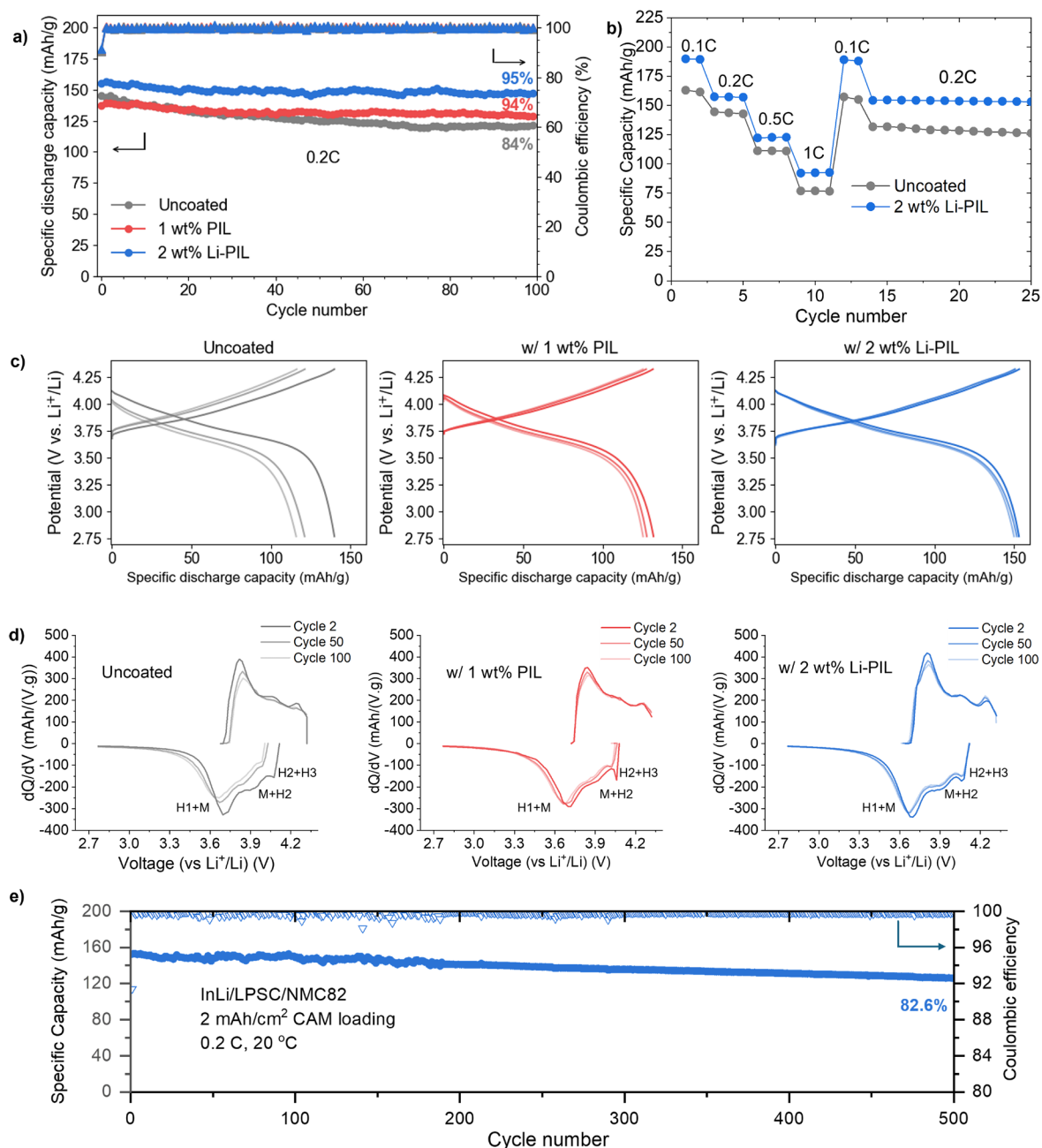


**Figure 3:** Electrochemical performance comparison: a) : Discharge capacities and Coulombic efficiencies for 100 cycles of InLi/ Li<sub>6</sub>PS<sub>5</sub>Cl/NMC82 cells for uncoated NMC, NMC with PIL, and NMC with Li-PIL, at 0.2C and 20 °C, and active mass loading of 10 mg/cm<sup>2</sup> b) Charge-discharge voltage profiles for the uncoated, PIL and Li-PIL cells at 0.2C for the 2<sup>nd</sup>, 50<sup>th</sup>, and the 100<sup>th</sup> cycle. c) First cycle coulombic efficiencies for the uncoated, PIL and Li-PIL cells at 0.05C. d) Rate performance comparison for the uncoated and Li-PIL cells. e) Long-term discharge capacity and coulombic efficiency of InLi/ Li<sub>6</sub>PS<sub>5</sub>Cl/NMC82 cells for NMC with Li-PIL, at 0.2C and 20°C, and NMC82 loading of 10 mg/cm<sup>2</sup> for 500 cycles.

### 3. Multifunctional ion-conductive polymer coatings for high-performance sulfide solid-state batteries

The improvement in initial capacity for the Li-PIL coated NMC82 is also reflected in the rate performance tests performed for C-rates from 0.1C up to 1C (**Figure 3b**). At all C-rates, the Li-PIL coated NMC82 outperforms the uncoated NMC82 (190 mAh/g vs 163 mAh/g at 0.1C, 92.7 mAh/g vs 76.6 mAh/g at 1C). On returning to lower C-rates, the capacity retention is observed to be much better (157.3 mAh/g to 154.5 mAh/g at 0.2 C vs 143.6 mAh/g to 131.8 mAh/g at 0.2C) for the Li-PIL coated NMC82.

The PIL and the Li-PIL coatings significantly improve the capacity retention of NMC82. **Figure 3c** shows the charge and discharge curves for the 2nd, 50th and 100th cycle of the three samples. For the sample with pristine NMC82, most of the capacity deterioration occurs in the first 50 cycles. With polymeric protective coatings PIL and Li-PIL, a lower capacity fade can be detected for the first 50 cycles, slowly heading towards a stable system with negligible capacity fade over the last 50 cycles. This is also reflected by the dq/dv plots for the three systems (**Figure 3d**), where a significant reduction of the reversibility in M to H2 and H2 to H3 phase transitions is observed for uncoated NMC82, whereas the Li-PIL coated NMC82 powder shows high reversibility of these transitions at cycle 100 (**Figure 3d**).

The application of coatings on NMC82 also improves the first cycle coulombic efficiency (**Figure S12**), which serves as an indicator of the extent of side reactions such as SE oxidation during the initial cycling.<sup>17</sup> Here, while the PIL coating results in an improvement of the 1<sup>st</sup> cycle CE from 77.3% to 78.7%, the Li-PIL results in further improvement to 79.5%. While this suggests that the PIL coating contributes towards improved (electro)chemical stability with Li<sub>6</sub>PS<sub>5</sub>Cl, the additional improvement in the Li-PIL coated NMC82 could also be coming from partial consumption of the Li<sup>+</sup> ions present in the coating. The Li-PIL coating improves both the rate performance and long-term stability of the LPSC/NMC system, and this is reflected in the excellent capacity retention of 82.7% at 0.2C and 20 °C for cells with 10 mg/cm<sup>2</sup> (~ 2 mAh/cm<sup>2</sup>) CAM loading after 500 cycles (**Figure 3e**).

Electrochemical Impedance Spectroscopy (EIS) results provide insights into the differences in resistance evolution at the Li<sub>6</sub>PS<sub>5</sub>Cl/NMC82 interfaces for the coated and uncoated powders.

### 3. Multifunctional ion-conductive polymer coatings for high-performance sulfide solid-state batteries

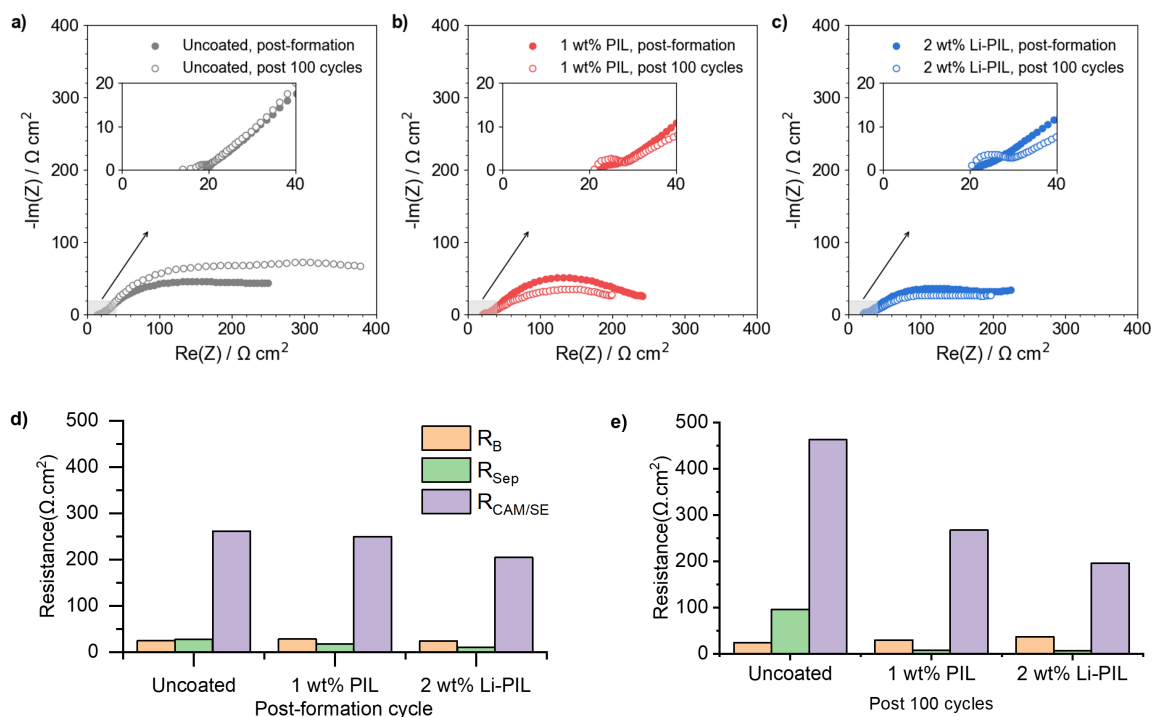


**Figure 4:** EIS Comparison: a) EIS Nyquist plots for uncoated NMC82, b) NMC82 coated with PIL, and c) NMC82 coated with Li-PIL, both post-formation cycles and post-100<sup>th</sup> cycle. All measurements were taken at 20°C and at 3 V (3.62 V vs Li<sup>+</sup>/Li) OCV. d) Resistances  $R_B$ ,  $R_{\text{Sep}}$ , and  $R_{\text{CAM/SE}}$ , post-formation, for the samples NMC82, NMC82 with PIL, and NMC82 with Li-PIL. e) Resistances  $R_B$ ,  $R_{\text{Sep}}$ , and  $R_{\text{CAM/SE}}$ , post-100 cycles, for the samples NMC82, NMC82 with PIL, and NMC82 with Li-PIL. The equivalent circuit and the resulting fits are shown in Figure S13.

Figure 4a-c show the Nyquist plots of the samples NMC82, NMC82 coated with PIL, and NMC82 coated with Li-PIL, post-formation cycles and post 100 cycles. All EIS measurements were performed after equilibration at an OCV of  $\approx 3.0$  V (or 3.62 V vs Li<sup>+</sup>/Li) to maintain a similar state of lithiation in the cathode composites. Given the similar range of time constants for different electrochemical processes in SSBs resulting in convoluted Nyquist plots, we also carried out Distribution of Relaxation Times (DRT) analysis to better deconvolute the individual processes and find an equivalent circuit.<sup>54</sup> The DRT analysis, the equivalent circuit for fitting the EIS measurements and the resulting fits are shown in Figure S13.

The resistances  $R_B$ ,  $R_{\text{Sep}}$ , and  $R_{\text{CAM/SE}}$ , determined using the fitted impedance data, are shown in Figures 4d and 4e.  $R_B$  corresponds to the bulk SE (Li<sub>6</sub>PS<sub>5</sub>Cl) resistance,  $R_{\text{Sep}}$  refers to the SE-separator/electrode interface resistance, and  $R_{\text{CAM/SE}}$  to the CAM/SE particle interface resistance.<sup>55</sup> The cell with the Li-PIL coatings shows the lowest  $R_{\text{CAM/SE}}$  and  $R_{\text{Sep}}$  post-formation. This agrees well with the cycling data (Figure 3a), where the sample with PIL had the lowest initial discharge capacity, and the cell with Li-PIL the highest. Post-cycling, the interface resistances for the uncoated NMC82 increase significantly, where  $R_{\text{Sep}}$  is nearly 4 times its value pre-cycling, and  $R_{\text{CAM/SE}}$  almost doubles. The increase of cell resistances is in line with the capacity fade the cell displayed during electrochemical cycling. In contrast,  $R_{\text{CAM/SE}}$  of the samples with PIL and Li-PIL coatings both decrease with cycling, with the Li-PIL coated NMC82 having the lowest  $R_{\text{CAM/SE}}$  value. The significant increase in  $R_{\text{CAM/SE}}$  for the uncoated NMC82

### 3. Multifunctional ion-conductive polymer coatings for high-performance sulfide solid-state batteries

could be caused by contact loss between the CAM/SE particles in the composite and/or the formation of a resistive CEI due to  $\text{Li}_6\text{PS}_5\text{Cl}$  decomposition, and the increase in  $R_{\text{Sep}}$  indicates possible contact loss at the separator/cathode composite interface. Both  $R_{\text{Sep}}$  and  $R_{\text{CAM/SE}}$  decrease with cycling for the samples with (Li)PIL coatings, which indicates that the coatings offer both enhanced (electro)chemical and mechanical stability to the interfaces involved.

#### 3.2.4 Effect on (electro)chemical stability

Li-PIL, with its high oxidative stability and interfacial compatibility with  $\text{Li}_6\text{PS}_5\text{Cl}$ , the latter demonstrated by 2D EXSY NMR (**Figure 1d-f**), is expected to alleviate the electrochemical degradation of the CAM/SE interface. To investigate this further, we performed XPS measurements on the cathode composites before and after cycling. The pre-cycling S2p and post-cycling S2p and P2p spectra are shown for the coated and uncoated samples in **Figure 5**.

For the S2p spectra (**Figure 5a,b,d,e**), four different peak doublets are observed. The main component is detected at a binding energy of  $\approx 161.7\text{eV}$ , corresponding to the  $\text{PS}_4^{3-}$  units of the  $\text{Li}_6\text{PS}_5\text{Cl}$ .<sup>56</sup> Oxidized species were detected at roughly 162.9 eV and 163.9 eV corresponding to the P-S-P ( $\text{P}_2\text{S}_x$ ) and  $\text{S}_x$ , respectively. P-S-P – or polysulfides, are known to form during the mixing of NMC with  $\text{Li}_6\text{PS}_5\text{Cl}$ .<sup>57</sup>  $\text{S}_x$  here could indicate multiple compounds, including elemental sulfur that can be responsible for the intensity at  $\approx 163.9\text{eV}$ .<sup>58</sup> In the case of the coated samples, an additional environment is observed at  $\approx 169.4\text{eV}$  corresponding to TFSI<sup>-</sup>.

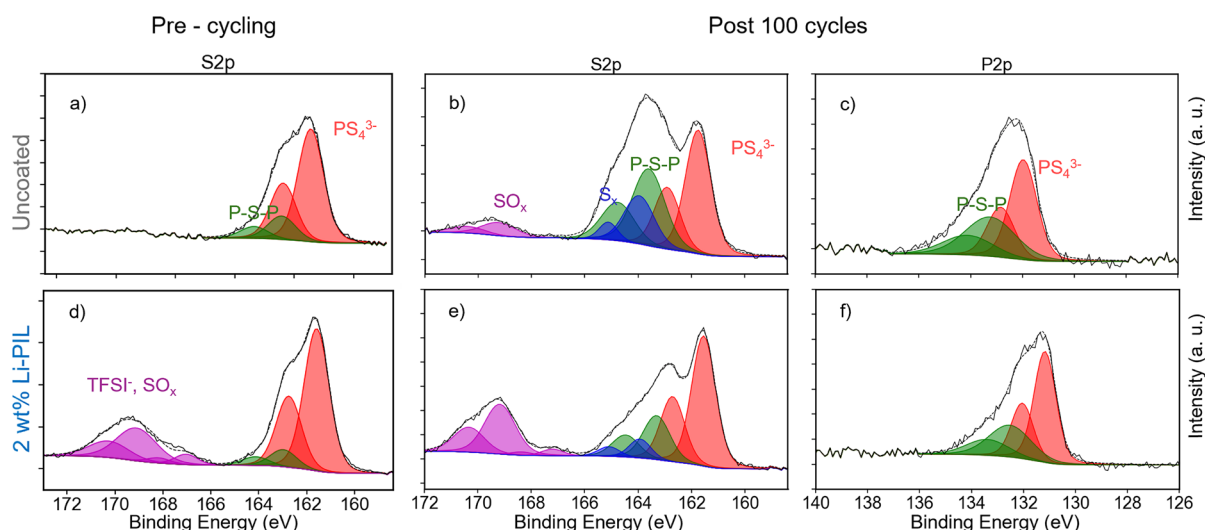


**Figure 5:** Pre-cycling S2p and Post-cycling S2p and P2p XPS spectra of a) - c) uncoated NMC82 and d) - f) NMC82 with Li-PIL coating.

For both composite cathodes, electrochemical cycling increased the intensities of oxidized species in the S2p spectra (**Figure 5 b, e**). However, in the case of uncoated NMC, the intensity of the oxidized species was greater than for the samples coated with Li-PIL. Additionally, oxidized sulfates were detected in the uncoated sample at  $\approx 169.0\text{eV}$ . However, the intensity at the same binding energy for coated samples corresponds to the units of TFSI<sup>-</sup> and therefore,

### 3. Multifunctional ion-conductive polymer coatings for high-performance sulfide solid-state batteries

it is hard to visually determine if the  $\text{SO}_x$  compounds were also formed in the case of the coated powders. However, a comparison of the area-wise percentages for the S2p components provided in **Figure S14** indicates that the TFSI<sup>-</sup>/ $\text{SO}_x$  environment stays nearly the same with cycling. This is also reflected in the ratios of the TFSI<sup>-</sup> environments in the F1s and S2p spectra remaining nearly the same with cycling (**Table S2**). It is also to be noted that  $\text{Li}_6\text{PS}_5\text{Cl}$  is known to display some degree of reversible redox upon charging and discharging,<sup>12</sup> and some part of the observed oxidized species might indeed be reversible. However, all the cells for post-mortem analysis were disassembled at an OCV of 3V (3.62 V vs  $\text{Li}^+/\text{Li}$ ) to ensure a uniform state of charge across these samples. Therefore, the reduction in the amount of P-S-P and  $\text{S}_x$  species post-cycling is evident for the powders coated with Li-PIL.

For the P2p spectra (**Figure 5c, f**), a similar trend is observed, with  $\text{PS}_4^{3-}$  at around 131 eV and polysulfides at approximately 132.5 eV. A similar ratio of  $\text{PS}_4^{3-}$  to P-S-P was detected as in the S2p spectra for all cells. The average signal position for the polysulfides shows slight deviations per cell, which is a result of the average chain length of the number of sulfide atoms, P- $[\text{S}]_n$ -P, in the polysulfides.<sup>57</sup> A signal shift towards higher binding energies with increasing  $n$  is assumed, which is observed in the uncoated NMC82 composite (**Figure 5c**). Again, the relative fraction of oxidized P- $[\text{S}]_n$ -P species is substantially higher for the uncoated samples than for the Li-PIL coated samples. Therefore, it can be concluded that the Li-PIL coatings on NMC82 reduce the amount of decomposition of the  $\text{Li}_6\text{PS}_5\text{Cl}$  solid-electrolyte at the NMC82 interface. Furthermore, the XPS spectra of pre-cycling and post-cycling PIL coated samples show identical trends as the Li-PIL coated samples (**Figure S15**), suggesting that the interfacial stability imparted by (Li)PIL coatings to NMC82 in sulfide SSBs might be independent of the Li salt concentration.

In addition, the F1s and N1s XPS spectra for the composites after cycling (**Figure S16a**) reveal minimal changes to the Li-PIL coating environment with cycling (compared to **Figure 2d,e**). To further verify this, we performed  $^{19}\text{F}$  NMR on the cathode composites of coated NMC82 before and after cycling (**Figure S16b**). Here, the environment corresponding to TFSI<sup>-</sup> is still present in the post-cycled spectrum with no additional  $^{19}\text{F}$  environments. While some reduction in the range of paramagnetic broadening is observed, this could have to do with the lower degree of paramagnetism at a partially delithiated state of NMC82(3.62 V vs  $\text{Li}^+/\text{Li}$ ). These findings corroborate the post-mortem F1s and N1s XPS results, implying that the applied Li-PIL coating is (electro)chemically stable with long-term cycling.

#### 3.2.5 Effect on mechanical and structural stability

A key advantage of polymeric surface coatings for cathodes in SSBs is their ability to buffer volume changes during cycling.<sup>18,36</sup> This is also reflected in the post-cycling SEM images of the uncoated and coated cathode composites (**Figure 6 and Figure S17**). In the case of uncoated NMC82, severe contact loss with several voids in the cathode composite is observed after cycling (**Figure 6a**). The yellow circles indicate the areas with significant contact loss. In contrast, for cathode composites with Li-PIL (**Figure 6b**) and PIL coatings (**Figure S17b**), the contact between the CAM and SE particles is still maintained after cycling, likely due to the volume buffering capacity of the polymer coating during the lithiation and delithiation of the NMC particles. The limited number of visible voids of the post-cycled samples compared to

### 3. Multifunctional ion-conductive polymer coatings for high-performance sulfide solid-state batteries

the pre-cycling uncoated NMC82 cathode composite (**Figure S17a**) indicates that initial particle contact could have been improved by the polymeric coating as well.

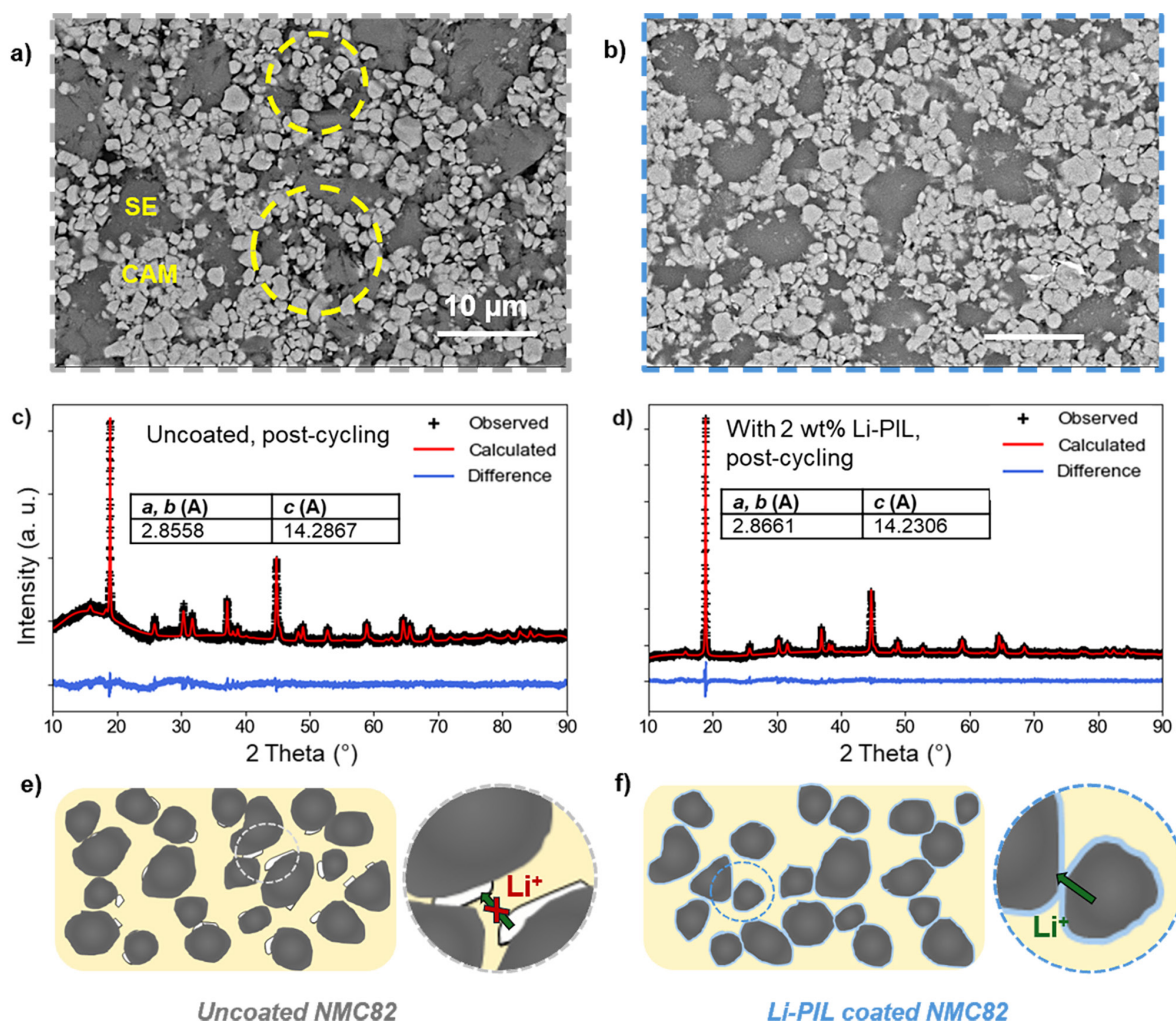


**Figure 6:** Top: SEM images of the NMC82/  $\text{Li}_6\text{PS}_5\text{Cl}$  composites with; a) NMC82 after cycling and b) NMC82 with Li-PIL after cycling. All images were taken with BED, and a 15kV acceleration voltage, with a magnification of 2500x. Yellow circles indicate the contact loss after cycling for uncoated NMC82. Middle: Post-cycling XRD patterns of c) Cathode composite with uncoated NMC82 d) Cathode composite with 2 wt% Li-PIL coated NMC82. Bottom: e) and f) provide schematic overview of the evolution of mechanical contact at the interfaces for LPSC/NMC82 composites without and with the Li-PIL coating respectively.

As Ni-rich layered oxides such as NMC82 can be highly prone to volume change-induced structural instabilities upon continuous cycling, we also performed XRD on coated and uncoated NMC82 cathode composites post-cycling to observe differences, if any, in the crystal structure retention (**Figure 6c,d**). The Pawley refinement results show a slightly greater (003) peak shift for the uncoated NMC82, as well as slightly increased peak broadening (**Figure S18**), associated with the presence of microstrain on the uncoated NMC.<sup>59</sup> On comparing the lattice parameters before and after cycling (**Figure S11** and **Figure 6c,d**), it is observed that the lattice parameters of the Li-PIL coated NMC82 show a lower degree of change with cycling compared to the uncoated NMC82 (c parameter: 14.2867 Å for uncoated

### 3. Multifunctional ion-conductive polymer coatings for high-performance sulfide solid-state batteries

vs 14.2306 Å for Li-PIL coated). While NMC particles are known to experience microstrain only at very high states of charge (delithiation),<sup>60</sup> it is plausible that the volume buffering offered by the polymeric coatings (as shown with SEM) alleviates the heterogeneities in the degree of (de)lithiation in the cathode composite otherwise caused due to contact loss, thereby reducing the overall extent of microstrain on the NMC particles present in the cathode composite.

To summarize, while uncoated NMC82 suffers from cycling-induced contact loss, resulting in poor ionic percolation through the cathode composite and capacity loss, the presence of Li-PIL coating on NMC82 improves contact retention between NMC82 and SE particles with cycling, and given the ion-conductive nature of the coating, this further helps in the retention of the ionic percolation pathways through the cathode composite (**Figure 6e,f**).

## 3

### 3.3 Conclusions

In this work, we investigate the incorporation of Li salt into polymerized ionic liquid surface coatings as a strategy for simultaneously addressing contact losses, electrochemical decomposition and Li<sup>+</sup> transport bottlenecks over the cathode-electrolyte interface in sulfide-based solid-state batteries with Ni-rich layered oxide cathodes. For the polymerized ionic liquid PDDATFSI, we show that the inclusion of LiTFSI in a 1:1 (mol%) ratio results in a good balance of Li<sup>+</sup> diffusivity and transference, as shown by PFG-NMR and electrochemical results. This translates to minimal Li<sup>+</sup> concentration and potential drops across the polymer at practical current densities, as shown by our analytical modelling results. The chemical compatibility of Li-PIL with the sulfide electrolyte Li<sub>6</sub>PS<sub>5</sub>Cl also results in facile Li<sup>+</sup> transport across the Li<sub>6</sub>PS<sub>5</sub>Cl/Li-PIL interface, as demonstrated by <sup>7</sup>Li 2D exchange NMR.

With 2 wt% Li-PIL (of the cathode active mass), thin (~10 nm) coatings of Li-PIL are obtained on Ni-rich NMC82, as confirmed by TEM, XPS, and ssNMR measurements. On testing in SSBs, the Li-PIL coating on NMC82 improves both the rate capability (190 mAh/g vs 163 mAh/g for uncoated at 0.1C, 92.7 mAh/g vs 76.6 mAh/g for uncoated at 1C) and the capacity retention (95% vs 84% after 100 cycles at 0.2C), while the PIL coating without LiTFSI improves only the capacity retention (94% after 100 cycles) with a reduction in the initial discharge capacity. An exceptional capacity retention of 82.7% is observed for the Li-PIL coated NMC82 after 500 cycles at 0.2C under ambient conditions (20 °C).

EIS measurements show minimal resistance evolution across the cathode electrolyte interface for the Li-PIL-coated sample, compared to a severe resistance increase for uncoated NMC82. Post-cycling XPS results show that the Li-PIL coating greatly reduces electrolyte oxidation at the NMC82/Li<sub>6</sub>PS<sub>5</sub>Cl interface. Furthermore, the presence of Li-PIL coatings also significantly improves CAM/SE particle contact retention with cycling, as established by the SEM images. In addition, the XRD results also indicate that the Li-PIL coating reduces the overall degree of structural deformation in the cathode composite, likely due to the improvements in contact retention and the preservation of ionic percolation pathways through the cathode composite. Our results establish Li salt incorporation into polymerized ionic liquid surface coatings as a highly effective strategy for overcoming both chemomechanical challenges and ion transport bottlenecks in sulfide-based solid-state

3. Multifunctional ion-conductive polymer coatings for high-performance sulfide solid-state batteries

batteries with Ni-rich layered oxide cathodes, particularly under ambient temperature conditions.

## 3.4 Experimental Procedures

### 3.4.1 Sample preparation

The cathode composites were prepared by adding argyrodite  $\text{Li}_6\text{PS}_5\text{Cl}$  (LPSC, NEI corporation,  $D50 = 5 \mu\text{m}$ ), with quasi-single crystal NMC82 ( $D50 = 3 - 5 \mu\text{m}$ , MSE Supplies LLC) to an agate pestle and mortar in the mass ratio of 30:70 and hand-mixing for 15 minutes. No conductive carbon additive was used in the cathode composite. The Polymerized ionic liquid of interest, Poly(diallyldimethylammonium) bis(trifluoromethanesulfonyl)imide (PDDATFSI, Solvionic), was coated on NMC82 either as a 1 wt% coating without the Li salt, or as a 2 wt% coating with the Li salt, i.e. Lithium bis(trifluoromethanesulfonyl)imide (LiTFSI, Solvionic). Due to the tendency of LiTFSI to absorb moisture from the air, the coating process was performed in an Argon-filled glovebox with water oxygen levels below 1 ppm. Either 15mg of Li-PIL or 7.5 mg of PIL was added to 5 mL of acetonitrile, which was mixed to form a homogeneous solution. To this, 0.75g of NMC82 was added, and the suspension was mixed for 60 minutes in a closed glass bottle. After 60 minutes, the bottle cap was removed and the suspension was dried at 60 °C, with continued mixing. Finally, the coated powder was dried under vacuum ( $< 10^{-3}$  mbar) at RT for 72 hours.

The LiTFSI:PDDATFSI (1:1 mole ratio) films for NMR characterization were prepared by adding the salt and polymer in the desired ratio to acetonitrile (1:1 solvent: solute weight ratio) and mixing until a clear solution was obtained. This solution was spread on a clean polytetrafluoroethylene (PTFE) dish and dried for 12 hours in an Ar filled Glovebox, after which the drying was carried out under vacuum ( $< 10^{-3}$  mbar) at RT for 72 hours to obtain the dried film. A similar procedure was repeated to obtain the hybrid film with  $\text{Li}_6\text{PS}_5\text{Cl}$ , where the weight of  $\text{Li}_6\text{PS}_5\text{Cl}$  in the film was set to 30% of the total dry weight of the film.

### 3.4.2 Electrochemical characterization

The cathode composites were tested in custom-made solid-state cells with two stainless steel cell parts surrounded by a PEEK sleeve with a cavity of 10 mm (assembly details are shown in **Figure S19**). First, 60 mg of LPSC was compressed at 125 MPa to form the separator. Cathode composites corresponding to  $10 \text{ mg/cm}^2$  ( $\approx 2 \text{ mAh/cm}^2$ ) of CAM loading were added to one side of the separator, and pressed at 312.5 MPa. Finally, the InLi alloy foil was prepared by placing an In foil with 8 mm diameter on the LPSC separator, followed by a Li foil with 5 mm diameter on top. The weight ratio of Indium to Lithium was optimized as per the work of Santhosha et al.<sup>37</sup> The final cell was closed at 60 MPa pressure.

The galvanostatic cycling of the batteries was performed on MACCOR 4300 cycler at 20 °C. The solid-state batteries were charged and discharged between 2.15V and 3.7V (corresponding to 4.3V vs  $\text{Li}^+/\text{Li}$ ). Two initial cycles were run at a C-rate of 0.05C ( $0.1 \text{ mA/cm}^2$ ), followed by further cycling at 0.2C ( $0.4 \text{ mA/cm}^2$ ). A minimum of two cells were tested for each NMC82 powder type. Electrochemical impedance spectroscopy measurements were performed on AUTOLAB potentiostat (Metrohm Inc.) at 20 °C, after the (two) initial cycles,

### 3. Multifunctional ion-conductive polymer coatings for high-performance sulfide solid-state batteries

and after 100 cycles. The cells were charged to an open circuit voltage (OCV) of 3.0 V (3.62 V vs Li<sup>+</sup>/Li). Measurements were taken between 10 MHz and 0.1 Hz. Further processing and analysis of the spectra were performed using RelaxIS 3 software (RHD Instruments). Distribution of Relaxation Times (DRT) analysis is conducted, also using RelaxIS 3, to serve as an aid in the fitting of equivalent circuits to the impedance data. Bruce-Vincent Li<sup>+</sup> transference number measurement at 60 °C was also performed on the AUTOLAB potentiostat in Li/Li symmetric cells with a 250 μm Li-PIL film as the separator. A DC amplitude of 5 mV was used for the potentiostatic polarization until steady-state conditions were reached.<sup>38</sup>

#### 3.4.3 Surface and Bulk Characterization

XPS measurements were performed on NMC82 powders before and after the coating, and on the cathode composites before and after cycling. For the post-cycling (100 cycles) XPS measurements, the samples were retrieved from cells after equilibration at an OCV of 3.0 V (3.62 V vs Li<sup>+</sup>/Li). The samples are handled in the glove box and placed into a vacuum transfer holder before being placed in the XPS apparatus. The XPS measurements were performed on a Thermo Scientific K-Alpha Spectrometer with an Al K-alpha monochromator. The spot diameter was set to 400 μm. Survey spectra were recorded with a pass energy of 200 eV and step size of 0.5 eV, while high-resolution spectra were recorded with a pass energy of 50 eV and step size of 0.1 eV. The binding energies were referenced to adventitious carbon at 284.8 eV. All the spectra were processed and analysed using the CasaXPS software using a Shirley background to account for inelastically scattered photoelectrons.

Scanning Electron Microscopy (SEM) measurements were performed on JEOL JSM-IT100 for samples in an airtight holder, and JEOL JSM-IT700HR FE-SEM for NMC powder investigations. For the investigation of cathode composites, Backscattered Electron Detection (BED) images were taken with electron acceleration voltages of 10 -15 keV to obtain sufficient contrast between Li<sub>6</sub>PS<sub>5</sub>Cl, NMC82, and voids. For the investigation of polymer coatings on NMC82, low electron acceleration voltages of 1 keV were used in the Secondary electron Detection (SED) mode.

X-ray Diffraction (XRD) measurements were performed on the X'Pert Pro X-ray diffractometer (PANalytical). Cu Kα X-rays (1.5406 Å at 45 kV and 40 mA) were used, with the absolute scan function and the XCelerator detector. The samples were tested in airtight holders with a Kapton window. Diffraction patterns were collected in a 2θ angular range from 10° to 90°, with a step size of 0.008°. Pawley refinement and fitting of the resulting spectra was performed using TOPAS software (Bruker).

For Transmission Electron Microscopy (TEM) measurements, a Thermo Fisher Scientific Titan Cs-corrected 80-300 kV TEM was used. The coated powders were gently crushed and put into hexane and the suspension was ultrasonically shaken for 2 minutes, and 2 droplets were loaded onto a TEM grid with a holey carbon foil. Elemental mapping in STEM mode was done, using the super-X in the ChemiSTEM™ configuration. In STEM mode, a small electron beam (~0.3 nm) scanned the specimen. For each beam position, the diffracted electrons were collected on a ring detector, thus forming a High Angle Annular Dark Field (HAADF) image

### 3. Multifunctional ion-conductive polymer coatings for high-performance sulfide solid-state batteries

after the complete area was scanned. At the same time, an EDX spectrum was collected for each beam position, and elemental maps were made. Two-pixel averaging was applied.

All solid-state NMR measurements were carried out on a Bruker Ascend 500 MHz (11.7 T) spectrometer equipped with a Neo console. For the Li-PIL polymer and the coated NMC82 powder, measurements were carried out on a 3.2 mm triple resonance probe at spinning speeds of 15-20 kHz, while for the cathode composites (pre and post-cycling), the measurements were performed on 1.9 mm double resonance probes at 35 kHz spinning speed.  $^{19}\text{F}$  and  $^1\text{H}$  MAS NMR measurements were acquired using a rotor-synchronized Hahn echo protocol, while  $^{13}\text{C}$  measurements were performed with direct excitation pulses with high power (30-60 W) proton decoupling. For  $^{13}\text{C}$  measurements, a pulse length of 3.1  $\mu\text{s}$  (145 W) was used with a recycle delay of 1-2 s.  $^1\text{H}$  measurements were carried out with a pulse length of 2.8  $\mu\text{s}$  (80 W) and recycle delay of 1-5 s.  $^1\text{H}$  and  $^{13}\text{C}$  measurements were referenced to adamantane at 1.77 ppm and 37.5 ppm respectively.  $^{19}\text{F}$  measurements were carried out with a pulse length of 2.8  $\mu\text{s}$  (80 W) and a recycle delay of 1-10 s.  $^1\text{H}\rightarrow^{13}\text{C}$  CP MAS experiments were performed at 10 kHz with an initial  $^1\text{H}$   $\pi/2$  pulse of 2.8  $\mu\text{s}$  and contact times ranging from 0.05 to 2 ms. A radio frequency field strength of 64 kHz was utilized, with a recycle delay of 2 s. The field amplitude of  $^1\text{H}$  was ramped from 70 to 100% and a TPPM15 sequence was used for proton decoupling.  $^7\text{Li}$ - $^7\text{Li}$  2D EXSY NMR measurements were performed at 60 °C with mixing times ranging from 10 ms to 250 ms and a recycle delay of 0.4s. The 2D spectra consisted of 32 scans each for 3000 transients, with each transient incremented by 514.6  $\mu\text{s}$ . The processing and analysis of the resulting spectra was performed using the Mestrenova 14 software.

For PFG NMR, a Bruker Ascend 600 ( $B_0= 14.1$  T) magnet equipped with a NEO console was used. The samples were measured using stimulated echo pulse field gradient procedure on  $^7\text{Li}$  ( $\pi/2$  pulse length of 17.5  $\mu\text{s}$ , 45 W and  $B_1=80$ -1600 Gauss/cm) and  $^{19}\text{F}$  ( $\pi/2$  pulse length of 23  $\mu\text{s}$ , 15.5 W and  $B_1=80$ -1600 Gauss/cm) using a linear gradient of 8 slices with typical diffusion times of 100-400 ms, gradient pulse durations of 1-2.5 ms, and 8-64 scans per slice for temperatures from 35 °C to 75 °C for every 5° – 10° increment in temperature. The data was fit using the Stejskal–Tanner equation, and Bruker Dynamics Center software was used.

## References

- (1) Janek, J.; Zeier, W. G. A Solid Future for Battery Development. *Nat. Energy* 2016, 1 (9), 1–4. <https://doi.org/10.1038/nenergy.2016.141>.
- (2) Han, Y.; Jung, S. H.; Kwak, H.; Jun, S.; Kwak, H. H.; Lee, J. H.; Hong, S.-T.; Jung, Y. S. Single- or Poly-Crystalline Ni-Rich Layered Cathode, Sulfide or Halide Solid Electrolyte: Which Will Be the Winners for All-Solid-State Batteries? *Adv. Energy Mater.* 2021, 11 (21), 2100126. <https://doi.org/10.1002/aenm.202100126>.
- (3) Chen, S.; Xie, D.; Liu, G.; Mwizerwa, J. P.; Zhang, Q.; Zhao, Y.; Xu, X.; Yao, X. Sulfide Solid Electrolytes for All-Solid-State Lithium Batteries: Structure, Conductivity, Stability and Application. *Energy Storage Mater.* 2018, 14, 58–74. <https://doi.org/10.1016/j.ensm.2018.02.020>.

### 3. Multifunctional ion-conductive polymer coatings for high-performance sulfide solid-state batteries

- (4) Kerman, K.; Luntz, A.; Viswanathan, V.; Chiang, Y.-M.; Chen, Z. Review—Practical Challenges Hindering the Development of Solid State Li Ion Batteries. *J. Electrochem. Soc.* 2017.
- (5) Pasta, M.; Armstrong, D.; Brown, Z. L.; Bu, J.; Castell, M. R.; Chen, P.; Cocks, A.; Corr, S. A.; Cussen, E. J.; Darnbrough, E.; Deshpande, V.; Doerrer, C.; Dyer, M. S.; El-Shinawi, H.; Fleck, N.; Grant, P.; Gregory, G. L.; Grovenor, C.; Hardwick, L. J.; Irvine, J. T. S.; Lee, H. J.; Li, G.; Liberti, E.; McClelland, I.; Monroe, C.; Nellist, P. D.; Shearing, P. R.; Shoko, E.; Song, W.; Jolly, D. S.; Thomas, C. I.; Turrell, S. J.; Vestli, M.; Williams, C. K.; Zhou, Y.; Bruce, P. G. 2020 Roadmap on Solid-State Batteries. *J. Phys. Energy* 2020, 2 (3), 032008. <https://doi.org/10.1088/2515-7655/ab95f4>.
- (6) Koerver, R.; Zhang, W.; de Biasi, L.; Schweidler, S.; Kondrakov, A. O.; Kolling, S.; Brezesinski, T.; Hartmann, P.; Zeier, W. G.; Janek, J. Chemo-Mechanical Expansion of Lithium Electrode Materials – on the Route to Mechanically Optimized All-Solid-State Batteries. *Energy Environ. Sci.* 2018, 11 (8), 2142–2158. <https://doi.org/10.1039/C8EE00907D>.
- (7) Janek, J.; Zeier, W. G. Challenges in Speeding up Solid-State Battery Development. *Nat. Energy* 2023, 8 (3), 230–240. <https://doi.org/10.1038/s41560-023-01208-9>.
- (8) Minnmann, P.; Strauss, F.; Bielefeld, A.; Ruess, R.; Adelhelm, P.; Burkhardt, S.; Dreyer, S. L.; Trevisanello, E.; Ehrenberg, H.; Brezesinski, T.; Richter, F. H.; Janek, J. Designing Cathodes and Cathode Active Materials for Solid-State Batteries. *Adv. Energy Mater.* 2022, 12 (35), 2201425. <https://doi.org/10.1002/aenm.202201425>.
- (9) Wang, C.; Yu, R.; Hwang, S.; Liang, J.; Li, X.; Zhao, C.; Sun, Y.; Wang, J.; Holmes, N.; Li, R.; Huang, H.; Zhao, S.; Zhang, L.; Lu, S.; Su, D.; Sun, X. Single Crystal Cathodes Enabling High-Performance All-Solid-State Lithium-Ion Batteries. *Energy Storage Mater.* 2020, 30, 98–103. <https://doi.org/10.1016/j.ensm.2020.05.007>.
- (10) Gregory, G. L.; Gao, H.; Liu, B.; Gao, X.; Rees, G. J.; Pasta, M.; Bruce, P. G.; Williams, C. K. Buffering Volume Change in Solid-State Battery Composite Cathodes with CO<sub>2</sub>-Derived Block Polycarbonate Ethers. *J. Am. Chem. Soc.* 2022, 144 (38), 17477–17486. <https://doi.org/10.1021/jacs.2c06138>.
- (11) Koerver, R.; Aygün, I.; Leichtweiß, T.; Dietrich, C.; Zhang, W.; Binder, J. O.; Hartmann, P.; Zeier, W. G.; Janek, J. Capacity Fade in Solid-State Batteries: Interphase Formation and Chemomechanical Processes in Nickel-Rich Layered Oxide Cathodes and Lithium Thiophosphate Solid Electrolytes. *Chem. Mater.* 2017, 29 (13), 5574–5582. <https://doi.org/10.1021/acs.chemmater.7b00931>.
- (12) Tan, D. H. S.; Wu, E. A.; Nguyen, H.; Chen, Z.; Marple, M. A. T.; Doux, J.-M.; Wang, X.; Yang, H.; Banerjee, A.; Meng, Y. S. Elucidating Reversible Electrochemical Redox of Li<sub>6</sub>PS<sub>5</sub>Cl Solid Electrolyte. *ACS Energy Lett.* 2019, 4 (10), 2418–2427. <https://doi.org/10.1021/acsenergylett.9b01693>.
- (13) Walther, F.; Koerver, R.; Fuchs, T.; Ohno, S.; Sann, J.; Rohnke, M.; Zeier, W. G.; Janek, J. Visualization of the Interfacial Decomposition of Composite Cathodes in Argyrodite-Based

### 3. Multifunctional ion-conductive polymer coatings for high-performance sulfide solid-state batteries

All-Solid-State Batteries Using Time-of-Flight Secondary-Ion Mass Spectrometry. *Chem. Mater.* 2019, 31 (10), 3745–3755. <https://doi.org/10.1021/acs.chemmater.9b00770>.

(14) Walther, F.; Strauss, F.; Wu, X.; Mogwitz, B.; Hertle, J.; Sann, J.; Rohnke, M.; Brezesinski, T.; Janek, J. The Working Principle of a Li<sub>2</sub>CO<sub>3</sub>/LiNbO<sub>3</sub> Coating on NCM for Thiophosphate-Based All-Solid-State Batteries. *Chem. Mater.* 2021, 33 (6), 2110–2125. <https://doi.org/10.1021/acs.chemmater.0c04660>.

(15) Kitsche, D.; Tang, Y.; Hemmelmann, H.; Walther, F.; Bianchini, M.; Kondrakov, A.; Janek, J.; Brezesinski, T. Atomic Layer Deposition Derived Zirconia Coatings on Ni-Rich Cathodes in Solid-State Batteries: Correlation Between Surface Constitution and Cycling Performance. *Small Sci.* 2023, 3 (2), 2200073. <https://doi.org/10.1002/smssc.202200073>.

(16) Ma, Y.; Zhang, R.; Tang, Y.; Ma, Y.; Teo, J. H.; Diemant, T.; Goonetilleke, D.; Janek, J.; Bianchini, M.; Kondrakov, A.; Brezesinski, T. Single- to Few-Layer Nanoparticle Cathode Coating for Thiophosphate-Based All-Solid-State Batteries. *ACS Nano* 2022, 16 (11), 18682–18694. <https://doi.org/10.1021/acsnano.2c07314>.

(17) Kitsche, D.; Tang, Y.; Ma, Y.; Goonetilleke, D.; Sann, J.; Walther, F.; Bianchini, M.; Janek, J.; Brezesinski, T. High Performance All-Solid-State Batteries with a Ni-Rich NCM Cathode Coated by Atomic Layer Deposition and Lithium Thiophosphate Solid Electrolyte. *ACS Appl. Energy Mater.* 2021. <https://doi.org/10.1021/acsaem.1c01487>.

(18) Amin, R.; Nisar, U.; Rahman, M. M.; Dixit, M.; Abouimrane, A.; Belharouak, I. Prospects of Polymer Coatings for All Solid-State and Emerging Li-Ion Batteries. *J. Mater. Chem. A* 2024, 12 (24), 14186–14205. <https://doi.org/10.1039/D4TA01061B>.

(19) Sen, S.; Trevisanello, E.; Niemöller, E.; Shi, B.-X.; Simon, F. J.; Richter, F. H. The Role of Polymers in Lithium Solid-State Batteries with Inorganic Solid Electrolytes. *J. Mater. Chem. A* 2021, 9 (35), 18701–18732. <https://doi.org/10.1039/D1TA02796D>.

(20) Xu, G.-L.; Liu, Q.; Lau, K. K. S.; Liu, Y.; Liu, X.; Gao, H.; Zhou, X.; Zhuang, M.; Ren, Y.; Li, J.; Shao, M.; Ouyang, M.; Pan, F.; Chen, Z.; Amine, K.; Chen, G. Building Ultraconformal Protective Layers on Both Secondary and Primary Particles of Layered Lithium Transition Metal Oxide Cathodes. *Nat. Energy* 2019, 4 (6), 484–494. <https://doi.org/10.1038/s41560-019-0387-1>.

(21) Deng, S.; Sun, Y.; Li, X.; Ren, Z.; Liang, J.; Doyle-Davis, K.; Liang, J.; Li, W.; Norouzi Banis, M.; Sun, Q.; Li, R.; Hu, Y.; Huang, H.; Zhang, L.; Lu, S.; Luo, J.; Sun, X. Eliminating the Detrimental Effects of Conductive Agents in Sulfide-Based Solid-State Batteries. *ACS Energy Lett.* 2020, 5 (4), 1243–1251. <https://doi.org/10.1021/acseenergylett.0c00256>.

(22) Gan, Q.; Qin, N.; Zhu, Y.; Huang, Z.; Zhang, F.; Gu, S.; Xie, J.; Zhang, K.; Lu, L.; Lu, Z. Polyvinylpyrrolidone-Induced Uniform Surface-Conductive Polymer Coating Endows Ni-Rich LiNi<sub>0.8</sub>Co<sub>0.1</sub>Mn<sub>0.1</sub>O<sub>2</sub> with Enhanced Cyclability for Lithium-Ion Batteries. *ACS Appl. Mater. Interfaces* 2019, 11 (13), 12594–12604. <https://doi.org/10.1021/acsaami.9b04050>.

(23) Lin, C.; Liu, Y.; Su, H.; Zhong, Y.; Wang, X.; Gu, C.; Tu, J. Elevating Cycle Stability and Reaction Kinetics in Ni-Rich Cathodes Through Tailored Bulk and Interface Chemistry for

### 3. Multifunctional ion-conductive polymer coatings for high-performance sulfide solid-state batteries

Sulfide-Based All-Solid-State Lithium Batteries. *Adv. Funct. Mater.* 2024, 34 (21), 2311564. <https://doi.org/10.1002/adfm.202311564>.

(24) Shi, B.-X.; Weber, F.; Yusim, Y.; Demuth, T.; Vettori, K.; Münchinger, A.; Titvinidze, G.; Volz, K.; Henss, A.; Berger, R.; Richter, F. H. Lithiated Polymer Coating for Interface Stabilization in Li6PS5Cl-Based Solid-State Batteries with High-Nickel NCM. *J. Mater. Chem. A* **2025**, 13 (4), 2600–2614. <https://doi.org/10.1039/D4TA07265K>.

(25) Sun, B.; Kazzi, M. E.; Müller, E.; Berg, E. J. Toward High-Performance Li(NixCoyMnz)O2 Cathodes: Facile Fabrication of an Artificial Polymeric Interphase Using Functional Polyacrylates. *J. Mater. Chem. A* 2018, 6 (36), 17778–17786. <https://doi.org/10.1039/C8TA03954B>.

(26) Eshetu, G. G.; Mecerreyes, D.; Forsyth, M.; Zhang, H.; Armand, M. Polymeric Ionic Liquids for Lithium-Based Rechargeable Batteries. *Mol. Syst. Des. Eng.* 2019, 4 (2), 294–309. <https://doi.org/10.1039/C8ME00103K>.

(27) Appetecchi, G. B.; Kim, G.-T.; Montanino, M.; Carewska, M.; Marcilla, R.; Mecerreyes, D.; De Meazza, I. Ternary Polymer Electrolytes Containing Pyrrolidinium-Based Polymeric Ionic Liquids for Lithium Batteries. *J. Power Sources* **2010**, 195 (11), 3668–3675. <https://doi.org/10.1016/j.jpowsour.2009.11.146>.

(28) Wang, X.; Zhu, H.; Girard, G. M. A.; Yunis, R.; MacFarlane, D. R.; Mecerreyes, D.; Bhattacharyya, A. J.; Howlett, P. C.; Forsyth, M. Preparation and Characterization of Gel Polymer Electrolytes Using Poly(Ionic Liquids) and High Lithium Salt Concentration Ionic Liquids. *J. Mater. Chem. A* 2017, 5 (45), 23844–23852. <https://doi.org/10.1039/C7TA08233A>.

(29) Wang, X.; Chen, F.; Girard, G. M. A.; Zhu, H.; MacFarlane, D. R.; Mecerreyes, D.; Armand, M.; Howlett, P. C.; Forsyth, M. Poly(Ionic Liquid)s-in-Salt Electrolytes with Co-Coordination-Assisted Lithium-Ion Transport for Safe Batteries. *Joule* 2019, 3 (11), 2687–2702. <https://doi.org/10.1016/j.joule.2019.07.008>.

(30) Song, X.; Wang, C.; Chen, J.; Xin, S.; Yuan, D.; Wang, Y.; Dong, K.; Yang, L.; Wang, G.; Zhang, H.; Zhang, S. Unraveling the Synergistic Coupling Mechanism of Li<sup>+</sup> Transport in an “Ionogel-in-Ceramic” Hybrid Solid Electrolyte for Rechargeable Lithium Metal Battery. *Adv. Funct. Mater.* 2022, 32 (10), 2108706. <https://doi.org/10.1002/adfm.202108706>.

(31) Vauthier, S.; Alvarez-Tirado, M.; Guzmán-González, G.; Tomé, L. C.; Cotte, S.; Castro, L.; Guéguen, A.; Mecerreyes, D.; Casado, N. High-Performance Pyrrolidinium-Based Poly(Ionic Liquid) Binders for Li-Ion and Li-Air Batteries. *Mater. Today Chem.* 2023, 27, 101293. <https://doi.org/10.1016/j.mtchem.2022.101293>.

(32) Fu, C.; Homann, G.; Grissa, R.; Rentsch, D.; Zhao, W.; Gouveia, T.; Falgayrat, A.; Lin, R.; Fantini, S.; Battaglia, C. A Polymerized-Ionic-Liquid-Based Polymer Electrolyte with High Oxidative Stability for 4 and 5 V Class Solid-State Lithium Metal Batteries. *Adv. Energy Mater.* 2022, 12 (27), 2200412. <https://doi.org/10.1002/aenm.202200412>.

### 3. Multifunctional ion-conductive polymer coatings for high-performance sulfide solid-state batteries

- (33) Homann, G.; Wang, Q.; Liu, S.; Devinenti, A.; Karanth, P.; Weijers, M.; Mulder, F. M.; Piesins, M.; Gouveia, T.; Ladam, A.; Fantini, S.; Battaglia, C. A Quasi-Solid-State Polymer Lithium–Metal Battery with Minimal Excess Lithium, Ultrathin Separator, and High-Mass Loading NMC811 Cathode. *ACS Appl. Energy Mater.* 2024. <https://doi.org/10.1021/acsaem.4c02099>.
- (34) Li, L.; Pascal, T. A.; Connell, J. G.; Fan, F. Y.; Meckler, S. M.; Ma, L.; Chiang, Y.-M.; Prendergast, D.; Helms, B. A. Molecular Understanding of Polyelectrolyte Binders That Actively Regulate Ion Transport in Sulfur Cathodes. *Nat. Commun.* 2017, 8 (1), 2277. <https://doi.org/10.1038/s41467-017-02410-6>.
- (35) Fan, X.; Wang, Y.; Zeng, M.; He, H.; Huang, J.; Feng, Z.; Li, J.; Liang, Z.; Zhou, T. Boosting the Polysulfides Adsorption-Catalysis Process on Carbon Nanotube Interlayer via a Simple Polyelectrolyte-Assisted Strategy for High-Performance Lithium Sulfur Batteries. *J. Alloys Compd.* 2022, 894, 162556. <https://doi.org/10.1016/j.jallcom.2021.162556>.
- (36) Shi, B.-X.; Yusim, Y.; Sen, S.; Demuth, T.; Ruess, R.; Volz, K.; Henss, A.; Richter, F. H. Mitigating Contact Loss in Li6PS5Cl-Based Solid-State Batteries Using a Thin Cationic Polymer Coating on NCM. *Adv. Energy Mater.* 2023, 13 (24), 2300310. <https://doi.org/10.1002/aenm.202300310>.
- (37) Santhosha, A. L.; Medenbach, L.; Buchheim, J. R.; Adelhelm, P. The Indium–Lithium Electrode in Solid-State Lithium-Ion Batteries: Phase Formation, Redox Potentials, and Interface Stability. *Batter. Supercaps* 2019, 2 (6), 524–529. <https://doi.org/10.1002/batt.201800149>.
- (38) Bruce, P. G.; Evans, J.; Vincent, C. A. Conductivity and Transference Number Measurements on Polymer Electrolytes. *Solid State Ion.* **1988**, 28–30, 918–922. [https://doi.org/10.1016/0167-2738\(88\)90304-9](https://doi.org/10.1016/0167-2738(88)90304-9).
- (39) De Vos, N.; Maton, C.; Stevens, C. V. Electrochemical Stability of Ionic Liquids: General Influences and Degradation Mechanisms. *ChemElectroChem* **2014**, 1 (8), 1258–1270. <https://doi.org/10.1002/celc.201402086>.
- (40) Zhao, Q.; Bennington, P.; Nealey, P. F.; Patel, S. N.; Evans, C. M. Ion Specific, Thin Film Confinement Effects on Conductivity in Polymerized Ionic Liquids. *Macromolecules* 2021, 54 (22), 10520–10528. <https://doi.org/10.1021/acs.macromol.1c01820>.
- (41) Cheng, J.; Fong, K. D.; Persson, K. A. Materials Design Principles of Amorphous Cathode Coatings for Lithium-Ion Battery Applications. *J. Mater. Chem. A* **2022**, 10 (41), 22245–22256. <https://doi.org/10.1039/D2TA06051E>.
- (42) Haverkort, W. *Electrolysers, Fuel Cells and Batteries: Analytical Modelling*; TU Delft OPEN Textbooks, 2024. <https://doi.org/10.59490/tb.93>.
- (43) Vargas-Barbosa, N. M.; Roling, B. Dynamic Ion Correlations in Solid and Liquid Electrolytes: How Do They Affect Charge and Mass Transport? *ChemElectroChem* **2020**, 7 (2), 367–385. <https://doi.org/10.1002/celc.201901627>.

### 3. Multifunctional ion-conductive polymer coatings for high-performance sulfide solid-state batteries

- (44) Stolz, L.; Hochstädt, S.; Röser, S.; Hansen, M. R.; Winter, M.; Kasnatscheew, J. Single-Ion versus Dual-Ion Conducting Electrolytes: The Relevance of Concentration Polarization in Solid-State Batteries. *ACS Appl. Mater. Interfaces* **2022**, *14* (9), 11559–11566. <https://doi.org/10.1021/acscami.2c00084>.
- (45) Liu, M.; Zhang, S.; van Eck, E. R. H.; Wang, C.; Ganapathy, S.; Wagemaker, M. Improving Li-Ion Interfacial Transport in Hybrid Solid Electrolytes. *Nat. Nanotechnol.* **2022**, *17* (9), 959–967. <https://doi.org/10.1038/s41565-022-01162-9>.
- (46) Simon, F. J.; Hanauer, M.; Henss, A.; Richter, F. H.; Janek, J. Properties of the Interphase Formed between Argyrodite-Type Li<sub>6</sub>PS<sub>5</sub>Cl and Polymer-Based PEO<sub>10</sub>:LiTFSI. *ACS Appl. Mater. Interfaces* **2019**, *11* (45), 42186–42196. <https://doi.org/10.1021/acscami.9b14506>.
- (47) Wagemaker, M.; Kentgens, A. P. M.; Mulder, F. M. Equilibrium Lithium Transport between Nanocrystalline Phases in Intercalated TiO<sub>2</sub> Anatase. *Nature* **2002**, *418* (6896), 397–399. <https://doi.org/10.1038/nature00901>.
- (48) Yu, C.; Ganapathy, S.; van Eck, E. R. H.; Wang, H.; Basak, S.; Li, Z.; Wagemaker, M. Accessing the Bottleneck in All-Solid State Batteries, Lithium-Ion Transport over the Solid-Electrolyte-Electrode Interface. *Nat. Commun.* **2017**, *8* (1), 1–9. <https://doi.org/10.1038/s41467-017-01187-y>.
- (49) Liu, M.; Wang, C.; Zhao, C.; van der Maas, E.; Lin, K.; Arszewska, V. A.; Li, B.; Ganapathy, S.; Wagemaker, M. Quantification of the Li-Ion Diffusion over an Interface Coating in All-Solid-State Batteries via NMR Measurements. *Nat. Commun.* **2021**, *12* (1), 5943. <https://doi.org/10.1038/s41467-021-26190-2>.
- (50) Yu, W.; Yu, Z.; Cui, Y.; Bao, Z. Degradation and Speciation of Li Salts during XPS Analysis for Battery Research. *ACS Energy Lett.* **2022**, *7* (10), 3270–3275. <https://doi.org/10.1021/acscenergylett.2c01587>.
- (51) Weber, I.; Kim, J.; Buchner, F.; Schnaidt, J.; Behm, R. J. Surface Science and Electrochemical Model Studies on the Interaction of Graphite and Li-Containing Ionic Liquids. *ChemSusChem* **2020**, *13* (10), 2589–2601. <https://doi.org/10.1002/cssc.202000495>.
- (52) Wickham, J. R.; Mason, R. N.; Rice, C. V. Solid-State NMR Studies of the Crystalline and Amorphous Domains within PEO and PEO: LiTf Systems. *Solid State Nucl. Magn. Reson.* **2007**, *31* (4), 184–192. <https://doi.org/10.1016/j.ssnmr.2007.05.001>.
- (53) Zhou, Y.-N.; Ma, J.; Hu, E.; Yu, X.; Gu, L.; Nam, K.-W.; Chen, L.; Wang, Z.; Yang, X.-Q. Tuning Charge–Discharge Induced Unit Cell Breathing in Layer-Structured Cathode Materials for Lithium-Ion Batteries. *Nat. Commun.* **2014**, *5* (1), 5381. <https://doi.org/10.1038/ncomms6381>.
- (54) Lu, Y.; Zhao, C.-Z.; Huang, J.-Q.; Zhang, Q. The Timescale Identification Decoupling Complicated Kinetic Processes in Lithium Batteries. *Joule* **2022**, *6* (6), 1172–1198. <https://doi.org/10.1016/j.joule.2022.05.005>.

### 3. Multifunctional ion-conductive polymer coatings for high-performance sulfide solid-state batteries

(55) Zhang, W.; Weber, D. A.; Weigand, H.; Arlt, T.; Manke, I.; Schröder, D.; Koerver, R.; Leichtweiss, T.; Hartmann, P.; Zeier, W. G.; Janek, J. Interfacial Processes and Influence of Composite Cathode Microstructure Controlling the Performance of All-Solid-State Lithium Batteries. *ACS Appl. Mater. Interfaces* 2017, 9 (21), 17835–17845. <https://doi.org/10.1021/acsami.7b01137>.

(56) Wu, X.; Mirolo, M.; Vaz, C. A. F.; Novák, P.; El Kazzi, M. Reactivity and Potential Profile across the Electrochemical LiCoO<sub>2</sub>–Li<sub>3</sub>PS<sub>4</sub> Interface Probed by Operando X-Ray Photoelectron Spectroscopy. *ACS Appl. Mater. Interfaces* 2021, 13 (36), 42670–42681. <https://doi.org/10.1021/acsami.1c09605>.

(57) Walther, F.; Randau, S.; Schneider, Y.; Sann, J.; Rohnke, M.; Richter, F. H.; Zeier, W. G.; Janek, J. Influence of Carbon Additives on the Decomposition Pathways in Cathodes of Lithium Thiophosphate-Based All-Solid-State Batteries. *Chem. Mater.* 2020, 32 (14), 6123–6136. <https://doi.org/10.1021/acs.chemmater.0c01825>.

(58) Wang, S.; Tang, M.; Zhang, Q.; Li, B.; Ohno, S.; Walther, F.; Pan, R.; Xu, X.; Xin, C.; Zhang, W.; Li, L.; Shen, Y.; Richter, F. H.; Janek, J.; Nan, C.-W. Lithium Argyrodite as Solid Electrolyte and Cathode Precursor for Solid-State Batteries with Long Cycle Life. *Adv. Energy Mater.* 2021, 11 (31), 2101370. <https://doi.org/10.1002/aenm.202101370>.

(59) Chung, H.; Li, Y.; Zhang, M.; Grenier, A.; Mejia, C.; Cheng, D.; Sayahpour, B.; Song, C.; Shen, M. H.; Huang, R.; Wu, E. A.; Chapman, K. W.; Kim, S. J.; Meng, Y. S. Mitigating Anisotropic Changes in Classical Layered Oxide Materials by Controlled Twin Boundary Defects for Long Cycle Life Li-Ion Batteries. *Chem. Mater.* 2022, 34 (16), 7302–7312. <https://doi.org/10.1021/acs.chemmater.2c01234>.

(60) Ryu, H.-H.; Park, N.-Y.; Noh, T.-C.; Kang, G.-C.; Maglia, F.; Kim, S.-J.; Yoon, C. S.; Sun, Y.-K. Microstrain Alleviation in High-Energy Ni-Rich NCMA Cathode for Long Battery Life. *ACS Energy Lett.* 2021, 6 (1), 216–223. <https://doi.org/10.1021/acsenergylett.0c02281>.

## Supplementary Information

3

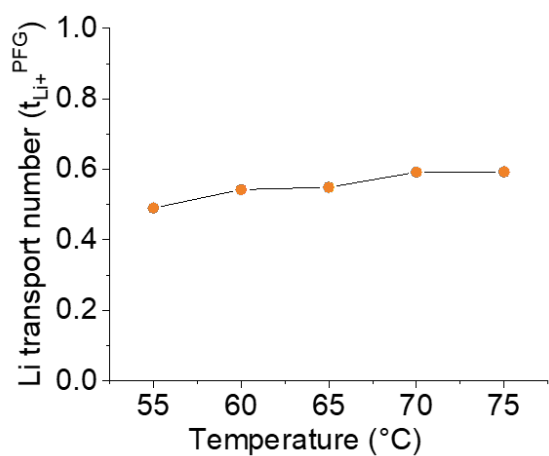


**Figure S1:**  $Li^*$  transport number of 1:1 Li-PIL (obtained from PFG NMR) as a function of temperature

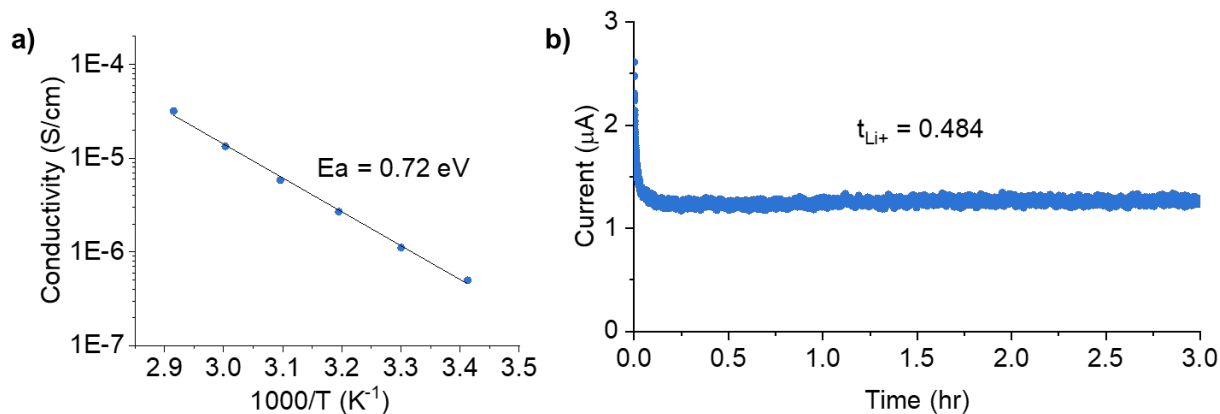


**Figure S2:** a) Ionic conductivity of 1:1 Li-PIL as a function of temperature and b) Chronoamperometry profile under a DC polarization of 5 mV for the determination of Bruce-Vincent  $Li^+$  transference number at 60  $^{\circ}C$

### 3. Multifunctional ion-conductive polymer coatings for high-performance sulfide solid-state batteries

#### Supplementary Note 1: Analytical solution of concentration and potential drop profiles in the Li-PIL coating

To evaluate the concentration and potential drop profiles in the Li-PIL coating, the Li-PIL coating is assumed to be an ideal binary electrolyte layer of thickness  $\delta$ , diffusivity  $D_+$  and concentration  $c_0$ . The steady-state concentration profile in the interface  $c_e$  can be calculated as a function of distance  $x$  (from the solid electrolyte interface), based on the Nernst-Planck transport equation,<sup>1</sup> as:

$$c_e(x) = c_0 - \frac{j}{2 F D_+} \left( x - \frac{\delta}{2} \right)$$

Where  $F$  is the Faraday constant and  $j$  is the specific current density, obtained by assuming a uniform current distribution across all the particle surfaces.

The potential drop  $\Delta\phi$ , defined as the difference between the potential at the solid electrolyte-coating interface and the coating-NMC82 interface, can also be analytically calculated as:

$$\Delta\phi(x) = \frac{RT}{F} \log \left( 1 - \frac{\frac{2}{\delta} x}{1 + \frac{2 c_0 F D_+}{j \delta}} \right)$$

It is to be noted however, that the assumption of ideal binary electrolyte is an approximation in the case of polymer electrolytes with high salt concentrations, as these systems typically also include cation-anion correlated motions, resulting in deviations from this ideal behavior.<sup>2,3</sup> Furthermore, ion diffusivity in thin film polymers is also known to drop due to confinement effects.<sup>4</sup> Therefore, while the extrapolation of diffusivities from PFG NMR (Figure 6a) results in Li\* diffusivity of around  $4 \times 10^{-14} \text{ m}^2/\text{s}$  at 20 °C, we assume a conservative lower bound of  $10^{-15} \text{ m}^2/\text{s}$  for  $D_+$ .

An overview of the values of parameters used for Figures 1b and 1c is shown below.

**Table S1:** Overview of parameters and values used for steady-state concentration and potential drop calculations

Parameter	Value, units
Cationic diffusivity, $D_+$	$10^{-15} \text{ m}^2/\text{s}$
Anionic diffusivity, $D_-$	$4 \times 10^{-15} \text{ m}^2/\text{s}$
Li-PIL thickness $\delta$	100 nm
Li+ initial concentration in Li-PIL, $c_0$	2 M (or mol/dm <sup>3</sup> )
Temperature, T	293 K
Total cycled capacity	2 mAh/cm <sup>2</sup>

### 3. Multifunctional ion-conductive polymer coatings for high-performance sulfide solid-state batteries

Specific surface area of NMC82	0.3 m <sup>2</sup> /g
--------------------------------	-----------------------

The concentration polarization occurs at the beginning of the discharge process since its characteristic time is  $\tau = \delta^2/D_{amb}$ , where  $D_{amb} = 2 \frac{D_+D_-}{D_+ + D_-}$ . For the case of  $D_+ = 10^{-15}$  m<sup>2</sup>/s and  $D_- = 4 \times 10^{-15}$  m<sup>2</sup>/s, the ambipolar diffusivity  $D_{amb} = 1.6 \times 10^{-15}$  m<sup>2</sup>/s. The relaxation time for a layer of thickness  $\delta = 100$  nm is then  $\tau = 6.25$  s. For  $\delta = 10$  nm,  $\tau = 0.06$  s. This means the Li<sup>+</sup> concentration in the coating quickly equilibrates at the beginning of the lithiation process, reaching the steady-state solution provided above.

Furthermore, the influence of  $D_+$  on concentration polarization and potential drops at different coating thicknesses is evaluated (Figure S14). Here, it can be observed that for a thickness of 10 nm, the target thickness of this work, these effects become significant only for  $D_+$  values below  $10^{-16}$  m<sup>2</sup>/s (with a current density of 2 mA/cm<sup>2</sup>).

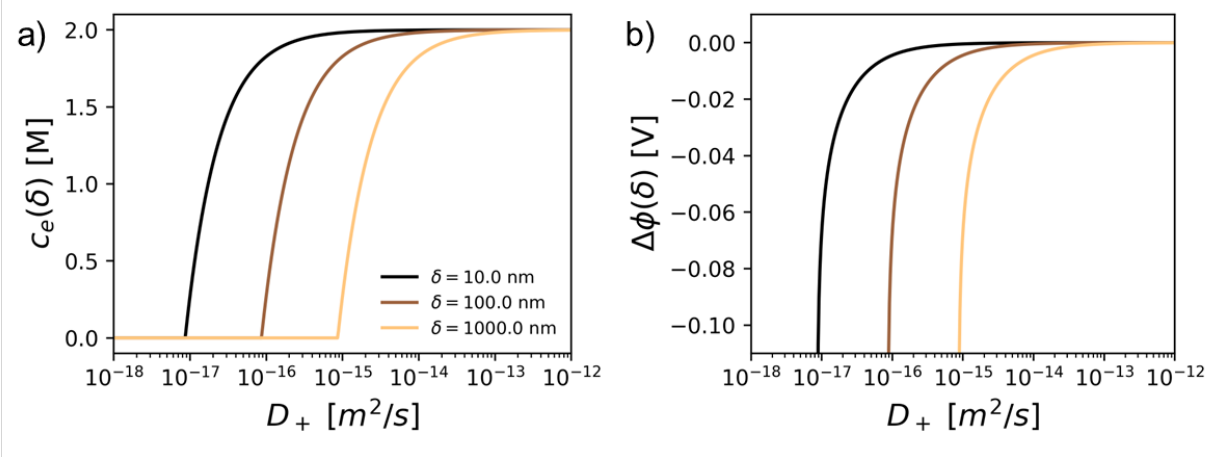


**Figure S3:** a) Steady-state electrolyte concentration at the cathode/Li-PIL interface and b) potential drop across the polymer coating as a function of Li<sup>+</sup> diffusivity at different Li-PIL coating thicknesses.

### 3. Multifunctional ion-conductive polymer coatings for high-performance sulfide solid-state batteries

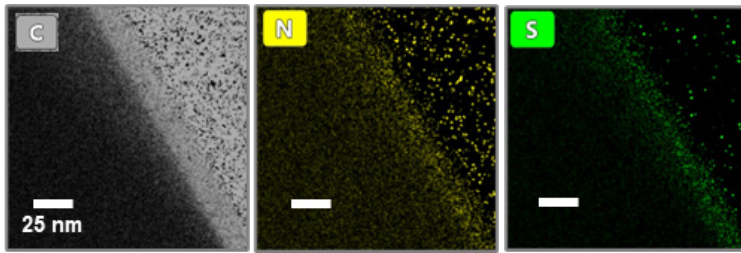


**Figure S4:** STEM-EDX elemental at% mapping of C, N and S, for Li-PIL coated on NMC82 (corresponding to the HAADF-STEM image shown in Figure 2b)

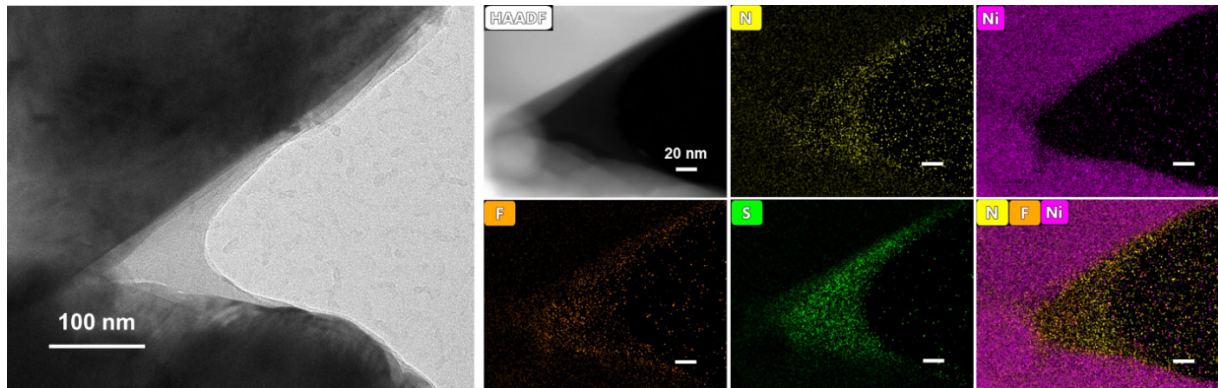


**Figure S5:** TEM image of Li-PIL between NMC82 grains (left) and HAADF, and STEM-EDX elemental at% mapping of Ni, Mn, F, and S, for Li-PIL between NMC82 grains (right). The scale bar for the EDX maps is 20 nm

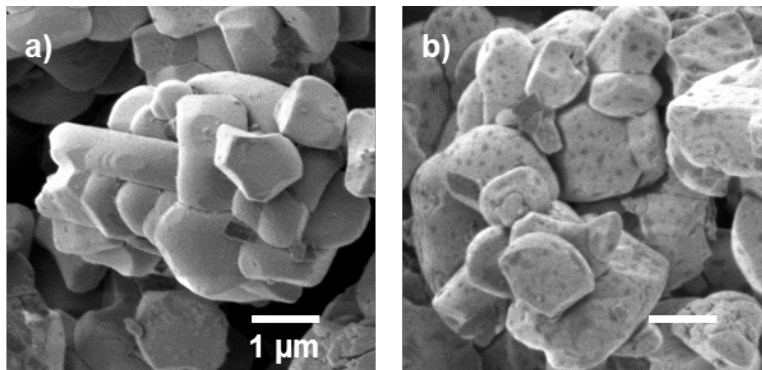


**Figure S6:** a) SEM image of NMC82 and b) SEM image of NMC82 with 2 wt% Li-PIL coating, a and b were taken with SED mode, and 1kV acceleration voltage.

3

### 3. Multifunctional ion-conductive polymer coatings for high-performance sulfide solid-state batteries

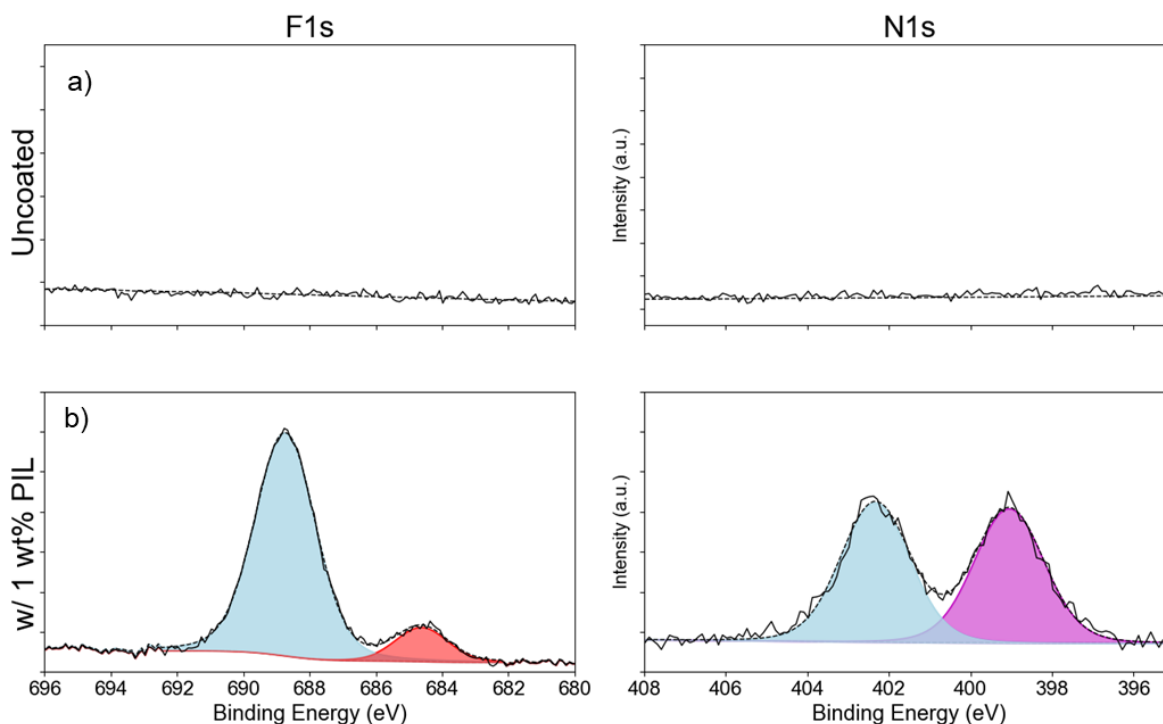


**Figure S7:** High resolution F1s and N1s XPS spectra of a) uncoated NMC82 powder and b) NMC82 powder coated with 1 wt% PIL

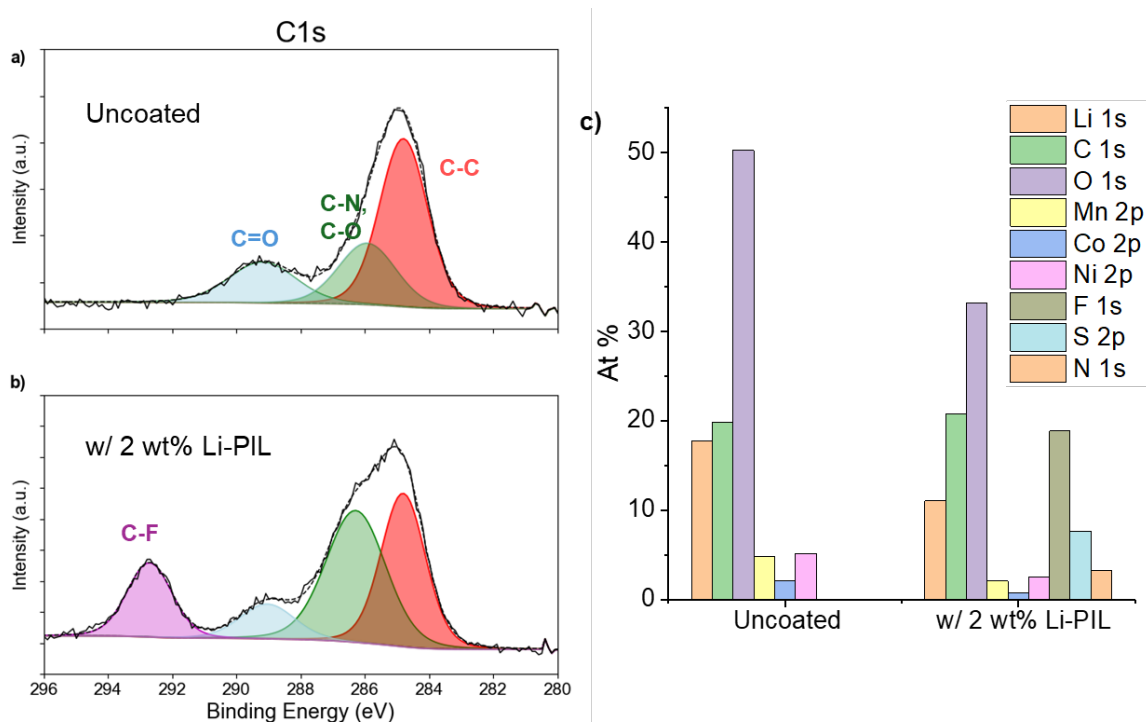


**Figure S8:** High-resolution C1s spectra of a) uncoated NMC82 and b) NMC82 with 2 wt% Li-PIL. c) XPS Survey elemental composition (in At%) of NMC82 and 2 wt% Li-PIL coated NMC82 powders

### 3. Multifunctional ion-conductive polymer coatings for high-performance sulfide solid-state batteries

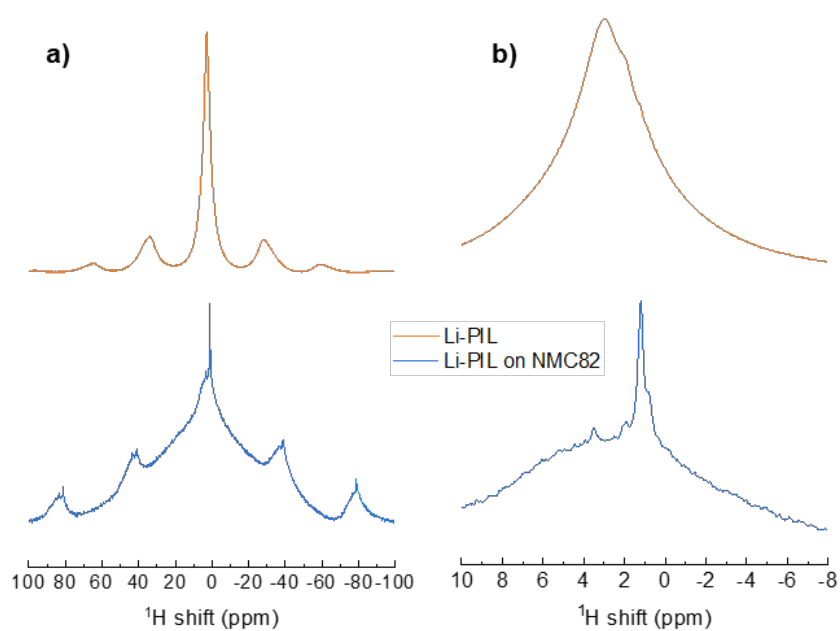


**Figure S9:** a)  $^1\text{H}$  Hahn echo MAS NMR spectra of Li-PIL film (top) and NMC82 coated with Li-PIL (bottom). b) Zoomed inset of  $^1\text{H}$  Hahn echo MAS NMR spectra of 2wt% Li-PIL film (top) and NMC82 coated with 2wt% Li-PIL (bottom)

### 3. Multifunctional ion-conductive polymer coatings for high-performance sulfide solid-state batteries

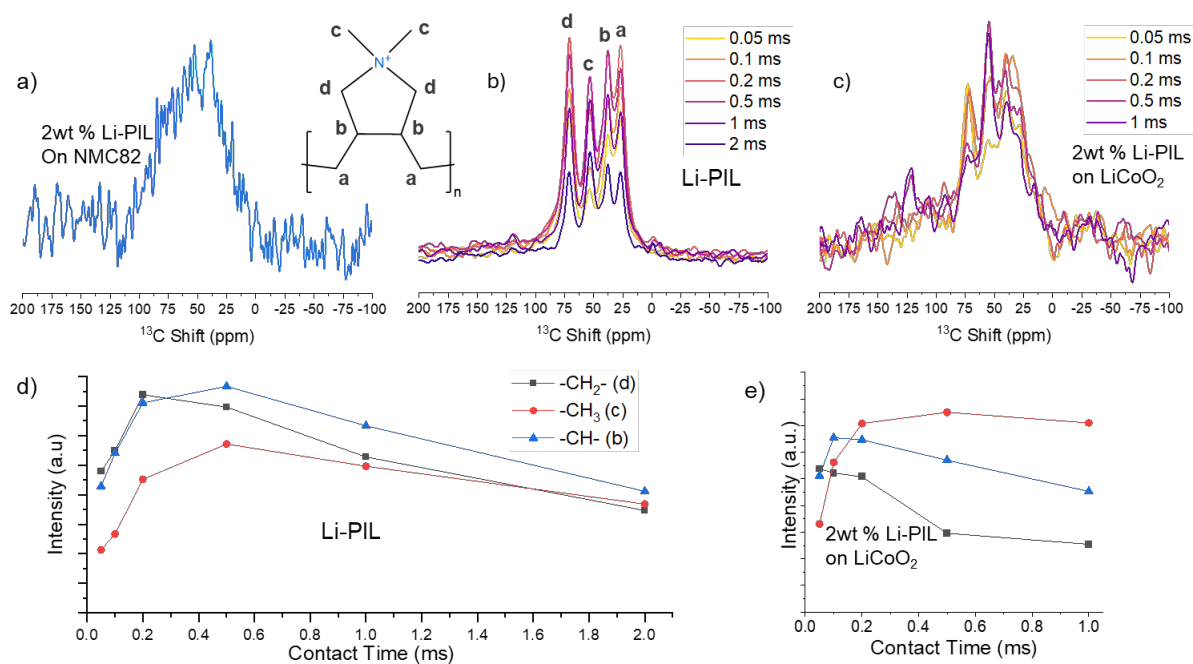


**Figure S10:** a)  $^1\text{H}$ - $^{13}\text{C}$  cross-polarization NMR spectra of 2wt% Li-PIL film (bottom) and NMC82 coated with 2wt% Li-PIL (top) at 15 kHz spinning speed b)  $^1\text{H}$ - $^{13}\text{C}$  CP NMR spectra of Li-PDDATFSI (Li-PIL) film at 10 kHz and contact times of 0.05 – 2 ms. c)  $^1\text{H}$ - $^{13}\text{C}$  CP NMR spectra of 2 wt% Li-PIL coated on  $\text{LiCoO}_2$  at 10 kHz and contact times of 0.05 – 1 ms. d) Intensities of  $^{13}\text{C}$  peaks as a function of contact time for the Li-PIL film e) Intensities of  $^{13}\text{C}$  peaks as a function of contact time for 2 wt% Li-PIL coated on  $\text{LiCoO}_2$ .

### 3. Multifunctional ion-conductive polymer coatings for high-performance sulfide solid-state batteries

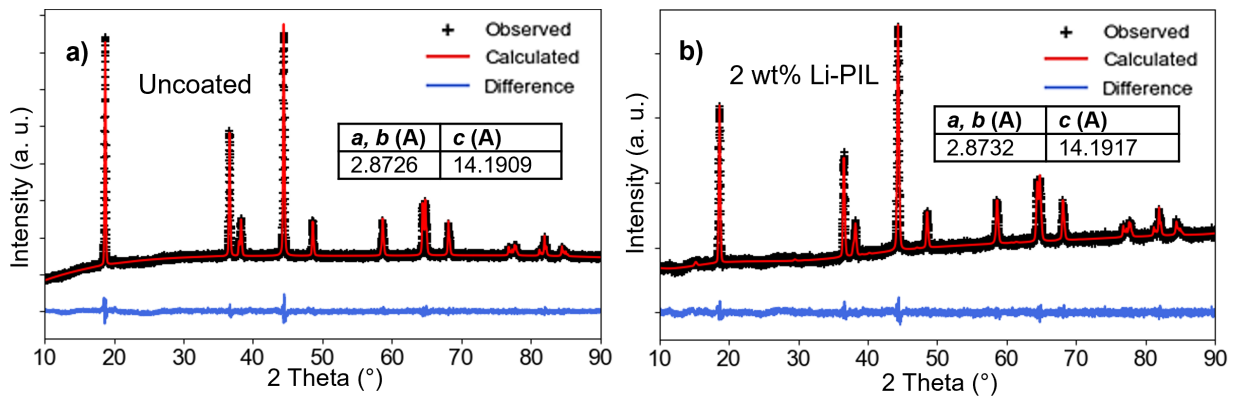


**Figure S11:** XRD spectra with Pawley refinement fit for a) uncoated NMC82 and b) NMC82 coated with Li-PIL

### 3. Multifunctional ion-conductive polymer coatings for high-performance sulfide solid-state batteries

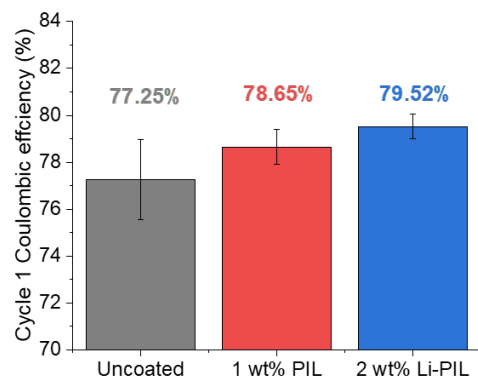


**Figure S12:** First cycle coulombic efficiencies for the uncoated, PIL and Li-PIL cells at 0.05C

### 3. Multifunctional ion-conductive polymer coatings for high-performance sulfide solid-state batteries

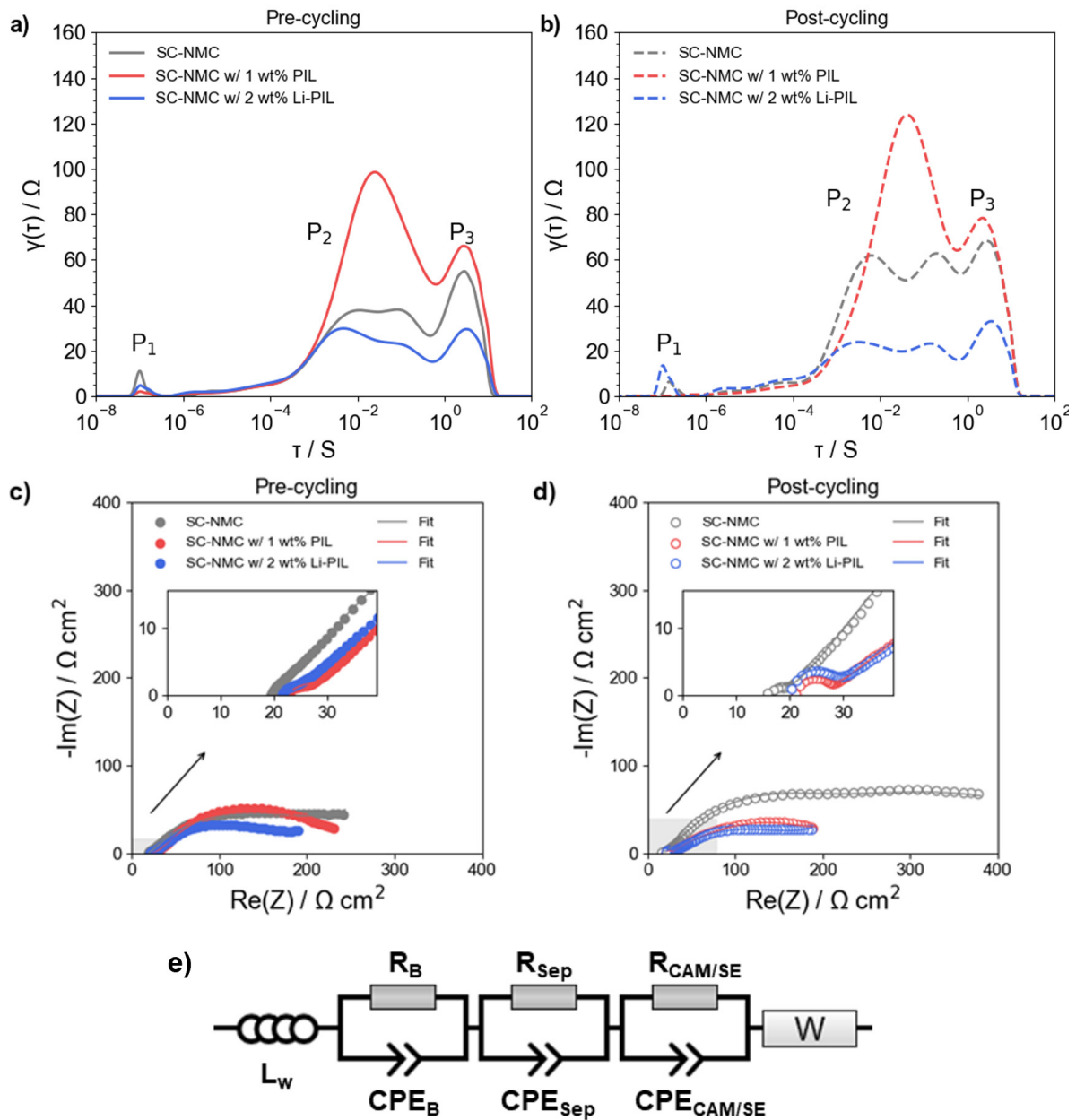


**Figure S13:** Top: Distribution of Relaxation Times (DRT) plots of a) pre-cycling and b) post-cycling for uncoated NMC82, NMC82 with a 1wt% PIL and 2wt% Li-PIL coatings. Middle: Top: Nyquist plots with fits for a) pre-cycling and b) post-cycling for uncoated NMC82, NMC82 with a 1wt% PIL and 2wt% Li-PIL coatings. Bottom: e) The equivalent circuit used for fitting the pre- and post-cycling Nyquist plots.

### 3. Multifunctional ion-conductive polymer coatings for high-performance sulfide solid-state batteries

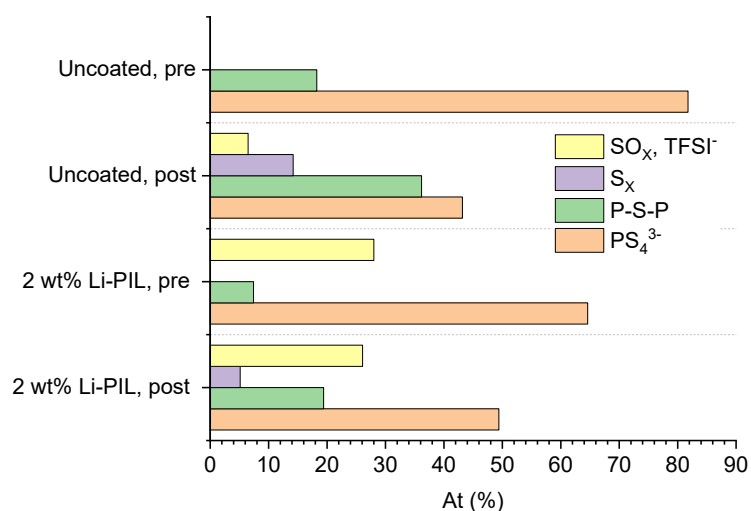


**Figure S14:** Comparison of pre and post-cycling atomic percentages of S-containing environments (normalized to total S2p at%) for cathode composites with and without the Li-PIL coating

**Table S2:** Comparison of total corrected areas corresponding to TFSI-/SO<sub>x</sub> environment in F1s and S2p spectra for the Li-PIL cathode composites

Name	Total Corrected Area, Raw Area/(RSF*T*MFP)	
	2 wt% Li-PIL, pre	2 wt% Li-PIL, post
F1s (TFSI <sup>-</sup> )	7732.49	8636.4
S2p (SO <sub>x</sub> , TFSI <sup>-</sup> )	6121.15	6319.68
Ratio	1.26	1.37

### 3. Multifunctional ion-conductive polymer coatings for high-performance sulfide solid-state batteries

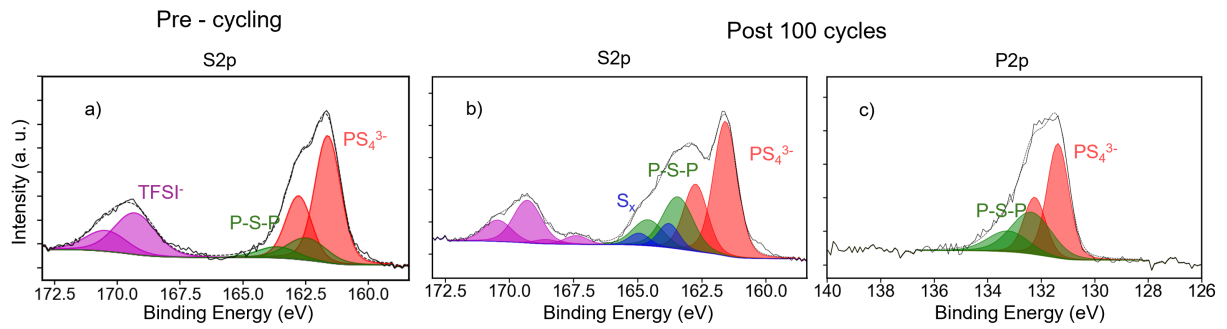


**Figure S15:** Pre-cycling S2p and Post-cycling S2p and P2p XPS spectra of NMC82 cathode composite with 1 wt% PIL coating

### 3. Multifunctional ion-conductive polymer coatings for high-performance sulfide solid-state batteries

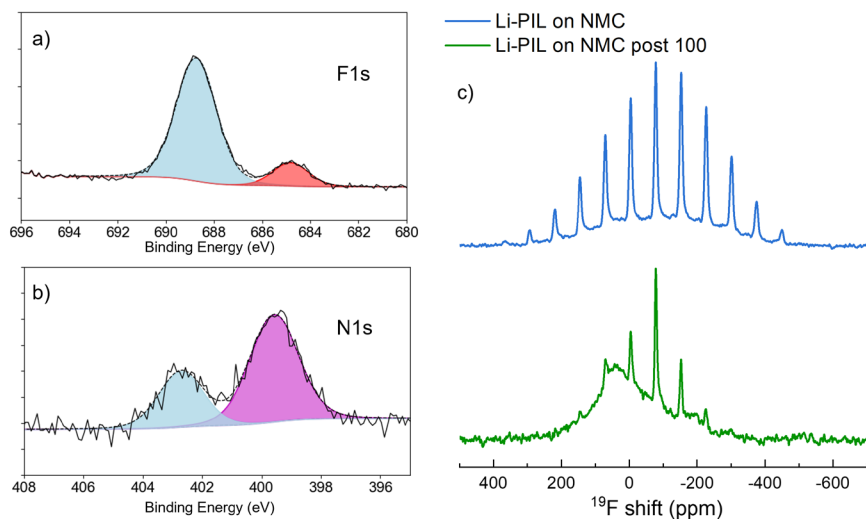


**Figure S16:** Post-cycling a) F1s and b) N1s XPS spectra of single-crystal NMC with 2wt% Li-PIL. c) <sup>19</sup>F MAS NMR spectra of the Li-PIL coated NMC82 cathode composite pre-cycling (top) and post 100 cycles (bottom)

### 3. Multifunctional ion-conductive polymer coatings for high-performance sulfide solid-state batteries

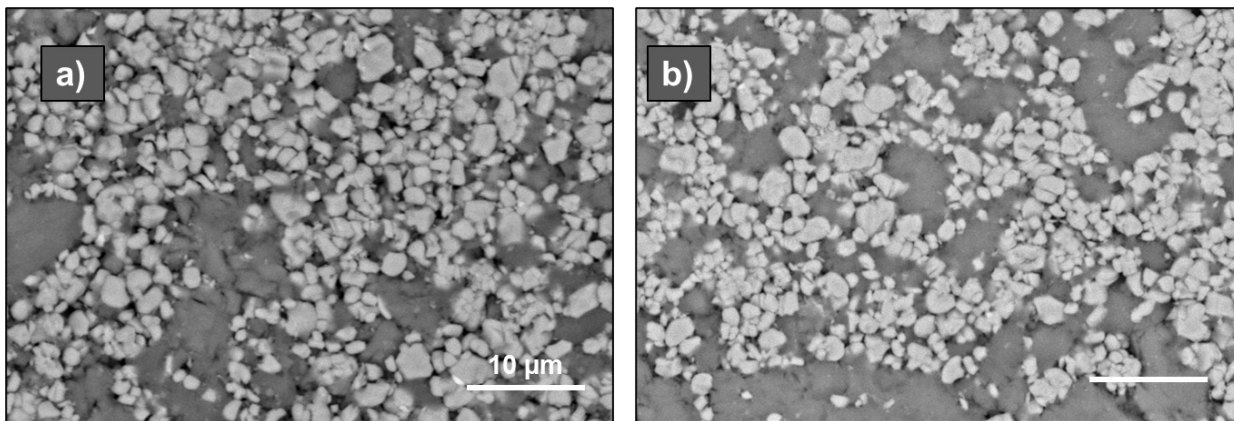


**Figure S17:** SEM images of the NMC82/LPSC composites with a) Uncoated NMC82 before cycling and b) NMC82 with 1 wt% PIL after cycling.

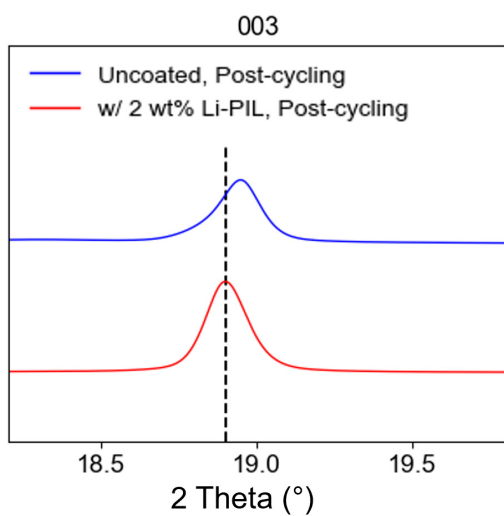


**Figure S18:** Zoomed inset of 003 peaks (of NMC82) for post-cycling uncoated NMC82, 2 wt% Li-PIL coated NMC82 cathode composites.

3

3. Multifunctional ion-conductive polymer coatings for high-performance sulfide solid-state batteries

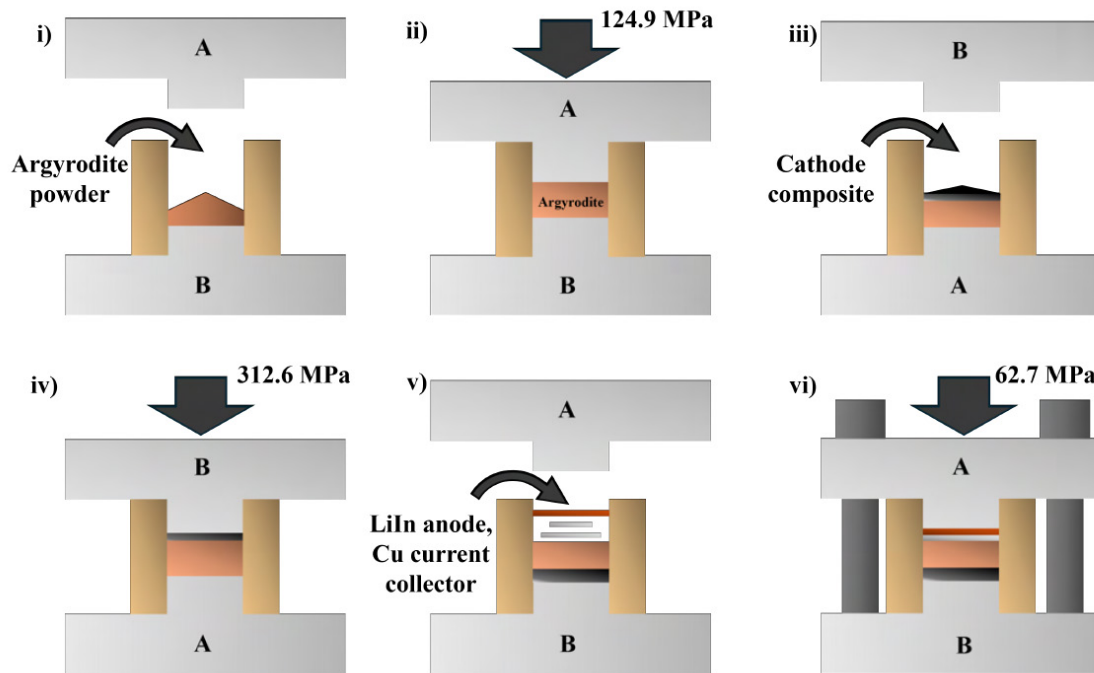


**Figure S19:** Schematic representation of the solid-state battery assembly procedure.

3

4. Understanding the effect of salt concentration on the Li metal interface in gel polymer electrolytes

## Abstract

Gel polymer electrolytes (GPEs) present an interesting class of materials for lithium metal batteries (LMBs), as they combine the benefits of improved mechanical stability against Lithium metal and sufficient ionic conductivity at room temperature. In particular, Polymerized Ionic Liquid (PIL) based GPEs are particularly interesting, given their electrochemical stability against high-voltage cathode materials. The effect of Li salt concentration in such systems has been previously studied in the context of bulk transport properties and ion correlations. However, the effect of salt concentration in GPEs on the chemomechanics of the Li/electrolyte interface is poorly understood.

Here, we study the effect of Lithium bis(fluorosulfonyl)imide (LiFSI salt) concentration in N-Propyl-N-methylpyrrolidinium Bis(fluorosulfonyl)imide (Pyr13FSI)/ Poly(diallyldimethylammonium Bis(fluorosulfonyl)imide)(PDDAFSI) (60:40 wt%) ternary PIL system on the Li/electrolyte interface, using a combination of ex-situ techniques and operando nuclear magnetic resonance (NMR). Here, the increase in salt concentration from 1M to 3M (in Pyr13FSI) resulted in a more inorganic solid electrolyte interphase (SEI) with improved Li<sup>+</sup> transfer, while Neutron Depth profiling (NDP) and operando NMR and showed denser and more uniform Li plating, resulting in improved coulombic efficiencies (CEs). In contrast, a further increase in LiFSI concentration to 4.5M results in minimal changes to the SEI composition, while the areal coverage and effective depth-wise density of Li deposits decrease. These factors, coupled with the deteriorating mechanical strength of the PIL surface layer with the increase in salt concentration, result in increased SEI/dead Lithium generation per cycle, lowering the CE. The results suggest that intermediate salt concentrations in GPEs offer the best balance in terms of chemomechanical stability at the Li interface and Li<sup>+</sup> conductivity/transference.

This chapter is in preparation for submission as a scientific paper:

## 4.1 Introduction

In the quest for safe, high energy density batteries, polymer electrolytes are often looked at as candidates that can offer enhanced safety in comparison to liquid electrolytes while also possessing reasonably good stability vs Li metal, which can enable Li metal as the anode<sup>1,2</sup>. Despite this promise, the commercialization of pure solid polymer electrolytes (SPEs) has been held back due to their poor conductivity. In this regard, gel polymer electrolytes (GPEs), i.e. electrolytes with additional liquid phase as plasticizers have been researched, as these could potentially offer both high ionic conductivity and safety<sup>3</sup>. While most polymer electrolytes studied so far have been based on polyethylene oxide (PEO)<sup>4,5</sup>, other candidates based on PMMA, polycarbonates, polyvinylidene difluoride (PVDF) etc. have also been studied for applications with high-voltage cathodes<sup>6</sup>. In this regard, Polymerized Ionic Liquids (PILs) (both the SPE and their GPEs, also referred to as ternary PILs) are of interest as compounds that display appreciable conductivity at room temperature, while also being stable over a wide electrochemical window, making them a suitable choice for high voltage lithium metal batteries LMBs<sup>7-10</sup>. Further, these electrolytes can also be infiltrated into commercial separators such as Celgard, making their roll-to-roll scale-up feasible.<sup>11</sup>

Salt concentration and its effects on Li transport properties (conductivity, transference number) as well as the Li metal interface (solid electrolyte interphase (SEI) composition and Li plating morphology) have been extensively studied in liquid electrolytes. While higher salt concentration has generally been observed to improve Li<sup>+</sup> transference and also result in an anion-derived inorganic-rich SEI<sup>12,13</sup> leading to stable Li metal plating with large grain size<sup>14</sup>, it does come at a cost of higher viscosity (leading to lower ionic conductivity). While recent studies suggest that an intermediate concentration could in fact result in an optimum in terms of both surface area coverage and grain size of Li deposits<sup>15</sup>, the general approach towards obtaining high coulombic efficiencies in liquid electrolytes has been increasing the salt concentration, either as a whole (High Concentration electrolytes (HCEs)) or locally (Localized High Concentration Electrolytes (LHCEs)<sup>16</sup>).

The effect of salt concentration has also been studied in polymer electrolytes with several studies focusing on the change in bulk transport properties with salt concentration.<sup>17,18</sup> Here, the general trends observed with increasing salt concentration are improvements in Li<sup>+</sup> transference number and/or correlated ion motion favoring constructive Li<sup>+</sup> transport. Interestingly, studies that focus on performance with Li metal do not necessarily show an improvement in the performance of such electrolytes with higher Li salt concentrations. For instance, studies performed on block copolymers have shown high salt concentrations to negatively affect the Li interface characteristics, where the cell lifetime was shown to be governed by the magnitude of the lithium salt concentration gradient.<sup>19,20</sup> For gel polymer electrolyte systems, where an additional plasticizer phase is involved, the effect of the salt concentration, particularly on the Li interface remains underexplored. GPEs present a complex system with typically both the solid and the liquid phase contributing to ion transport and mechanical properties, and a better understanding of the interplay between changes to

#### 4. Understanding the effect of salt concentration on the Li metal interface in gel polymer electrolytes

the SEI composition and the Li microstructure evolution is desired. Further, these systems can be particularly difficult to explore with conventional ex-situ techniques because of the buried interfaces that are difficult to retrieve undamaged<sup>21,22</sup>.

In this work, we study three different salt concentrations in a ternary PIL, i.e. Lithium bis(fluorosulfonyl)imide (LiFSI) in N-Propyl-N-methylpyrrolidinium Bis(fluorosulfonyl)imide (Pyr13FSI)/ Poly(diallyldimethylammonium Bis(fluorosulfonyl)imide)(PDDAFSI (60:40 wt%) system, at moderate to high current densities and capacities. The effect of LiFSI salt concentration on the SEI composition and the Li morphology is studied using operando and ex-situ techniques that complement one another, providing unprecedented insights into the differences between the Li metal/electrolyte interface properties at these salt concentrations and their implications on long-term cycling.

## 4.2 System Definition

The gel polymer electrolyte investigated in this study, i.e., LiFSI in Pyr13FSI/PDDAFSI was previously shown to exhibit excellent electrochemical stability both against Li metal anode and 4V/5V class cathode materials, making it an interesting system for further exploration<sup>10</sup>. Here, the use of ionic liquid Pyr13FSI as a plasticizer/solvent contributes to the improved room temperature conductivity of the electrolyte, and a mass ratio of 60:40 (IL:PIL) was shown to result in a good balance of ionic conductivity and mechanical properties<sup>10</sup>. For this study, the IL:PIL ratio is, therefore, maintained constant at this ratio.

The salt concentration is expected to change the bulk conductivity and Li<sup>+</sup> transference numbers. The electrolytes with three different salt concentrations studied here are provided below in **Table 1**. While the ionic conductivity and Li<sup>+</sup> transference numbers have been measured similar to the previous work on these systems.<sup>11</sup> This work mainly focuses on studying the Li metal/electrolyte interface characteristics with changing salt concentrations, and therefore a detailed investigation of the change in bulk properties and ion correlations is beyond the current scope.

**Table 1:** Compositions and bulk properties of the three studied ternary PILs

Abbreviation	m/m% Polymer PDDA FSI	m/m% Ionic Liquid PYR 13FSI	m/m% Salt Li FSI	Molarity LiFSI in Pyr13FSI	Li+ Conductivity at 20 °C (mS/cm)	Li+ transference number (20 °C)
<b>1M PIL</b>	36.9%	55.4%	7.7%	1	0.185	0.12
<b>3M PIL</b>	32%	48%	20%	3	0.191	0.19
<b>4.5M PIL</b>	29%	43.6%	27.4%	4.5	0.135	0.2

To further enhance the mechanical strength of the PIL, the electrolytes were infiltrated into commercial Celgard 2500 separators, which are a more practical alternative to previously reported separators such as glass fibre and electrospun fibres.<sup>10,11,23</sup>

### 4.3 Electrochemical Performance

The electrochemical performances of PILs with 1M, 3M, and 4.5M LiFSI in Pyr13FSI/PDDAFSI (60:40 wt%) are evaluated in Li/Cu cells. A modification of the method by Adams et. al. was used to determine the Coulombic efficiencies (CEs)<sup>24</sup>. Here, after the initial conditioning cycle (4 mAh/cm<sup>2</sup> of plating at 0.1 mA/cm<sup>2</sup> and stripping at 0.1 mA/cm<sup>2</sup> to 1.5 V, the CEs are evaluated over 50 cycles under 3 conditions, i.e. **a)** 0.2 mA/cm<sup>2</sup>, 1 mAh/cm<sup>2</sup> at 20 °C (referred to as '0.2 mA/cm<sup>2</sup> – 20°C') **b)** 0.2 mA/cm<sup>2</sup>, 1 mAh/cm<sup>2</sup> at 40 °C (referred to as '0.2 mA/cm<sup>2</sup> - 40 °C'), and **c)** 0.5 mA/cm<sup>2</sup>, 2 mAh/cm<sup>2</sup> at 40 °C (referred to as '0.5 mA/cm<sup>2</sup> - 40°C'). In all cases, an initial Li reservoir plating at 0.2 mA/cm<sup>2</sup> and 3 mAh/cm<sup>2</sup> was carried out, followed by 50 cycles at the desired condition, and finally Li stripping was carried out at 0.2 mA/cm<sup>2</sup> until a cutoff potential of 1.5V was reached. The results are shown in **Figure 1a, d, and g**, with the zoomed inset of the voltage traces shown in **Figure 1b, e, and h-i**, and the resulting coulombic efficiencies are displayed in **Figure 1c,f, and j**, respectively.

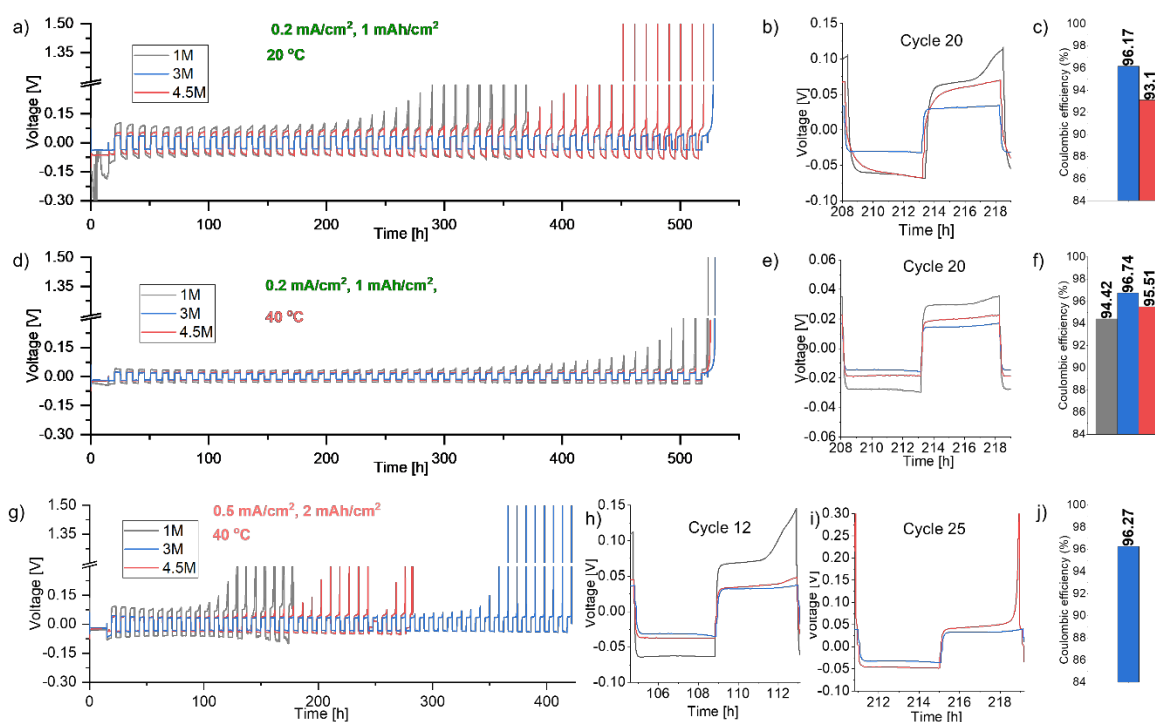


**Figure 1: Electrochemical performance of PILs in Li/Cu cells:** Top: a) Voltage traces of Galvanostatic plating/stripping in Li/PIL/Cu cells for 50 cycles at 0.2 mA/cm<sup>2</sup>, 1 mAh/cm<sup>2</sup> at 20 °C, with b) showing the voltage traces at cycle 20 and c) the overall coulombic efficiencies. Middle: d) Voltage traces for 50 cycles at d) 0.2 mA/cm<sup>2</sup>, 1 mAh/cm<sup>2</sup> at 40 °C, with e) showing the voltage traces at cycle 20 and f) the overall coulombic efficiencies. Bottom: g) Voltage traces for 50 cycles at 0.5 mA/cm<sup>2</sup>, 2 mAh/cm<sup>2</sup> at 40 °C with h) showing the voltage traces at cycle 12, i) showing the voltage traces at cycle 25 and j) the overall coulombic efficiencies

For the 1M and 4.5 PIL cells cycling at 0.2 mA/cm<sup>2</sup> – 20°C, the plating/stripping overpotentials are always higher as compared to the 3M PIL. With extended cycling, there is a considerable

#### 4. Understanding the effect of salt concentration on the Li metal interface in gel polymer electrolytes

difference in the voltage traces for the three electrolytes (**Figure 1b**). For the 1M PIL, the shape of the voltage trace transforms to that with a diverging peak towards the end of stripping, typical of mass transfer limitations in the electrolyte bulk (ion depletion close to the electrode interface). Considering the low charge carrier concentration and  $\text{Li}^+$  transference number for this system, this is plausible. For the 4.5 M PIL, the voltage trace continues to have an arcing pattern, and such a voltage trace has previously been attributed to Li transport through tortuous layers of dead lithium<sup>25</sup>. In contrast, the 3M PIL maintains a stable, nearly flat voltage trace throughout cycling, indicative of stable Li plating/stripping. At 0.2 mA/cm<sup>2</sup> - 40 °C, the overpotentials are initially low for all three electrolytes, with nearly flat voltage traces (**Figure 1e**). However, a diverging voltage trace is observed for the 1M PIL beyond cycle 40 (hour 400).

With a more aggressive cycling condition, i.e. 0.5 mA/cm<sup>2</sup> - 40°C (**Figure 1g**), a diverging voltage trace is observed much earlier for the 1M PIL (**Figure 1h**). For the 4.5M PIL, while the voltage trace is initially comparable to that of the 3M PIL, the coulombic efficiency per cycle eventually lowers, resulting in sharp voltage cutoffs much earlier compared to the 3M PIL (**Figure 1i**). In contrast, the 3M PIL shows the lowest overpotential and a flat voltage trace under all three testing conditions, indicative of stable cycling with no mass transfer limitations in either the electrolyte bulk or at the Li/electrolyte interface.

These differences in the electrochemical performance are also reflected in the average CEs over 50 cycles (**Figure 1d**). While all electrolytes display the best CEs at 0.2 mA/cm<sup>2</sup> - 40 °C, the 3M LiFSI PIL consistently shows the best coulombic efficiencies (of above 96%) under all testing conditions, with the best CE of 96.74% obtained under condition 0.2 mA/cm<sup>2</sup> - 40 °C.

#### 4.4 Differences at the Li interface with initial (formation) cycling:

Looking at the electrochemical performances under different conditions, it is clear that the cell polarization/failure modes can change depending on the salt concentration and the cycling conditions. While 1M PIL with low carrier concentration and transference number suffers from ion depletion-induced gradients and possibly other factors such as (comparatively) organic-rich SEI,<sup>11</sup> the 4.5M PIL appears to suffer from lower CEs with continued cycling, possibly either due to dead Li generation and/or uneven SEI formation. The intermediate concentration of 3M performs the best under the probed conditions, and the reasons behind this are investigated further.

##### 4.4.1 Charge transfer kinetics

In previous works, high CEs for Li plating/stripping have been shown to have a positive correlation with kinetics at the Li/electrolyte interface<sup>26</sup>. This observation is also reflected in the Electrochemical Impedance Spectroscopy (EIS) Nyquist plots of the Li/Cu coin cells after the initial conditioning cycle (**Figure 2a**), with the higher salt concentration cells showing lower overall charge transfer resistance ( $R_{CT}$ ) values (i.e. the real axis length of the depressed semicircle) as compared to the 1M PIL. In liquid electrolytes, higher salt concentrations are

#### 4. Understanding the effect of salt concentration on the Li metal interface in gel polymer electrolytes

expected to result in a thin inorganic-rich SEI with high  $\text{Li}^+$  conductivity, as opposed to an organic-rich, porous SEI typically formed due to higher solvent decomposition for lower salt concentrations<sup>14</sup>. It is to be noted, however, that the value of  $R_{CT}$  decreases in the order of  $1\text{M} > 4.5\text{M} > 3\text{M}$  at  $20\text{ }^\circ\text{C}$  (**Figure 3a**) and at higher temperatures (**Figure 3b**), as opposed to a monotonic decrease with increase in salt concentration.

The overall  $R_{CT}$  contains contributions from both the desolvation kinetics at the Li/electrolyte interface ( $R_{de}$ ) and  $\text{Li}^+$  transport through the SEI ( $R_{SEI}$ ), the latter typically having lower time constants.<sup>27</sup> While deconvoluting the two contributions from Nyquist plots obtained for Li/Cu and Li/Li cells can be difficult, Distribution of Relaxation Times (DRT) analysis has been previously employed to guide such deconvolution<sup>27</sup>. Here, the DRT analysis of the EIS plots reveals that SEI resistance has a much higher contribution to  $R_{CT}$  than desolvation ( $R_{de}$ ) for all the salt concentrations (**Figure 2c**). It is also observed that while the ( $R_{de}$ ) seems to decrease with the increase in salt concentration,  $R_{SEI}$  has the same trend as the overall  $R_{CT}$ .

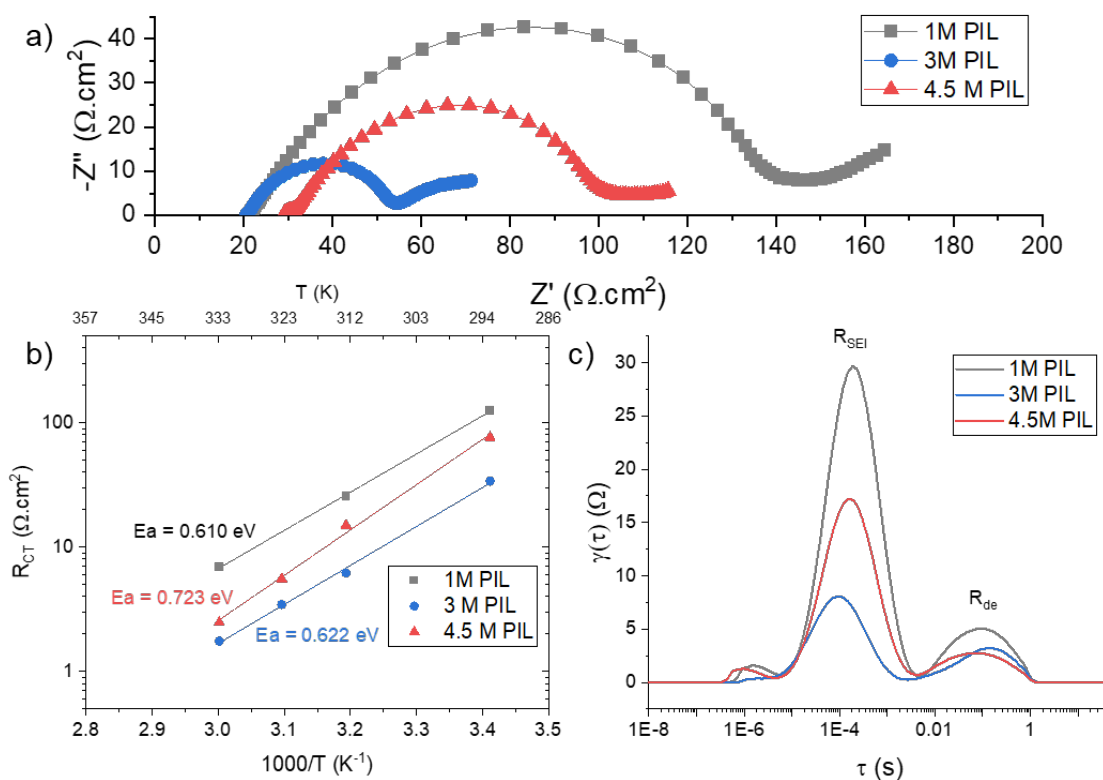


**Figure 2: Kinetics at the PIL/Li interface:** a) EIS Nyquist plot of Li/Cu cells after the initial conditioning cycle at  $20\text{ }^\circ\text{C}$  (measured at  $T = 20\text{ }^\circ\text{C}$ ). b) Comparison of  $R_{CT}$  values as a function of temperature and the calculated activation energies for the Li/PIL interface c) Distribution of Relaxation Times (DRT) analysis of EIS spectra of Li/PIL/Cu cells after the formation protocol.

Furthermore, the activation energies ( $E_a$ ) for the overall charge transfer, while nearly the same for 1M and 3M PILs (0.610 eV and 0.622 eV) also show an increase going from 3M to 4.5M

#### 4. Understanding the effect of salt concentration on the Li metal interface in gel polymer electrolytes

4.5 M LiFSI (0.622 eV to 0.723 eV). It is important to note that the value of  $R_{CT}$  and its components obtained from the EIS can be influenced both by the changes in the SEI composition/structure and the surface area of active and dead Li. Therefore, an increase in the  $R_{SEI}$  could be a combination of SEI thickening and the changes in the deposited Li surface area, and both of these aspects will be addressed in the coming sections.

##### 4.4.2 SEI Composition

As previously stated, the characterization of Li interfaces in gel polymer electrolytes can be challenging given the difficulties involved in efficiently separating and analyzing the electrode/electrolyte interface in these systems<sup>22</sup>. Therefore, we employ two complementary techniques, i.e., solid-state nuclear magnetic resonance spectroscopy (ssNMR) and X-ray photoelectron spectroscopy (XPS). While ssNMR is utilized to look at the Li interface composition in its unaltered state, i.e. with the salt/PIL traces adhering to the electrodeposited Lithium (EDLi) scraped off from the Cu current collectors, XPS is used to study the depth-dependent elemental composition of the SEI in its washed state. Here, the Cu foils with EDLi were washed and dried prior to analysis to remove the salt/polymer traces, as  $Ar^+$  sputtering could lead to in-situ speciation of salt/polymer traces, making the results erroneous.<sup>28</sup> Further, the typical probing depth of XPS is only 3-5 nm for inorganic materials typically found in Li SEI<sup>29</sup> and having much thicker PIL traces (in the micron range) on top would make the analysis difficult.

For the ssNMR spectra shown in **Figure 3 a,b**, spectra are normalized to the area of LiFSI peak in the  $^7Li$  spectrum (**Figure 3b-d, S1**) for the sake of a semi-quantitative comparison.

**Figure 3a** shows the  $^{19}F$  spectra for the three PILs. A relatively higher amount of LiF is formed in the case of 3 and 4.5 M PILs, while a third significant environment is observed at  $\sim 78$  ppm, which could be attributed to the  $SO_2F^-$  intermediate fragments resulting from the stepwise decomposition of LiFSI.<sup>30</sup> Further, in comparison to 1M and 3M PILs, the 3M PIL shows a much higher amount of 'mobile'  $FSI^-$  (coming mainly from LiFSI and Pyr13FSI), which could be indicative of relatively higher amounts of PIL traces being present on/within the Li deposits of these systems. A significant portion of the diamagnetic peak in the  $^7Li$  spectra (**Figure 3b-c**) comes from the SEI components in the case of 1M and 3M PILs, which is evident from the extent of broad features observed downfield of the LiFSI salt peak (at -2 ppm). The broader SEI-associated peak still forms a major fraction of the diamagnetic peak in the case of the 4.5 M PIL (**Figure 3d**), but the relative abundance of PIL/salt traces in this case is also evident from the lower  $A_{SEI}/A_{Salt}$  ratio (2.03 for the 4.5M PIL as opposed to 4.16 for the 1M PIL and 3.45 for the 3M PIL).

The XPS results provide further insights into the chemical environment of the SEI as a function of depth. XPS survey spectra (with depth profiling) indicate a clear shift towards a more inorganic SEI with higher salt concentrations (**Figure 3 e,f,g**). It is observed that for the 1M PIL, the atomic percentage of the SEI is dominated by C (**Figure 3e**), whereas 3M and 4.5M PILs show higher inorganic content (Li and O content) in comparison (**Figure 3f, g**). While all

#### 4. Understanding the effect of salt concentration on the Li metal interface in gel polymer electrolytes

samples are shown to have a high amount of LiF in the inner SEI (**Figure S1-S3**), consistent with the ssNMR observations, the Li<sub>2</sub>O content in the inner part of the SEI is observed to be higher for 3M and 4.5M samples (**Figure S1-S3**), along with the presence of Li<sub>x</sub>O<sub>y</sub> and -SO<sub>2</sub>F based compounds. For the 1M sample, the C1s spectra at the surface (**Figure S1**) shows a higher ratio of C-O/C-N environment (at ~286 eV), which could be coming from either the PIL traces or the decomposition products of Pyr13FSI with a quaternary N<sup>+</sup> ion.<sup>31</sup>

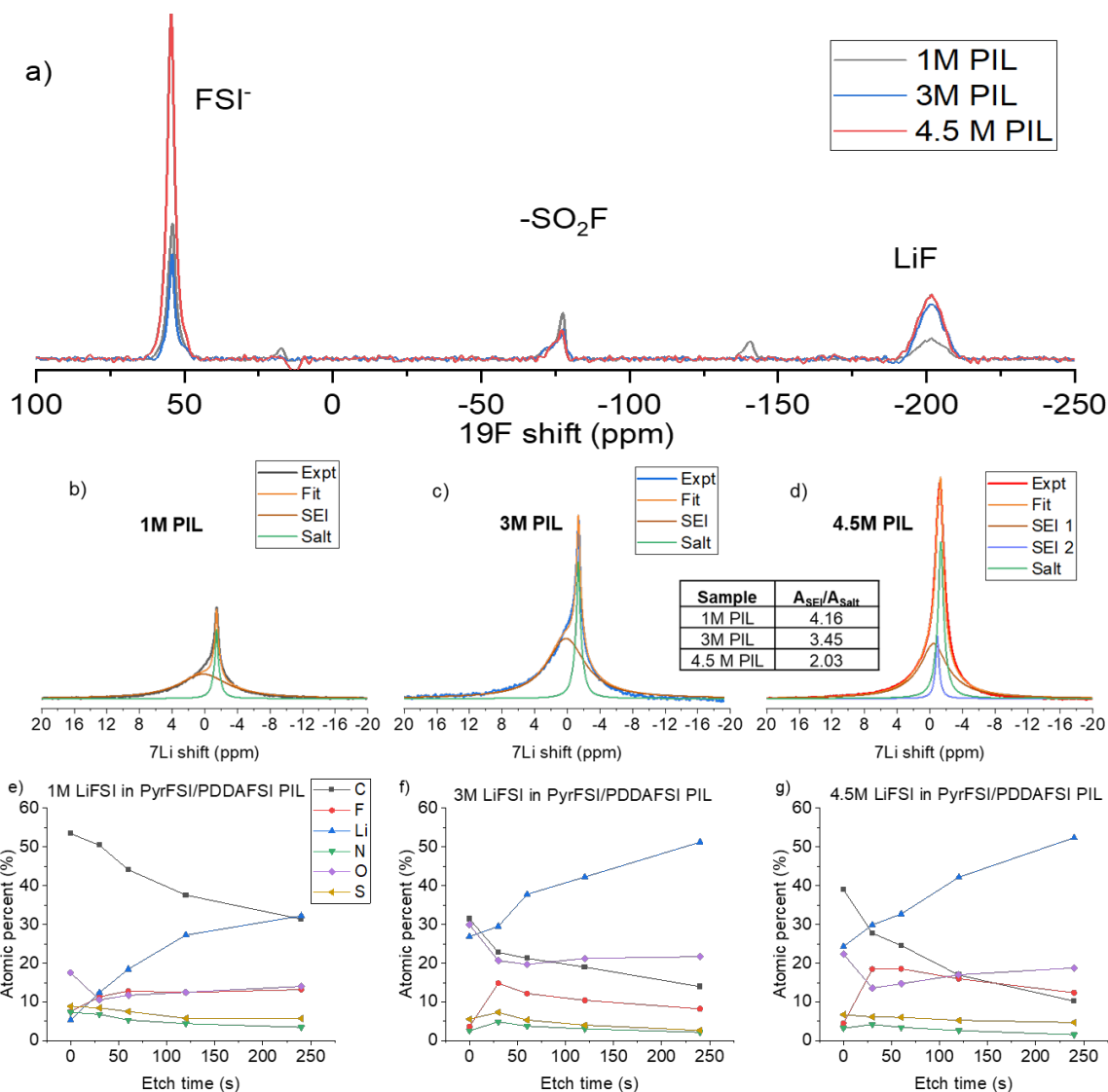


**Figure 3: SEI composition at the Li/PIL interface after the initial conditioning cycle: a)** <sup>19</sup>F NMR of the Li/PIL interface **b)** <sup>7</sup>Li NMR of the Li/PIL interface for 1M PIL **c)** <sup>7</sup>Li NMR of the Li/PIL interface for 3M PIL **d)** <sup>7</sup>Li NMR of the Li/PIL interface for 4.5M PIL **e)** XPS survey atomic percentage (with depth profiling) for 1M PIL/Li interface, **f)** XPS survey atomic percentage (with depth profiling) for 3M PIL/Li interface, **g)** XPS survey atomic percentage (with depth profiling) for 4.5M PIL/Li interface

The organic C-C environment is still found (with depth profiling to 120 s) in the inner part of the SEI for the 1M sample, while this environment drops rapidly for the 3M and 4.5M samples.

#### 4. Understanding the effect of salt concentration on the Li metal interface in gel polymer electrolytes

These results suggest that the initial SEI composition significantly changes in terms of elemental percentages going from 1M to 3M, with minimal changes going from 3M to 4.5M suggesting that the extent of difference in  $R_{CT}$  observed in the case of 3M and 4.5M PILs could additionally be linked to the Li morphology differences.

##### 4.4.3 Lithium morphology evolution

While relatively simple techniques such as operando optical microscopy can be used to track Li plating and stripping in liquid electrolytes<sup>32</sup>, this can be hard to achieve with solid and polymer electrolytes, owing to the relative opacity of the electrolytes and buried interfaces. Here, a combination of operando and ex-situ techniques was applied to study the evolution of Li morphology on Cu with cycling. Operando NMR has been recently employed as a technique to study Li plating/stripping behavior in liquid electrolytes by harnessing the ability of NMR to be sensitive to different morphology/orientation of Lithium with respect to the magnetic field<sup>15,33,34</sup>. In contrast, neutron depth profiling (NDP), a nondestructive technique based on the neutron capture reaction by  $^6\text{Li}$ , can be sensitive to the differences in Li plating density and can distinguish between porous and compact Li deposition as a function of depth and experiment time<sup>35,36</sup>. Results from operando NMR are compared to images from ex-situ scanning electron microscopy (SEM) and results from NDP to obtain insights into the Li morphology evolution.

The operando NMR results for the Li/Cu cells with 1M, 3M and 4.5M PIL as the electrolyte are shown in **Figures 4** and **6**. Here, the Li/Cu cells were cycled for 5 cycles at a low current density  $0.1 \text{ mA/cm}^2$ ,  $0.5 \text{ mAh/cm}^2$ , followed by 4 cycles at a higher current density  $0.2 \text{ mAh/cm}^2$ ,  $0.5 \text{ mAh/cm}^2$ , all at  $20 \text{ }^\circ\text{C}$ . **Figure 4** shows the voltage traces, alongside the contour plots of Li metal chemical shifts for the first two cycles, and a 1D overlay of the Li metal spectra after 0, 1, 2 and 4 cycles at  $0.1 \text{ mA/cm}^2$ , while **Figure 6** shows these for the current density of  $0.2 \text{ mA/cm}^2$  and for 1M and 3M PILs.

At low current densities, Li plating is observed to occur at  $\sim 253 \text{ ppm}$  for the 1M PIL, while this occurs at a slightly higher chemical shift, i.e.  $258 \text{ ppm}$  for the 3M PIL (**Figure 4 a, b**). A comparable amount of signal remaining (after stripping), corresponding to the dead Li generated, is observed for both salt concentrations after 1, 2 and 4 cycles (**Fig 4a and b**, right). It can also be noticed that the amount of Li metal plating (Li plating intensity on the contour plot) for the first two hours is a bit lower for the 3M PIL (**Figure 4b**), suggesting that a higher share of capacity applied could be dedicated to SEI formation at this stage, which is also reflected in the slightly lower coulombic efficiencies at  $0.1 \text{ mA/cm}^2$  for the 3M PIL (**Figure S5**). This trend is also observed with a further increase in PIL salt concentration, i.e. for the 4.5 M PIL, which has a much lesser coulombic efficiency for the first few cycles, and also a lower intensity of Li metal plating from the contour plots (**Figure 4c**), suggesting an even higher extent of SEI formation.

#### 4. Understanding the effect of salt concentration on the Li metal interface in gel polymer electrolytes

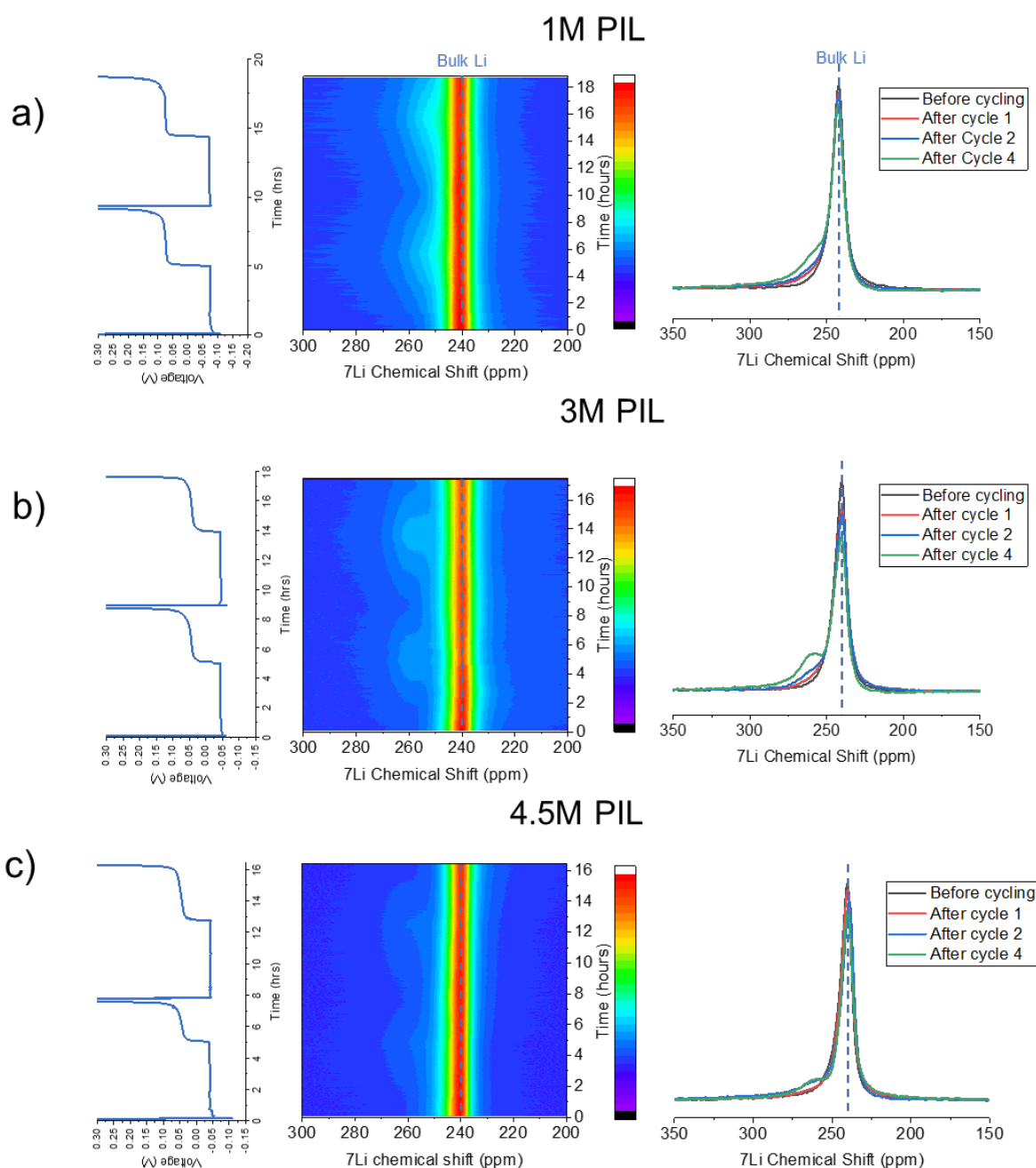


**Figure 4: Operando  $^7\text{Li}$  NMR of Li/PIL/Cu cells at  $0.1 \text{ mA/cm}^2$ : Voltage traces (left), 2D contour plot of Li metal intensities (middle), and Li metal spectra at different cycling stages (right) for a) 1M PIL at  $0.1 \text{ mA/cm}^2$  b) 3M PIL at  $0.1 \text{ mA/cm}^2$  c) 4.5M PIL at  $0.1 \text{ mA/cm}^2$**

To rule out the possibility that the signal from some of the EDLi is indistinguishable from that of the bulk Li (i.e. around 240 ppm), ex-situ NMR of the  $2 \text{ mAh/cm}^2$  Li deposits at  $0.1 \text{ mA/cm}^2$  was also performed (**Figure S6**), which show nearly the same chemical shifts for the EDLi as with the operando NMR, again showing different chemical shifts of EDLi for every salt concentration, suggesting possible differences in the morphology and nucleation/growth mode for these deposits.

#### 4. Understanding the effect of salt concentration on the Li metal interface in gel polymer electrolytes

These differences in the morphology and depth-wise density of EDLi for the three PILs can be further understood with the help of ex-situ Neutron Depth Profiling (NDP) for 1 mAh/cm<sup>2</sup> deposits (**Figure 5a-c**) and Scanning electron Microscopy (SEM) for 1 and 2 mAh/cm<sup>2</sup> deposits (**Figures 5d**), all plated at 0.1 mA/cm<sup>2</sup> at 20 °C. For the NDP, the EDLi on Cu with the PIL separator attached to it was analyzed under the Neutron beam with the configuration shown in **Figure 5a**, whereas for the SEM, the EDLi samples were washed and dried to remove the PIL/salt traces. Further information on the conversion of obtained NDP data from energy to depth-wise (normalized) Li density is further described in Supplementary Note S1.

With NDP, the 1M PIL deposits show a gradual increase in (normalized) Li density towards the current collector, but this density stays low (<0.3 of bulk Li). In contrast, the density for the 3M PIL deposit shows a sharp increase towards the current collector and a high value (>0.4 of bulk Li) at the edge of the current collector. In comparison, the 4.5M PIL deposit has a Li density greater than that for the 1M, but this density flattens and shows a small drop towards the current collector, where its density is lower than that for the 3M PIL. With an increased amount of plating of 3 mAh/cm<sup>2</sup>, the 3M PIL deposit now shows a high (>0.4 of bulk Li) nearly uniform Li density throughout the observable window.

With ex-situ SEM, it is observed that the grain size of deposited Li and area coverage progressively change with salt concentration for the 1 mAh/cm<sup>2</sup> deposits, consistent with literature on liquid electrolytes<sup>14,15</sup>. With further plating to 2 mAh/cm<sup>2</sup>, the deposits nearly follow the initial template, and while the 1M PIL Li morphology transforms from low grain size compact deposits to nodule-like/mossy deposits with a high surface coverage, 3M and 4.5M PILs result in Li deposits with larger grain sizes and lower surface coverage. In terms of shape, the 3M deposits appear globular as opposed to being layered like in the case of the 1M PIL. With further Li deposition, growth/thickening of initial deposits occurs, which further explains why the depth-wise density of the deposit is now nearly the same as observed with NDP.

In comparison, the 4.5M sample displays an even larger grain size, but also a higher percentage of voids in between the deposits, suggesting an even lower geometric area coverage on the current collector (**Figure S8** shows the SEM images over a wider area for 3M and 4.5M PIL samples). This, coupled with the NDP observations of Li density slightly dropping close to the current collector for the 4.5M sample suggests a drop in the number of nucleation sites with the increase in salt concentration, leading to the observed morphology with SEM.

#### 4. Understanding the effect of salt concentration on the Li metal interface in gel polymer electrolytes

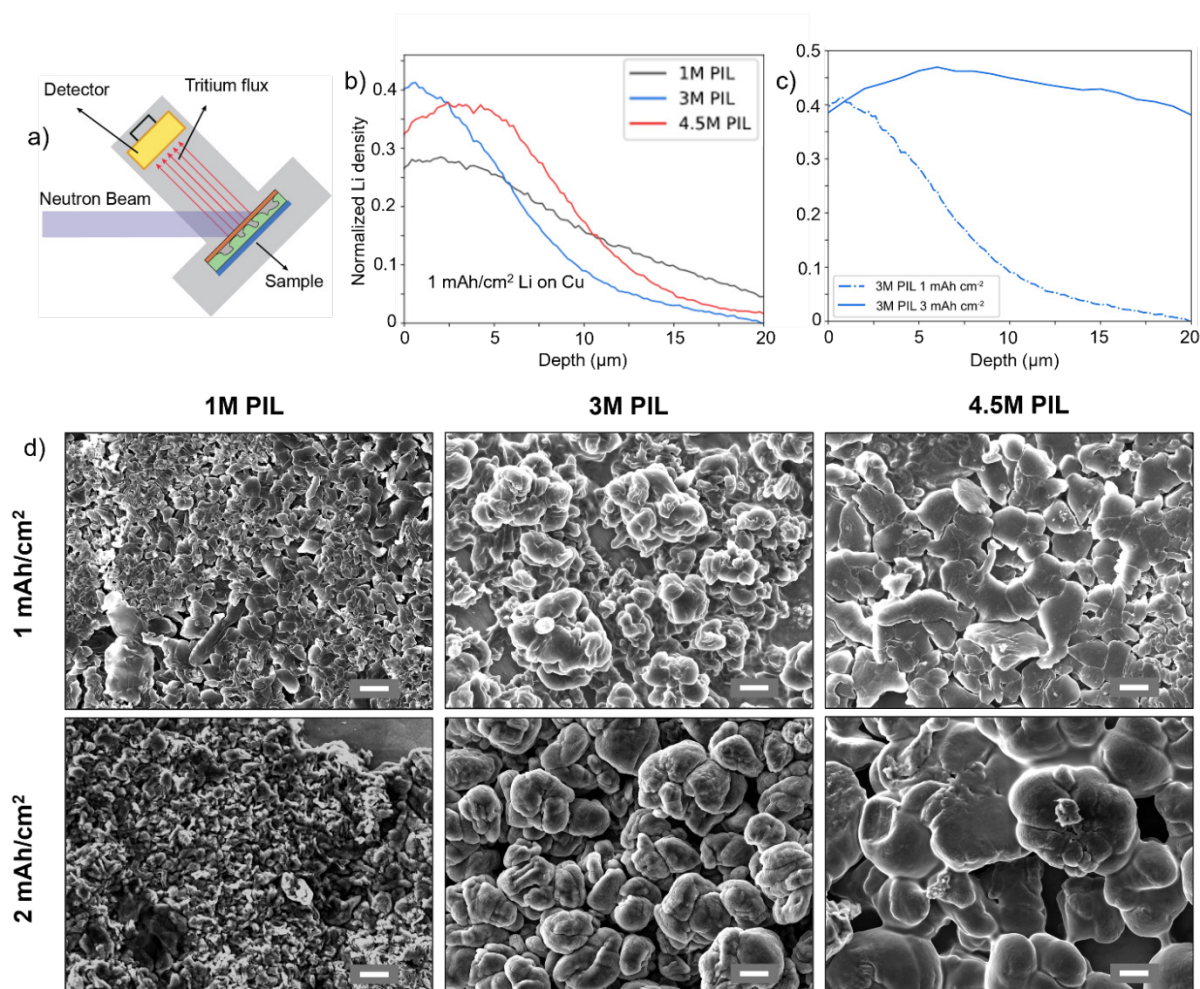


**Figure 5:** Ex-situ characterization of electrodeposited Li from Li/PIL/Cu cells a) b) ex-situ Neutron Depth Profiling derived normalized Li density of electrodeposited Li on Cu from Li/Cu cells with 1 mAh/cm<sup>2</sup> deposited Li c) Comparison of normalized Li densities for 3M PIL with 1 mAh/cm<sup>2</sup> and 3 mAh/cm<sup>2</sup> deposited Li d) Morphology of Li plated on Cu at 1 mAh/cm<sup>2</sup> (top) and 2 mAh/cm<sup>2</sup> (bottom) with a current density of 0.1 mA/cm<sup>2</sup> for 1M, 3M and 4.5 M PILs. The scale bar indicates 10 μm.

#### 4.5 Lithium interface evolution with extended cycling

Having understood the differences in Li morphology and SEI composition with LiFSI salt concentration at low currents (0.1 mA/cm<sup>2</sup>) typically used in formation cycling protocols, we now look at their evolution with extended cycling at higher currents (0.2 mA/cm<sup>2</sup> and higher). While the initial SEI and Li morphology play a major role in dictating further Li plating/stripping, they can undergo changes with cycling for longer and/or at higher currents, this is also observed for the PIL EDLi samples. Particularly for the 3M and 4.5M samples, where the initial differences between the SEI and Li morphology are lesser compared to those between the 1M and 3M samples, it is of interest to carefully monitor these changes.

As observed with operando NMR at 0.2 mA/cm<sup>2</sup> (Figure 6) following the initial cycles at 0.1 mA/cm<sup>2</sup> (Figure 4), clear differences emerge in terms of plating morphologies, leading to

#### 4. Understanding the effect of salt concentration on the Li metal interface in gel polymer electrolytes

different coulombic efficiencies for the 1M and 3M PILs. In the 1M PIL, the coulombic efficiency drops and the overpotential increases significantly (**Figure 6a**). In terms of electrodeposition, Li plating is observed to occur over a wide chemical shift range, characteristic of mossy/high surface area Lithium deposition with randomly oriented deposits with respect to the magnetic field. The 3M PIL, on the other hand, maintains a consistent and narrow plating/stripping chemical shift, still centered around 260 ppm, with better coulombic efficiencies (**Figure 6b**). A consistent and narrow Li plating/stripping chemical shift with high coulombic efficiencies is also observed in the case of the 4.5M PIL, These changes in coulombic efficiencies observed at a higher current also agree well with the values obtained in coin cells under the same conditions (**Figure S8**), implying that the morphological changes observed with operando NMR are fairly representative of the changes occurring under more standard cell architectures.

It is to be noted, however, that in a Li-Cu configuration, stripping of Li from the EDLi side coincides with the plating of Li on bulk Li foil. Furthermore, the Li metal is subject to skin depth effects (about  $6.7 \mu\text{m}$  for a magnetic field of  $11.7 \text{ T}$ )<sup>37</sup> and as observed with SEM, the grain size of Li can exceed this value at 3M and 4.5M salt concentrations. This makes the quantification of dead Li on the Cu side in absolute terms, particularly in terms of volume, difficult. Nevertheless, NMR is sensitive to changes in the surface area of Li, and therefore, the intensities of the non-bulk Li peak at the end of each half-cycle at  $0.2 \text{ mA/cm}^2$  are normalized to the non-bulk Li intensity at the end of low current ( $0.1 \text{ mA/cm}^2$ ) cycling in order to compare the relative increase in non-bulk Li concentration with cycling for the three samples (**Figure 6d**). Here, the 1M sample shows the highest increase in the amount of non-bulk Li after 4 cycles, and 3M the lowest, with the 4.5M sample showing a slightly higher non-bulk Li increase in comparison. This trend agrees well with that of the CEs for the three salt concentrations, suggesting that these differences in CEs could be linked to differences in the amount of dead Li generation.

4. Understanding the effect of salt concentration on the Li metal interface in gel polymer electrolytes

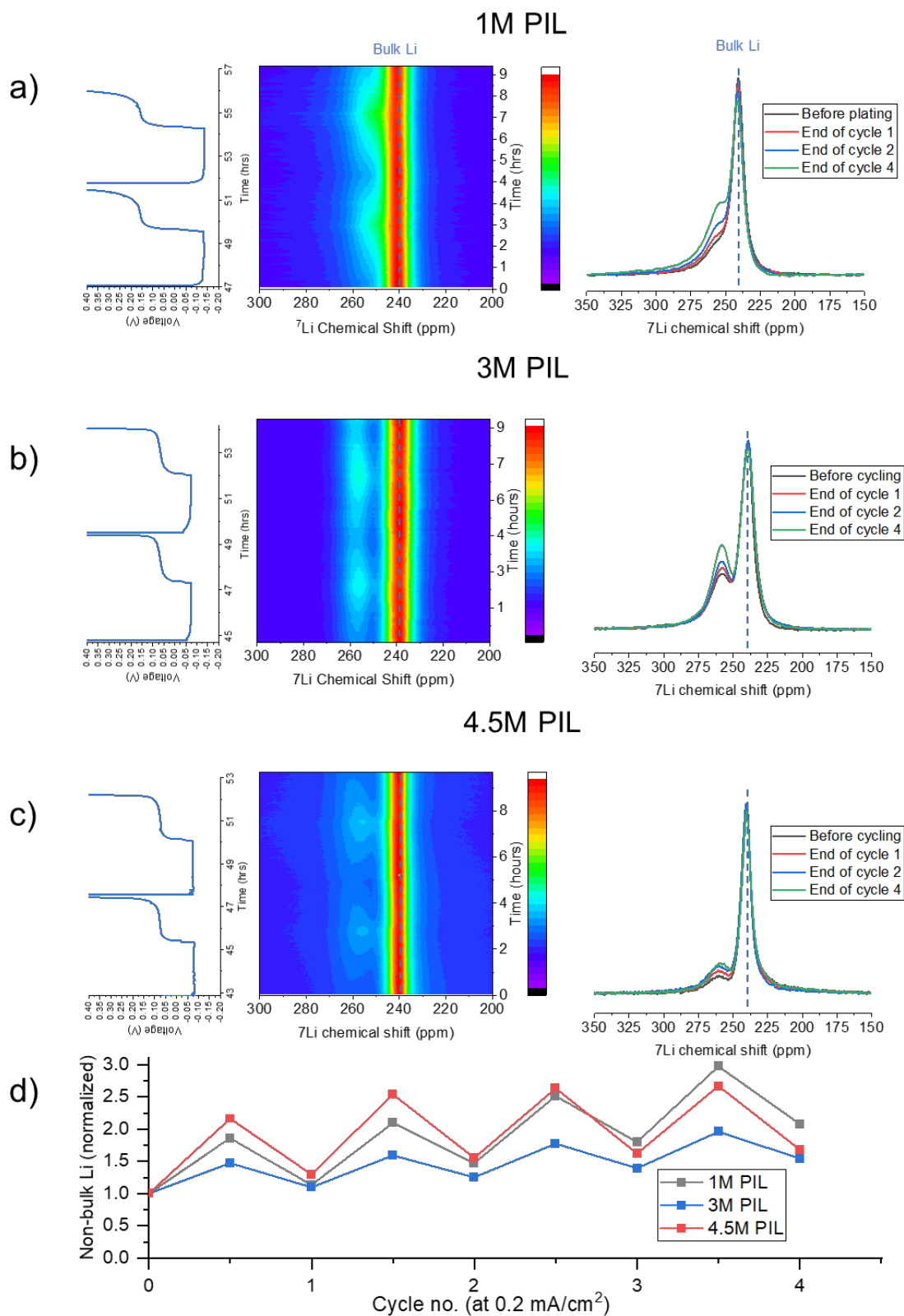


**Figure 6: Operando  ${}^7\text{Li}$  NMR of Li/PIL/Cu cells at 0.2 mA/cm<sup>2</sup>: Voltage traces  $t$ (left), 2D contour plot of Li metal intensities (middle), and Li metal spectra at different cycling stages (right) for a) 1M PIL at 0.2 mA/cm<sup>2</sup> b) 3M PIL at 0.2 mA/cm<sup>2</sup>**

#### 4. Understanding the effect of salt concentration on the Li metal interface in gel polymer electrolytes

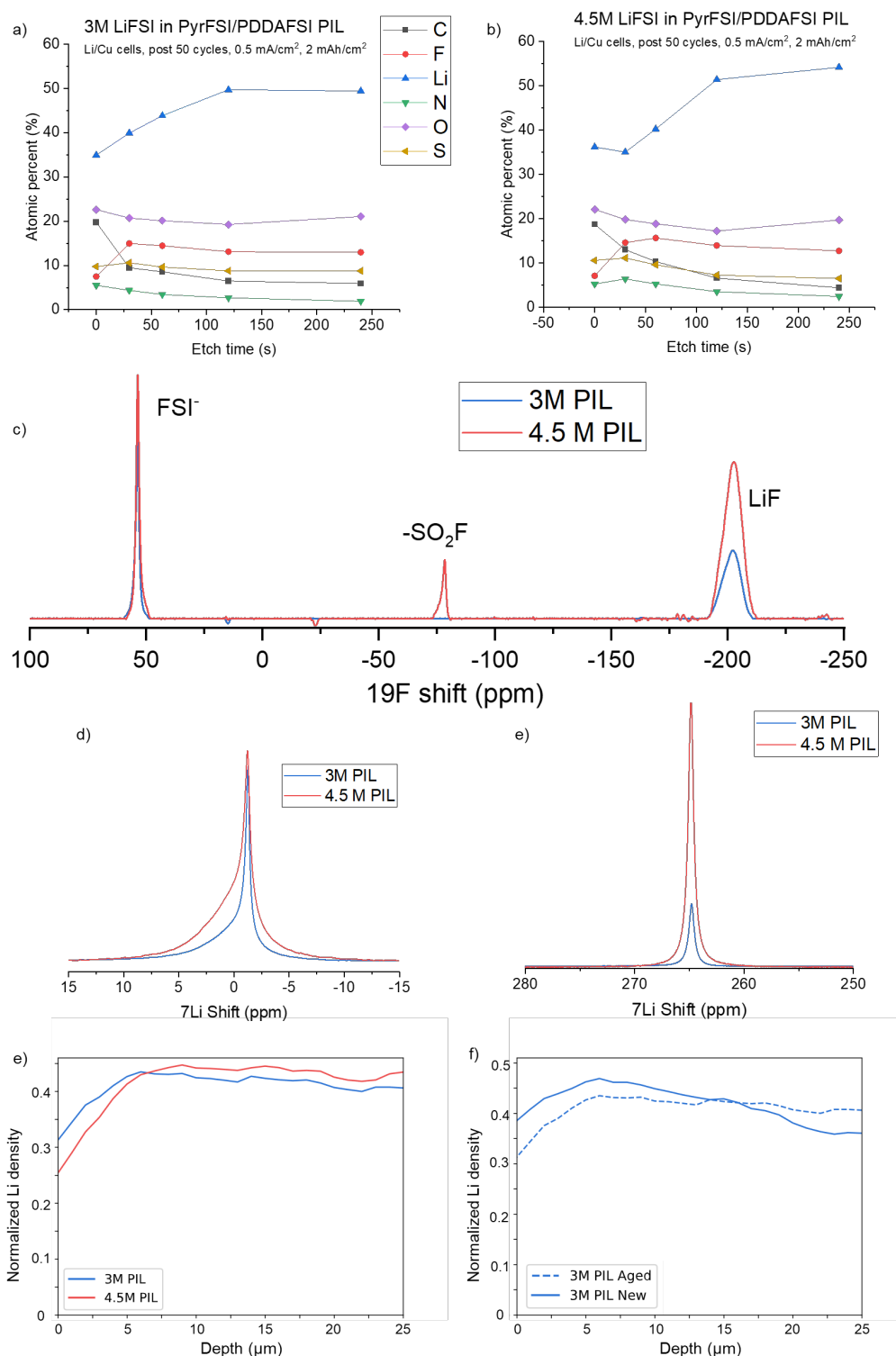


**Figure 7: SEI composition at the Li/PIL interface after 50 cycles at 0.5 mA/cm<sup>2</sup> - 40°C:** a) XPS survey atomic percentage (with depth profiling) for 3M PIL/Li interface, b) XPS survey atomic percentage (with depth profiling) for 4.5M PIL/Li interface. c) <sup>19</sup>F NMR of the Li/PIL interface d) <sup>7</sup>Li NMR (diamagnetic part) of the Li/PIL interface e) <sup>7</sup>Li NMR (Li metal region) of the Li/PIL interface f) Neutron Depth Profiling derived Li density of post-cycling EDLi on Cu from Li/Cu cells for 3M and 4.5 M PILs g) Li density comparison of post-formation and post-50 cycles EDLi on Cu from Li/Cu cells for 3M PIL

#### 4. Understanding the effect of salt concentration on the Li metal interface in gel polymer electrolytes

For 3M and 4.5M samples, solid-state NMR and XPS were also carried out after the most aggressive cycling condition used in this study, i.e. 50 cycles at 0.5 mA/cm<sup>2</sup> and 40°C, to study the changes to the SEI composition with cycling. The XPS survey spectra now show a very similar composition as a function of depth (**Fig 7 a,b**), suggesting that the SEI atomic percentages do not change by much between these two concentrations. However, for the NMR spectra, when a LiFSI normalization approach is used (as with the post-formation cycle spectra in Figure 3), it is observed that the 4.5M sample now has a higher LiF content, both in absolute terms and relative to the mobile FSI<sup>-</sup> peak when compared to the 3M sample (**Figure S7a**). In the case of the 3M PIL, the peak at ~-78 ppm corresponding to -SO<sub>2</sub>F is no longer observed, in line with previous research that suggests that this might be an intermediate product<sup>30</sup>. For the 4.5M PIL, however, this environment is still observed. A higher amount of Li-containing SEI relative to the salt peak is also observed in the case of <sup>7</sup>Li NMR of the 4.5M sample (**Figure S6b**), indicating a higher amount of SEI present. Further, a relatively higher amount of metallic Li is observed for the 4.5M sample (**Figure S7b**). Given the NMR sample preparation procedure for post-50 cycle samples (See **Supplementary Note 2**), this metallic Li almost entirely corresponds to dead Li, thereby indicating a substantial increase in the amount of dead Li generation for the 4.5 M PIL at this condition, explaining the higher SEI generation and the lower CE. Furthermore, a comparison of normalized Li densities for post-cycling EDLi on Cu obtained from NDP (**Figure 7f**) shows a sharper drop of Li intensity close to the Cu current collector for the 4.5 M PIL, further supporting the higher dead Li argument. The 3M sample, on the other hand, maintains nearly the same Li density distribution post-cycling (**Figure 7g**).

While Li deposition at high salt concentrations in liquid electrolytes also results in larger grains with reduced current collector area coverage<sup>15</sup>, the facile wetting of surfaces by the liquid electrolytes offsets any potential performance drawbacks. In polymer and gel polymer systems, however, this could be a potential performance bottleneck, resulting in contact loss during stripping and/or Li protrusion into the separator, particularly if the polymer possesses poor mechanical strength. The increase of salt concentration to 4.5M is expected to lower the mechanical strength of the polymer, and despite its infiltration into Celgard, the relative softness of the PIL at the surface could accelerate these degradation modes. Indeed, the SEM images of EDLi for the 4.5M PIL after the formation cycle with incomplete washing (**Figure S9**) show the PIL surface layer deposited on both the Li deposits and the Cu current collector. This chemomechanical instability is typically further aggravated at higher temperatures and currents, resulting in continuous loss of Li to SEI and dead Li.

## 4.6 Conclusion

Increasing the salt concentration to obtain an inorganic-rich SEI and achieve stable Li metal plating/stripping has been a strategy that has worked well for liquid electrolytes. With polymer electrolytes, and with gel polymer electrolytes in particular, such as the PDDAFSI-based ternary PILs investigated here, the long-term cycling stability and CE seem to have a nontrivial relationship with the salt concentration.

#### 4. Understanding the effect of salt concentration on the Li metal interface in gel polymer electrolytes

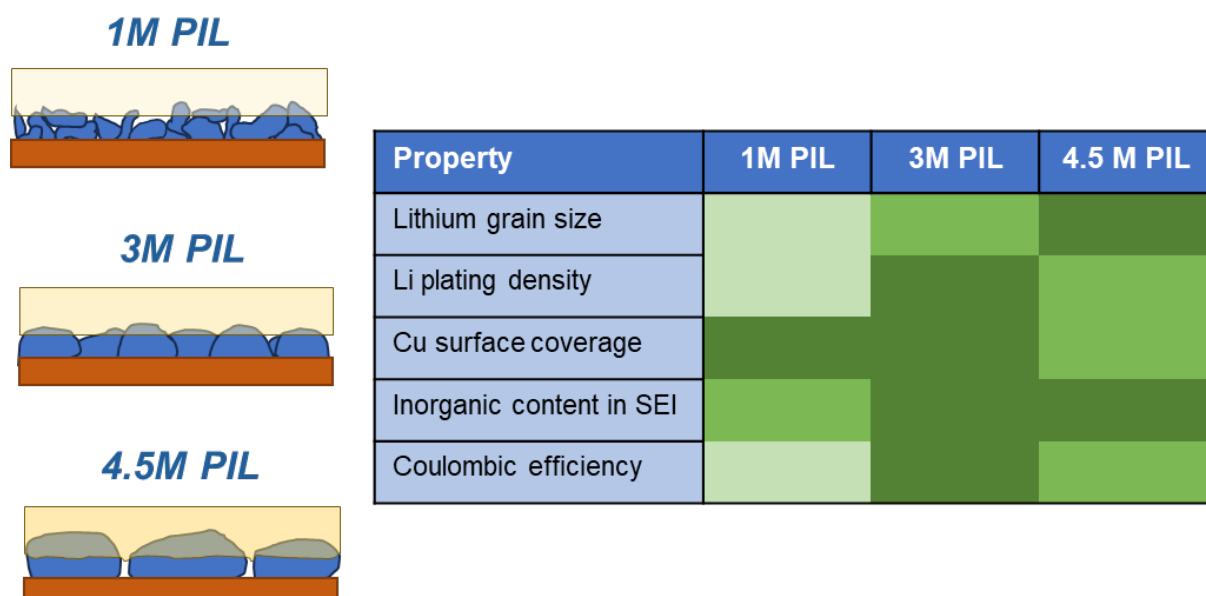


**Figure 8:** Schematic diagram showing the evolution of Li morphology as a function of PIL salt concentration. A comparison of various Li interface properties is provided on the right. Lighter shade of green implies less favorable and a darker shade of green implies more favorable.

4

Increasing the LiFSI salt concentration in Pyr13FSI/PDDAFSI ternary PILs from 1M to 3M results in beneficial changes to both the SEI composition and Li microstructure, in addition to improved  $\text{Li}^+$  transference number. The operando NMR shows a lower coulombic efficiency for initial cycles owing to increased SEI formation, which, as shown by XPS and ssNMR, is inorganic rich, and shows lower  $R_{\text{SEI}}$  from the EIS measurements. With plating/stripping at higher currents, 3M PIL outperforms the 1M PIL and maintains a Li metal morphology with a narrow chemical shift range. The Li deposits obtained for 3M PIL are revealed to be denser through ex-situ NDP, and the SEM images show a larger grain size for the 3M deposits with good area coverage, as opposed to low-density, nodule-like deposits for the 1M PIL, likely influenced by the higher organic content in the SEI and lower  $\text{Li}^+$  transference.

On further increasing the concentration to 4.5M, the elemental composition of the SEI stays nearly the same. However, a higher  $R_{\text{SEI}}$  is observed post-formation, and operando NMR shows a further increase in the extent of SEI formation in the initial cycles. The generated Li microstructure, while having a larger grain size, shows lower nucleation sites and a higher extent of voids, resulting in a lower surface coverage. This, coupled with the reduced mechanical strength of the PIL surface layer with the increase in salt concentration causes the accelerated chemomechanical degradation of the Li/PIL interface, resulting in higher dead Li generation and SEI formation as suggested by ssNMR, resulting in lower coulombic efficiencies than for the 3M.

#### 4. Understanding the effect of salt concentration on the Li metal interface in gel polymer electrolytes

The results highlight the importance of optimizing salt concentration in gel polymer electrolytes by paying attention to not only the conductivity/Li<sup>+</sup> transference balance, but more importantly to the SEI composition, and the Li morphology/area coverage which would influence the interface kinetics and long-term chemomechanical stability of the Li/PIL interface respectively.

### 4.7 Experimental Procedures

#### 4.7.1 PIL separator synthesis

The PIL-infiltrated Celgard separators were prepared according to the procedure previously reported by Homann et. al.<sup>11</sup>. LiFSI, Pyr13FSI, and PDDAFSI were obtained from Solvionic. A 25  $\mu\text{m}$  thick porous polypropylene separator (Celgard 2500) was punched into a disc with a diameter of 19 mm, dried in vacuum ( $< 10^{-3}$  mbar) for 12 h, and soaked in a solution containing  $x$  M LiFSI ( $x = 1, 3, 4.5$ ) in PYR13FSI (60 wt.%) and PDDAFSI (40 wt.%) in acetonitrile (1:1wt. ratio) for 1 h, dried for 12 hours in an Ar filled Glovebox on a polytetrafluoroethylene (PTFE) dish, after which the drying was carried out under vacuum ( $< 10^{-3}$  mbar) at RT for 72 hours to obtain the dried separators.

#### 4.7.2 Cell assembly and electrochemical characterization

The Li|Cu coin cells (CR2032) were assembled using Li discs (250  $\mu\text{m}$ ) of 15.4 mm diameter, PIL infiltrated Celgard separator of 19 mm diameter and a Cu foil (9  $\mu\text{m}$  thick) of 12.7 mm diameter in an Ar filled glovebox. The galvanostatic cycling was carried out either at 20 °C or 40 °C in climate chambers connected to a Maccor 4300 cycler. Electrochemical impedance spectroscopy measurements were performed at different target temperatures on an Autolab (Metrohm Inc.) potentiostat between frequencies of 500 kHz and 0.1 Hz. Lithium-ion transference numbers were determined in Li/Li symmetric cells using the Bruce-Vincent method, subjecting the cells to a polarization of 10 mV and measuring the current response for 12 h<sup>38</sup>.

#### 4.7.3 SEI Characterization

To obtain solid electrolyte interphase samples for MAS solid-state NMR measurements, Li|Cu coin cells containing the Celgard separator with the 1M/3M/4.5M LiFSI PIL electrolyte subjected to the initial conditioning cycle (4 mAh/cm<sup>2</sup> of plating at 0.1 mA/cm<sup>2</sup>, stripping at 0.1 mA/cm<sup>2</sup> to 1.5 V and then 3 mAh/cm<sup>2</sup> Li reservoir plating at 0.2 mA/cm<sup>2</sup>), and subsequently the Cu foils containing the Li deposits were extracted from these cells. The deposited Li layer plus its solid electrolyte interphase was then scraped off from the Cu foils (unwashed) and was packed into 3.2 mm airtight ZrO<sub>2</sub> rotors with KBr as the inert filler.

All solid-state NMR measurements were carried out on a Bruker Ascend 500 MHz (11.7 T) spectrometer equipped with a Neo console. <sup>7</sup>Li, <sup>19</sup>F, and <sup>1</sup>H MAS NMR measurements were carried out on a 3.2 mm triple resonance probe at spinning speeds of 18 kHz using direct excitation pulses. For <sup>7</sup>Li measurements, a pulse length of 5  $\mu\text{s}$  (45 W) was used with a recycle

#### 4. Understanding the effect of salt concentration on the Li metal interface in gel polymer electrolytes

delay of 30 s. All measurements were referenced to a LiCl solution at 0 ppm.  $^{19}\text{F}$  measurements were carried out with a pulse length of 3.25  $\mu\text{s}$  (107.75 W) and recycle delay of 10 s. The processing and analysis of the resulting spectra was performed using the Mestrenova 14 software.

XPS measurements with depth profiling were also carried out on Li deposited on Cu, collected from Li|Cu cells as described above. Before XPS measurements, the foils were washed with propylene carbonate (Sigma Aldrich, 99.5%), dimethyl carbonate (Sigma Aldrich, 99%) to remove polymer and LiFSI salt deposits, and dried in a glovebox antechamber overnight at room temperature. Instead of scraping off the Li, the washed Cu foils were directly used for the analysis. The samples were transferred to the XPS chamber using a vacuum transfer holder.

The XPS measurements were performed on a Thermo Scientific K-Alpha Spectrometer with an Al K-alpha monochromator. The spot diameter was set to 400  $\mu\text{m}$ . Survey spectra were recorded with a pass energy of 200 eV and step size of 0.5 eV, while high-resolution spectra were recorded with a pass energy of 50 eV and step size of 0.1 eV. The binding energies were referenced to adventitious carbon at 284.8 eV. For the depth profiling measurements, argon ion sputtering was performed (1 keV ion energy, 1.5  $\mu\text{A}$  and 1x1  $\text{mm}^2$  raster size). All the spectra were processed and analyzed using the CasaXPS software using a U2 Tougaard background to account for inelastically scattered photoelectrons.

#### 4.7.4 Operando NMR

The operando Li/Cu half-cells were assembled using Li foil (250  $\mu\text{m}$ ) of 0.4x1 cm, PIL infiltrated Celgard separator of 0.6x1.2 cm and a Cu foil (9  $\mu\text{m}$ ) of 0.5 x 1 cm. A plastic capsule cell made out of polyether ether ketone (PEEK) with Cu wire connections to the external circuit was used for the cell assembly. More details regarding the cell setup and assembly can be found in the work of Pecher et. al.<sup>39</sup> The operando NMR experiments were performed at room temperature ( $\sim 20$  °C) on a Bruker Avance 500 MHz spectrometer using a solenoidal silver-coated Cu coil, which was synchronized with the external galvanostatic cycler (Maccor). The spectra were recorded using an in situ NMR probe with automatic tuning and matching control (ATMC) (NMR Service) that enables automatic recalibration of the NMR RF circuit during the measurement.

A 2D array of Single pulse experiments was used to collect the operando NMR spectra, with each transient having a recycle delay of 1s and 256 scans. The shift of  $^7\text{Li}$  was internally referenced to LiFSI salt peak at  $-2$  ppm. Further processing of the spectra was performed using Mestrenova 14.

#### 4.7.5 Li density and morphology characterization

Neutron depth profiling is used to monitor the lithium plating density in situ. Lithium plating density was monitored by subjecting the battery to a neutron beam, measuring the  $^6\text{Li}+^1_0\text{n}\rightarrow^3_1\text{H}+^4_2\text{He}$  reaction product residual energies coming from the battery, specifically

#### 4. Understanding the effect of salt concentration on the Li metal interface in gel polymer electrolytes

the  $^3\text{H}$ . The charged particle residual energy is obtained after the particles travelled from the position where lithium fissions in the battery cell to the PIPS detector (Mirion). The tritium particles lose energy as they travel through matter. The rate of tritium energy loss, called the stopping power is different for various materials and can be accurately calculated.<sup>40</sup> The trajectory of tritium passing from the point of fission through possibly: PIL, deposited lithium, 10  $\mu\text{m}$  copper sheet, and helium gas to the detector thus yields only a limited set of possible trajectories with a set of possible detected energies. During analysis, lower detector energies are cut off as they may also originate from electrical noise, gamma rays or beta particles. For this study, the tritium particles' energy and counts are collected during intervals of 1 minute. The energy loss in the trajectory from the pouch to the detector is minimized by flushing helium gas in an in-house made pouch holder with PIPS detector mount. The fission rate of lithium (and thus the formation rate of tritium particles) from the neutron beam flux is normalized using a secondary detector monitoring the fission rate from irradiating a pure Lithium source with the same neutron beam simultaneously. The conversion from channel to energy and the conversion from counts to Li concentration is done employing a standard Si sample containing a known quantity of  $^5\text{B}$ .

Scanning electron microscopy (SEM) pictures were taken using a JEOL JSM-IT700HR FE-SEM setup in scattering electron imaging (acceleration voltage: 10 -15 kV) mode. The Cu foils with plated Li were first washed using the same procedure as that for the XPS sample preparation to remove the salt/polymer traces.

## References

- (1) Zhou, D.; Shanmukaraj, D.; Tkacheva, A.; Armand, M.; Wang, G. Polymer Electrolytes for Lithium-Based Batteries: Advances and Prospects. *Chem* **2019**, *5* (9), 2326–2352. <https://doi.org/10.1016/j.chempr.2019.05.009>.
- (2) Song, Z.; Chen, F.; Martinez-Ibañez, M.; Feng, W.; Forsyth, M.; Zhou, Z.; Armand, M.; Zhang, H. A Reflection on Polymer Electrolytes for Solid-State Lithium Metal Batteries. *Nat. Commun.* **2023**, *14* (1), 4884. <https://doi.org/10.1038/s41467-023-40609-y>.
- (3) Song, J. Y.; Wang, Y. Y.; Wan, C. C. Review of Gel-Type Polymer Electrolytes for Lithium-Ion Batteries. *J. Power Sources* **1999**, *77* (2), 183–197. [https://doi.org/10.1016/S0378-7753\(98\)00193-1](https://doi.org/10.1016/S0378-7753(98)00193-1).
- (4) Fenton, D. E.; Parker, J. M.; Wright, P. V. Complexes of Alkali Metal Ions with Poly(Ethylene Oxide). *Polymer* **1973**, *14* (11), 589. [https://doi.org/10.1016/0032-3861\(73\)90146-8](https://doi.org/10.1016/0032-3861(73)90146-8).
- (5) Xue, Z.; He, D.; Xie, X. Poly(Ethylene Oxide)-Based Electrolytes for Lithium-Ion Batteries. *J. Mater. Chem. A* **2015**, *3* (38), 19218–19253. <https://doi.org/10.1039/C5TA03471J>.
- (6) Cabañero Martínez, M. A.; Boaretto, N.; Naylor, A. J.; Alcaide, F.; Salian, G. D.; Palombarini, F.; Ayerbe, E.; Borrás, M.; Casas-Cabanas, M. Are Polymer-Based Electrolytes Ready for High-Voltage Lithium Battery Applications? An Overview of Degradation Mechanisms and Battery Performance. *Adv. Energy Mater.* **2022**, *12* (32), 2201264. <https://doi.org/10.1002/aenm.202201264>.
- (7) Pont, A.-L.; Marcilla, R.; De Meatza, I.; Grande, H.; Mecerreyes, D. Pyrrolidinium-Based Polymeric Ionic Liquids as Mechanically and Electrochemically Stable Polymer Electrolytes. *J. Power Sources* **2009**, *188* (2), 558–563. <https://doi.org/10.1016/j.jpowsour.2008.11.115>.
- (8) Appetecchi, G. B.; Kim, G.-T.; Montanino, M.; Carewska, M.; Marcilla, R.; Mecerreyes, D.; De Meatza, I. Ternary Polymer Electrolytes Containing Pyrrolidinium-Based Polymeric Ionic Liquids for Lithium Batteries. *J. Power Sources* **2010**, *195* (11), 3668–3675. <https://doi.org/10.1016/j.jpowsour.2009.11.146>.
- (9) Eshetu, G. G.; Mecerreyes, D.; Forsyth, M.; Zhang, H.; Armand, M. Polymeric Ionic Liquids for Lithium-Based Rechargeable Batteries. *Mol. Syst. Des. Eng.* **2019**, *4* (2), 294–309. <https://doi.org/10.1039/C8ME00103K>.
- (10) Fu, C.; Homann, G.; Grissa, R.; Rentsch, D.; Zhao, W.; Gouveia, T.; Falgayrat, A.; Lin, R.; Fantini, S.; Battaglia, C. A Polymerized-Ionic-Liquid-Based Polymer Electrolyte with High Oxidative Stability for 4 and 5 V Class Solid-State Lithium Metal Batteries. *Adv. Energy Mater.* **2022**, *12* (27), 2200412. <https://doi.org/10.1002/aenm.202200412>.

#### 4. Understanding the effect of salt concentration on the Li metal interface in gel polymer electrolytes

(11) Homann, G.; Wang, Q.; Liu, S.; Devinenti, A.; Karanth, P.; Weijers, M.; Mulder, F. M.; Piesins, M.; Gouveia, T.; Ladam, A.; Fantini, S.; Battaglia, C. A Quasi-Solid-State Polymer Lithium–Metal Battery with Minimal Excess Lithium, Ultrathin Separator, and High-Mass Loading NMC811 Cathode. *ACS Appl. Energy Mater.* **2024**.

<https://doi.org/10.1021/acsaem.4c02099>.

(12) Yamada, Y.; Yamada, A. Review—Superconcentrated Electrolytes for Lithium Batteries. *J. Electrochem. Soc.* **2015**, *162* (14), A2406. <https://doi.org/10.1149/2.0041514jes>.

(13) Camacho-Forero, L. E.; Smith, T. W.; Balbuena, P. B. Effects of High and Low Salt Concentration in Electrolytes at Lithium–Metal Anode Surfaces. *J. Phys. Chem. C* **2017**, *121* (1), 182–194. <https://doi.org/10.1021/acs.jpcc.6b10774>.

(14) Qian, J.; Henderson, W. A.; Xu, W.; Bhattacharya, P.; Engelhard, M.; Borodin, O.; Zhang, J.-G. High Rate and Stable Cycling of Lithium Metal Anode. *Nat. Commun.* **2015**, *6* (1), 6362. <https://doi.org/10.1038/ncomms7362>.

(15) Wang, Q.; Zhao, C.; Wang, S.; Wang, J.; Liu, M.; Ganapathy, S.; Bai, X.; Li, B.; Wagemaker, M. Clarifying the Relationship between the Lithium Deposition Coverage and Microstructure in Lithium Metal Batteries. *J. Am. Chem. Soc.* **2022**, *144* (48), 21961–21971. <https://doi.org/10.1021/jacs.2c08849>.

(16) Cao, X.; Jia, H.; Xu, W.; Zhang, J.-G. Review—Localized High-Concentration Electrolytes for Lithium Batteries. *J. Electrochem. Soc.* **2021**, *168* (1), 010522. <https://doi.org/10.1149/1945-7111/abd60e>.

(17) Molinari, N.; Mailoa, J. P.; Kozinsky, B. Effect of Salt Concentration on Ion Clustering and Transport in Polymer Solid Electrolytes: A Molecular Dynamics Study of PEO–LiTFSI. *Chem. Mater.* **2018**, *30* (18), 6298–6306. <https://doi.org/10.1021/acs.chemmater.8b01955>.

(18) Wang, X.; Chen, F.; Girard, G. M. A.; Zhu, H.; MacFarlane, D. R.; Mecerreyes, D.; Armand, M.; Howlett, P. C.; Forsyth, M. Poly(Ionic Liquid)s-in-Salt Electrolytes with Co-Coordination-Assisted Lithium-Ion Transport for Safe Batteries. *Joule* **2019**, *3* (11), 2687–2702. <https://doi.org/10.1016/j.joule.2019.07.008>.

(19) Frenck, L.; Maslyn, J. A.; Loo, W. S.; Parkinson, D. Y.; Balsara, N. P. Impact of Salt Concentration on Nonuniform Lithium Electrodeposition through Rigid Block Copolymer Electrolytes. *ACS Appl. Mater. Interfaces* **2019**, *11* (51), 47878–47885. <https://doi.org/10.1021/acsaami.9b15606>.

(20) Frenck, L.; Veeraraghavan, V. D.; Maslyn, J. A.; Müller, A.; Ho, A. S.; Loo, W. S.; Minor, A. M.; Balsara, N. P. Effect of Salt Concentration Profiles on Protrusion Growth in Lithium–Polymer–lithium Cells. *Solid State Ion.* **2020**, *358*, 115517. <https://doi.org/10.1016/j.ssi.2020.115517>.

#### 4. Understanding the effect of salt concentration on the Li metal interface in gel polymer electrolytes

(21) López, I.; Morey, J.; Ledeuil, J. B.; Madec, L.; Martinez, H. A Critical Discussion on the Analysis of Buried Interfaces in Li Solid-State Batteries. Ex Situ and in Situ/Operando Studies. *J. Mater. Chem. A* **2021**, *9* (45), 25341–25368. <https://doi.org/10.1039/D1TA04532F>.

(22) Cabañero, M. A.; Orive, J.; Bustinza, A.; Gómez, G.; Celaya, A.; Bonilla, F.; de Meatza, I.; López del Amo, J. M.; Casas-Cabanas, M. Diagnostic Protocols for Evaluating the Degradation Mechanisms in Gel-Polymer Lithium Batteries. *Small n/a* (n/a), 2404063. <https://doi.org/10.1002/sml.202404063>.

(23) Martínez-Ibañez, M.; Boaretto, N.; Santiago, A.; Meabe, L.; Wang, X.; Zugazua, O.; Raposo, I.; Forsyth, M.; Armand, M.; Zhang, H. Highly-Concentrated Bis(Fluorosulfonyl)Imide-Based Ternary Gel Polymer Electrolytes for High-Voltage Lithium Metal Batteries. *J. Power Sources* **2023**, *557*, 232554. <https://doi.org/10.1016/j.jpowsour.2022.232554>.

(24) Adams, B. D.; Zheng, J.; Ren, X.; Xu, W.; Zhang, J.-G. Accurate Determination of Coulombic Efficiency for Lithium Metal Anodes and Lithium Metal Batteries. *Adv. Energy Mater.* **2018**, *8* (7), 1702097. <https://doi.org/10.1002/aenm.201702097>.

(25) Chen, K.-H.; N. Wood, K.; Kazyak, E.; S. LePage, W.; L. Davis, A.; J. Sanchez, A.; P. Dasgupta, N. Dead Lithium: Mass Transport Effects on Voltage, Capacity, and Failure of Lithium Metal Anodes. *J. Mater. Chem. A* **2017**, *5* (23), 11671–11681. <https://doi.org/10.1039/C7TA00371D>.

(26) May, R.; Fritzsche, K. J.; Livitz, D.; Denny, S. R.; Marbella, L. E. Rapid Interfacial Exchange of Li Ions Dictates High Coulombic Efficiency in Li Metal Anodes. *ACS Energy Lett.* **2021**, *6* (4), 1162–1169. <https://doi.org/10.1021/acseenergylett.1c00112>.

(27) Weng, S.; Zhang, X.; Yang, G.; Zhang, S.; Ma, B.; Liu, Q.; Liu, Y.; Peng, C.; Chen, H.; Yu, H.; Fan, X.; Cheng, T.; Chen, L.; Li, Y.; Wang, Z.; Wang, X. Temperature-Dependent Interphase Formation and Li<sup>+</sup> Transport in Lithium Metal Batteries. *Nat. Commun.* **2023**, *14* (1), 4474. <https://doi.org/10.1038/s41467-023-40221-0>.

(28) Yu, W.; Yu, Z.; Cui, Y.; Bao, Z. Degradation and Speciation of Li Salts during XPS Analysis for Battery Research. *ACS Energy Lett.* **2022**, *7* (10), 3270–3275. <https://doi.org/10.1021/acseenergylett.2c01587>.

(29) Jagger, B.; Pasta, M. Solid Electrolyte Interphases in Lithium Metal Batteries. *Joule* **2023**, *7* (10), 2228–2244. <https://doi.org/10.1016/j.joule.2023.08.007>.

(30) Arano, K.; Begic, S.; Chen, F.; Rakov, D.; Mazouzi, D.; Gautier, N.; Kerr, R.; Lestriez, B.; Le Bideau, J.; Howlett, P. C.; Guyomard, D.; Forsyth, M.; Dupre, N. Tuning the Formation and Structure of the Silicon Electrode/Ionic Liquid Electrolyte Interphase in Superconcentrated Ionic Liquids. *ACS Appl. Mater. Interfaces* **2021**, *13* (24), 28281–28294. <https://doi.org/10.1021/acsmi.1c06465>.

#### 4. Understanding the effect of salt concentration on the Li metal interface in gel polymer electrolytes

- (31) Basile, A.; Bhatt, A. I.; O'Mullane, A. P. Stabilizing Lithium Metal Using Ionic Liquids for Long-Lived Batteries. *Nat. Commun.* **2016**, *7* (1), ncomms11794. <https://doi.org/10.1038/ncomms11794>.
- (32) Wood, K. N.; Kazyak, E.; Chadwick, A. F.; Chen, K.-H.; Zhang, J.-G.; Thornton, K.; Dasgupta, N. P. Dendrites and Pits: Untangling the Complex Behavior of Lithium Metal Anodes through Operando Video Microscopy. *ACS Cent. Sci.* **2016**, *2* (11), 790–801. <https://doi.org/10.1021/acscentsci.6b00260>.
- (33) Gunnarsdóttir, A. B.; Amanchukwu, C. V.; Menkin, S.; Grey, C. P. Noninvasive In Situ NMR Study of “Dead Lithium” Formation and Lithium Corrosion in Full-Cell Lithium Metal Batteries. *J. Am. Chem. Soc.* **2020**, *142* (49), 20814–20827. <https://doi.org/10.1021/jacs.0c10258>.
- (34) Xiang, Y.; Tao, M.; Zhong, G.; Liang, Z.; Zheng, G.; Huang, X.; Liu, X.; Jin, Y.; Xu, N.; Armand, M.; Zhang, J.-G.; Xu, K.; Fu, R.; Yang, Y. Quantitatively Analyzing the Failure Processes of Rechargeable Li Metal Batteries. *Sci. Adv.* **2021**, *7* (46), eabj3423. <https://doi.org/10.1126/sciadv.abj3423>.
- (35) Lv, S.; Verhallen, T.; Vasileiadis, A.; Ooms, F.; Xu, Y.; Li, Z.; Li, Z.; Wagemaker, M. Operando Monitoring the Lithium Spatial Distribution of Lithium Metal Anodes. *Nat. Commun.* **2018**, *9* (1), 1–12. <https://doi.org/10.1038/s41467-018-04394-3>.
- (36) Wang, Q.; Yao, Z.; Zhao, C.; Verhallen, T.; Tabor, D. P.; Liu, M.; Ooms, F.; Kang, F.; Aspuru-Guzik, A.; Hu, Y.-S.; Wagemaker, M.; Li, B. Interface Chemistry of an Amide Electrolyte for Highly Reversible Lithium Metal Batteries. *Nat. Commun.* **2020**, *11* (1), 4188. <https://doi.org/10.1038/s41467-020-17976-x>.
- (37) Bhattacharyya, R.; Key, B.; Chen, H.; Best, A. S.; Hollenkamp, A. F.; Grey, C. P. In Situ NMR Observation of the Formation of Metallic Lithium Microstructures in Lithium Batteries. *Nat. Mater.* **2010**, *9* (6), 504–510. <https://doi.org/10.1038/nmat2764>.
- (38) Bruce, P. G.; Evans, J.; Vincent, C. A. Conductivity and Transference Number Measurements on Polymer Electrolytes. *Solid State Ion.* **1988**, *28–30*, 918–922. [https://doi.org/10.1016/0167-2738\(88\)90304-9](https://doi.org/10.1016/0167-2738(88)90304-9).
- (39) Pecher, O.; Carretero-González, J.; Griffith, K. J.; Grey, C. P. Materials' Methods: NMR in Battery Research. *Chem. Mater.* **2017**, *29* (1), 213–242. <https://doi.org/10.1021/acs.chemmater.6b03183>.
- (40) Liu, M.; Cheng, Z.; Qian, K.; Verhallen, T.; Wang, C.; Wagemaker, M. Efficient Li-Metal Plating/Stripping in Carbonate Electrolytes Using a LiNO<sub>3</sub>-Gel Polymer Electrolyte, Monitored by Operando Neutron Depth Profiling. *Chem. Mater.* **2019**, *31* (12), 4564–4574. <https://doi.org/10.1021/acs.chemmater.9b01325>.

#### 4. Understanding the effect of salt concentration on the Li metal interface in gel polymer electrolytes

(41) Verhallen, T. Neutron Depth Profiling: Following the Lithium Distribution in Rechargeable Batteries. Dissertation (TU Delft), 2019.

<https://doi.org/10.4233/uuid:debbe50e-27bb-4e57-805f-db30bb8a61bb>.

(42) Ziegler, J. F.; Ziegler, M. D.; Biersack, J. P. SRIM – The Stopping and Range of Ions in Matter (2010). *Nucl. Instrum. Methods Phys. Res. Sect. B Beam Interact. Mater. At.* **2010**, *268* (11), 1818–1823. <https://doi.org/10.1016/j.nimb.2010.02.091>.

## Supplementary Information

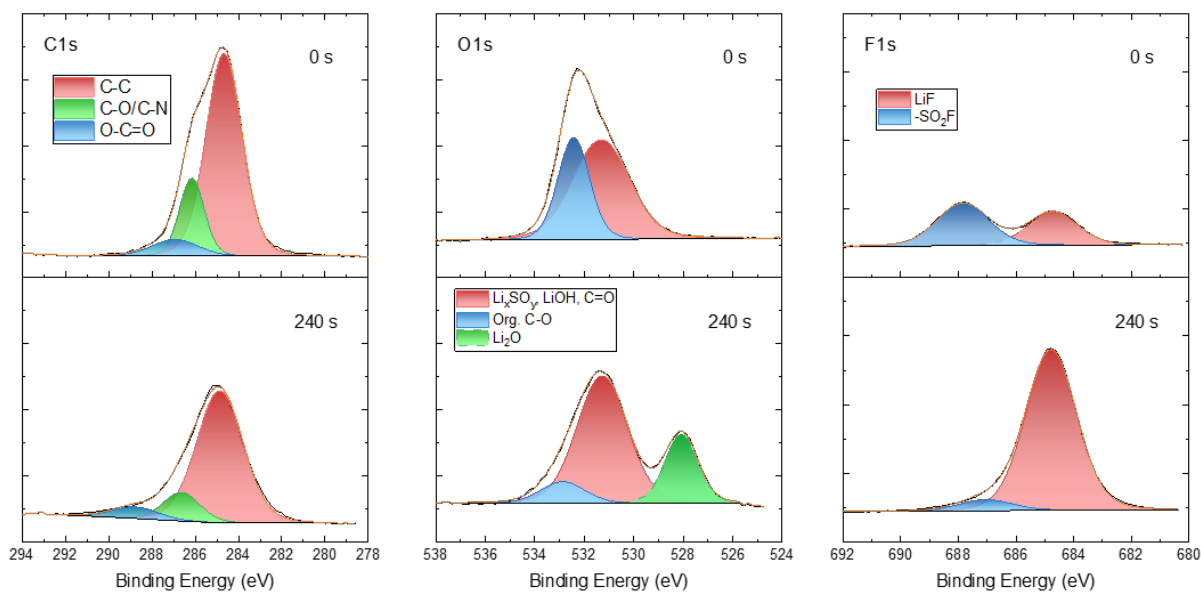


**Figure S1:** C1s, O1s and F1s spectra before (top) and after 240 s of depth profiling (bottom) of the 1M PIL/Li SEI after the initial conditioning cycle

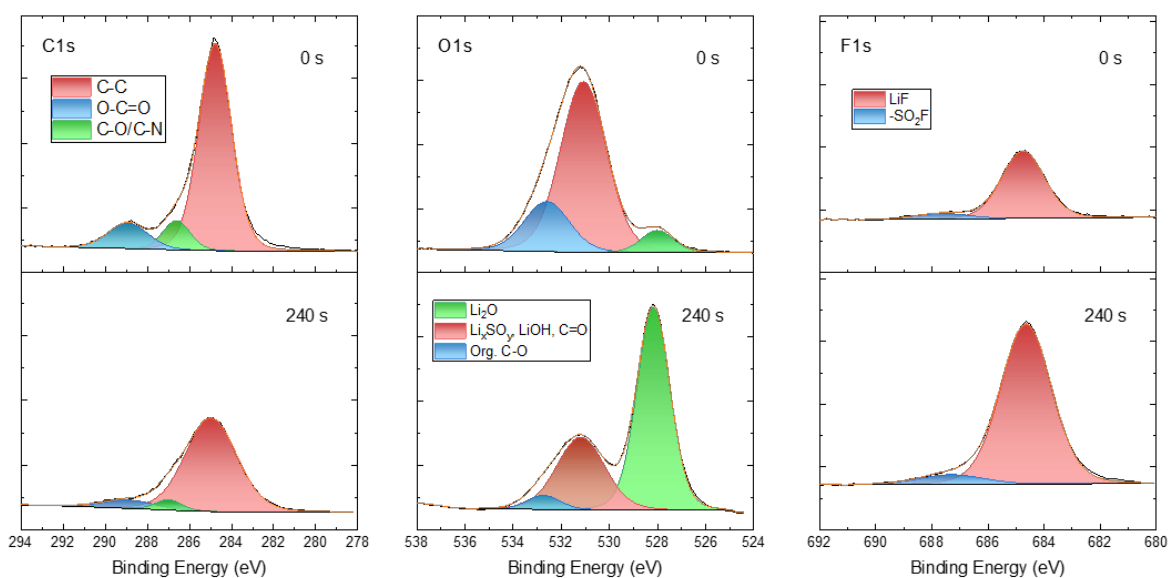


**Figure S2:** C1s, O1s and F1s spectra before (top) and after 240 s of depth profiling (bottom) of the 3M PIL/Li SEI after the initial conditioning cycle

#### 4. Understanding the effect of salt concentration on the Li metal interface in gel polymer electrolytes

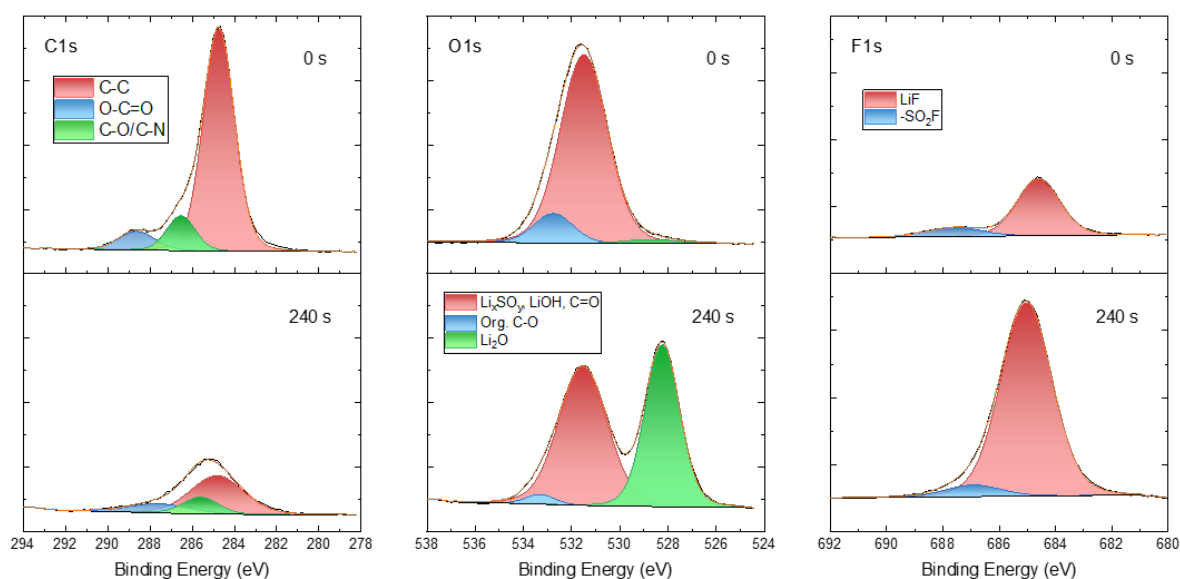


**Figure S3:** C1s, O1s and F1s spectra before (top) and after 240 s of depth profiling (bottom) of the 4.5M PIL/Li SEI after the initial conditioning cycle

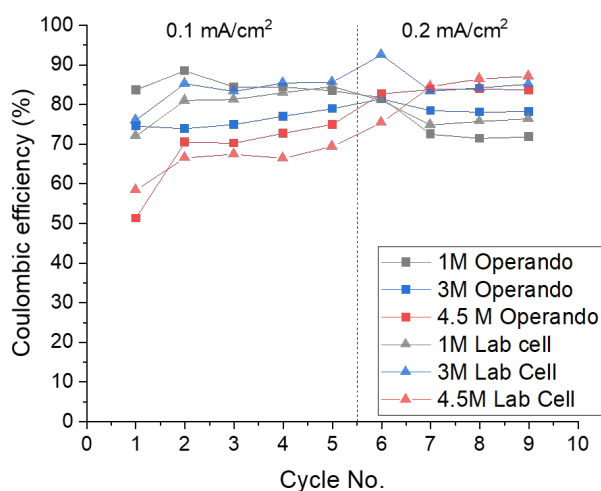


**Figure S4:** a) Relative percentages of Li consumption towards different processes for the 1st Operando NMR cycle for 1M, 3M and 4.5M PILs. b) Comparison of coulombic efficiencies per cycle for 1M, 3M and 4.5 M Operando NMR cells and their coin cell counterparts

#### 4. Understanding the effect of salt concentration on the Li metal interface in gel polymer electrolytes

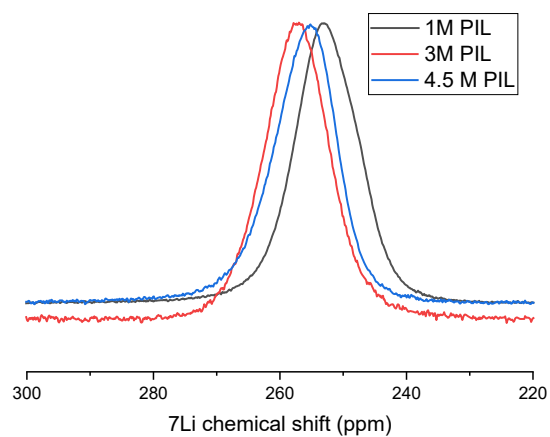


**Figure S5:** Static  ${}^7\text{Li}$  NMR performed on Operando NMR cells containing  $2 \text{ mAh/cm}^2$  (at  $0.1 \text{ mA/cm}^2$ ) of plated Li on Cu

### Supplementary Note 1: Neutron depth profiling methodology

The spectra acquired during the operando Neutron Depth Profiling, consisting of counts vs energy, were converted into a depth-resolved Li concentration by extending the methodology described by Verhallen.<sup>41</sup>

The conversion from channel to energy and the conversion from counts to Li concentration is done employing a standard Si sample containing a known quantity of <sup>5</sup>B. This sample is measured at low pressure (1 mPa), and the energy of the detected product (He at 1472 keV) is assigned to the channel corresponding to the measured peak. The remaining channels are linearly interpolated. Moreover, a Li-containing sample was also measured at low pressure and the energy of resulting peaks (He and tritium) was confirmed to be corresponding to the expected values. The counts under the <sup>5</sup>B peak are integrated to obtain conversion between counts and areal density. Moreover, in every experiment, a spectrum is acquired before the Li plating so that the obtained spectrum can be considered a representative background and subtracted from the subsequently obtained spectra. During the experiments, the sample holder is either used in low pressure (for ex-situ samples) or in 1 atm He (for operando experiments).

The conversion between energy and depth requires considering the charged particle path is composed of two steps, the path within the electrode and the path in the current collector, the conversion algorithm is also composed of two steps. The first converts the energy at the detector to the energy the incoming ion had before passing the current collector; the second exploits the known stopping power to convert the resulting energy spectrum into a depth profile within the electrode.

Given that the energy losses within the current collector (10  $\mu$ m Cu) is highly dependent on the incoming energy, the software TRIM is used to calculate the energy losses in the current collector, creating a function that maps the detected energies to the energies the ions had before crossing the current collector.

#### 4. Understanding the effect of salt concentration on the Li metal interface in gel polymer electrolytes

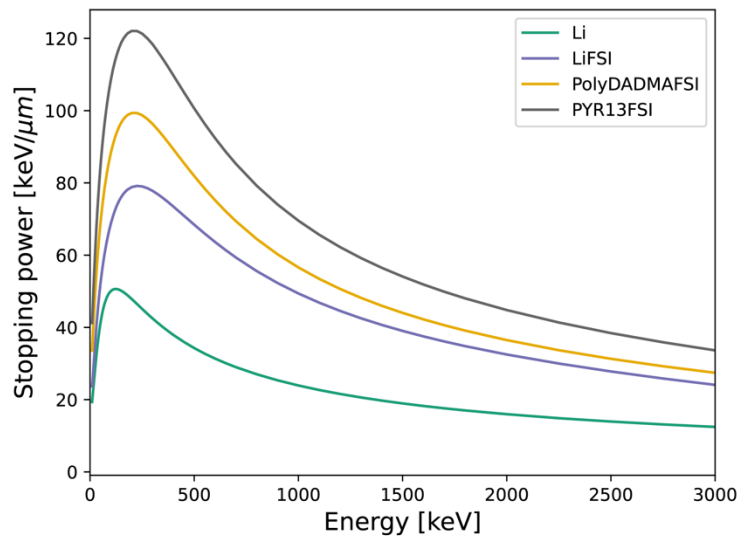


**Figure S6:** Stopping power dependence on energy of the various species present in the study, calculated using SRIM<sup>42</sup>.

4

Subsequently, the notion of stopping power can be used to convert the energy spectrum (counts vs energy) in a depth profile (Li concentration vs depth). In fact, ionized particles traveling in a media are known to lose energy due to the coulomb repulsions with the atoms in the media. These energy losses depend on the density and the chemical species of the media and on the energy of the ionized particle. The quantity of energy the particle loses per unit of space in a specific material is called stopping power  $S(E) = \frac{dE}{dx} |_E$ . In general, the stopping power of a compound can be calculated as the average of the stopping powers of the single species in the compound  $S_i(E)$ , weighted by their volume fraction  $v_i$ :  $S(E) = \sum_{i=1}^n v_i S_i(E)$ . Each stopping power function  $S_i(E)$  can be calculated using SRIM<sup>42</sup> by inserting the list of covalent bonds and the density of the material. The resulting stopping power will be a highly non-linear function of the energy (Figure S9), therefore preventing a direct conversion between energy and depth and instead imposing the use of a specific algorithm.

The algorithm, taking into account the discrete nature of the obtained spectra, consists of the following steps.

The counts at a given discrete position  $x_n$  are calculated starting from obtained counts vs energy spectrum  $C(E)$  and the total stopping power of the compound  $S_{tot}(E)$ , as

$$C(x_n) = \int_{E_n}^{E_{n+1}} C(E) dE .$$

#### 4. Understanding the effect of salt concentration on the Li metal interface in gel polymer electrolytes

Setting the initial depth  $x_0$  to 0 and the corresponding energy  $E_0$  to 2727 keV (the maximum value of the tritium energy),  $E_{n+1}$  is calculated by selecting  $\Delta x$ :

$$E_{n+1} = E_n - S_{tot}(x_n, E_n) \Delta x ,$$

$$x_{n+1} = x_n + \Delta x ,$$

Where

$$S_{tot}(x_n, E_n) = v_{Li}(x_n) S_{Li}(E_n) + (1 - v_{Li}(x_n)) S_{elyte}(E_n)$$

can be computed by knowing the Li metal volume fraction  $v_{Li}$  at a specific position  $x_n$  and the stopping power of the Li metal  $S_{Li}$  and the electrolyte  $S_{elyte}$ . The composition of the SEI is unknown and therefore its stopping power is unknown and therefore cannot be considered in the conversion, the sample is so assumed to be only composed of electrolyte and Li metal.

4

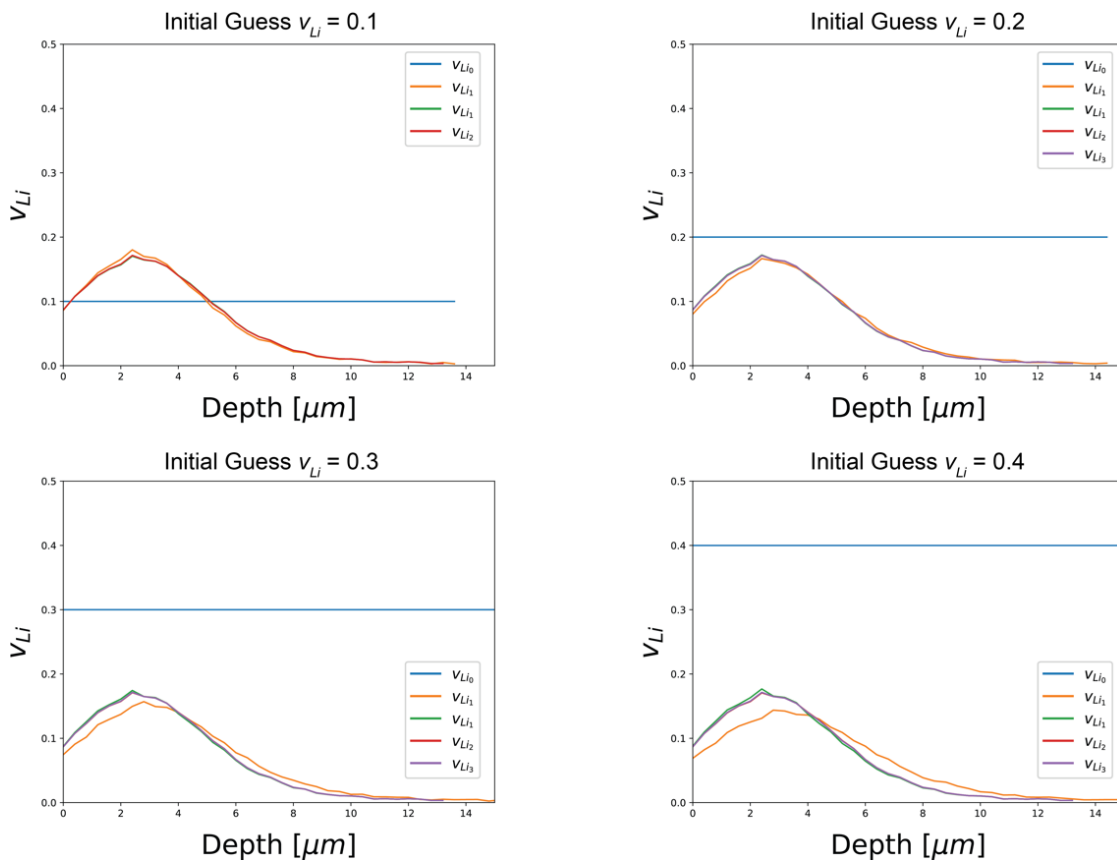


**Figure S7:** Results of the iteration scheme starting from different initial guesses for the lithium volume fraction.

#### 4. Understanding the effect of salt concentration on the Li metal interface in gel polymer electrolytes

The volume fraction of Li metal is also generally not known since it is itself the desired result of the neutron depth profiling. To overcome this, it is necessary to imply an iterative scheme:

- the spectrum  $C(E)$  is converted to an initial guess  $C_0(x)$  by considering an initial constant volume fraction set by the user  $v_{Li_0}(x)$  that allows the computation of  $S_{tot_0}$ .
- the obtained  $C_0(x)$  is then used to calculate  $v_{Li_1}(x)$  and in turn  $S_{tot_1}(x)$ .
- the procedure is repeated until the absolute value of the difference between the integral of two subsequent volume fractions is less than 1%:

$$\Delta v = \frac{1}{tL} \iint |v_{Li_n} - v_{Li_{n-1}}| dx dt < 0.01$$

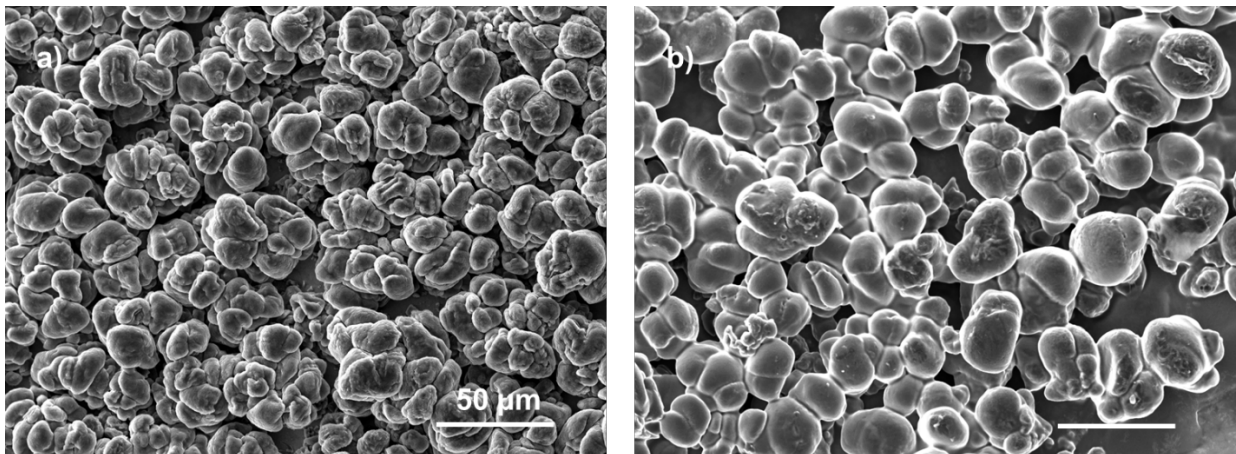


**Figure S8:** Morphology of Li plated on Cu at  $0.1 \text{ mA/cm}^2$ ,  $2 \text{ mAh/cm}^2$  for a) 3M PIL and b) 4.5M PIL. The scale bar is  $50 \mu\text{m}$

4. Understanding the effect of salt concentration on the Li metal interface in gel polymer electrolytes

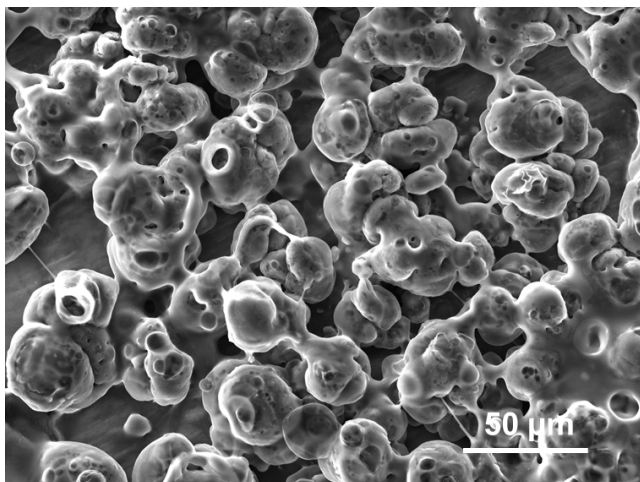


**Figure S9:** Morphology of Li plated on Cu at  $0.1 \text{ mA/cm}^2$ ,  $2 \text{ mAh/cm}^2$  for 4.5M PIL with incomplete washing. The scale bar is  $50 \mu\text{m}$

#### 4. Understanding the effect of salt concentration on the Li metal interface in gel polymer electrolytes

##### **Supplementary Note 2: Preparation of samples for post-mortem ssNMR (after 50 cycles at condition 0.5 mA/cm<sup>2</sup> - 40°C)**

For the 3M and 4.5M samples retrieved from coin cells after 50 cycles at 0.5 mA/cm<sup>2</sup>, 2 mAh/cm<sup>2</sup> at 40 °C, the dead Li was found mostly adhered to the PIL separator rather than the Cu foil as shown in Figure S6. Therefore, the NMR samples were prepared by scraping off the Li deposits from the separator, which also introduces an excess amount of PIL into the sample. This is in contrast to the approach followed for the sNMR after the formation cycle, where Li was scraped off from the Cu foil. Therefore, for the post-mortem comparison of the PIL samples, the spectra were normalized such that the areas of LiFSI peaks in the <sup>7</sup>Li NMR spectra are in the ratio 3:4.5 (Figure S7b).

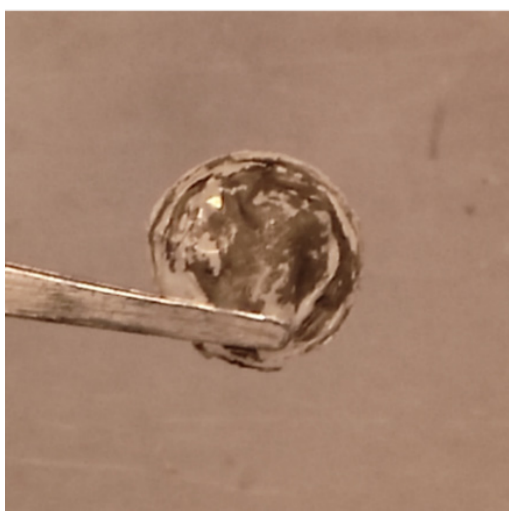


**Figure S10:** Li deposits on the PIL separator after cycling at 0.5 mA/cm<sup>2</sup>, 2 mAh/cm<sup>2</sup> for 50 cycles at 40 °C

#### 4. Understanding the effect of salt concentration on the Li metal interface in gel polymer electrolytes

5. Rational design of safe,  
fluorine-free dual salt  
electrolytes for Lithium  
metal batteries

## Abstract

While fluorination of electrolytes has been a widely used strategy to enable stable cycling in Lithium metal batteries, a move towards perfluoroalkyl substances (PFAS) and fluorine-free electrolytes is desirable given the safety and environmental concerns surrounding fluorinated materials. Lithium Nitrate ( $\text{LiNO}_3$ ) has been previously employed as an electrolyte additive, thanks to its role in generating a highly conductive  $\text{Li}_2\text{O}$ -rich solid electrolyte interface SEI on Lithium. However, its rapid consumption, owing to its (electro)chemical instability of  $\text{LiNO}_3$  with fresh Lithium, has hindered its usage as the main salt without employing fluorinated solvents/additives.

In this work, we develop diglyme based fluorine-free electrolytes with  $\text{LiNO}_3$  and lithium bis(oxalato)borate (LiBOB) as the two constituent salts. We observed that increasing the amount of LiBOB in the electrolyte improved the electrolyte conductivity despite a reduction in bulk properties (viscosity, self-diffusivity). This increase is mainly attributed to the increase in the heterogeneity of Li solvation structures. Further, this also significantly improved Li cycling stability, due to the chemomechanical stabilization of  $\text{LiNO}_3$ -derived inner Solid Electrolyte Interphase (SEI) by LiBOB-derived SEI components. The optimized dual salt F-free electrolyte enables stable Li plating/stripping at  $1 \text{ mA/cm}^2$  ( $1 \text{ mAh/cm}^2$ ) for over 700 hours at  $20 \text{ }^\circ\text{C}$ , and shows good capacity retention (77%) after 100 cycles at 0.5C ( $1 \text{ mA/cm}^2$ ) in Li/LFP cells with Li reservoir of  $100 \text{ }\mu\text{m}$ , and commercial LFP cathode ( $2 \text{ mAh/cm}^2$  active mass loading) at  $25 \text{ }^\circ\text{C}$ . These results present a significant step forward in the design of room-temperature fluorine-free electrolytes, highlighting the importance of tailoring the SEI properties to achieve the desired electrochemical performance.

This chapter has been submitted for publication.

## 5.1 Introduction

Lithium metal batteries (LMBs) have been subject to significant research and commercial interest over the last two decades, owing to the promise of improved cell-level energy densities when employing Lithium metal as the anode<sup>1</sup>. A major challenge in realizing LMBs has been stabilizing lithium plating and stripping, particularly due to the (electro) chemical instability of Li metal in traditional carbonate electrolytes and dendritic metal growth at moderate to high current densities<sup>2,3</sup>. However, a reasonable amount of success has been achieved in this regard by modifying the fluorine content in electrolytes, either by changing the salt (for example to LiFSI)<sup>4</sup>, having fluorinated cosolvents/additives (like FEC)<sup>5,6</sup>, fluorinating traditional solvents<sup>7,8</sup> and having fluorinated diluents<sup>9–12</sup>.

The improved Li metal stability in these reports is often attributed to the LiF-rich SEI<sup>4</sup>, while the use of fluorinated solvents/cosolvents was also shown to additionally improve the electrochemical stability windows (ESW) for electrolytes that would otherwise be unstable at high voltages<sup>7,8</sup>. Further, non-solvating fluorinated compounds possessing a high ESW have been used as diluents to enable localized high-concentration electrolytes (LHCEs) that have demonstrated some of the highest coulombic efficiencies known to date for Li metal plating<sup>13</sup>.

However, fluorination of battery electrolytes gives rise to several environmental and safety hazards. Several fluorinated components in batteries belong to a class of compounds called perfluoroalkyl substances (PFAS), which are compounds with multiple F-atoms attached an alkyl chain. Thanks to the very strong C-F bond, these compounds are extremely durable.<sup>14</sup> However, this property also makes them very difficult to recycle. Exposure to PFAS materials has been linked to a range of health disorders in animals and humans, including cancer,<sup>15,16</sup> and therefore several global organizations, including the European Union, have proposed a ban on the use of PFAS materials<sup>17</sup>. This move would, however, put the decarbonization and energy transition at risk, given the abundance of PFAS materials in batteries, electrolyzers, and other 'clean' technology devices<sup>18</sup>.

Besides PFAS, several other fluorinated materials such as LiPF<sub>6</sub> and FEC are known to produce toxic hydrogen fluoride (HF) during cycling, and in substantially higher amounts during accidents such as battery fires<sup>19</sup>. Another factor to be considered here is the cost, as fluorinated salts, solvents and diluents are more expensive compared to their non-fluorinated counterparts, particularly the fluorinated diluents typically used in LHCEs (Figure S1), putting the commercial feasibility of fluorinated LHCEs into question. Therefore, while fluorinated electrolytes possess several benefits, moving towards cleaner and safer fluorine-free electrolytes is highly desirable.

Furthermore, while a bulk of high-performance LMB electrolytes indeed have high F content, fluorine may not necessarily be indispensable to stable Li metal performance. Growing evidence suggests that LiF does not form a continuous passivation layer in the SEI of fluorinated electrolytes, and could be acting 'as an indirect SEI/inert block that can stabilize Li electrodeposition by increasing Li<sup>+</sup> surface diffusivity or homogenizing the Li<sup>+</sup> diffusion field gradient'<sup>20,21</sup>. Lithium oxide (Li<sub>2</sub>O), typically also found as an SEI component in most high-performance LMB electrolytes, is more conductive than LiF<sup>22</sup> and has been shown to form a

continuous layer in high coulombic efficiency (CE) electrolytes. A recent study by Hobold et al. also suggested that the CEs in LMBs correlate much better with the  $\text{Li}_2\text{O}$  content in the SEI rather than the LiF content, and the nature of  $\text{Li}_2\text{O}$  layers in the SEI dictates the CE. High  $\text{Li}_2\text{O}$  content in the SEI, therefore, could be a crucial factor in the design of highly efficient F-free electrolytes<sup>23</sup>.

Lithium nitrate ( $\text{LiNO}_3$ ) and Lithium bis(oxalato)borate (LiBOB) are two often studied cheap non-corrosive fluorine free salts for Lithium ion batteries. LiBOB has previously been looked at as an alternative to  $\text{LiPF}_6$  in carbonate electrolytes<sup>24</sup> and shows similar properties such as passivation of the Al current collector<sup>25</sup>, and comparable electrochemical performances<sup>26</sup>. In addition, it also displays enhanced temperature stability<sup>24</sup>. However, LiBOB-based electrolytes suffer from poor bulk conductivity at room temperature, and the reaction of LiBOB with Li metal also leads to a significant amount of organic SEI components that lead to low  $\text{Li}^+$  conductivity over the interphase<sup>27</sup>. As a result, most works employing LiBOB as the main salt focusses on performance at higher temperatures<sup>28,29</sup>. Solubility is another challenge, as conventional carbonate-based electrolytes can only dissolve up to 0.7 M of the salt<sup>26</sup>.

$\text{LiNO}_3$  is a salt additive often used in high CE electrolytes for LMBs, and is known to preferentially reduce to form a highly conducting  $\text{Li}_2\text{O}$ -rich interphase<sup>23</sup>. However, its use as the main electrolyte salt is hindered by several challenges.  $\text{LiNO}_3$  possesses a high donor number ( $\sim 20$ ) and is, as a result, poorly soluble in most traditional solvents, including carbonates<sup>30</sup>. Works employing  $\text{LiNO}_3$  as the main salt, therefore, use high donor number solvents such as Diethylene Glycol Dimethyl Ether (diglyme DEGDME)<sup>31,32</sup>, Triethyl Phosphate (TEP)<sup>33,34</sup>, and Dimethyl Sulfoxide (DMSO)<sup>30</sup>. Furthermore,  $\text{LiNO}_3$  is known to react with freshly deposited Li metal in every cycle<sup>32</sup>. While this could be due to the chemical reactivity or the mechanical fragility of the  $\text{LiNO}_3$  derived SEI<sup>33,35</sup>, more research is necessary to fully elucidate the mechanism of  $\text{LiNO}_3$  consumption in different electrolyte systems and its prevention. Nevertheless, several strategies have been used to enable  $\text{LiNO}_3$  as the main salt in LMB electrolytes, and these have typically involved the use of fluorinated cosolvents. Liao et al and Zheng et al. used  $\text{LiNO}_3$  in TEP, and in both cases, the best cycling performance was obtained when FEC was used as a cosolvent<sup>33,34</sup>. In addition to the increase in the LiF content in the SEI the addition of film-forming SEI is likely to have also improved the chemomechanical properties of the SEI. Adams et al. showed stable cycling in Li-S batteries with fluorinated LiTFSI salt in addition to high concentration  $\text{LiNO}_3$  (3M) in diglyme<sup>32</sup>. Further, Choudhury et al. used  $\text{LiNO}_3$  in diglyme as the electrolyte, where the use of fluorinated hexafluoroisopropanol (HfIP) as the polymerization inhibitor significantly improved the long-term stability of Li plating and stripping process in these electrolytes<sup>31</sup>. In summary, while the chemomechanical stability of the SEI layer appears to play a key role in enabling  $\text{LiNO}_3$  based electrolytes, achieving this without using fluorinated additives still remains a challenge.

In this work, we design a high-performance fluorine-free (F-free) dual salt electrolyte for LMBs by tuning the ratio of  $\text{LiNO}_3$  and LiBOB in diglyme. The bulk properties and the solvation structures of resulting electrolytes are studied using nuclear magnetic resonance (NMR), rheometry, Raman spectroscopy, and molecular dynamics. The SEI formed on Li metal is characterized using X-ray photoelectron spectroscopy (XPS), scanning electron microscopy

(SEM) and solid-state NMR (ssNMR) to study its composition and structural arrangement. The obtained dual salt F-free electrolyte achieves a high coulombic efficiency of 98%, enables stable Li plating/stripping at 1 mA/cm<sup>2</sup> (1 mAh/cm<sup>2</sup>) for over 700 hours at 20 °C, and shows good capacity retention (77%) after 100 cycles in Li/LFP cells with Li reservoir of 100 μm, and commercial LFP cathode (2 mAh/cm<sup>2</sup> active mass loading) at 25 °C. These results present an important step forward in the design of room-temperature F-free electrolytes.

## 5.2 Results and discussion

### 5.2.1 Choice of salts, solvents and salt concentration

The choice of constituents for the F-free electrolytes is made with electrochemical performance versus Li metal and safety as the two main criteria. LiNO<sub>3</sub> is chosen as the main salt owing to its beneficial SEI passivation of Lithium metal.<sup>23</sup> LiBOB, known for its thermal stability and cathode passivation properties,<sup>31</sup> is selected as the secondary salt. While LiClO<sub>4</sub> has also been recently shown to result in high-CE F-free electrolytes,<sup>23</sup> it is not considered in this study given its strong oxidative property, thermal instability<sup>36</sup> (higher than LiNO<sub>3</sub>), and halogen content. In terms of solvent, diglyme (G2) presents a good balance of solvent properties, given their high donor number (~24)<sup>37</sup>, a higher flash point compared to most commonly used solvents (57.3 °C), and a moderate viscosity (1 mPa.s)<sup>38</sup>. This choice of solvent also results in reduced flammability for this class of electrolytes in comparison to conventional carbonate electrolytes such as 1M LiPF<sub>6</sub> in EC:DMC (1:1 vol%), hereafter referred to as LP30 (**Figure S2**). While high electrolyte concentrations are known to result in high CE due to their anion-derived SEI, excessively high salt concentrations could also affect the ion transport properties of the electrolyte, owing to an increase in viscosity. An overall salt:solvent ratio of 2.4:7 was chosen based on the optimum transport properties previously obtained for LiNO<sub>3</sub>-based electrolytes at similar concentrations<sup>31</sup>. The series of salt concentrations tested in this work is provided in **Table 1**.

**Table 1:** Electrolytes studied and their compositions. Molarities were calculated based on density measurements at 25 °C.

Electrolyte name	LiNO <sub>3</sub> (mol)	LiBOB (mol)	DEGDME (mol)	Molarity (M)
<b>2.4LN-0LB</b>	2.4	0	7	2.24
<b>2LN-0.4LB</b>	2	0.4	7	2.20
<b>1.6LN-0.8LB</b>	1.6	0.8	7	
<b>1.2LN-1.2LB</b>	1.2	1.2	7	2.12

For the rheometry measurements (**Figure 1a**), we observe that the dynamic viscosity rises with the increase in LiBOB content. This is expected, given the increase in steric effect due to the bulkier BOB<sup>-</sup> anion, but it could also be due to a higher degree of aggregation. The Pulsed Field Gradient (PFG) <sup>7</sup>Li NMR results (**Figure 1b**) also show a decrease in Li diffusion with increasing LiBOB concentration. Further, pulsed field gradient (PFG) NMR provides insights into the mobilities of Li and the solvent (G2) at these concentrations. While <sup>13</sup>C PFG NMR shows relatively higher diffusivities for G2 compared to Li, a stronger reduction in G2 diffusivity is

observed with increasing LiBOB content. Interestingly, despite the high salt concentration (2.12M – 2.24 M), the density measurements performed at 25 °C (**Figure 1c**) show lower gravimetric densities for all the F-free electrolytes in comparison to the standard 1M LiPF<sub>6</sub> in EC:DMC electrolyte (LP30), which suggests that these electrolytes could improve the cell level gravimetric energy densities of LMBs. Nevertheless, an increase in density with increasing LiBOB content is also observed, going from 1.03 g/cc for the 2.4LN-0LB electrolyte to 1.11 g/cc for the 1.2LN-1.2LB electrolyte.

In contrast to the diffusivity/viscosity results, the electrochemically measured total ionic conductivity of the electrolytes increases with the increasing LiBOB content, from 1.1 mS/cm for the 2.4LN-0LB electrolyte to 4.2 mS/cm for the 1.2LN-1.2LB electrolyte (**Figure 1d**), suggesting that the trend in the ionic conductivity cannot be explained solely on the basis of the individual physical properties of its constituents. In concentrated electrolytes (>2 M), the solvation structures can be anion-dominated, and the ion transport properties can be strongly influenced by the solvation structures, aggregation, and possible correlated/anticorrelated motion.<sup>39</sup> Therefore, the solvation structure of these electrolytes was investigated in further detail.

## 5. Rational design of safe, fluorine-free dual salt electrolytes for Lithium metal batteries

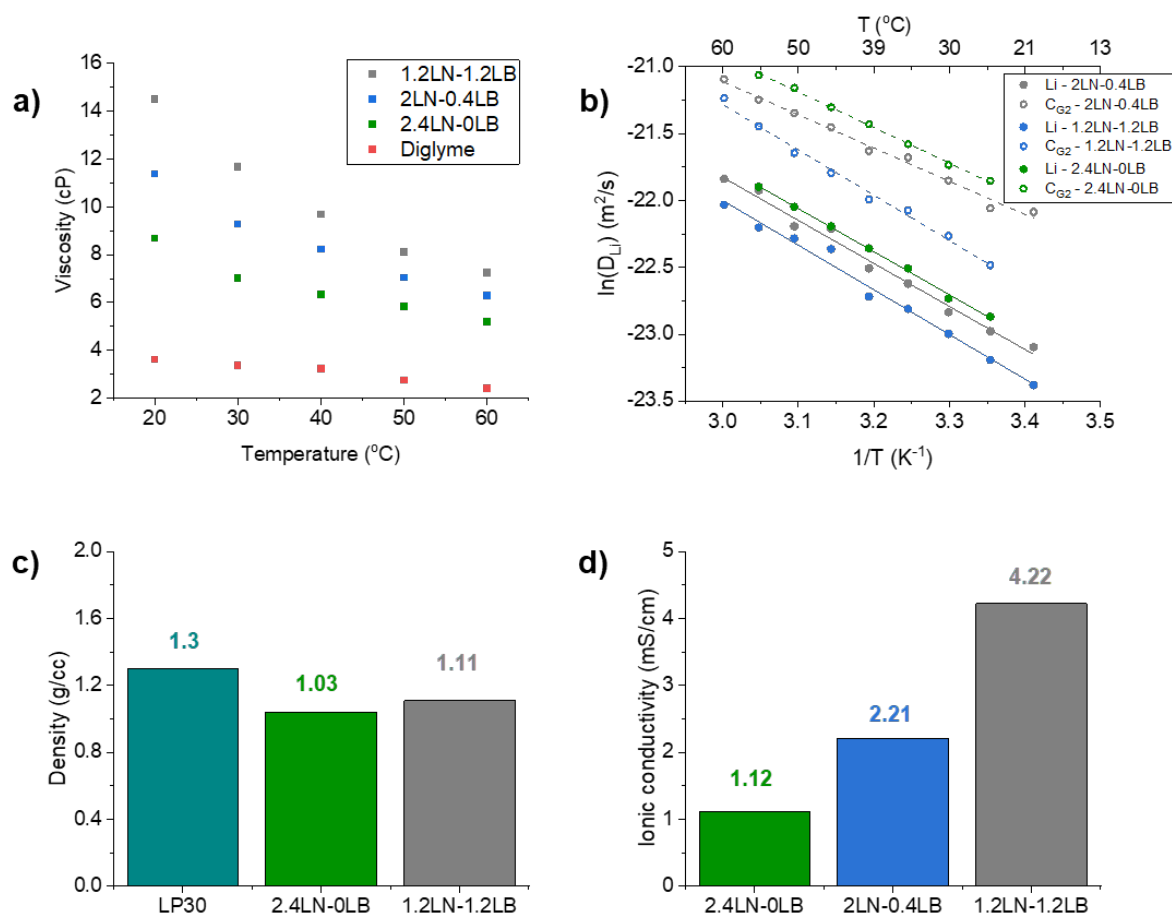


**Figure 1:** Physical and chemical characterization of F-free glyme electrolytes: a) Viscosity vs shear rate b) PFG NMR self-diffusion coefficients for <sup>7</sup>Li and glyme <sup>13</sup>C as a function of temperature, c) Density at 25 °C, d) Ionic conductivity (electrochemically measured) at 20 °C.

**Figure 2a**, shows a Walden plot (a log–log plot of molar ionic conductivities against dynamic viscosities at different temperatures) for the F-free electrolytes for a temperature range of 20 – 60 °C. Here, the resulting plot lines are compared with the ‘ideal KCl’ line resulting from a 1M aqueous solution, to roughly estimate the ‘ionicity’ of the electrolytes.<sup>40–42</sup> Ionicity is a measure of the extent to which ionic self-diffusion contributes to ionic conductivity and provides an estimate of ion dissociation, with the ‘ideal KCl’ line representing a fully ion-dissociated system.<sup>40</sup> Here, a low ionicity of 7.6% is obtained for the 2.4LN-0LB electrolyte, and this value increases with the amount of LiBOB in the system, i.e., to 35.1% for the 2LN-0.4LB electrolyte and to 57.8% for the 1.2LN-1.2LB electrolyte. For anions with high Lewis basicity such as NO<sub>3</sub><sup>-</sup>, Li<sup>+</sup> - anion interactions are known to be strong, resulting in less ion dissociation in concentrated glyme solutions.<sup>40</sup> The addition of LiBOB into the systems results in higher overall ion dissociation, which is likely due to the combined effect of easier salt dissociation with LiBOB and weakened Li<sup>+</sup> - NO<sub>3</sub><sup>-</sup> interactions, the mechanism of which is investigated further.

## 5. Rational design of safe, fluorine-free dual salt electrolytes for Lithium metal batteries

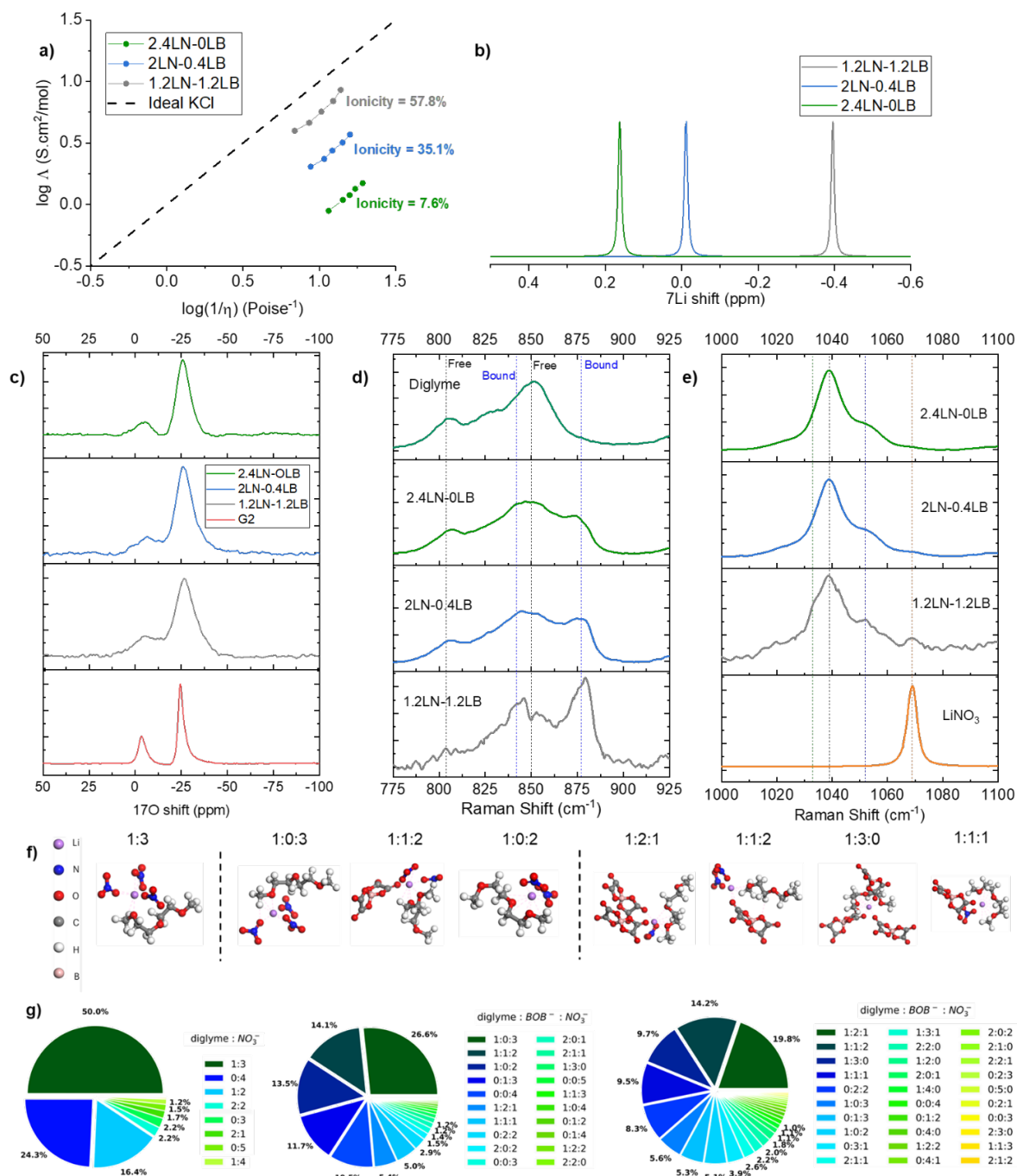


**Figure 2:** Investigation of solvation structures in F-free glyme electrolytes: a) Walden plot for the electrolytes alongside the 'ideal KCl' line b) <sup>7</sup>Li NMR at 25 °C c) Zoomed inset of <sup>17</sup>O solution NMR at 40 °C d) Raman spectra for electrolytes and diglyme in the region corresponding to CH<sub>2</sub> rocking and C-O-C stretching vibrations e) Raman spectra for electrolytes and LiNO<sub>3</sub> in the region corresponding to NO<sub>3</sub><sup>-</sup> stretching vibrations f) Dominant solvation structures (making up ~50% of all the solvation structures) obtained from MD simulations for 2LN-0.4LB (left) and 1.2LN-1.2LB (right) electrolytes. i) Pie charts of Li<sup>+</sup> coordination environments determined from MD simulations from left to right for 2.4LN-0LB, 2LN-0.4LB and 1.2LN-1.2LB electrolytes. For 2.4LN-0LB electrolyte, the ratios indicate  $N_{Dig} : N_{NO_3^-}$  while for the other two, the ratios indicate  $N_{Dig} : N_{BOB^-} : N_{NO_3^-}$

With  $^7\text{Li}$  NMR (**Figure 2b**), an upfield shift (i.e. shift to lower ppm values) is observed with increasing LiBOB content (from 0.2 ppm for 2.4LN-0LB electrolyte to -0.32 ppm for the 1.2LN-1.2LB electrolyte). The upfield shift indicates a higher shielding, likely due to the chelating oxygen groups (with a higher electron density) on the  $\text{BOB}^-$  ion, indicating the increased involvement of the  $\text{BOB}^-$  ion in the  $\text{Li}^+$  solvation structure. For the  $^{17}\text{O}$  NMR measurements conducted at 40 °C (**Figure 2c**), an increased broadening of the peaks corresponding to G2 oxygens (0 to -50 ppm) is observed with increasing LiBOB content, along with a slight upfield shift of the environment corresponding to terminal G2 oxygen (-25.73 ppm for 2.4LN-0LB to -26.62 ppm for 1.2LN-1.2LB). While the peak broadening could indicate lower G2 mobility, it could also indicate the formation of ion pairs/aggregates<sup>43</sup> and/or a high degree of heterogeneity in the possible solvation structures.

Raman spectroscopy results (**Figure 2d,e**) provide further evidence of the altered solvation structures with LiBOB addition. In the 775-925  $\text{cm}^{-1}$  region corresponding to  $\text{CH}_2$  rocking and C-O-C stretching vibrations in glymes,<sup>44</sup> For all the F-free electrolytes, in addition to the 'free' glyme environment at around 803 and 850  $\text{cm}^{-1}$ , additional 'bound' glyme peaks emerge at 840 and 877  $\text{cm}^{-1}$ , with the amount of bound glyme progressively increasing from 2.4LN-0LB to 1.2LN-1.2LB electrolytes. This suggests an increased participation of G2 molecules in the overall solvation structure. Furthermore, in comparison to pristine  $\text{LiNO}_3$ , the peak corresponding to  $\text{NO}_3^-$  stretching vibrations at 1069  $\text{cm}^{-1}$  shifts to a lower wavenumber of around 1039  $\text{cm}^{-1}$  for all the electrolytes with a second environment at around 1052  $\text{cm}^{-1}$ . For the 1.2LN-1.2LB electrolyte, however, additional features emerge both at lower (1033  $\text{cm}^{-1}$ ) and higher (1069  $\text{cm}^{-1}$ ) wavenumbers, which indicates an increased heterogeneity of  $\text{NO}_3^-$ -containing solvation structures.

Molecular dynamics (MD) results provide a deeper understanding of the solvation structures obtained in the F-free electrolytes. For the three simulated electrolytes, the radial distribution function (RDF) analysis (**Figure S4**) suggests that the  $\text{NO}_3^-$  species has the strongest interaction with  $\text{Li}^+$  followed by  $\text{BOB}^-$ . G2 has the lowest  $g(r)$  values, indicating that G2 has relatively lower coordination with  $\text{Li}^+$  in comparison. The RDF results suggest that the inner solvation sheath of  $\text{Li}^+$  would be anion-dominated, particularly with  $\text{NO}_3^-$ , for all three electrolytes. The closer and more defined peaks for  $\text{NO}_3^-$  compared to  $\text{BOB}^-$  can be attributed to the smaller size of the  $\text{NO}_3^-$  anion, which allows it to pack more closely around the  $\text{Li}^+$  ion. In contrast, the steric effects of the larger  $\text{BOB}^-$  anion may limit its interaction with  $\text{Li}^+$ , resulting in broader RDF peaks and causing no significant alterations in the  $\text{Li}^+$ - $\text{BOB}^-$  RDF with increasing  $\text{BOB}^-$  concentration. The relatively stronger reduction in Diglyme self-diffusion for 1.2LN-1.2LB electrolyte, previously observed with PFG NMR (**Figure 1b**), is also reflected in the mean square displacement (MSD) values calculated from the MD simulation (**Figure S4**).

Looking at the possible solvation structures (**Figure 2f,g**), it is clear that the solvation structures in most cases are anion-rich, and having  $\text{LiNO}_3$  and LiBOB in equimolar quantities results in a higher diversity of solvation structures and a higher participation of  $\text{BOB}^-$  in the solvation structures for the 1.2LN-1.2LB electrolyte, as indicated by the pie charts. A high diversity of solvation structures has been previously observed to result in decreased solvation

strength and higher ionic conductivity, which has been attributed to the increase in configurational entropy.<sup>45</sup>

While the Raman results suggest an increased amount of bound G2 for the 1.2LN-1.2LB electrolyte, the MD results suggest that the inner solvation structures are still anion-dominated. This indicates that this additional bound G2 contributes to the outer solvation shell, resulting in larger aggregates, which could explain the observed lower self-diffusivities (for Li and C). Despite this, the addition of large, weakly co-ordinating BOB<sup>-</sup> ions into the inner solvation sheath (as observed with MD), coupled with the progressive increase in the heterogeneity of solvation structures with the inclusion of LiBOB, could be contributing to the weakening of interactions between Li<sup>+</sup> and NO<sub>3</sub><sup>-</sup> (observed by Raman), and the improved ion dissociation and conductivity. Moreover, the aggregates formed in the case of 1.2LN-1.2LB electrolyte could also have a higher degree of correlated motion, which would further enhance ionic conductivity in these systems.<sup>39</sup> These results suggest that the inclusion of the bulky LiBOB salt in the system, despite causing a reduction in the bulk self-diffusion properties, results in an overall improvement in the ionic conductivity, rendering it suitable for applications in room temperature lithium metal batteries.

### 5.2.2 Lithium plating/stripping in Li/Li and Li/Cu cells

While the bulk properties of F-free electrolytes are comparable to standard carbonate electrolytes as previously discussed, they are further tested electrochemically to evaluate the rate performance and stability against Li metal. **Figure 3a** shows the voltage traces of Li plating/stripping cycles at 1 mA/cm<sup>2</sup> and 1 mAh/cm<sup>2</sup> (post-formation at 0.1 mA/cm<sup>2</sup> 4 mAh/cm<sup>2</sup>) at 20 °C as a function of salt ratios, with the zoomed insets at different timestamps displayed in **Figure 3b,c**, and **d**. Further, the cycling performance of the best F-free electrolyte is compared to that of standard LP30 in **Figure S5**.

For the 2.4LN-0LB electrolyte, a high overpotential (>0.1V) is observed from the beginning, and the cell already fails by 55 hours. In comparison, all the electrolytes with LiBOB show much lower and more stable overpotentials. The 2LN-0.4LB electrolyte has the lowest overpotential initially (**Figure 3b**), but this gradually increases, leading to cell failure by around 300 hours. With the introduction of higher amounts of LiBOB, the overpotential slightly increases, particularly towards the end of the plating/stripping cycle, where the divergence in the voltage trace becomes more pronounced. Previously, this behaviour has been attributed to concentration polarization-induced overpotential for lithium plating and stripping<sup>46</sup>. The MD results showed an increased participation of BOB<sup>-</sup> in the solvation shell for the 1.2LN-1.2LB electrolyte, and it is likely that desolvation from BOB<sup>-</sup>-dominated solvation structures requires slightly higher overpotentials. However, the cycle life of the F-free electrolytes significantly improves with increasing LiBOB content, with the 1.2LN-1.2LB electrolyte showing stable cycling for over 700 hours.

Electrochemical impedance spectroscopy sheds further light on the evolution of bulk electrolyte resistance (i.e., the high-frequency real axis intercept) and Li interface resistance (i.e., the real axis length of the large semicircle) with cycling (**Figure 3e, f, g**). Comparing the Nyquist plots right after formation cycling, it is observed that the 2.4LN-0LB electrolyte has

the highest Li interface resistance, while the LiBOB-containing electrolytes have lower values, in line with the initial cycling trends. In the case of 1.2LN-1.2LB electrolyte, a small secondary feature is observed at medium to low frequencies (**Figure 3g**), which could indicate the presence of an additional SEI component with a different time constant. Further, the bulk electrolyte resistance also follows the same trend as that observed with the bulk ionic conductivity measurements (**Figure 1d**), with the 1.2LN-1.2LB having the lowest bulk resistance. The Li interface R drops with cycling for all the electrolytes; however, the bulk electrolyte resistance also increases. For the 2.4LN-OLB electrolyte, this increase is the most severe, ( 4.5  $\Omega$  to 18  $\Omega$  after 50 cycles), while the bulk R barely changes for the 1.2LN-1.2LB electrolyte ( 2.5  $\Omega$  to 3  $\Omega$  after 50 cycles). This could indicate rapid LiNO<sub>3</sub> consumption in the case of the 2.4LN-OLB electrolyte, while the additional semicircle at high frequency could be indicative of (partially) electronically conducting organic decomposition layers on Li and/or dead Li following significant LiNO<sub>3</sub> consumption. This additional feature is not observed for the 1.2LN-1.2LB electrolyte even after 150 cycles, indicating the electrochemically stable nature of the Li interphase. While LiNO<sub>3</sub> is known to react with freshly plated Li in every cycle resulting in its rapid consumption, the presence of LiBOB seems to have a profound effect on stabilizing the Li interphase, the mechanism of which will be explored further.

## 5. Rational design of safe, fluorine-free dual salt electrolytes for Lithium metal batteries

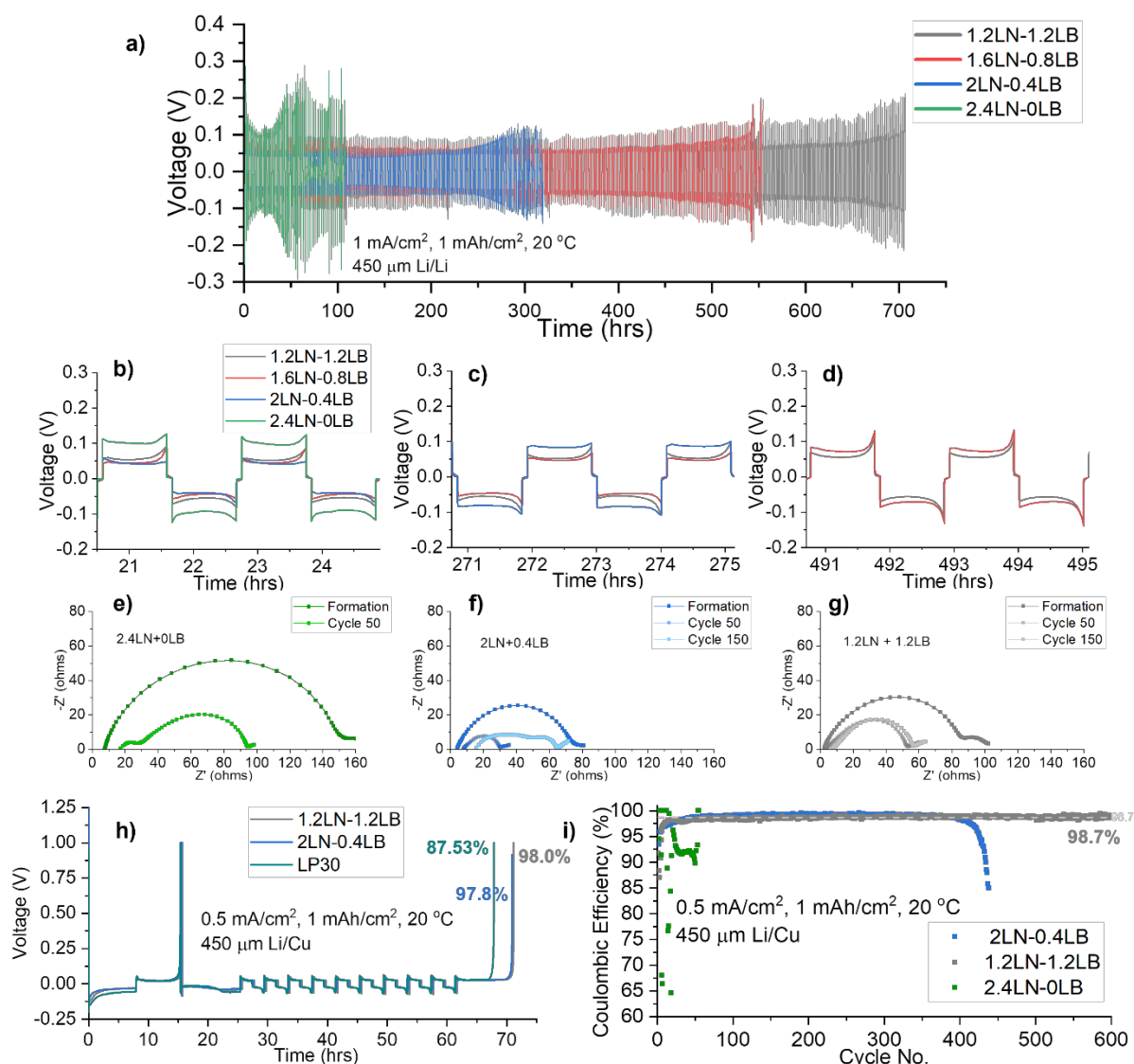


**Figure 3:** Electrochemical performance in Li/Li and Li/Cu cells: a) Voltage profiles of Li/Li cells at 1 mA/cm<sup>2</sup> (capacity 1 mAh/cm<sup>2</sup>) after two formation cycles at 0.1 mA/cm<sup>2</sup>, capacity 4 mAh/cm<sup>2</sup> (not shown). Zoomed inset of the voltage profiles are provided for b) 20.5-25 hrs, c) 270.8-275.2 hrs and d) 490.8-495.2 hrs. EIS Nyquist plots of Li/Li cells after formation, cycle 50 and cycle 150 are provided for e) 2.4 LN- 0LB f) 2LN-0.4LB and g) 1.2LN-1.2LB cells. h) Coulombic efficiency measurements in Li/Cu cells at 0.5 mA/cm<sup>2</sup> and 1 mAh/cm<sup>2</sup> with a reservoir plating of 5 mAh/cm<sup>2</sup> i) Coulombic efficiency measurements in Li/Cu cells at 0.5 mA/cm<sup>2</sup> and 1 mAh/cm<sup>2</sup> without reservoir plating

Further, coulombic efficiency (CE) measurements were performed in Li/Cu cells at 0.5 mA/cm<sup>2</sup> and 1 mAh/cm<sup>2</sup> according to the protocol by Adams et al.,<sup>47</sup> with a reservoir plating of 5 mAh/cm<sup>2</sup> (**Figure 3h**). Here, all the F-free electrolytes perform better than the conventional LP30 electrolyte, with the 1.2LN-1.2LB electrolyte showing a CE of 98.0%. On long-term cycling without reservoir plating, the CE value briefly increases to 99.2% for the 2LN-0.4LB electrolyte, but the cell fails after 440 cycles. In contrast, the 1.2LN-1.2LB cell cycles for over 600 cycles with a CE of 98.7%, in line with the trends observed for Li/Li cells (**Figure 3i**). While this value is lower than those recently reported for the highly fluorinated LHCEs,<sup>13</sup>

it nevertheless presents a very promising avenue for further development of F-free electrolytes with high CEs for Lithium plating/stripping.

### 5.2.3 Effect of salt ratios on SEI composition and Li microstructure

The electrochemical cycling and the EIS results suggest that the improvements in (electro)chemical stability for the F-free electrolytes with the inclusion of LiBOB are linked to changes in characteristics of the Li/electrolyte interface in terms of Li morphology on plating/stripping, SEI composition or possibly both, as the properties of the SEI have been known to strongly influence Li plating/stripping characteristics, particularly with high current density.

Scanning electron microscopy (SEM) top view images of the Li surface morphology, and the SEI compositions based on X-ray Photoelectron spectroscopy (XPS) for the F-free electrolytes are shown in **Figure 4**. Here, samples from all three electrolytes are compared post 50 cycles at 1 mA/cm<sup>2</sup> current and 1 mAh/cm<sup>2</sup> capacity.

**Figure 4a** shows the SEM top view of the electrodeposited Li surface after 50 cycles at 1mA/cm<sup>2</sup> and 1mAh/cm<sup>2</sup>, and **Figures 4b** and **4c** show the corresponding survey and C1s XPS compositions of the surfaces respectively. For the 2.4LN-OLB electrolyte, the Li deposition is significantly uneven, with the formation of a surface layer on top. The corresponding XPS survey spectrum shows a high concentration of C at the surface, which decreases drastically with etching, along with an increase in Li and O concentrations. In the high-resolution C1s spectrum (**Figure 4c**), in addition to the adventitious C-C carbon peak at 284.8 eV, another significant environment is observed at 286.8 eV, which could correspond to Li alkoxides (R-CO-Li) typically known to form with ether decomposition at the Li surface,<sup>49</sup> This possibility is also supported by the O1s spectrum (**Figure S6**), where a significant peak is observed in the region corresponding to alkoxides ( ~531 eV), alongside Li<sub>2</sub>O (~528 eV), formed upon LiNO<sub>3</sub> reduction.<sup>32</sup> Nevertheless, some contributions from the adventitious carbon environments, also occurring with similar binding energies for the C1s and O1s spectra, cannot be ruled out. An environment is also observed at 283 eV, which could correspond to components like Li<sub>2</sub>C<sub>2</sub> which can be formed by further reduction of organic SEI components on lithium.<sup>50</sup> This might also explain the additional high-frequency semicircle in the EIS post-50 cycles.

## 5. Rational design of safe, fluorine-free dual salt electrolytes for Lithium metal batteries

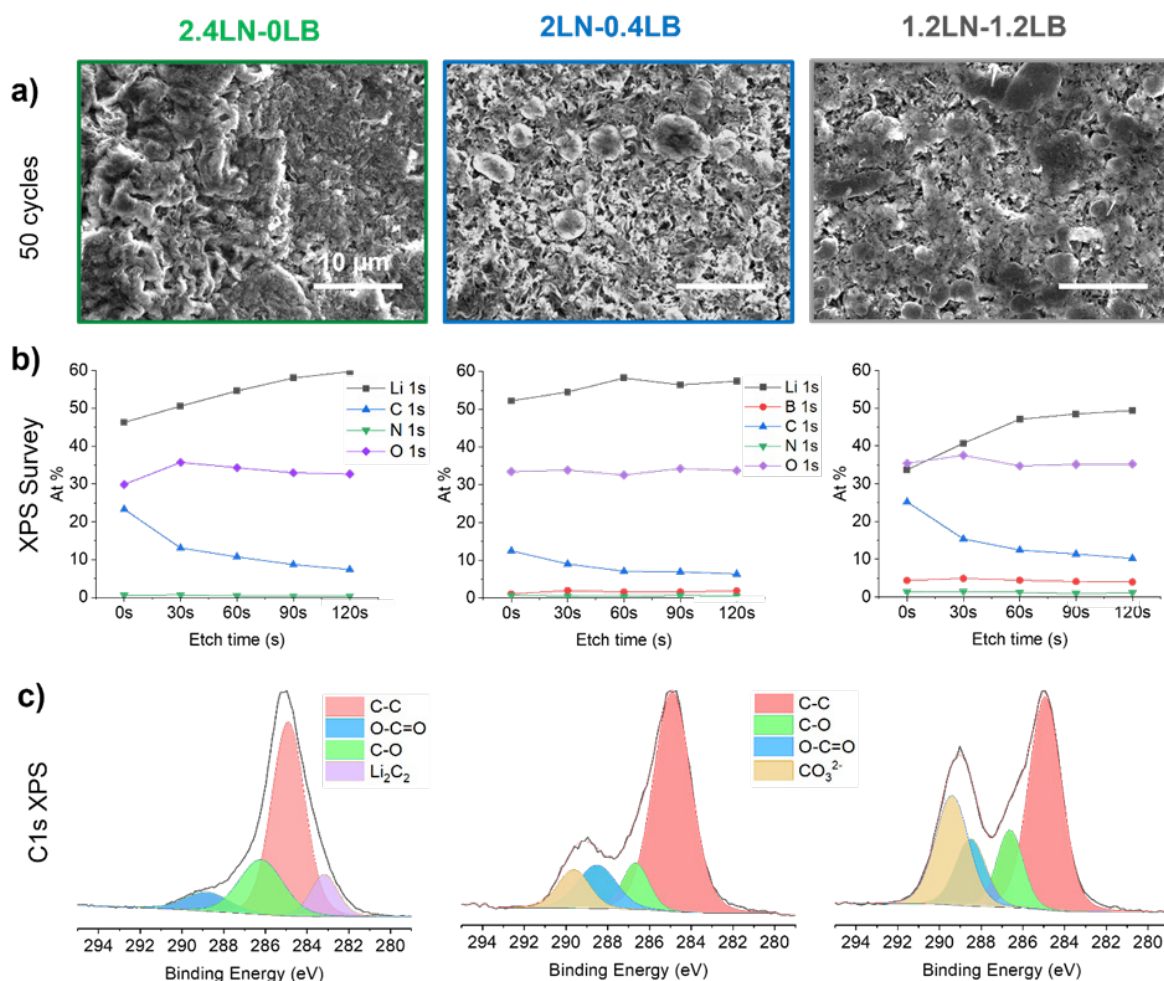


**Figure 4:** Li morphology and interphase composition after 50 cycles in Li/Cu cells at  $1 \text{ mA/cm}^2$ ,  $1 \text{ mAh/cm}^2$ : Top - SEM images of a) 2.4LN-0LB b) 2LN-0.4LB and c) 1.2LN-1.2LB samples. The scale bar is  $20 \mu\text{m}$ . Middle - XPS survey atomic percentage (with depth profiling) for d) 2.4LN-0LB e) 2LN-0.4LB and f) 1.2LN-1.2LB samples. Bottom - C1s XPS spectra of g) 2.4LN-0LB h) 2LN-0.4LB and i) 1.2LN-1.2LB samples

In contrast, the 2LN-0.4LB and 1.2LN-1.2LB electrolytes show a more uniform Li surface morphology, where the Li deposits are surrounded or covered by a scaffold-like structure. For the 2LN-0.4LB electrolyte, this structure appears porous, whereas for the 1.2LN-1.2LB electrolyte, this structure appears more compact, with Li plating visible below the structure. The chemical compositions of these surfaces are also different. The 2LN-0.4LB electrolyte results in a much lesser C content throughout the SEI, with Li and O dominating the SEI composition. The C1s spectrum reveals the emergence of a new environment around 289.5 eV, corresponding to  $\text{Li}_2\text{CO}_3$ , and a relative increase in the O-C=O peak at 288.5 eV, which could be due to the presence of  $\text{Li}_2\text{C}_2\text{O}_4$  and/or organic borate intermediates known to form with LiBOB decomposition at Li surface.<sup>51</sup> In the O1s spectrum (**Figure S6**) at the top surface, a dominant contribution from  $\text{Li}_2\text{O}$  (528.5 eV) is observed, alongside Li alkoxides/LiOH ( $\sim 531$  eV) and a new environment at 531.5 eV corresponding to  $\text{Li}_2\text{CO}_3$ , and other C=O derivatives from LiBOB.<sup>52</sup> The presence of LiBOB derivatives in the SEI is further confirmed by B1s XPS (**Figure S7**), where a peak is observed at lower binding energies ( $\sim 191$  eV) than that for the

BOB<sup>-</sup> anion (193.7 eV). However, the XPS spectra close to cell failure post 150 cycles (**Figure S8**) show similar depth-wise composition and top-layer composition as the 2.4LN-0LB electrolyte after 50 cycles. This further confirms the hypothesis that the cell failure in these electrolytes possibly occurs due to solvent decomposition at the Li surface following LiNO<sub>3</sub> consumption and also suggests that the presence of LiBOB-derived products in the SEI could be delaying its onset.

For the 1.2LN-1.2LB electrolyte, the top surface shows a high C, but this value drops more steadily with etching compared to that of the 2.4LN-0LB electrolyte, suggesting a more uniform depth-wise distribution of C in the SEI. Furthermore, the relatively lower Li content in the outer SEI layers (0 -30 s etching) and an increased presence of B (4-5%) suggest that these outer SEI layers could be primarily made up of LiBOB derivatives. The C1s spectrum reveals a strong increase amount of Li<sub>2</sub>CO<sub>3</sub> (289.5 eV) in the SEI. In the O1s spectrum, the Li<sub>2</sub>CO<sub>3</sub>/C=O peak is now the most dominant, with an additional peak at 532.5 eV, which could correspond to less-reduced intermediates of the salts, particularly LiBOB. The B1s XPS also indicates a less-reduced environment on the outer SEI layers (192 eV) covering the more reduced LiBOB derivatives at 191 eV. The amount of B in the SEI also increases from ~1.5% to 4-5% throughout the SEI thickness probed.

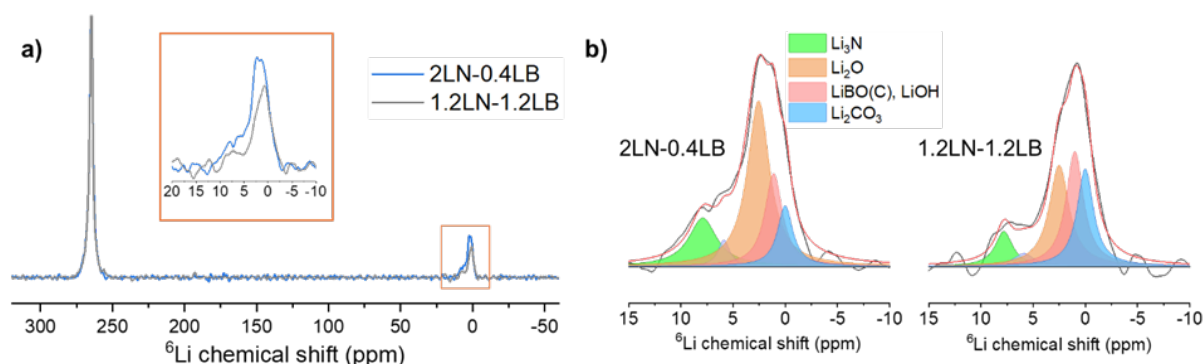


**Figure 5:** a) <sup>6</sup>Li MAS NMR of the SEI after 440 cycles in Li/Cu cells at 0.5 mA/cm<sup>2</sup>, 1 mAh/cm<sup>2</sup> normalized to the intensity of dead Li. b) <sup>6</sup>Li NMR diamagnetic (SEI) region of 2LN-0.4LB and 1.2LN-1.2LB samples with fits.

It is to be noted, however, that lab-scale XPS (with Al source) typically has a penetration depth of only around 5 nm, while the SEI in Li metal cells post-cycling could be 10 nm and higher.<sup>53</sup> While depth profiling can access the elemental compositions at higher depths, the chemical environments of the SEI can change significantly under the influence of X-rays/Ar<sup>+</sup> etching.<sup>54</sup> Obtaining quantitative information on the SEI composition with XPS can, therefore, be difficult. In this regard, we employed natural abundance <sup>6</sup>Li MAS NMR to probe the composition of the SEI (for Li-containing components) in a non-destructive manner, and complemented this with cross-section SEM to obtain a visual estimate of the overall dead Li/SEI residue generated. <sup>6</sup>Li was chosen over <sup>7</sup>Li NMR to obtain a better chemical shift resolution on the SEI components.

The post-cycling cross-section SEM images (**Figure S9**) reveal that the amount of dead Li/SEI residue generated after 440 cycles is nearly the same (around 64.5 μm) for the 2LN-0.4LB and 1.2LN 1.2LB electrolytes, justifying our choice of <sup>6</sup>Li NMR spectra normalization with respect

to the dead Li peak at  $\sim 260$  ppm for the sake of comparison. With this approach, we observe that the 2LN-0.4LB electrolyte has a relatively higher area of the diamagnetic peak at  $\sim 0$  ppm, corresponding to Li-containing SEI components. The compositions of the SEI are also different.  $\text{Li}_2\text{O}$  (at 2.6 ppm) is the dominant SEI component for the 2LN-0.4LB electrolyte, with minor peaks for Li-borates/LiOH ( $\sim 1$  ppm),  $\text{Li}_2\text{CO}_3$  (0 ppm) and  $\text{Li}_3\text{N}$  (6.5 ppm).<sup>55,56</sup> In comparison, the ratio of Li-borate/LiOH and  $\text{Li}_2\text{CO}_3$  peaks increases for the 1.2LN 1.2LB electrolyte, with reduced contributions from  $\text{Li}_2\text{O}$  and  $\text{Li}_3\text{N}$ .

To sum up, the addition of LiBOB into  $\text{LiNO}_3$ /diglyme electrolytes improves Li plating/stripping both in terms of homogenizing Li deposition at high current densities and regulating  $\text{Li}^+$  consumption from the electrolyte with cycling. While the addition of LiBOB as a minor secondary salt already improves  $\text{Li}^+$  dissociation, leading to homogenous Li plating/stripping with high CE, the formed Li-rich SEI scaffold does not sufficiently passivate fresh Li deposits with subsequent cycling, leading to  $\text{Li}^+$  consumption-induced cell failure. On increasing the LiBOB concentration further, the initial and subsequent Li deposition (below the SEI structure) are observed to be more compact. LiBOB-derived borate derivatives are observed in the outer layers of the SEI, which chemomechanically reinforce the SEI, and regulate  $\text{Li}^+$  consumption from the electrolyte towards the continuous formation of Li-rich inner SEI components such as  $\text{Li}_2\text{O}$  and  $\text{Li}_3\text{N}$  with cycling.

### 5.2.4 Electrochemical performance in half and full cells

The electrochemical performance of the optimized 1.2LN-1.2LB electrolyte is tested in half and full cells to further evaluate its practical applicability. The linear sweep voltammetry (LSV) measurements performed in Li/stainless steel cells at 0.1 mV/s at 25 °C (**Figure S10**) show that the 1.2LN-1.2LB electrolyte has an electrochemical stability of up to 4.3 V. In comparison, the electrolytes with lower amounts of LiBOB show similar stability, but the leakage current beyond 4.3V appears to be higher, implying that the inclusion of LiBOB imparts some additional electrochemical stability at high potentials, similar to previous reports<sup>31</sup>. As such, the scope of this work is limited to testing of the 1.2LN-1.2LB electrolyte with a moderate potential cathode material, i.e.  $\text{LiFePO}_4$  (LFP). A rate performance comparison of 1.2LN-1.2LB and LP30 electrolytes is performed in Li/LFP half cells with commercially supplied 1 mAh/cm<sup>2</sup> LFP cathodes at 20 °C (**Figure 6a**). It is observed that the rate performance of the 1.2LN-1.2LB electrolyte is very similar to that of LP30 (176 mAh/g vs 171 mAh/g at 0.1C, 44.24 mAh/g vs 44.6 mAh/g at 5C) despite the high salt concentration and high LiBOB content of the former. With continued cycling at 1C for another 200 cycles (**Figure 6b**), the standard LP30 electrolyte undergoes a rapid capacity fade, while the 1.2LN-1.2LB electrolyte continues to display stable cycling with high average coulombic efficiency of 99.47% over the 200 cycles (versus 98.48% for LP30). These results suggest that the high-current induced Li surface degradation is much lower in the case of the 1.2LN-1.2LB electrolyte.

## 5. Rational design of safe, fluorine-free dual salt electrolytes for Lithium metal batteries

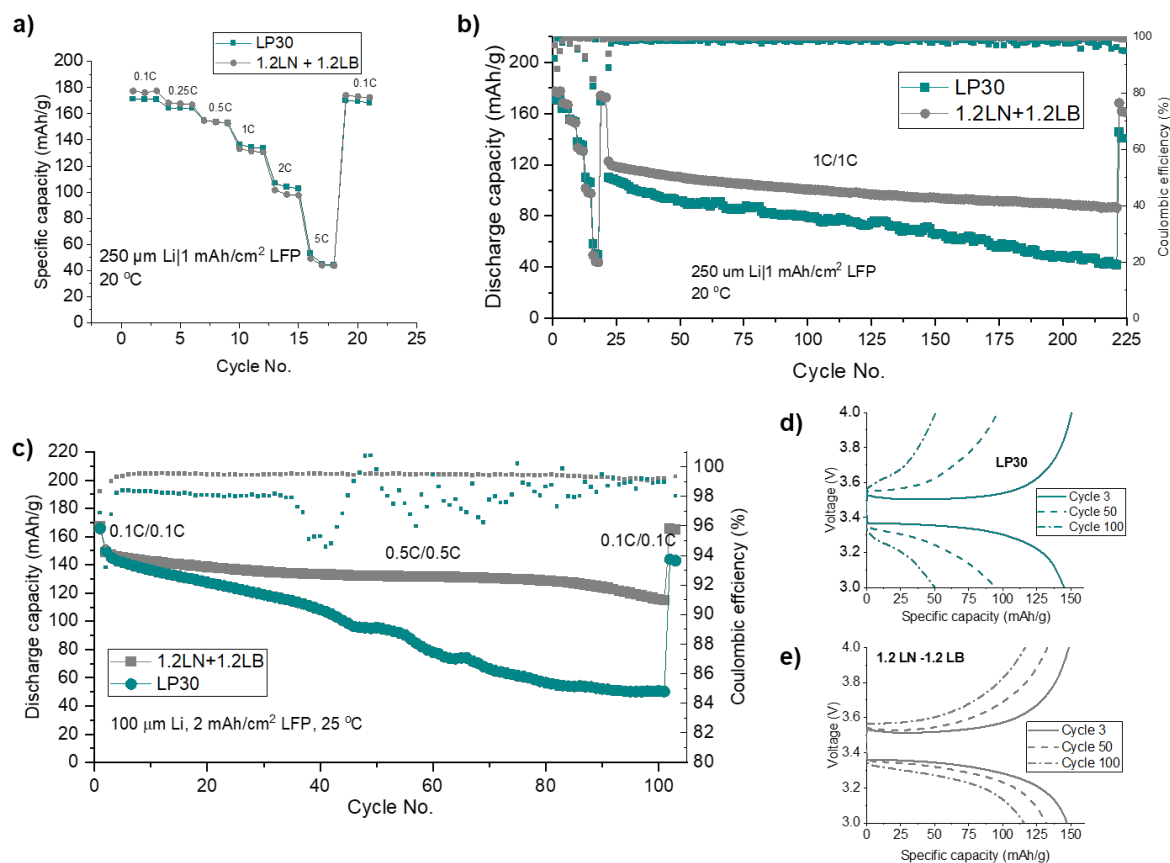


**Figure 6:** a) Rate performances of Li/LFP ( $1 \text{ mAh/cm}^2$ ) half cells at varying charge/discharge rates at  $20 \text{ }^\circ\text{C}$  b) Discharge capacities and coulombic efficiencies for the Li/LFP ( $1 \text{ mAh/cm}^2$ ) half cells with extended cycling at 1C for 200 cycles and 0.1C for 2 cycles at  $20 \text{ }^\circ\text{C}$  c) Discharge capacities and coulombic efficiencies in Li/LFP ( $2 \text{ mAh/cm}^2$ ) full cells with LP30 and 1.2LN-1.2LB electrolytes at  $25 \text{ }^\circ\text{C}$  d) Voltage traces for the LP30 Li/LFP cells at 3, 50, and 100 cycles. e) Voltage traces for the 1.2LN-1.2LB Li/LFP cells at 3, 50, and 100 cycles

Furthermore, the electrochemical performance of 1.2LN-1.2LB electrolyte was evaluated under more realistic full-cell conditions, i.e. with a lower lithium reservoir of  $100 \text{ }\mu\text{m}$ , commercial LFP cathodes with an active mass loading of  $2 \text{ mAh/cm}^2$  and at  $25 \text{ }^\circ\text{C}$  (**Figure 6c**). Here, the 1.2LN-1.2LB electrolyte significantly outperforms LP30 with a capacity retention of 77.15%, average discharge capacity of  $132.36 \text{ mAh/g}$  and average coulombic efficiency of 99.38% (versus a capacity retention of 33.49%, average discharge capacity of  $92.47 \text{ mAh/g}$  and average coulombic efficiency of 98.07% for LP30) after 100 cycles at 0.5C. On return to 0.1C, the capacity retention further increases to 98.69% for the 1.2LN-1.2LB electrolyte (versus 86.23% for LP30). From the voltage traces shown for cycle 3, 50 and 100 (**Figure 6d,e**), it can be observed that the capacity degradation for LP30 appears to be mainly from electrolyte consumption at the anode/cathode interfaces, resulting in both a high ohmic drop and steeper voltage traces at the latter cycles. The 1.2LN-1.2LB likely benefits from the presence of LiBOB which, in addition to stabilizing the Li SEI as previously discussed, is also known to contribute towards a robust CEI in LFP electrodes,<sup>57</sup> thereby inhibiting electrolyte consumption at either of the electrodes.

## 5.3 Conclusions

In this work, we have developed diglyme-based fluorine-free electrolytes for lithium metal batteries, employing LiNO<sub>3</sub> and LiBOB as the two Li salts, with a focus on studying the effect of salt ratios on bulk electrolyte properties, Li-metal interface stability and electrochemical performance. Here, while increasing the amount of LiBOB resulted in a drop in transport properties such as viscosity and self-diffusivity, owing to the steric effects imparted by LiBOB and a possible increase in aggregation, the increase in the number of charge carriers due to both easier dissociation of LiBOB and weakening of Li<sup>+</sup>-NO<sub>3</sub><sup>-</sup> interactions, and an increase in heterogeneity of solvation structures as suggested by molecular dynamics, solution NMR and Raman spectroscopy result in an increase in ionic conductivity. The inclusion of LiBOB also significantly improved the cycling stability in Li/Li symmetric cells, with the 1.2LN-1.2LB electrolyte showing stable cycling for over 700 hours at 1 mA/cm<sup>2</sup>, 1 mAh/cm<sup>2</sup>, 20 °C. Li microstructural analysis with SEM shows dense Li plating with high surface coverage for this electrolyte, while the Li interphase composition studied by XPS and MAS NMR reveals the role played by LiBOB-derived SEI components in the chemomechanical stabilization of the Li<sub>2</sub>O rich inner SEI. The 1.2LN-1.2LB electrolyte performs well in Li-LFP half cells and full cells, with a capacity retention of 77% after 100 cycles at 0.5C (1 mA/cm<sup>2</sup>) in a 100 μm Li/2 mAh/cm<sup>2</sup> commercial LFP cell at 25 °C, with an average CE of 99.38%. These results open up an interesting avenue towards the development of green, safe, affordable electrolytes for Li metal batteries, while also highlighting the importance of tailoring the chemomechanical properties of the Li-metal SEI in the absence of fluorinated compounds.

5

## 5.4 Experimental Details

### 5.4.1 Electrolyte preparation

The salts LiNO<sub>3</sub> (battery grade, anhydrous), LiBOB (battery grade) and solvent DEGDME (anhydrous, 99.5%) were all purchased from Sigma Aldrich. To prepare the electrolytes with different salt ratios, the salts and the solvent are in the ratios described in Table 1, and mixed in pre-dried glass vials using a magnetic stirrer until a homogenous solution was obtained. The mixing was carried out inside an Argon-filled glove box.

### 5.4.2 Electrolyte characterization

Rheometry was performed on the liquids using a 40-mm Peltier plate with a 0° cone angle and 500 μm gap width on a Discovery HR10 rheometer (TA Instruments). The shear rate was varied between 0.01 and 10/s.

For solution and pulsed field gradient (PFG) NMR, a Bruker Ascend 600 (B<sub>0</sub>= 14.1 T) magnet equipped with a NEO console was used. 5 mm NMR sample tubes (Wilmad) were filled with the liquid sample. Glass capillaries filled with C<sub>6</sub>D<sub>6</sub> were inserted into these tubes for solvent locking and shimming. <sup>7</sup>Li solution NMR was performed at 25 °C with a π/2 pulse length of 17.5 μs, 45 W and a recycle delay of 5 s with 16-32 scans per measurement. Natural abundance <sup>17</sup>O solution NMR was performed at 40 °C as a balance between signal/noise ratio

## 5. Rational design of safe, fluorine-free dual salt electrolytes for Lithium metal batteries

and measurement time. A  $\pi/2$  pulse length of 14.7  $\mu\text{s}$  at 190 W and a recycle delay of 0.5s were used with 60000-100000 scans per measurement.

For PFG NMR, the samples were measured using stimulated echo pulse field gradient procedure on  $^7\text{Li}$  ( $\pi/2$  pulse length of 17.5  $\mu\text{s}$ , 45 W and  $B_1=84\text{-}1680$  Gauss/cm) and  $^{13}\text{C}$  ( $\pi/2$  pulse length of 12  $\mu\text{s}$ , 100 W and  $B_1=84\text{-}1680$  Gauss/cm) using a linear gradient of 8 slices with typical mixing times of 10-20  $\mu\text{s}$  and 8-32 scans per slice for temperatures from 20 °C to 60 °C for every 5° increment in temperature. The data was fit using the Stejskal–Tanner equation, and Bruker Dynamics center software was used.

Raman spectroscopy was performed on a Horiba Jobin Yvon LabRAM HR800 Raman Spectroscopy system, using an excitation wavelength of 515 nm (Cobolt Fandango™ 50) and a 50x objective lens. Raman measurements were recorded between 100 and 2000  $\text{cm}^{-1}$  using an acquisition time of 20 s and 5 accumulations. The maximum slit and hole opening (1000), a 10% neutral density (ND) filter and a grating of 1800 were used. To avoid air exposure, the specimens were transferred (in an Ar glovebox) to an air-tight homemade optical sample holder.

Molecular dynamics (MD) simulations were conducted using the GROMACS 2022.3 package<sup>58–60</sup> on the DelftBlue high-performance cluster.<sup>61</sup> Molecular forces were calculated using the Generation Amber Force Field (GAFF).<sup>62</sup> The ACPYPE code<sup>63</sup> was utilized to generate the desired force field parameters for the simulation systems. The ORCA 5.0.4 software<sup>64,65</sup> was employed to optimize the molecular geometries at B3LYP D3 def2-TZVP def2/J RIJCOSX level. Partial charges on atoms were obtained with the restrained electrostatic potential (RESP) method calculated using ORCA and Multiwfn 3.8 software.<sup>66</sup> The molecules were mixed in a cubic box  $60\times 60\times 60$  Å<sup>3</sup> with periodic boundary conditions using the PACKMOL package.<sup>67,68</sup>

The simulation protocol started with steepest-descent energy minimizations with maximum number of steps of 100000. Equilibration was performed in two stages, the first stage in the canonical ensemble (NVT) for 200 ps (time step = 1 fs) and the subsequent stage in the isothermal–isobaric ensemble (NPT) for 200 ps (time step = 1 fs). Convergence of the system energy, temperature, and box size were checked to verify equilibration. After that, a production run under NVT ensemble lasting 20 ns (time step = 2 fs) was carried out. The minimizations and simulations were run using the long-range fast smooth particle-mesh Ewald (SPME) electrostatics<sup>69</sup> with Fourier spacing of 0.1 nm, order of 4, and cut-off of 1.0 nm. A cutoff set to 1.0 nm was used for van der Waals interactions. The Verlet cut-off scheme was used to generate pair lists. A cut-off of 1.0 nm was used for non-bonded Lennard-Jones interactions. The LINCS algorithm<sup>70</sup> was used to constrain the hydrogen bonds. The temperature during the simulations was 300 K, controlled using a velocity rescaling thermostat,<sup>71</sup> and the pressure (when running NPT) was 1 bar, controlled using a stochastic cell rescaling barostat.<sup>72</sup>

## 5. Rational design of safe, fluorine-free dual salt electrolytes for Lithium metal batteries

Mean square displacements (MSDs) and radial distribution functions (RDFs) were generated using GROMACS. Solvation shell statistics were calculated using the MDAnalysis Python library<sup>73,74</sup> with a cut-off distance of 2.5 Å.

### 5.4.3 Cell assembly and electrochemical characterization

The Li/Li coin cells (CR2032) were assembled using Li discs (450 µm) of 15.4 mm diameter, a surfactant-coated polypropylene separator of 19 mm diameter, and 60 µl of the electrolyte. For Li/Cu cells, Li discs (450 µm) and a Cu foil (9 µm thick) of 12.7 mm diameter were used as electrodes. For Li/LFP half cells, commercial 1 mAh/cm<sup>2</sup> LFP sheets (Customcells, Germany) were cut into 12.7 mm diameter discs, and Li discs (250 µm) of 15.4 mm diameter were used as counter electrodes. For Li-LFP full cells, commercial 2 mAh/cm<sup>2</sup> LFP sheets (Customcells, Germany) were cut into 12.7 mm diameter discs, and Li discs (100 µm) of 15 mm diameter were used as counter electrodes. All cells were assembled in an Argon-filled glovebox.

Linear Sweep Voltammetry (LSV) measurements were performed in Li/Stainless steel cells at 25 °C on a Lahne G340A battery testing system, with a scan rate of 0.1 mV/s up to a potential of 5V (vs Li<sup>+</sup>/Li).

Electrochemical impedance spectroscopy measurements on Li/Li symmetric cells were performed at 20 °C on a Biologic VMP3 potentiostat between frequencies of 7 MHz and 0.1 Hz, with an AC amplitude of 10 mV and 10 points per decade.

Ionic conductivity of electrolytes was measured in symmetric stainless steel/stainless steel cells with a 500 µm PTFE ring with 10 mm inner diameter in between, by measuring the electrochemical impedance ( $R$ ) at 25 °C, and calculated using the equation:

$$\sigma = \frac{L}{R \times S}$$

where  $\sigma$  is ionic conductivity,  $S$  is the effective area of electrodes,  $L$  stands for the thickness of the PTFE ring, respectively.

The galvanostatic cycling of Li/Li symmetric cells, and Li/Cu and Li/LFP half cells was carried out at 20 °C using a Maccor 4300 cycler. The Li/Li symmetric cells were subjected to a formation cycle of 40 hours of plating and stripping each at 0.1 mA/cm<sup>2</sup> (4 mAh/cm<sup>2</sup>), following which the cells were subjected to plating/stripping at 1 mA/cm<sup>2</sup> and 1 mAh/cm<sup>2</sup>. The coulombic efficiencies of the electrolytes were evaluated in Li/Cu cells according to the protocol by Adams et. al.,<sup>47</sup> where an initial formation cycle of 0.5 mA/cm<sup>2</sup>, 4 mAh/cm<sup>2</sup> was followed by a reservoir plating of 5 mAh/cm<sup>2</sup> at 0.5 mA/cm<sup>2</sup>, followed by subsequent stripping/plating at 0.5 mA/cm<sup>2</sup>, 1 mAh/cm<sup>2</sup>, with the terminating condition for the last stripping half cycle being 1V (vs Li<sup>+</sup>/Li). The Li-LFP half cells were subjected to charge/discharge rates (3 cycles each) of 0.1C, 0.2C, 0.5C, 1C, 2C, 5C, 0.1C, followed by 200 cycles at 1C and then two cycles at 0.1C between 2.5 and 4.0 V (vs Li<sup>+</sup>/Li). Galvanostatic (long-term) cycling of Li-LFP full cells was performed at 25 °C on the Lahne G340A battery testing system between 3 and 4.0 V (vs Li<sup>+</sup>/Li). The cell was subjected to 2 formation cycles at 0.1C

(not shown), followed by one cycle at 0.1C, 100 cycles at 0.5 C charge/discharge (constant current), and finally two cycles at 0.1C.

#### 5.4.4 Li interface characterization

Li/Cu coin cells were subjected to 50 cycles at 1 mA/cm<sup>2</sup>, 1 mAh/cm<sup>2</sup>, and subsequently, the Cu foils containing the Li deposits were extracted from these cells. The Li foils were washed multiple times with Dimethoxyethane (DME, Sigma Aldrich, 99.5%) to remove the salt traces, and then dried under vacuum to evaporate the DME. The washed foils were directly used for the SEM and XPS analysis. The samples were transferred to the XPS chamber using a vacuum transfer holder.

Scanning electron microscopy (SEM) pictures were taken using a JEOL JSM-IT700HR FE-SEM setup in scattering electron imaging (acceleration voltage: 10 -15 kV) mode.

The XPS measurements were performed on a Thermo Scientific K-Alpha Spectrometer with an Al K-alpha monochromator. The spot diameter was set to 400 μm. Survey spectra were recorded with a pass energy of 200 eV and step size of 0.5 eV, while high-resolution spectra were recorded with a pass energy of 50 eV and step size of 0.1 eV. The binding energies were referenced to adventitious carbon at 284.8 eV. For the depth profiling measurements, argon ion sputtering was performed (1 keV ion energy, 1.5 μA and 1x1 mm<sup>2</sup> raster size). All the spectra were processed and analyzed using the CasaXPS software using a U2 Tougaard background to account for inelastically scattered photoelectrons.

To obtain solid electrolyte interphase samples for MAS solid-state NMR measurements, Li foils Li/Cu coin cells were subjected to 440 cycles at 0.5 mA/cm<sup>2</sup>, 1 mAh/cm<sup>2</sup> were retrieved, washed and dried similar to those for the XPS measurements. Thereafter, the deposited Li layer plus its solid electrolyte interphase was scraped off from the Li foils and packed into 3.2 mm airtight ZrO<sub>2</sub> rotors with KBr as the inert filler.

All solid-state NMR measurements were carried out on a Bruker Ascend 500 MHz (11.7 T) spectrometer equipped with a Neo console. <sup>6</sup>Li MAS NMR measurements were carried out on a 3.2 mm triple resonance probe at spinning speeds of 18 kHz using direct excitation pulses. For <sup>6</sup>Li measurements, a pulse length of 2 μs (200 W) was used with a recycle delay of 150 s and 600-1000 scans. All measurements were referenced to a LiCl solution at 0 ppm. The processing and analysis of the resulting spectra was performed using the Mestrenova 14 software.

## References

(1) Liu, J.; Bao, Z.; Cui, Y.; Dufek, E. J.; Goodenough, J. B.; Khalifah, P.; Li, Q.; Liaw, B. Y.; Liu, P.; Manthiram, A.; Meng, Y. S.; Subramanian, V. R.; Toney, M. F.; Viswanathan, V. V.; Whittingham, M. S.; Xiao, J.; Xu, W.; Yang, J.; Yang, X.-Q.; Zhang, J.-G. Pathways for Practical High-Energy Long-Cycling Lithium Metal Batteries. *Nat. Energy* **2019**, *4* (3), 180–186. <https://doi.org/10.1038/s41560-019-0338-x>.

## 5. Rational design of safe, fluorine-free dual salt electrolytes for Lithium metal batteries

- (2) Lin, D.; Liu, Y.; Cui, Y. Reviving the Lithium Metal Anode for High-Energy Batteries. *Nat. Nanotechnol.* **2017**, *12* (3), 194–206. <https://doi.org/10.1038/nnano.2017.16>.
- (3) Cheng, X.-B.; Zhang, R.; Zhao, C.-Z.; Zhang, Q. Toward Safe Lithium Metal Anode in Rechargeable Batteries: A Review. *Chem. Rev.* **2017**, *117* (15), 10403–10473. <https://doi.org/10.1021/acs.chemrev.7b00115>.
- (4) Qian, J.; Henderson, W. A.; Xu, W.; Bhattacharya, P.; Engelhard, M.; Borodin, O.; Zhang, J.-G. High Rate and Stable Cycling of Lithium Metal Anode. *Nat. Commun.* **2015**, *6* (1), 6362. <https://doi.org/10.1038/ncomms7362>.
- (5) Su, C.-C.; He, M.; Amine, R.; Rojas, T.; Cheng, L.; Ngo, A. T.; Amine, K. Solvating Power Series of Electrolyte Solvents for Lithium Batteries. *Energy Environ. Sci.* **2019**, *12* (4), 1249–1254. <https://doi.org/10.1039/C9EE00141G>.
- (6) Weber, R.; Genovese, M.; Louli, A. J.; Hames, S.; Martin, C.; Hill, I. G.; Dahn, J. R. Long Cycle Life and Dendrite-Free Lithium Morphology in Anode-Free Lithium Pouch Cells Enabled by a Dual-Salt Liquid Electrolyte. *Nat. Energy* **2019**, *4* (8), 683–689. <https://doi.org/10.1038/s41560-019-0428-9>.
- (7) Yu, Z.; Wang, H.; Kong, X.; Huang, W.; Tsao, Y.; Mackanic, D. G.; Wang, K.; Wang, X.; Huang, W.; Choudhury, S.; Zheng, Y.; Amanchukwu, C. V.; Hung, S. T.; Ma, Y.; Lomeli, E. G.; Qin, J.; Cui, Y.; Bao, Z. Molecular Design for Electrolyte Solvents Enabling Energy-Dense and Long-Cycling Lithium Metal Batteries. *Nat. Energy* **2020**, *5* (7), 526–533. <https://doi.org/10.1038/s41560-020-0634-5>.
- (8) Yu, Z.; Rudnicki, P. E.; Zhang, Z.; Huang, Z.; Celik, H.; Oyakhire, S. T.; Chen, Y.; Kong, X.; Kim, S. C.; Xiao, X.; Wang, H.; Zheng, Y.; Kamat, G. A.; Kim, M. S.; Bent, S. F.; Qin, J.; Cui, Y.; Bao, Z. Rational Solvent Molecule Tuning for High-Performance Lithium Metal Battery Electrolytes. *Nat. Energy* **2022**, *7* (1), 94–106. <https://doi.org/10.1038/s41560-021-00962-y>.
- (9) Cao, X.; Jia, H.; Xu, W.; Zhang, J.-G. Review—Localized High-Concentration Electrolytes for Lithium Batteries. *J. Electrochem. Soc.* **2021**, *168* (1), 010522. <https://doi.org/10.1149/1945-7111/abd60e>.
- (10) Cao, X.; Ren, X.; Zou, L.; Engelhard, M. H.; Huang, W.; Wang, H.; Matthews, B. E.; Lee, H.; Niu, C.; Arey, B. W.; Cui, Y.; Wang, C.; Xiao, J.; Liu, J.; Xu, W.; Zhang, J.-G. Monolithic Solid–Electrolyte Interphases Formed in Fluorinated Orthoformate-Based Electrolytes Minimize Li Depletion and Pulverization. *Nat. Energy* **2019**, *4* (9), 796–805. <https://doi.org/10.1038/s41560-019-0464-5>.
- (11) Chen, S.; Zheng, J.; Yu, L.; Ren, X.; Engelhard, M. H.; Niu, C.; Lee, H.; Xu, W.; Xiao, J.; Liu, J.; Zhang, J.-G. High-Efficiency Lithium Metal Batteries with Fire-Retardant Electrolytes. *Joule* **2018**, *2* (8), 1548–1558. <https://doi.org/10.1016/j.joule.2018.05.002>.

## 5. Rational design of safe, fluorine-free dual salt electrolytes for Lithium metal batteries

- (12) Yu, L.; Chen, S.; Lee, H.; Zhang, L.; Engelhard, M. H.; Li, Q.; Jiao, S.; Liu, J.; Xu, W.; Zhang, J.-G. A Localized High-Concentration Electrolyte with Optimized Solvents and Lithium Difluoro(Oxalate)Borate Additive for Stable Lithium Metal Batteries. *ACS Energy Lett.* **2018**, *3* (9), 2059–2067. <https://doi.org/10.1021/acsenergylett.8b00935>.
- (13) Hobold, G. M.; Lopez, J.; Guo, R.; Minafra, N.; Banerjee, A.; Shirley Meng, Y.; Shao-Horn, Y.; Gallant, B. M. Moving beyond 99.9% Coulombic Efficiency for Lithium Anodes in Liquid Electrolytes. *Nat. Energy* **2021**, *6* (10), 951–960. <https://doi.org/10.1038/s41560-021-00910-w>.
- (14) *Perfluoroalkyl and Polyfluoroalkyl Substances (PFAS)*. National Institute of Environmental Health Sciences. <https://www.niehs.nih.gov/health/topics/agents/pfc> (accessed 2024-08-23).
- (15) Fenton, S. E.; Ducatman, A.; Boobis, A.; DeWitt, J. C.; Lau, C.; Ng, C.; Smith, J. S.; Roberts, S. M. Per- and Polyfluoroalkyl Substance Toxicity and Human Health Review: Current State of Knowledge and Strategies for Informing Future Research. *Environ. Toxicol. Chem.* **2021**, *40* (3), 606–630. <https://doi.org/10.1002/etc.4890>.
- (16) Vieira, V. M.; Hoffman, K.; Shin, H.-M.; Weinberg, J. M.; Webster, T. F.; Fletcher, T. Perfluorooctanoic Acid Exposure and Cancer Outcomes in a Contaminated Community: A Geographic Analysis. *Environ. Health Perspect.* **2013**, *121* (3), 318–323. <https://doi.org/10.1289/ehp.1205829>.
- (17) *Registry of restriction intentions until outcome - ECHA*. <https://echa.europa.eu/registry-of-restriction-intentions/-/dislist/details/0b0236e18663449b> (accessed 2024-08-23).
- (18) Collins, P. *Hydrogen Europe*. Hydrogen Europe. <https://hydrogeneurope.eu/joint-statement-on-the-importance-of-fluoropolymers-to-the-energy-transition/> (accessed 2024-08-23).
- (19) Larsson, F.; Andersson, P.; Blomqvist, P.; Mellander, B.-E. Toxic Fluoride Gas Emissions from Lithium-Ion Battery Fires. *Sci. Rep.* **2017**, *7* (1), 10018. <https://doi.org/10.1038/s41598-017-09784-z>.
- (20) Huang, W.; Wang, H.; Boyle, D. T.; Li, Y.; Cui, Y. Resolving Nanoscopic and Mesoscopic Heterogeneity of Fluorinated Species in Battery Solid-Electrolyte Interphases by Cryogenic Electron Microscopy. *ACS Energy Lett.* **2020**, *5* (4), 1128–1135. <https://doi.org/10.1021/acsenergylett.0c00194>.
- (21) Surace, Y.; Leanza, D.; Mirolo, M.; Kondracki, Ł.; Vaz, C. A. F.; El Kazzi, M.; Novák, P.; Trabesinger, S. Evidence for Stepwise Formation of Solid Electrolyte Interphase in a Li-Ion Battery. *Energy Storage Mater.* **2022**, *44*, 156–167. <https://doi.org/10.1016/j.ensm.2021.10.013>.

## 5. Rational design of safe, fluorine-free dual salt electrolytes for Lithium metal batteries

- (22) Guo, R.; Gallant, B. M. Li<sub>2</sub>O Solid Electrolyte Interphase: Probing Transport Properties at the Chemical Potential of Lithium. *Chem. Mater.* **2020**, *32* (13), 5525–5533. <https://doi.org/10.1021/acs.chemmater.0c00333>.
- (23) Hobold, G. M.; Wang, C.; Steinberg, K.; Li, Y.; Gallant, B. M. High Lithium Oxide Prevalence in the Lithium Solid–Electrolyte Interphase for High Coulombic Efficiency. *Nat. Energy* **2024**, *9* (5), 580–591. <https://doi.org/10.1038/s41560-024-01494-x>.
- (24) Xu, K.; Zhang, S. S.; Lee, U.; Allen, J. L.; Jow, T. R. LiBOB: Is It an Alternative Salt for Lithium Ion Chemistry? *J. Power Sources* **2005**, *146* (1), 79–85. <https://doi.org/10.1016/j.jpowsour.2005.03.153>.
- (25) Zhang, X.; Devine, T. M. Passivation of Aluminum in Lithium-Ion Battery Electrolytes with LiBOB. *J. Electrochem. Soc.* **2006**, *153* (9), B365. <https://doi.org/10.1149/1.2218269>.
- (26) Hernández, G.; Naylor, A. J.; Chien, Y.-C.; Brandell, D.; Mindemark, J.; Edström, K. Elimination of Fluorination: The Influence of Fluorine-Free Electrolytes on the Performance of LiNi<sub>1/3</sub>Mn<sub>1/3</sub>Co<sub>1/3</sub>O<sub>2</sub>/Silicon–Graphite Li-Ion Battery Cells. *ACS Sustain. Chem. Eng.* **2020**, *8* (27), 10041–10052. <https://doi.org/10.1021/acssuschemeng.0c01733>.
- (27) Jürg, S.; Brown, Z. L.; Kim, J.; Lucht, B. L. Effect of Electrolyte on the Nanostructure of the Solid Electrolyte Interphase (SEI) and Performance of Lithium Metal Anodes. *Energy Environ. Sci.* **2018**, *11* (9), 2600–2608. <https://doi.org/10.1039/C8EE00364E>.
- (28) Kreth, F. A.; Köps, L.; Leibing, C.; Darlami Magar, S.; Hermesdorf, M.; Schutjajew, K.; Neumann, C.; Leistenschneider, D.; Turchanin, A.; Oschatz, M.; Gómez Urbano, J. L.; Balducci, A. Enabling Fluorine-Free Lithium-Ion Capacitors and Lithium-Ion Batteries for High-Temperature Applications by the Implementation of Lithium Bis(Oxalato)Borate and Ethyl Isopropyl Sulfone as Electrolyte. *Adv. Energy Mater.* **2024**, *14* (13), 2303909. <https://doi.org/10.1002/aenm.202303909>.
- (29) Jiang, Z.; Li, C.; Yang, T.; Deng, Y.; Zou, J.; Zhang, Q.; Li, Y. Fluorine-Free Lithium Metal Batteries with a Stable LiF-Free Solid Electrolyte Interphase. *ACS Energy Lett.* **2024**, *9* (4), 1389–1396. <https://doi.org/10.1021/acsenergylett.3c02724>.
- (30) Chen, H.; Chen, K.; Luo, L.; Liu, X.; Wang, Z.; Zhao, A.; Li, H.; Ai, X.; Fang, Y.; Cao, Y. LiNO<sub>3</sub>-Based Electrolytes via Electron-Donation Modulation for Sustainable Nonaqueous Lithium Rechargeable Batteries. *Angew. Chem. Int. Ed.* **2024**, *63* (10), e202316966. <https://doi.org/10.1002/anie.202316966>.
- (31) Choudhury, S.; Tu, Z.; Nijamudheen, A.; Zachman, M. J.; Stalin, S.; Deng, Y.; Zhao, Q.; Vu, D.; Kourkoutis, L. F.; Mendoza-Cortes, J. L.; Archer, L. A. Stabilizing Polymer Electrolytes in High-Voltage Lithium Batteries. *Nat. Commun.* **2019**, *10* (1), 3091. <https://doi.org/10.1038/s41467-019-11015-0>.

## 5. Rational design of safe, fluorine-free dual salt electrolytes for Lithium metal batteries

- (32) Adams, B. D.; Carino, E. V.; Connell, J. G.; Han, K. S.; Cao, R.; Chen, J.; Zheng, J.; Li, Q.; Mueller, K. T.; Henderson, W. A.; Zhang, J.-G. Long Term Stability of Li-S Batteries Using High Concentration Lithium Nitrate Electrolytes. *Nano Energy* **2017**, *40*, 607–617. <https://doi.org/10.1016/j.nanoen.2017.09.015>.
- (33) Zheng, T.; Zhu, B.; Xiong, J.; Xu, T.; Zhu, C.; Liao, C.; Yin, S.; Pan, G.; Liang, Y.; Shi, X.; Zhao, H.; Berger, R.; Cheng, Y.-J.; Xia, Y.; Müller-Buschbaum, P. When Audience Takes Stage: Pseudo-Localized-High-Concentration Electrolyte with Lithium Nitrate as the Only Salt Enables Lithium Metal Batteries with Excellent Temperature and Cathode Adaptability. *Energy Storage Mater.* **2023**, *59*, 102782. <https://doi.org/10.1016/j.ensm.2023.102782>.
- (34) Liao, C.; Han, L.; Wang, W.; Li, W.; Mu, X.; Kan, Y.; Zhu, J.; Gui, Z.; He, X.; Song, L.; Hu, Y. Non-Flammable Electrolyte with Lithium Nitrate as the Only Lithium Salt for Boosting Ultra-Stable Cycling and Fire-Safety Lithium Metal Batteries. *Adv. Funct. Mater.* **2023**, *33* (17), 2212605. <https://doi.org/10.1002/adfm.202212605>.
- (35) Guo, R.; Wang, D.; Zuin, L.; Gallant, B. M. Reactivity and Evolution of Ionic Phases in the Lithium Solid–Electrolyte Interphase. *ACS Energy Lett.* **2021**, *6* (3), 877–885. <https://doi.org/10.1021/acsenergylett.1c00117>.
- (36) Xu, K. Nonaqueous Liquid Electrolytes for Lithium-Based Rechargeable Batteries. *Chem. Rev.* **2004**, *104* (10), 4303–4418. <https://doi.org/10.1021/cr030203g>.
- (37) Ortiz Vitoriano, N.; Ruiz de Larramendi, I.; Sacci, R. L.; Lozano, I.; Bridges, C. A.; Arcelus, O.; Enterría, M.; Carrasco, J.; Rojo, T.; Veith, G. M. Goldilocks and the Three Glymes: How Na+ Solvation Controls Na–O<sub>2</sub> Battery Cycling. *Energy Storage Mater.* **2020**, *29*, 235–245. <https://doi.org/10.1016/j.ensm.2020.04.034>.
- (38) Lecce, D. D.; Marangon, V.; Jung, H.-G.; Tominaga, Y.; Greenbaum, S.; Hassoun, J. Glyme-Based Electrolytes: Suitable Solutions for next-Generation Lithium Batteries. *Green Chem.* **2022**, *24* (3), 1021–1048. <https://doi.org/10.1039/D1GC03996B>.
- (39) Vargas-Barbosa, N. M.; Roling, B. Dynamic Ion Correlations in Solid and Liquid Electrolytes: How Do They Affect Charge and Mass Transport? *ChemElectroChem* **2020**, *7* (2), 367–385. <https://doi.org/10.1002/celec.201901627>.
- (40) Ueno, K.; Yoshida, K.; Tsuchiya, M.; Tachikawa, N.; Dokko, K.; Watanabe, M. Glyme–Lithium Salt Equimolar Molten Mixtures: Concentrated Solutions or Solvate Ionic Liquids? *J. Phys. Chem. B* **2012**, *116* (36), 11323–11331. <https://doi.org/10.1021/jp307378j>.
- (41) Shigenobu, K.; Shibata, M.; Dokko, K.; Watanabe, M.; Fujii, K.; Ueno, K. Anion Effects on Li Ion Transference Number and Dynamic Ion Correlations in Glyme–Li Salt Equimolar Mixtures. *Phys. Chem. Chem. Phys.* **2021**, *23* (4), 2622–2629. <https://doi.org/10.1039/D0CP06381A>.

## 5. Rational design of safe, fluorine-free dual salt electrolytes for Lithium metal batteries

(42) MacFarlane, D. R.; Forsyth, M.; Izgorodina, E. I.; Abbott, A. P.; Annat, G.; Fraser, K. On the Concept of Ionicity in Ionic Liquids. *Phys. Chem. Chem. Phys.* **2009**, *11* (25), 4962–4967. <https://doi.org/10.1039/B900201D>.

(43) Chen, Y.; Yu, Z.; Rudnicki, P.; Gong, H.; Huang, Z.; Kim, S. C.; Lai, J.-C.; Kong, X.; Qin, J.; Cui, Y.; Bao, Z. Steric Effect Tuned Ion Solvation Enabling Stable Cycling of High-Voltage Lithium Metal Battery. *J. Am. Chem. Soc.* **2021**, *143* (44), 18703–18713. <https://doi.org/10.1021/jacs.1c09006>.

(44) Hosaka, T.; Matsuyama, T.; Kubota, K.; Tatara, R.; Komaba, S. KFSA/Glyme Electrolytes for 4 V-Class K-Ion Batteries. *J. Mater. Chem. A* **2020**, *8* (45), 23766–23771. <https://doi.org/10.1039/D0TA08851J>.

(45) Wang, Q.; Zhao, C.; Wang, J.; Yao, Z.; Wang, S.; Kumar, S. G. H.; Ganapathy, S.; Eustace, S.; Bai, X.; Li, B.; Wagemaker, M. High Entropy Liquid Electrolytes for Lithium Batteries. *Nat. Commun.* **2023**, *14* (1), 440. <https://doi.org/10.1038/s41467-023-36075-1>.

(46) Wood, K. N.; Kazyak, E.; Chadwick, A. F.; Chen, K.-H.; Zhang, J.-G.; Thornton, K.; Dasgupta, N. P. Dendrites and Pits: Untangling the Complex Behavior of Lithium Metal Anodes through Operando Video Microscopy. *ACS Cent. Sci.* **2016**, *2* (11), 790–801. <https://doi.org/10.1021/acscentsci.6b00260>.

(47) Adams, B. D.; Zheng, J.; Ren, X.; Xu, W.; Zhang, J.-G. Accurate Determination of Coulombic Efficiency for Lithium Metal Anodes and Lithium Metal Batteries. *Adv. Energy Mater.* **2018**, *8* (7), 1702097. <https://doi.org/10.1002/aenm.201702097>.

(48) Wang, Q.; Zhao, C.; Wang, S.; Wang, J.; Liu, M.; Ganapathy, S.; Bai, X.; Li, B.; Wagemaker, M. Clarifying the Relationship between the Lithium Deposition Coverage and Microstructure in Lithium Metal Batteries. *J. Am. Chem. Soc.* **2022**, *144* (48), 21961–21971. <https://doi.org/10.1021/jacs.2c08849>.

(49) Aurbach, D.; Daroux, M. L.; Faguy, P. W.; Yeager, E. Identification of Surface Films Formed on Lithium in Dimethoxyethane and Tetrahydrofuran Solutions. *J. Electrochem. Soc.* **1988**, *135* (8), 1863. <https://doi.org/10.1149/1.2096170>.

(50) Menkin, S.; O’Keefe, C. A.; Gunnarsdóttir, A. B.; Dey, S.; Pesci, F. M.; Shen, Z.; Agudero, A.; Grey, C. P. Toward an Understanding of SEI Formation and Lithium Plating on Copper in Anode-Free Batteries. *J. Phys. Chem. C* **2021**, *125* (30), 16719–16732. <https://doi.org/10.1021/acs.jpcc.1c03877>.

(51) Melin, T.; Lundström, R.; Berg, E. J. Elucidating the Reduction Mechanism of Lithium Bis(Oxalato)Borate. *J. Phys. Chem. Lett.* **2024**, *15* (9), 2537–2541. <https://doi.org/10.1021/acs.jpcclett.4c00328>.

## 5. Rational design of safe, fluorine-free dual salt electrolytes for Lithium metal batteries

- (52) Hernández, G.; Mogensen, R.; Younesi, R.; Mindemark, J. Fluorine-Free Electrolytes for Lithium and Sodium Batteries. *Batter. Supercaps* **2022**, *5* (6), e202100373. <https://doi.org/10.1002/batt.202100373>.
- (53) Jagger, B.; Pasta, M. Solid Electrolyte Interphases in Lithium Metal Batteries. *Joule* **2023**, *7* (10), 2228–2244. <https://doi.org/10.1016/j.joule.2023.08.007>.
- (54) Yu, W.; Yu, Z.; Cui, Y.; Bao, Z. Degradation and Speciation of Li Salts during XPS Analysis for Battery Research. *ACS Energy Lett.* **2022**, *7* (10), 3270–3275. <https://doi.org/10.1021/acsenergylett.2c01587>.
- (55) Meyer, B. M.; Leifer, N.; Sakamoto, S.; Greenbaum, S. G.; Grey, C. P. High Field Multinuclear NMR Investigation of the SEI Layer in Lithium Rechargeable Batteries. *Electrochem. Solid State Lett.* **2005**, *8* (3), A145. <https://doi.org/10.1149/1.1854117>.
- (56) Michan, A. L.; Parimalam, Bharathy. S.; Leskes, M.; Kerber, R. N.; Yoon, T.; Grey, C. P.; Lucht, B. L. Fluoroethylene Carbonate and Vinylene Carbonate Reduction: Understanding Lithium-Ion Battery Electrolyte Additives and Solid Electrolyte Interphase Formation. *Chem. Mater.* **2016**, *28* (22), 8149–8159. <https://doi.org/10.1021/acs.chemmater.6b02282>.
- (57) Liao, Y.; Li, G.; Xu, N.; Chen, T.; Wang, X.; Li, W. Synergistic Effect of Electrolyte Additives on the Improvement in Interfacial Stability between Ionic Liquid Based Gel Electrolyte and LiFePO<sub>4</sub> Cathode. *Solid State Ion.* **2019**, *329*, 31–39. <https://doi.org/10.1016/j.ssi.2018.11.013>.
- (58) Berendsen, H. J. C.; van der Spoel, D.; van Drunen, R. GROMACS: A Message-Passing Parallel Molecular Dynamics Implementation. *Comput. Phys. Commun.* **1995**, *91* (1), 43–56. [https://doi.org/10.1016/0010-4655\(95\)00042-E](https://doi.org/10.1016/0010-4655(95)00042-E).
- (59) Van Der Spoel, D.; Lindahl, E.; Hess, B.; Groenhof, G.; Mark, A. E.; Berendsen, H. J. C. GROMACS: Fast, Flexible, and Free. *J. Comput. Chem.* **2005**, *26* (16), 1701–1718. <https://doi.org/10.1002/jcc.20291>.
- (60) Abraham, M. J.; Murtola, T.; Schulz, R.; Páll, S.; Smith, J. C.; Hess, B.; Lindahl, E. GROMACS: High Performance Molecular Simulations through Multi-Level Parallelism from Laptops to Supercomputers. *SoftwareX* **2015**, *1–2*, 19–25. <https://doi.org/10.1016/j.softx.2015.06.001>.
- (61) *Delft High Performance Computing Centre (DHPC), DelftBlue Supercomputer (Phase 2)*. TU Delft. <https://www.tudelft.nl/dhpc/ark/delftbluephase2> (accessed 2024-09-03).
- (62) Wang, J.; Wolf, R. M.; Caldwell, J. W.; Kollman, P. A.; Case, D. A. Development and Testing of a General Amber Force Field. *J. Comput. Chem.* **2004**, *25* (9), 1157–1174. <https://doi.org/10.1002/jcc.20035>.
- (63) Sousa da Silva, A. W.; Vranken, W. F. ACPYPE - AnteChamber PYthon Parser InterfacE. *BMC Res. Notes* **2012**, *5* (1), 367. <https://doi.org/10.1186/1756-0500-5-367>.

## 5. Rational design of safe, fluorine-free dual salt electrolytes for Lithium metal batteries

- (64) Neese, F. The ORCA Program System. *WIREs Comput. Mol. Sci.* **2012**, 2 (1), 73–78. <https://doi.org/10.1002/wcms.81>.
- (65) Neese, F. Software Update: The ORCA Program System—Version 5.0. *WIREs Comput. Mol. Sci.* **2022**, 12 (5), e1606. <https://doi.org/10.1002/wcms.1606>.
- (66) Lu, T.; Chen, F. Multiwfn: A Multifunctional Wavefunction Analyzer. *J. Comput. Chem.* **2012**, 33 (5), 580–592. <https://doi.org/10.1002/jcc.22885>.
- (67) Martínez, J. M.; Martínez, L. Packing Optimization for Automated Generation of Complex System's Initial Configurations for Molecular Dynamics and Docking. *J. Comput. Chem.* **2003**, 24 (7), 819–825. <https://doi.org/10.1002/jcc.10216>.
- (68) Martínez, L.; Andrade, R.; Birgin, E. G.; Martínez, J. M. PACKMOL: A package for building initial configurations for molecular dynamics simulations. *J. Comput. Chem.* **2009**, 30 (13), 2157–2164. <https://doi.org/10.1002/jcc.21224>.
- (69) Essmann, U.; Perera, L.; Berkowitz, M. L.; Darden, T.; Lee, H.; Pedersen, L. G. A Smooth Particle Mesh Ewald Method. *J. Chem. Phys.* **1995**, 103 (19), 8577–8593. <https://doi.org/10.1063/1.470117>.
- (70) Hess, B.; Bekker, H.; Berendsen, H. J. C.; Fraaije, J. G. E. M. LINCS: A Linear Constraint Solver for Molecular Simulations. *J. Comput. Chem.* **1997**, 18 (12), 1463–1472. [https://doi.org/10.1002/\(SICI\)1096-987X\(199709\)18:12<1463::AID-JCC4>3.0.CO;2-H](https://doi.org/10.1002/(SICI)1096-987X(199709)18:12<1463::AID-JCC4>3.0.CO;2-H).
- (71) Bussi, G.; Donadio, D.; Parrinello, M. Canonical Sampling through Velocity Rescaling. *J. Chem. Phys.* **2007**, 126 (1), 014101. <https://doi.org/10.1063/1.2408420>.
- (72) Bernetti, M.; Bussi, G. Pressure Control Using Stochastic Cell Rescaling. *J. Chem. Phys.* **2020**, 153 (11), 114107. <https://doi.org/10.1063/5.0020514>.
- (73) Michaud-Agrawal, N.; Denning, E. J.; Woolf, T. B.; Beckstein, O. MDAAnalysis: A Toolkit for the Analysis of Molecular Dynamics Simulations. *J. Comput. Chem.* **2011**, 32 (10), 2319–2327. <https://doi.org/10.1002/jcc.21787>.
- (74) *MDAnalysis: A Python Package for the Rapid Analysis of Molecular Dynamics Simulations - SciPy Proceedings*. <https://proceedings.scipy.org/articles/Majora-629e541a-00e> (accessed 2024-09-03).
- (75) Merck | Netherlands | Life Science Products & Service Solutions. <https://www.sigmaaldrich.com/NL/en> (accessed 2024-09-06).

## Supplementary Information

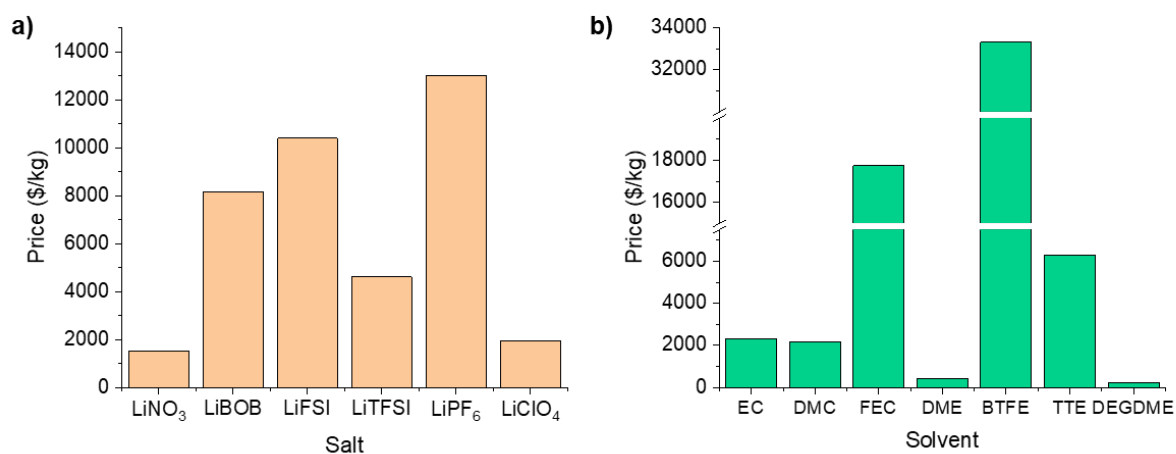


**Figure S1:** a) Prices of 'battery grade' (or 99.9% pure unless indicated so) Li salts as of 1 Sept. 2024. b) Prices of 'battery grade' (or 99.5% pure and higher unless indicated so) solvents as of 1 Sept. 2024. Source: SigmaAldrich<sup>75</sup>

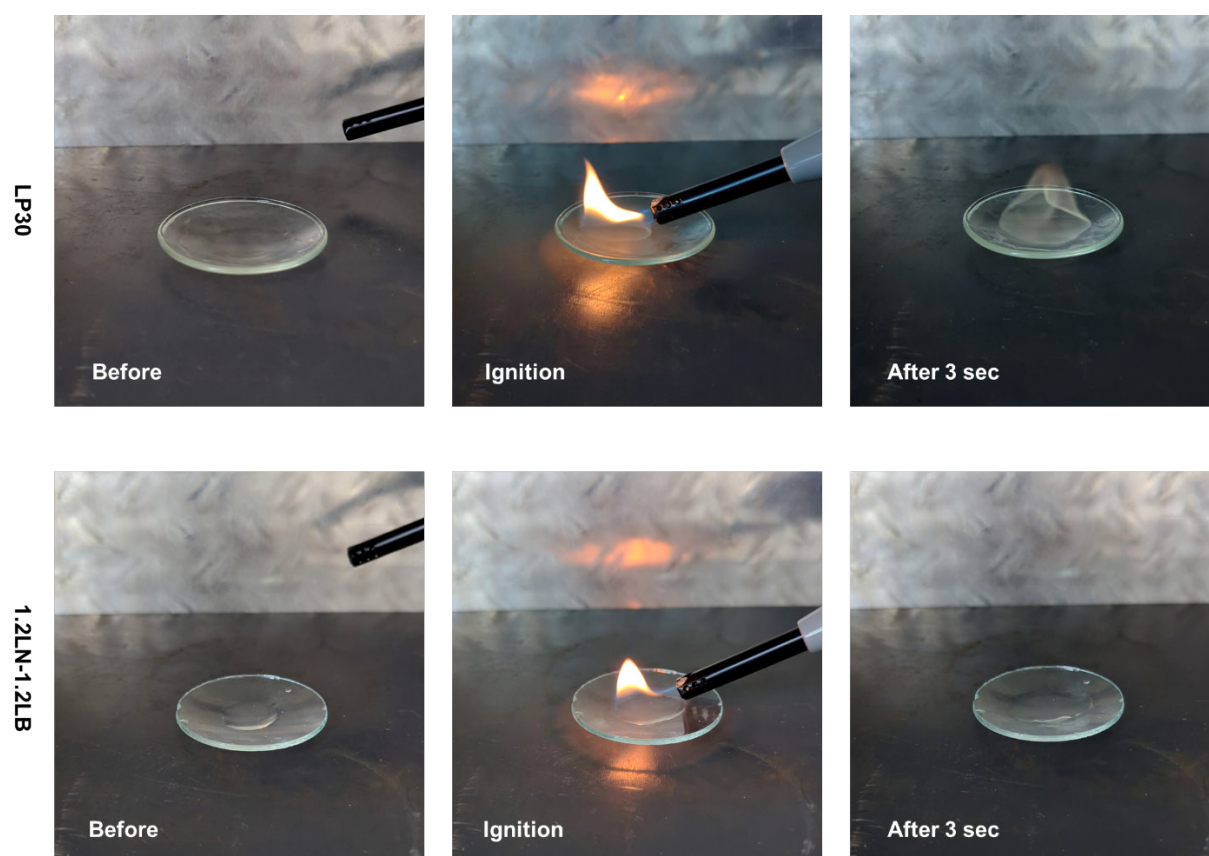
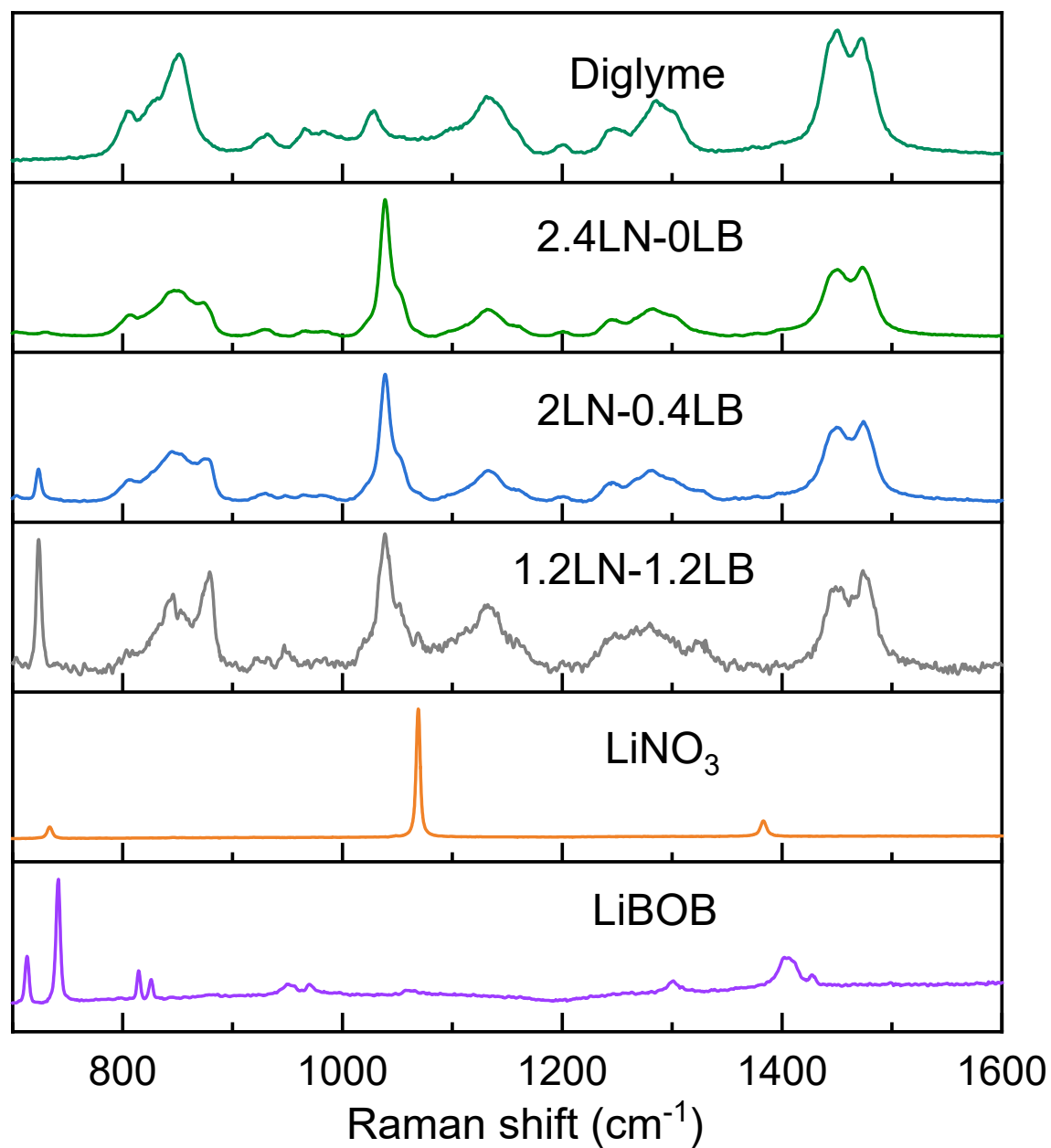


**Figure S2:** Snapshots of the Flammability test performed at 20 °C for LP30 and 1.2 LN-LB electrolytes



5

**Figure S3:** Raman spectra for electrolytes and salts/solvents

## 5. Rational design of safe, fluorine-free dual salt electrolytes for Lithium metal batteries

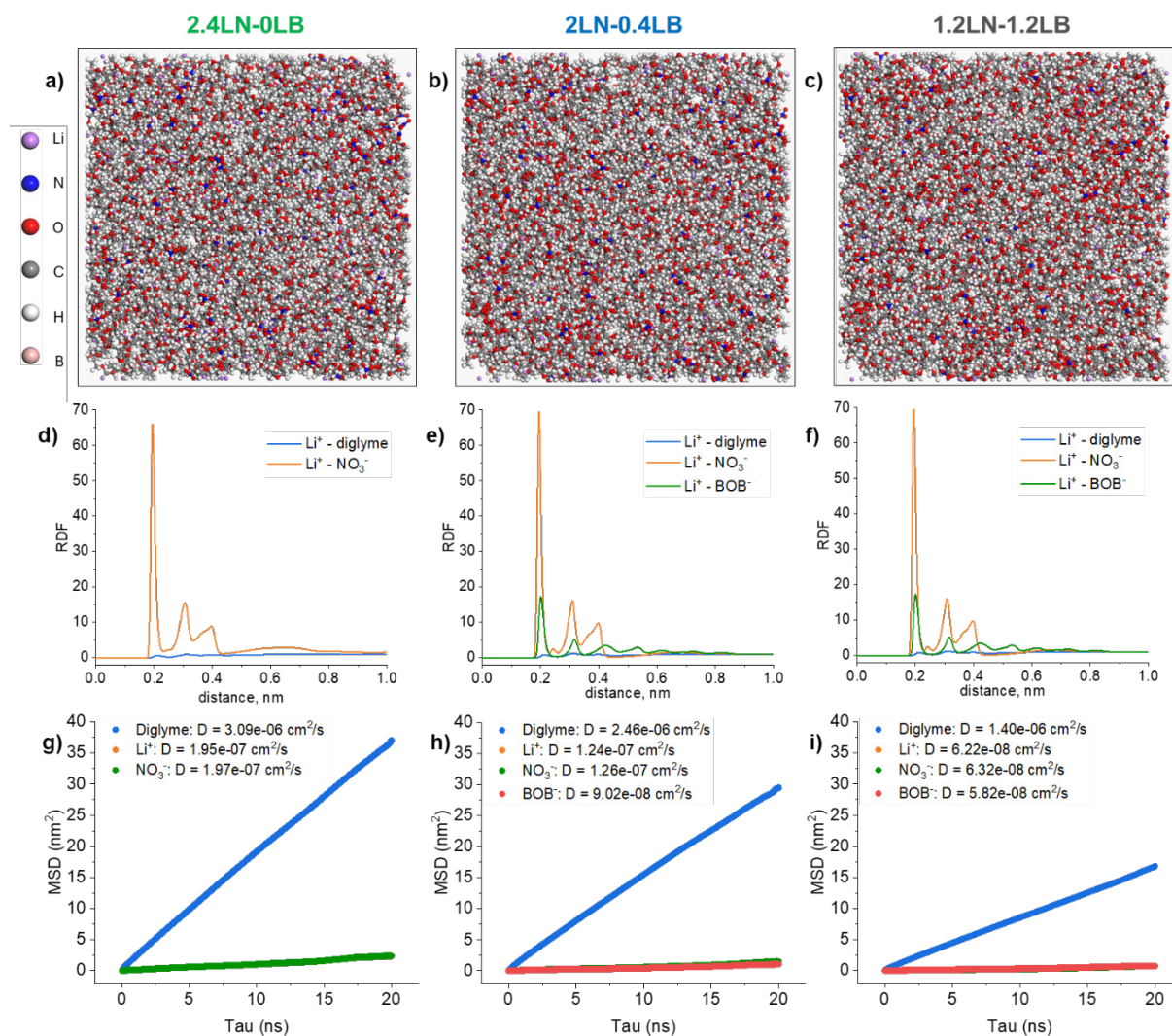


**Figure S4: Molecular Dynamics (MD) Simulation settings and results:** Top - Snapshots of the MD simulated boxes of a) 2.4LN-0LB b) 2LN-0.4LB and c) 1.2LN-1.2LB electrolytes. The color nomenclature for the spheres is shown on the right. Middle: Radial Distribution Function (RDF) w.r.t Li<sup>+</sup> for molecules and ions in d) 2.4LN-0LB e) 2LN-0.4LB and f) 1.2LN-1.2LB electrolytes. Bottom: Mean Square Displacement (MSD) values for molecules and ions in g) 2.4LN-0LB h) 2LN-0.4LB and i) 1.2LN-1.2LB electrolytes.

## 5. Rational design of safe, fluorine-free dual salt electrolytes for Lithium metal batteries

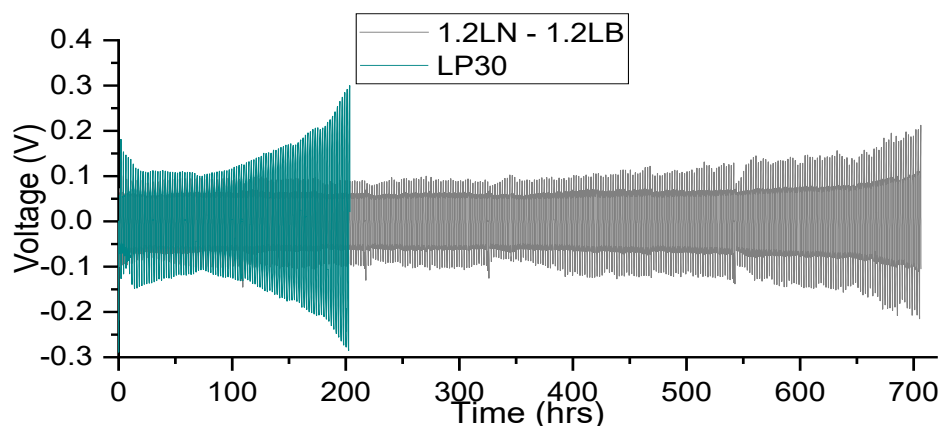


**Figure S5:** Voltage profiles of Li/Li cells at  $1 \text{ mA/cm}^2$  (capacity  $1 \text{ mAh/cm}^2$ ) after two formation cycles at  $0.1 \text{ mA/cm}^2$ , capacity  $4 \text{ mAh/cm}^2$  (not shown).

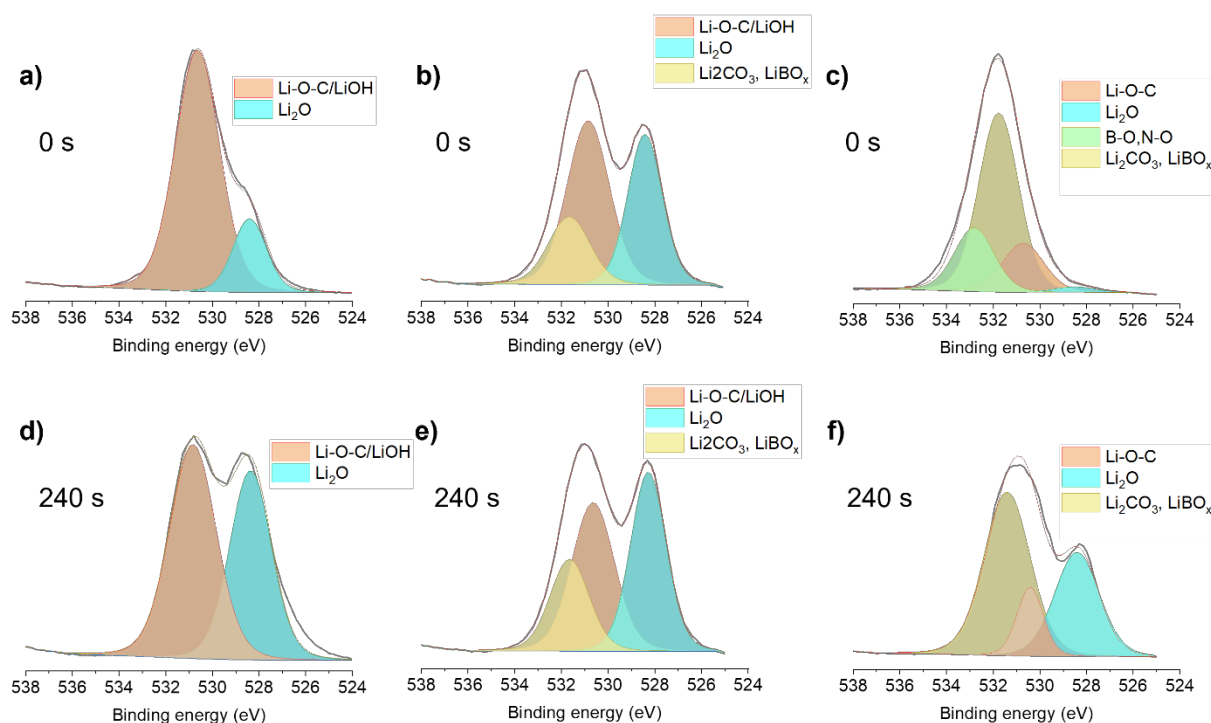


**Figure S6:** Li interphase O1s composition after 50 cycles in Li/Cu cells at  $1 \text{ mA/cm}^2$ ,  $1 \text{ mAh/cm}^2$ : Top - O1s XPS Spectra before depth profiling for a) 2.4LN-0LB b) 2LN-0.4LB and c) 1.2LN-1.2LB samples. Bottom: O1s XPS Spectra after 240s of depth profiling for d) 2.4LN-0LB e) 2LN-0.4LB and f) 1.2LN-1.2LB samples

## 5. Rational design of safe, fluorine-free dual salt electrolytes for Lithium metal batteries

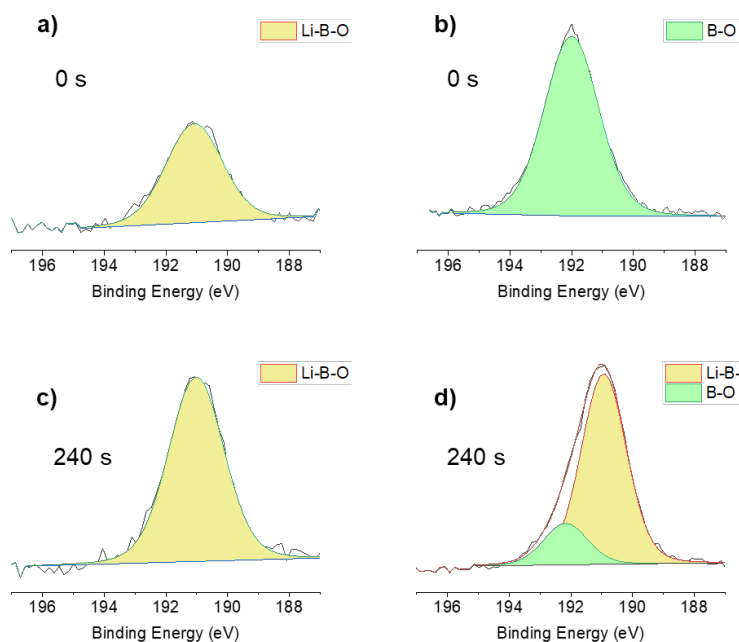


**Figure S7:** Li interphase B1s composition after 50 cycles at  $1 \text{ mA/cm}^2$ ,  $1 \text{ mAh/cm}^2$ , before (above) and after (below) depth profiling for a) 2LN-0.4LB and b) 1.2LN-1.2LB samples.

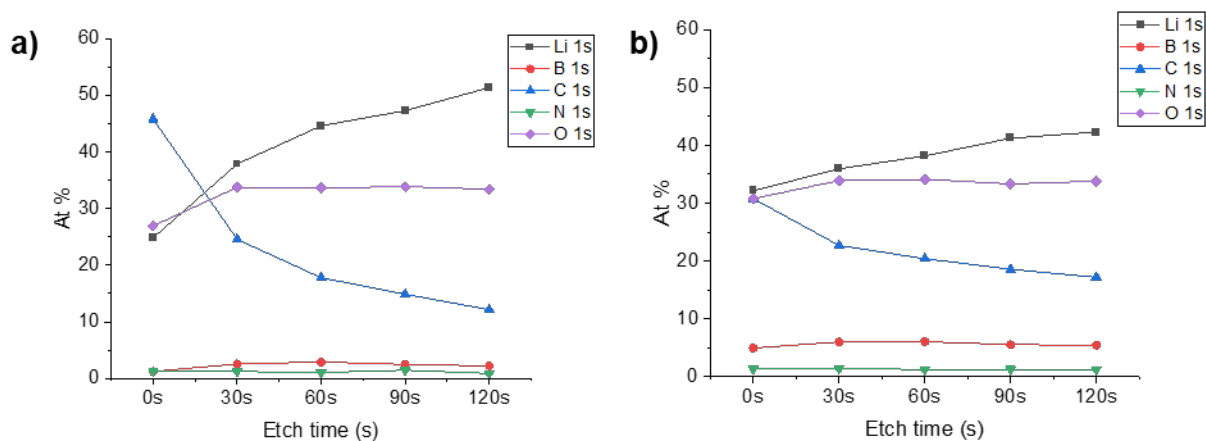


**Figure S8:** - XPS survey atomic percentage (with depth profiling) for g) 2.4LN-0LB h) 2LN-0.4LB sample after 150 cycles at  $1 \text{ mA/cm}^2$ ,  $1 \text{ mAh/cm}^2$  and i) 1.2LN-1.2LB samples after 250 cycles at  $1 \text{ mA/cm}^2$ ,  $1 \text{ mAh/cm}^2$

5. Rational design of safe, fluorine-free dual salt electrolytes for Lithium metal batteries

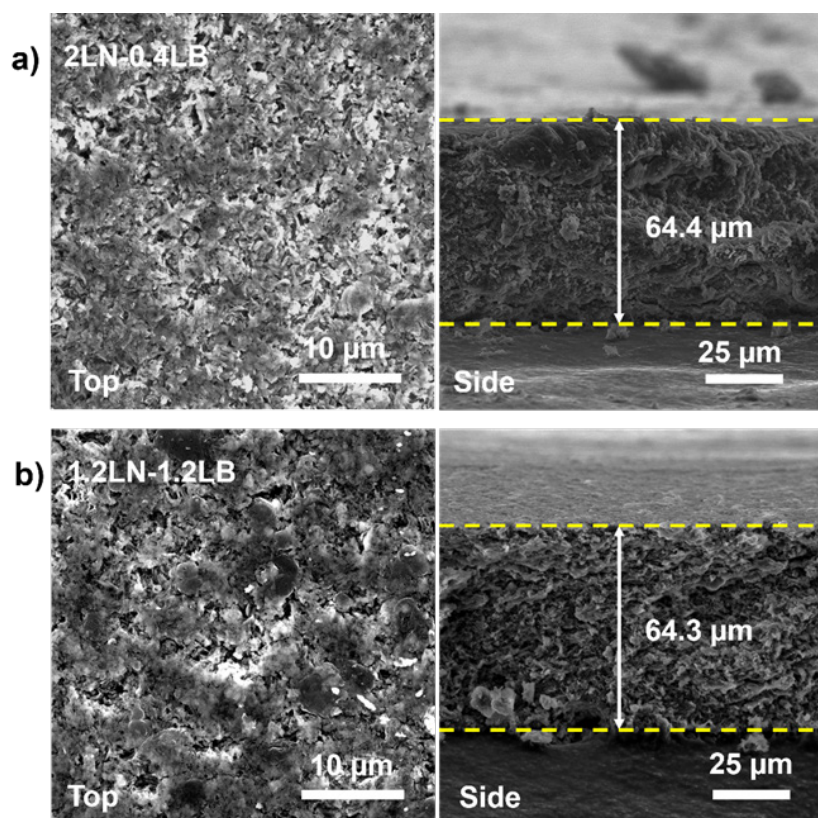


**Figure S9:** Top-view and cross-section SEM images of Li/SEI residues on Cu foils after 440 cycles at 0.5 mA/cm<sup>2</sup>, 1mAh/cm<sup>2</sup>

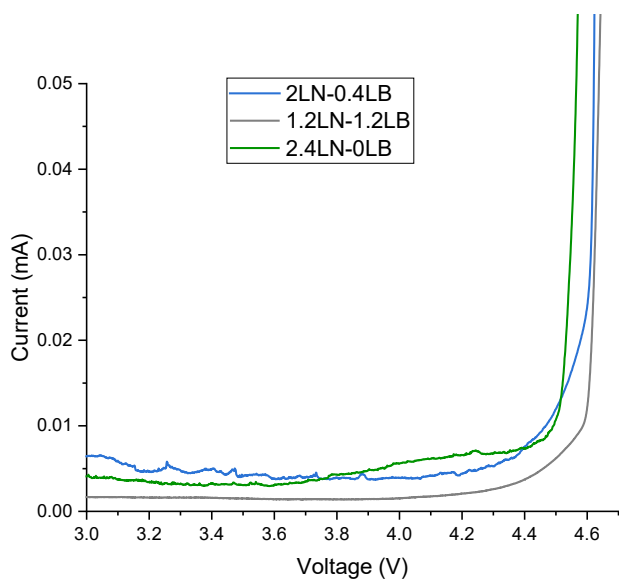


**Figure S10:** Linear Sweep Voltammetry (LSV) of F-free glyme electrolytes in Li/Stainless Steel cells at 25 °C. The scan rate was 0.1 mV/s and the voltage window was OCP- 5V

## Summary

Energy storage technologies are critical to the global energy transition, given the need to reduce carbon emissions and the ever-increasing demand for energy. The need for energy storage is particularly crucial in the automotive and electricity generation sectors, where a shift from fossil fuels to renewable sources is imperative. Lithium-ion batteries are central contributors to this transition, powering electric vehicles (EVs) and supporting renewable energy integration into electricity grids. Historically, lithium-ion batteries evolved from using Li metal as a negative electrode to safer alternatives like graphite, and positive electrode materials such as  $\text{LiNi}_{0.8}\text{Mn}_{0.1}\text{Co}_{0.1}\text{O}_2$  (NMC811) and  $\text{LiFePO}_4$  (LFP). However, despite these advancements, several challenges still need to be addressed.

First, increasing the energy density of lithium-ion batteries is a priority, particularly for EVs, where higher energy densities can extend the driving range and improve market adoption. Feasible solutions in this regard could be increasing the thickness of electrodes and switching to higher energy density materials such as Li metal. Second, safety remains a key concern, as current batteries use liquid electrolytes that are prone to thermal runaway, leading to fires or explosions. Solid-state electrolytes offer a safer alternative with higher thermal stability. However, they also present their own challenges at the electrode/electrolyte interfaces. Third, there is a growing emphasis on developing environmentally friendly batteries, as many of the materials and manufacturing processes for current lithium-ion batteries are not sustainable. Efforts are being made to eliminate fluorinated compounds and other toxic components from batteries, but this needs to be done without compromising performance. The optimization of the electrode-electrolyte interfaces in batteries holds the key to enabling batteries of the future. Optimizing Li morphology during plating/stripping, improving interfacial stability, and ensuring sufficient ion and electron percolation in cathode composites are key to improving battery capacity, lifetime, safety, and efficiency.

Increasing the electrode thickness is an often-considered strategy to achieve higher energy density Li-ion batteries since this can improve the ratio of active material over inactive supporting materials such as the current collectors and separators. However, for the same charging times, this would now result in higher current densities, and, therefore, also in higher electronic and ionic overpotentials. The use of conventional slurry-casting/drying procedures to manufacture thick electrodes can also result in mechanical failure of these electrodes induced by binder migration during prolonged solvent drying times. In **Chapter 2**, an Ethanol phase inversion (EPI) strategy was developed for making ultrathick, high-performance electrodes out of Ni-rich layered oxide materials. The EPI NMC811 electrodes significantly outperform conventionally slurry cast/dried electrodes with similar active mass loading ( $35 \text{ mg/cm}^2$ ) and porosity (30%) in Li/NMC811 half cells at 1C discharge. The binder structure induced by the nonsolvent improves the pore connectivity and results in lower tortuosity factors, as shown by electrochemical measurements and pseudo-2-dimensional modeling. The rapid solvent removal also reduces the binder migration during drying, enabling active

## Summary

mass loadings up to 60 mg/cm<sup>2</sup> without delamination or cracking. The EPI electrodes show a higher capacity and similar capacity retention as the conventional electrodes with long-term cycling, implying that the processing does not negatively impact the Ni-rich cathode active material. Moreover, the excellent compatibility of the phase inversion processes with the current roll-to-roll coating infrastructure makes this a technique with high industrial feasibility toward future batteries with both high energy and power densities.

Solid-state batteries (SSBs) based on Sulfide-based electrolytes such as Li<sub>6</sub>PS<sub>5</sub>Cl argyrodite are considered one of the top contenders for next-generation batteries with improved safety and energy density. However, Sulfide-based SSBs with Nickel-rich cathode materials exhibit several cathode interface-related challenges such as mechanical and chemical instability, resulting in particle cracking, contact loss, and electrolyte decomposition. In **Chapter 3**, polymerized ionic liquid coatings were employed at the cathode surface to overcome these challenges. Herein, the single-crystal LiNi<sub>0.82</sub>Mn<sub>0.07</sub>Co<sub>0.11</sub>O<sub>2</sub> (SC-NMC82) was coated with poly(diallyldimethylammonium) bis(trifluoromethanesulfonyl)imide (PDDATFSI) with and without LiTFSI salt (Li-PIL and PIL respectively). In both cases, a thin nanometer-scale coating was formed around most of the SC-NMC82 aggregates. The PIL-coated SC-NMC82 showed improved capacity retention in InLi/Li<sub>6</sub>PS<sub>5</sub>Cl/SC-NMC82 solid-state cells, and the Li-PIL coating additionally improved the cathode active mass utilization, with a capacity retention of 82.7% observed after 500 cycles at 0.2C charge and discharge rates and 20 °C. The polymer-coated samples showed minimal resistance increase at the cathode-electrolyte interface, compared to a severe resistance increase for uncoated NMC. X-ray Photoelectron Spectroscopy (XPS) post-cycling indicated that the polymer coatings effectively suppressed the formation of Li<sub>6</sub>PS<sub>5</sub>Cl oxidation products and electrochemically passivated the cathode-electrolyte interface. Furthermore, the cathode composites with polymer coatings exhibited minimal contact loss after electrochemical cycling. <sup>7</sup>Li 2-Dimensional exchange Nuclear Magnetic Resonance (NMR) provided evidence of Li ion transport across the Li<sub>6</sub>PS<sub>5</sub>Cl /Li-PIL interface at longer timescales, which agrees well with the performance improvements observed for the Li-PIL coated NMC82. Overall, the results showcase the effectiveness of lithiated polymers as multifunctional cathode coatings in sulfide-based SSBs.

Having a stable solid electrolyte interphase (SEI) and highly reversible Li plating/stripping are key to enabling Li metal as the anode. Chapters 4 and 5 deal with the optimization of lithium electrolyte salt concentration or molar ratio to achieve prolonged cycling in two promising electrolyte classes for lithium metal batteries (LMBs). In **Chapter 4**, the focus is on gel polymer electrolytes (GPEs), with Lithium bis(fluorosulfonyl)imide (LiFSI) electrolyte salt with several different concentrations in the ternary polymerized ionic liquid N-Propyl-N-methylpyrrolidinium Bis(fluorosulfonyl)imide (Pyr13FSI)/ Poly(diallyldimethylammonium Bis(fluorosulfonyl)imide)(PDADMAFSI) (60:40 wt%). Using a combination of ex-situ techniques, operando NMR and operando neutron depth profiling (NDP), the reasons underlying the nontrivial relationship of long-term cycling stability and coulombic efficiency (CE) with the salt concentration are studied. The increase in salt concentration from 1M to

## Summary

3M (in Pyr13FSI) increases the inorganic content in the SEI and the Li<sup>+</sup> conductivity, while operando NMR and NDP revealed a denser and more uniform Li deposition at 3M, correlating with higher electrochemically observed CEs. However, a further increase in LiFSI concentration to 4.5M does not result in significant changes to the SEI composition, whereas the number of nucleation sites and the areal coverage Li deposits decrease as observed with SEM. These factors, combined with the reduced mechanical strength of the PIL surface layer at the highest salt concentration, appear to result in increased SEI as well as increased dead lithium metal generation per cycle, as observed from operando and post-mortem solid-state NMR. Both these factors contribute to the lowering of the CE. The findings indicate that intermediate salt concentrations of 3M in GPEs result in the best overall performance, balancing Li interface stability and Li<sup>+</sup> conductivity/transference.

As previously mentioned, a move towards fluorine-free battery electrolytes is desirable given the safety and environmental concerns surrounding fluorinated materials. But this comes at a time when fluorination of electrolytes continues to be a widely used strategy to extend the lifetime of LMBs as this leads to relatively stable electrolyte salts and SEI components. **Chapter 5** focuses on the development of fluorine-free electrolytes with lithium nitrate (LiNO<sub>3</sub>) and Lithium bis(oxalato)borate (LiBOB) as the two Li salts, and Diglyme as the solvent. With LiNO<sub>3</sub> as the main salt, increasing the amount of LiBOB while keeping the overall salt concentration constant resulted in a drop in transport properties such as viscosity and Li self-diffusivity, owing to the steric effects imparted by LiBOB and a possible increase in ionic coordination shell or aggregation. However, the increase in ion dissociation (due to weakened Li<sup>+</sup> - NO<sub>3</sub><sup>-</sup> interactions) and heterogeneity of solvation structures, as indicated by molecular dynamics simulations, NMR, and Raman spectroscopy, result in an increase in ionic conductivity with increasing LiBOB content. The inclusion of LiBOB also significantly improved the cycling stability in Li/Li symmetric cells, with the electrolyte with equimolar LiNO<sub>3</sub>:LiBOB concentration showing the most stable cycling in Li/Li symmetric coin cells. The Li interphase composition, studied using XPS and solid-state NMR, reveals the role played by LiBOB-derived SEI compounds such as Li<sub>2</sub>CO<sub>3</sub> and Li-borates in chemomechanically stabilizing the Li<sub>2</sub>O-rich inner SEI that is formed upon LiNO<sub>3</sub> decomposition. The optimized dual salt F-free electrolyte also shows good long-term capacity retention (77% after 100 cycles) in Li/dual salt electrolyte/LFP cells with a limited Li metal reservoir (100 μm) and a commercial LFP cathode cycled at 25 °C, with a high average CE (99.38%). These findings represent a significant advancement in the development of safe, fluorine-free electrolytes for LMBs capable of operating at room temperature. Optimizing the SEI composition in terms of Li<sup>+</sup> conduction and chemomechanical stability to attain the targeted electrochemical performance plays a critical role in these investigations.

# Samenvatting

Energy opslag technologieën zijn essentieel voor de wereldwijde energietransitie, door de noodzaak om koolstof emissie te reduceren en de altijd groeiende vraag naar energie. De noodzaak voor energie opslag is vooral cruciaal in de transport en elektriciteit productie sectoren, waar een migratie vanuit fossiele naar hernieuwbare bronnen dient te gebeuren. Lithium-ion batterijen zijn centraal in deze transitie, als accu in elektrische voertuigen (EV) en om support te geven bij hernieuwbare energie integratie in elektrische grids. Historisch zijn lithium-ion batterijen geëvolueerd vanuit het gebruik van lithium metaal aan de negatieve electrode, naar veiligere alternatieven zoals grafiet, en positieve electrode materialen zoals  $\text{LiNi}_{0.8}\text{Mn}_{0.1}\text{Co}_{0.1}\text{O}_2$  (NMC811) en  $\text{LiFePO}_4$  (LFP). Ondanks deze progressie zijn er nog verschillende uitdagingen die geaddresserd moeten worden.

Allereerst is het verhogen van de energiedichtheid van lithium-ion batterijen een prioriteit. Specifiek voor EV waarin een hogere energie dichtheid het bereik van auto's kan verhogen, wat beter aansluit op de huidige markt. Mogelijke oplossingen kunnen het verhogen van de electrode dikte zijn of het veranderen van de actieve materialen naar materialen met hogere energie dichtheden, zoals lithium metaal. Als tweede blijft veiligheid een zorg, aangezien huidige batterijen vloeibare electrolyten gebruiken die vatbaar zijn voor thermal runaways die leiden tot brand of explosies. Vaste stof electrolyten zijn een veiliger alternatief met een hogere thermische stabiliteit. Echter, ze hebben hun eigen uitdagingen bij het contact oppervlak tussen electrode en electrolyt. Als derde is er een groeiende nadruk op het ontwikkelen van milieuvriendelijke batterijen, omdat veel van de materialen en procesvoering voor het vervaardigen van lithium-ion batterijen niet duurzaam zijn. Er wordt getracht om gefluoreerde materialen en andere toxische elementen uit batterijen te verbannen, maar dit kan niet worden gedaan zonder een compromis te vinden tussen deze wens en de batterij prestatie. Het optimaliseren van de electrode/electrolyt contactoppervlak in batterijen is de sleutel om de volgende generatie batterijen mogelijk te maken. Het optimaliseren van lithium structuurvorming tijdens het platen/strippen, het verbeteren van de oppervlaktestabiliteit en het verzorgen van voldoende ion- en elektronenpercolatie in cathode composieten zijn de sleutel voor het verbeteren van batterij capaciteit, levensduur, veiligheid en efficiëntie.

Het dikker maken van de electrode is een vaak overwogen strategie om hogere dichtheid lithium-ion batterijen te verkrijgen, omdat het de balans tussen actieve materialen en inactieve support materialen zoals current collectors en separators kan verbeteren. Echter, voor dezelfde laadtijd moet hiervoor een hogere stroom worden gebruikt en, hierom, ook een hogere elektronen en ionen overpotentiaal. Het gebruik van conventionele slurrydepositie- en droogprocedures om dikke electrodes te vervaardigen leidt ook tot mechanische problemen omdat het bindmiddel migreert tijdens verlengde droogtijden voor het verwijderen van het solvent. In **Hoofdstuk 2** is een ethanol phase inversie (EPI) strategie

ontwikkeld om extreem dikke, goed presterende electrodes te vervaardigen die bestaan uit Ni-rijke gelaagde oxides. De EPI NMC811 electrodes zijn significant beter dan conventionele electrodes met vergelijkbare belading ( $35 \text{ mg/cm}^2$ ) en porositeit (30%) in Li/NMC811 half cellen tijdens 1C laadtijd. De structuur van de binder is verbeterd door een nonsolvent, wat leidt tot een verbeterde connectiviteit en resulteert in lagere tortuositeit factoren zoals wordt aangetoond door electrochemische metingen en pseudo-2 dimensionale modellering. De snelle solvent verwijdering reduceert ook de mate van bindmiddel migratie tijdens het drogen, wat belading tot  $60 \text{ mg/cm}^2$  toelaat zonder dat de electrode delamineert of breekt. De EPI electrodes vertonen een hogere capaciteit en vergelijkbare capaciteitsbehoud in vergelijking met conventionele electrodes tijdens lange termijn cycling testen, wat impliceert dat de toegevoegde processtap geen negatieve impact heeft op het Ni-rijke cathode materiaal. Het phase inversie proces zelf past voortreffelijk in de huidige roll-to-roll procesvoering voor het vervaardigen van electrodes, wat het een techniek maakt met een hoge geschiktheid in de huidige industrie, die naar de volgende generatie batterijen met hoge energie en stroomdichtheid migreren.

Vaste stof batterijen (VSB) gebaseerd op sulfide gebaseerde electrolyten als  $\text{Li}_6\text{PS}_5\text{Cl}$  argyrodite worden als top kandidaten geëvalueerd voor de volgende generatie batterijen met verbeterde veiligheid en energiedichtheid. Echter, sulfide gebaseerde VSB met Nickel-rijke cathode materialen hebben specifieke oppervlakte gerelateerde uitdagingen zoals mechanische en chemische instabiliteit, wat resulteert in fractionering van de deeltjes, contactverlies en electrolyt ontleding. In **Hoofdstuk 3** worden gepolymeriseerde ionische vloeistofcoatings gebruikt op het cathode oppervlak om deze uitdagingen te adresseren. Hier is monokristallijne  $\text{LiNi}_{0.82}\text{Mn}_{0.07}\text{Co}_{0.11}\text{O}_2$  (SC-NMC82) gecoat met poly(diallyldimethylammonium) bis(trifluoro-methanesulfonyl)imide (PDDATFSI) met en zonder LiTFSI zout (Li-PIL en PIL respectievelijk). In beide gevallen werd een nanometer-schaal dikke coating gevormd over de meeste SC-NMC82 aggregaten. De PIL-gecoated SC-NMC82 liet een verbeterde capaciteitsretentie zien in InLi/Li<sub>6</sub>PS<sub>5</sub>Cl/SC-NMC82 vaste stof cellen, en de Li-PIL coating gaf initieel een verbeterde utilisatie van actief materiaal, met een capaciteit retentie van 82.7% geobserveerd na 500 cycli bij 0.2C laad- en ontlaadsnelheid en 20 °C. De polymeer gecoate samples lieten een minimale toename in weerstand zien bij de cathode/electrolyt oppervlak in vergelijking met ongecoate NMC. X-ray photoelectron spectroscopy (XPS) na cyclen liet zien dat de polymeer coatings effectief de formering van Li<sub>6</sub>PS<sub>5</sub>Cl oxidatieproducten tegenhield en de cathode/electrolyte oppervlakte passiverde. Ook lieten de cathode composieten met polymeercoating minimale contactverlies zien na electrochemisch cyclen. <sup>7</sup>Li 2-Dimensional exchange Nuclear Magnetic Resonance (NMR) liet zien dat Li ion transport over het Li<sub>6</sub>PS<sub>5</sub>Cl /Li-PIL contactoppervlak bij langere tijdschalen gebeurde, wat in overeenkomst is met de verbeterde prestatie van de Li-PIL gecoate NMC82. Deze resultaten laten de effectiviteit zien van gelithieerde polymeren als multifunctionele cathode coatings in sulfide gebaseerde VSB.

Het verkrijgen van een stabiele 'solid electrolyte interphase' (SEI) en reversibele lithium plating/stripping zijn essentieel om lithium metaal anodes mogelijk te maken. Hoofdstuk 4 en 5 adresseren het optimaliseren van lithium zout concentraties (of molaire ratio) om de levensduur te verlengen van twee veelbelovende electrolyt klassen voor lithium metaal batterijen (LMB). In **Hoofdstuk 4** de focus is een gel polymeer electrolyte (GPE) met Lithium bis(fluorosulfonyl)imide (LiFSI) electrolyt zout met verschillende concentraties gepolymeriseerde ionische vloeistof N-Propyl-N-methylpyrrolidinium Bis(fluorosulfonyl)imide (Pyr13FSI)/ Poly(diallyldimethylammonium Bis(fluorosulfonyl)imide)(PDADMAFSI) (60:40 wt%). Een combinatie van ex-situ technieken, operando NMR en operando neutronen diepte profilering (NDP) wordt gebruikt om de niet-triviale relatie tussen lange termijn stabiliteit, coulombic efficiency (CE) en de zoutconcentratie te bestuderen. Het verhogen van de zoutconcentratie van 1M naar 3M (in Pyr13FSI) verhoogt de inorganische fractie in het SEI en de  $\text{Li}^+$  conductiviteit, terwijl operando NMR en NDP lieten zien dat er een dichter en meer homogene lithium depositie plaatsvindt bij 3M wat gecorreleerd wordt met de hogere geobserveerde electrochemische CE. Echter, een hogere LiFSI concentratie naar 4.5M laat geen significante verandering zien in SEI compositie, terwijl SEM laat zien dat het aantal nucleatie locaties en homogeniteit van lithium depositie is verlaagd. Deze factoren, gecombineerd met een verlaagde mechanische sterkte van de PIL oppervlaktelaag bij de hoogste zoutconcentratie lijken het resultaat van een verhoogde SEI en een verhoogde hoeveelheid inactief lithium vorming per (ont)laadcyclus, wat wordt geobserveerd met operando en post-mortem solid-state NMR. Beide factoren leiden tot een verlaagde CE. Deze bevinding geeft aan dat er een tussenliggende zoutconcentratie is van 3M in GPE die resulteren in de beste prestatie, balancerend tussen oppervlakttestabiliteit en  $\text{Li}^+$  conductiviteit en transference.

Zoals eerder benoemd is het migreren naar fluorvrije batterij electrolyten wenselijk aangezien de zorgen rondom veiligheid en milieu in combinatie met gefluorineerde materialen. Dit komt echter gedurende een periode waarin gefluorineerde electrolyten een veelgebruikte strategie is om de levensduur van LMB te verlengen, gezien de relatieve stabiele electrolyt zouten en SEI componenten die van deze klasse beschikbaar zijn. **Hoofdstuk 5** focust op het ontwikkelen van fluorvrije electrolyten met lithium nitraat ( $\text{LiNO}_3$ ) en Lithium bis(oxalato)borate (LiBOB) als twee lithium zouten, met diglyme als oplosmiddel. Met het verhogen van de LiBOB in een oplossing met  $\text{LiNO}_3$  als voornaamste zout, met het behoud van dezelfde totale zoutconcentratie, werd een verlaging van de transporteigenschappen als viscositeit en Lithium zelf-diffusiviteit geobserveerd. Dit wordt veroorzaakt door sterische effecten die LiBOB induceert en mogelijk ook door een verhoging van de ionische coordinatie schil of aggregatie toestand. Echter, de verhoging van ion dissociatie (door verzwakte  $\text{Li}^+ - \text{NO}_3^-$  interacties) en heterogeniteit door solvatiestructuren, zoals wordt voorspeld door moleculaire dynamica simulaties, NMR en Raman spectroscopie, resulteert in een verhoogde ionische geleidbaarheid bij verhoogde LiBOB concentratie. De toevoeging van LiBOB verbeterd ook de stabiliteit tijdens het (ont)laden, waarbij een equimolaire concentratie van  $\text{LiNO}_3:\text{LiBOB}$  de hoogste stabiliteit laat zien in Li/Li symmetrische knooppellen. De compositie

## Samenvatting

van het lithium oppervlakte, bestudeerd met XPS en solid-state NMR laat de rol zien van LiBOB-afgeleide componenten als  $\text{Li}_2\text{CO}_3$  en Li-boraat in chemomechanische stabilisatie en  $\text{Li}_2\text{O}$  rijke SEI die gevormd is vanuit  $\text{LiNO}_3$  decompositie. De geoptimaliseerde twee-zouten electrolyte die fluorvrij is, laat met een gelimiteerde lithium metaal reservoir (100  $\mu\text{m}$ ) en een commerciële LFP cathode bij 25 °C een hoge CE (99.38%) zien. Deze bevinding geeft een significante verbetering voor het verbeteren van veilige, fluorvrije electrolyten voor LMB die in staat zijn om bij kamertemperatuur te werken. Het optimaliseren van SEI compositie voor  $\text{Li}^+$  conductiviteit en chemomechanische stabiliteit, om de gewenste electrochemische prestatie te verkrijgen speelt een essentieel rol in dit onderzoek.

# Acknowledgements

When I started my journey as a PhD researcher at TU Delft in February 2020, I was determined to carry forward the insights gained from my MEP on Li (and Zn) metal battery interfaces into the SOLiDIFY project; however, I was absolutely not prepared for what was to follow shortly after. The last 5 years have been a roller-coaster ride, thanks in no small part to the complications brought upon by the COVID-19 pandemic. Furthermore, with Li-ion battery technology being one of the most heavily researched topics globally, making meaningful contributions to this crucial topic and ‘moving the needle’ seemed a Herculean challenge at times. Nevertheless, here I am, looking back at the most challenging phase of my life/career so far with a sense of fulfilment and gratitude. I have several people to thank for, without whom this journey would have been impossible.

My main supervisor, Fokko, thank you for the opportunity to pursue this PhD under your supervision as part of the SOLiDIFY project. The scientific discussions, guidance and feedback on various topics provided through both weekly and impromptu meetings whenever necessary, were instrumental in shaping this thesis. I will always be grateful to the freedom you provided and the faith you showed in me to pursue my academic interests for some of the PhD topics. Thanks again for the additional assistance you offered to ensure my PhD carried on smoothly despite the several setbacks (COVID lockdown, health and SOLiDIFY related) that I had to go through.

My co-supervisor, Marnix, thank you for allowing us to carry out a major part of the PhD work in the SEE group/labs. I believe working closely with you and other SEE members has significantly improved the quality and impact of my PhD work. I will always be grateful to timely feedback and insights you provided me on my different PhD topics, and for other forms of support provided throughout my PhD. I am excited to continue my journey as a Postdoctoral Researcher under your guidance, and look forward to the scientific mysteries we can unravel in the coming years.

Special thanks also go to my Master thesis supervisors (also from SEE) Erik and Shiv. The guidance, support and encouragement I received during my MEP played a major role in my decision to continue with a PhD on Li-ion batteries and at TU Delft. Swapna, thank you for teaching me solid state NMR, and for being available whenever necessary to help me out with scientific discussions and feedback on my PhD chapters/manuscripts despite your busy schedule. I am also grateful to the career advice and the moral support you have provided me over the years. I am also indebted to Bernard, Tom, Hans, Andreas, Gabriele, Ruud (van Ommen), Stephen (Picken) and Andrea from ChemE, and Pedro, Xuehang, Lars and Jouke from RST, for the scientific feedback/advice and other forms of help I have received from you during my PhD.

## Acknowledgements

Next, I would like to express my deepest gratitude to Frans, whose constant guidance and support with designing cells/setup, setting up experiments, overseeing purchase orders and whatnot have been integral to the completion of this thesis. You are truly one of a kind with the all-round support you provide me and the rest of the SEE group on a regular basis. I would also like to sincerely thank Herman and Joost, for having played a similar role from the MECS side, and for also keeping the daily coffee-breaks and the weekly borrels engaging. Special thanks to the other (present and former) technicians from SEE: Katarina, Nirmal, Dan, Esther, Baukje and Michel for the for countless occasions you have helped me out with various lab-related issues. Bart, thank you for teaching me XPS and for the several interesting conversations. Stephen, thank you for all your help with liquid NMR and for the fun chats. Furthermore, I would like to thank the following for their help with various techniques/equipment: Duco and Astrid for SEM, Frans (Tichelaar) and MengYue for TEM, Robert, Xiaohui and Kees for XRD, Aleksandra for DSC/Rheometry, Dave and Chantal (from DASML) for the mechanical characterization, Suriya (P&E) for the spray dryer and Arjan (from MicroLab) for the porosimetry. My big thanks to the secretaries Roos (MECS) and Martine (SEE) for their continuous assistance with several administrative tasks/challenges during my PhD, particularly over the last year. Also, thanks to Ilse, Nicole and Adinda for their assistance during this period.

Besides this, I have several fellow PhD-ers, PostDocs and students to thank for their contributions in making this PhD a fruitful and a memorable one. Mark, we started our PhDs on the 'SOLIDIFY' project about 2 months apart and just as the pandemic was beginning to take hold; we have since faced multiple challenges along the road, but your presence as a reliable colleague and a friend made a huge difference in navigating them. Apart from having collaborated scientifically over several topics, our common interests beyond science also made for some interesting discussions. I have always admired your work ethic and the ability to balance work and personal life, the latter being quite important but equally challenging to maintain during a PhD. Thanks again for being a great friend/colleague over the past years, and I wish you and your family a great future ahead! Ajay, your insights to sulfide solid state electrolytes helped me significantly improve my understanding of the topic and venture into it with confidence. Also, your inputs on scientific publishing, academia in Europe/India and a variety of other topics have also helped me gain a better perspective on them. Apart from your sharp scientific acumen, I was also amazed by your innate ability to seamlessly network with several researchers at conferences we attended together. Thank you for everything, and I hope our paths cross again. Pier, my neighbour both at work and home, thank you for being someone I could always call upon for help, sometimes on very short notice. The physics-driven insights that you bring forth to any given discussion, coupled with your expertise in modelling battery materials across multiple time/length scales are truly remarkable. Meera, your critical analysis of various topics related to polymers/energy storage and conversations we've had about academia/life in general have been of great help to me, thank you. Hanan, I have always been a fan of your meticulous approach to scientific research and brilliance in terms of scientific communication. Thanks for all the help and for making the lunchtime conversations

## Acknowledgements

so lively. Chaofan, I find your optimism, work ethic and curiosity for science truly admirable. Thanks for the delicious snacks and the nice chats on a wide range of topics. Hao, your calm, systematic approach to research is exemplary, thanks for being a helpful officemate. Anastasiia, thank you so much for your help with the MD simulations. Zhu and Jef, thank you guys for your valuable inputs into the solid-state/NMC manuscript. Shengnan, thanks for being a great colleague, willing to help out with the smallest of queries. Alex, thanks for arranging my first visit to the SEE group as a Master student, which led to everything thereafter. Biffo, thanks again for the engaging conversations on NMR and a range of other topics. Remco, thanks for helping me out with several technical queries ever since my MEP days, and for lending me your office spot. Katarina, thanks a lot for organizing the Dutch speaking sessions close to my exams, I think we should organize these more often. Xavier, Victor and Peter, thanks for organizing the amazing group outings/game nights and hosting us at your place on different occasions. Besides, I would also thank the other RST colleagues from past and present: Eveline, Tammo, Viola, Ming, Chao, Zhaolong, Peter-Paul, Tomas, Angie, Martijn, Walter, Qidi, Chenglong, Mark K., Wenxuan, Luca, Lucas, MengFu, Albert, Rui, Tian, Rijk, Vignesh, Ziqing, Ilse, Kaouther, Zamran and others.

Coming to the MECSicans; Davide, thanks for making me a part of the synchrotron XPS session at ALBA, this was a great learning experience for me. Also, thanks for the FIB-SEM measurements. Boaz, thanks for being a very reliable collaborator, and I always enjoyed the discussions we had on Nitrogen reduction, Li metal batteries and other topics which helped me expand my horizons on these. Audrey, thank you for teaching us the phase inversion method, and showing us around Toulouse during our visit. Bernhard, Sid, Santosh and Vineesh, thanks for all the insightful discussions on electrochemistry and academia, and for being of help with various matters. Besides these, I would also like to thank the other colleagues from the MECS group who I have interacted with over the years: Robin, Martin, Dylan, Peter, Hugo, Erdem, Giorgio, Diana, Kailun, Marijn, Aaron, Maryam, Anirudh, Sanjana, Mark S, Jesse, Jasper, Henri, Nikita, Julia, Gerard, Elena and others.

This thesis would be incomplete without the dedicated hard work of students who I have had the honor and pleasure of supervising. Jelle, thank you for being the driving force behind the solid-state electrolyte/NMC work, your contributions have helped us explore the topic in great detail. My thanks also goes to Marilène, Nimra and Samar, whose works helped us better understand the ion transport properties in Ni-rich layered oxide electrodes and their dependence on various parameters. I would also like to thank our collaborators from the SOLiDIFY project: Corsin, Gerrit and Qing from EMPA, Alix and Sebastien from Solvionic, Felix and Andreas from Fraunhofer ISC, Sebastien and Matteo from Powall, Daniele, Ishamol, Mohammed, Amelia, Hans, Veroni, Philippe and others from Imec, and other consortium members. Being part of this project constantly served as a reminder of the bigger picture when it comes to battery research, and I am grateful for the things we have learnt and achieved together.

## Acknowledgements

I would also to thank my friends from the SET Masters who have greatly helped me in this transition from Masters to PhD and also thereafter: Yashwanth, Ashwin, Asvin, Sachin, Aditya, Syed, Sameep, Arya and many others. Special thanks also to my friends from Bachelors, Mervyn and Praveen; it was nice meeting you guys in person after a long time. I am also grateful to my extended family members back in India for cheering me on in my ventures from afar. Last but not the least, I would like to thank my parents for the unconditional love, support and advice you have offered me over these years. None of this would have been possible without you, and I will forever be thankful.

# List of Publications

## Related to this Thesis:

4. **Karant, P.**; Weijers, M.; Ombrini, P.; Homann, G.; Ganapathy, S.; Battaglia, C.; Wagemaker, M.; Mulder, F. M. **Understanding the effect of salt concentration on the Li metal interface in gel polymer electrolytes**, *to be submitted*

3. **Karant, P.**; Weijers, M.; Lavrinenko, A.; Izelaar, B.; Kortlever, R.; Ganapathy, S.; Wagemaker, M.; Mulder, F. M. **Designing safe, fluorine-free electrolytes for Lithium metal batteries**, *submitted*

2. **Karant, P.**; Prins, J. H.; Gautam, A.; Cheng, Z.; Canals-Riclot, J.; Ombrini, P.; Ganapathy, S.; Ladam, A.; Fantini, S.; Wagemaker, M.; Mulder, F. M. **Multifunctional ion-conductive polymer coatings for high-performance sulfide solid-state batteries with Ni-rich cathodes**, *Journal of Materials Chemistry A*, *under review*

1. **Karant, P.**; Weijers, M.; Ombrini, P.; Ripepi, D.; Ooms, F.; Mulder, F. M. **A Phase Inversion Strategy for Low-Tortuosity and Ultrahigh-Mass-Loading Nickel-Rich Layered Oxide Electrodes**. *Cell Rep. Phys. Sci.* **2024**, 5 (6), 101972.

## Other Publications

13. Ombrini, P.; Pathak, S.; Ntagkras, D.; Pal, S. K.; **Karant, P.**; Wagemaker, M.; Bazant, M. Z.; Vasileiadis, A. Modeling Single-Crystal LFP Electrodes as a Network of Particles, *to be submitted*

12. Mohankumar, M.; **Karant, P.**; Zhang, S.; Cheng, Z.; Ooms, F.; Ganapathy, S.; Wagemaker, M. Demystifying the complex Li ion transport pathways in plastic crystal embedded polymer electrolytes: Insights from NMR spectroscopy. *to be submitted*

11. Izelaar, B.; **Karant, P.**; Toghraei, A.; Girichandran, N.; Weijers, M.; Hendrikx, R. W. A.; Mulder, F. M.; Kortlever, R. The Effect of Potent/al on the Li-mediated NRR Performance, *submitted*

10. Weijers, M.; **Karant, P.**; Borninkhof, J.; Mulder, F. M. Fluorine-free Lithium Ion Batteries: A Working Alternative. *submitted*

9. Weijers, M.; **Karant, P.**; Homann, G.; Izelaar, B.; Kondakova, A.; Ganapathy, S.; Kortlever, R.; Battaglia, C.; Mulder, F. M. Trade-off between Lithium Diffusivity and Transference in Solid Ternary Polymer Ionic Liquid Electrolytes. *Solid State Ion.* **2025**, 424, 116854.

8. Homann, G.; Wang, Q.; Liu, S.; Devinenti, A.; **Karant, P.**; Weijers, M.; Mulder, F. M.; Piesins, M.; Gouveia, T.; Ladam, A.; Fantini, S.; Battaglia, C. A Quasi-Solid-State Polymer Lithium–Metal Battery with Minimal Excess Lithium, Ultrathin Separator, and High-Mass Loading NMC811 Cathode. *ACS Appl. Energy Mater.* **2024**, 7 (21), 10037–10043.

## List of Publications

7. Park, J.; Dutta, S.; Sun, H.; Jo, J.; **Karanth, P.**; Weber, D.; Tavabi, A. H.; Durmus, Y. E.; Dzieciol, K.; Jodat, E.; Karl, A.; Kungl, H.; Pivak, Y.; Garza, H. H. P.; George, C.; Mayer, J.; Dunin-Borkowski, R. E.; Basak, S.; Eichel, R.-A. Toward Quantitative Electrodeposition via In Situ Liquid Phase Transmission Electron Microscopy: Studying Electroplated Zinc Using Basic Image Processing and 4D STEM. *Small Methods* **2024**, *8* (12), 2400081.

6. Weijers, M.; **Karanth, P.**; Ganapathy, S.; Mulder, F. M. Elucidation of Enhanced Lithium Conductivity in Nanoporous Ionogel Using Solid State NMR. *Adv. Mater. Interfaces* **2023**, *10* (2), 2201646.

5. Ripepi, D.; Izelaar, B.; van Noordenne, D. D.; Jungbacker, P.; Kolen, M.; **Karanth, P.**; Cruz, D.; Zeller, P.; Pérez-Dieste, V.; Villar-Garcia, I. J.; Smith, W. A.; Mulder, F. M. In Situ Study of Hydrogen Permeable Electrodes for Electrolytic Ammonia Synthesis Using Near Ambient Pressure XPS. *ACS Catal.* **2022**, *12* (21), 13781–13791.



# Curriculum Vitae

Pranav Karanth was born in Mangalore, India on 20 June 1993. He obtained his B.Tech in Chemical Engineering from National Institute of Technology Karnataka, Surathkal, India, in 2015. Shortly after, he joined Reliance Industries Limited, India as a Graduate Engineer Trainee (GET), where he worked at the Polypropylene Copolymer (PPCP) production unit in Vadodara. On completion of the GET period, he worked as Operations Manager at PPCP (Vadodara) and Fluidized Catalytic Cracker (Jamnagar) units. In August 2017, he moved to the Netherlands to pursue his Masters.

In 2019, he obtained his M. Sc. degree (cum laude) in Sustainable Energy Technology from Delft University of Technology. For his MSc thesis project, he worked in the Storage of Electrochemical Energy (SEE) group under Dr. Erik Kelder, and studied the microstructural evolution of zinc and lithium metal anodes in batteries with operando and ex-situ microscopy. In February 2020, he joined the Materials for Energy Storage and Conversion (MECS) group at the Department of Chemical Engineering, Delft University of Technology, as a PhD candidate under the supervision of Prof. Fokko Mulder (MECS) and Prof. Marnix Wagemaker (SEE). His PhD project focused on the optimization of electrode-electrolyte interfaces in next-generation Lithium batteries, and was part of the EU H2020 project *SOLIDIFY*. The results of the research during his PhD are presented in this thesis. He is currently working as a post-doctoral researcher in the SEE group under Prof. Wagemaker on the NEXTGEN-Hightech project concerning the production of 3D solid-state batteries.

